Resistance Welding of Advanced Materials and Micro Components

Friis, Kasper Storgaard

Publication date:
2010

Document Version
Publisher's PDF, also known as Version of record

Resistance Welding of Advanced Materials and Micro Components

by

Kasper Storgaard Friis

For fullfilment of the degree

Philosophiæ Doctor

Department of Mechanical Engineering

Technical University of Denmark

May 2010

Title
Resistance Welding of Advanced Materials and Micro Components

Manuscript by
M.Sc. Kasper Storgaard Friis

Examining Committee

Aff. Prof., PhD, M.Sc., Jens Klæstrup Kristensen
Project coordinator
Division of Materials and Welding
FORCE Technology
Park Allé 345
DK-2605 Brøndby
Denmark

Dr. Norbert Joseph Link
Professor
Technische Informatik und Embedded Systems
Karlsruhe University of Applied Sciences
Moltkestraße 30
76133 Karlsruhe
Germany

Dr.-Ing. Karen Pantleon
Associate Professor
Department of Mechanical Engineering
Technical University of Denmark
Kemitorvet, Building 204
DK-2800 Kongens Lyngby
Denmark

DTU Mechanical Engineering
Section of Manufacturing Engineering
Technical University of Denmark

Produtionstorvet
Bygning 427S
DK-2800 Kgs. Lyngby
Denmark

www.me.mek.dtu.dk
Tel: (+45) 45 25 47 63
Fax: (+45) 45 93 01 90

Category:	PhD dissertation
Version:	1. edition
ISBN:	978-87-89502-92-2
Printed:	2010
Printed by:	Rosendahls - Schultz Grafisk

| Layout: | By Kasper Storgaard Friis using LaTeX and the memoir class. Graphics made with GnuPlot version 4.2(4) and Microsoft Visio 2003. |

Abstract

With the use of the Finite Element Method it has become possible to analyse and better understand complex physical processes such as the resistance welding by numerical simulation. However, simulation of resistance welding is a very complex matter due to the strong interaction between mechanical, thermal, electrical and metallurgical effects all significantly influencing the process. Modelling is further complicated when down-scaling the process for welding micro components or when welding new advanced high strength steels in the automotive industry. The current project deals with three main themes aimed at improving the understanding of resistance welding for increasing the accuracy of numerical simulation of the process. Firstly methods for measuring and modelling mechanical and electrical properties at a wide range of temperatures is investigated, and especially the electrical contact resistance is addressed both theoretically and experimentally. Secondly the consequences of downscaling the process is investigated experimentally and discussed in relation to simulation of the process. Finally resistance welding of advanced high strength steels is addressed aimed at improving the simulation of the final weld properties. The temperature dependent material rheology of different advanced high strength steels and other materials, often resistance welded, were measured using hot tensile testing and hot compression testing. It is found that the Hollomon equation is capable of modelling material rheology at discrete temperatures with sufficient accuracy. Investigation of theoretical contact resistance models revealed that most models build on the classic theory by Greenwood and Holm. However, extensive simplifications and assumptions raise questions regarding the theoretical foundation of the models. Experimental measurements of contact resistance was performed on a Gleeble 1500 system, and the measurements revealed that surface hardness and film resistance interacts with the effect of pressure on the contact resistance. Numerical simulation of downscaled joints introduce problems not observed for large scale welding. Especially the relatively small electrode force and the formation of the actual contact area is found to cause discrepancies in simulation of micro spot welding, as well as in micro welding of joints of complex geometry where simulation of the collapse of the geometric projections presented problems. Simulation of two- and three sheet spot welding of advanced high strength steels DP600 and TRIP700 did generally agree well with experimental observations. Microstructure characterisation revealed that martensite was the main constituent in the final weld. By using empirical formulae by Blondeau et al. predicting martensite hardness, and a proposed average volume weighted material composition function, the predicted post weld hardness corresponded well with experimental observations.

Resume

Ved at benytte Finite Element metoden er det via numerisk simulering blevet muligt i langt højere grad at kunne analysere og forstå komplekse processer som modstandssvejsning. Grundet den stærke interaktion mellem mekaniske, termiske, elektriske og metallurgiske fænomener, er simulering af modstands-svejsning yderst kompleks. Modelleringen er yderligere kompliceret i forbindelse med nedskalering og svejsning af mikro komponenter samt ved svejsning af nye avancerede materialer så som højstyrkestål til bilindustrien. Nærværende projekt omhandler tre temaer og har til formål at øge forståelsen af modstandssvejsning med henblik på at forbedre modellering og simulering af processen. Først undersøges metoder for måling af materialers mekaniske og elektriske egenskaber ved en bred vifte af temperaturer. Herunder undersøges specielt kontaktmodstand både teoretisk og eksperimentelt. Derefter omhandler projektet konsekvenserne af nedskalering af processen i relation til simulering, og til sidst fokuseres på svejsning af højstyrkestål med henblik på at forbedre modelleringen af den færdige svejsnings mekaniske egenskaber. Den temperatur- og tøjningsafhængige flydespænding af forskellige højstyrkestål samt af andre ofte anvendte materialer er blevet målt ved brug af varm-trækprøvning og varm-kompressionstest. Det blev fundet, at Hollomon's ligning er tilstrækkelige til at beskrive materialernes plastiske opførsel ved udvalgte temperaturer. En litteratur-undersøgelse af kontaktmodstand afslører, at de fleste modeller bygger på de klassiske teorier af Greenwood og Holm. Omfattende simplificeringer i udledningen af nyere modeller stiller dog spørgsmålstegn ved det teoretiske fundament bag modellerne. Eksperimentelle undersøgelser af kontaktmodstand er gennemført på et Gleeble 1500 system. Målingerne viser, at overflade hårdhed og elektrisk modstand af overfladefilm interagerer med effekten af kontakttrykket på kontaktmodstanden. Numerisk simulering af nedskalerede svejsninger introducerer problemer, der ikke ses ved normal størrelse. Specielt den lave elektrodekraft og etableringen af det egentlige kontaktareal blev identificeret som problematisk ved simulering af mikrosvejsninger. Derudover viser forsøg, at simuleringen af det mekaniske kollaps af projektionen i trådsvejsning er utilstrækkelig. Simulering af punktsvejsning af to- og trelags højstyrkestål viser generelt god overensstemmelse med eksperimentelle forsøg. Karakterisering af mikrostrukturen af svejsningerne afslører, at martensit er den dominerende fase. Ved brug af empiriske formler af Blondeau et al. til forudsigelse af hårdheden af martensit, samt en foreslået funktion til udregning af det gennemsnitlige legeringsindhold, vises det, hvorledes hårdheden af svejsningerne kan forudsiges.

to my daughter
Alison

Contents

Preface

This thesis is submitted in partial fulfilment of the requirements for obtaining the degree of PhD at the Department of Mechanical Engineering at the Technical University of Denmark (DTU). The project is part of the INNOJoint project and has been carried out from March 2007 until February 2010. The supervisors of the project has been Prof. Niels Bay and Prof. Marcel A.J. Somers from the Department of Mechanical Engineering.

The creation of this thesis and the entire course of events leading to the completion of this PhD project has been a very educational experience for me. I have learnt a lot about myself, about research, and the life in the academic community, and of course a lot about resistance welding. It is not until now, standing at the very end of the project period, that I have come to realise what a PhD-project is actually all about. I find myself thinking: *"If only I had known this from the beginning, then I would have done things quite differently..."* However, I choose to take this as a good sign indicating that I have fulfilled the overall objective of the PhD process - to learn how to run a research project.

I would like to extent my heartfelt thanks to my closest family - especially my wonderful wife Ann-Katrine, who gave me a well needed perspective on the project and helped me keep my spirits up in periods of hard time and frustration - and without whom I would most likely have lost my touch on reality.

Kasper Storgaard Friis

Kongens Lyngby, May 31st 2010

Acknowledgements

First of all the project supervisors Prof. Marcel A.J. Somers and Prof. Niels Bay are thanked for all the great help and the pleasant collaboration during the course of the project.

The experimental work at the DIMEG department in Padova, Italy, was conducted during a four week stay in June 2008. In this context the author would like to thank Prof. Stefania Bruschi, Ing. Silvio Fanini, Ing. Andrea Ghiotti and Ing. Daniele Pellegrini. The experimental and theoretical work regarding micro welding of stainless steel wire to a block was conducted at the Center for Advanced Materials Joining at the University of Waterloo, Ontario, Canada. In this context the author would like to express his heartfelt gratitude to Prof. Norman Y. Zhou for the invitation. Furthermore M.Sc. Ibraheem Khan is thanked for his great help, good collaboration and fruitful discussions.

At DTU the author would like to acknowledge the pleasant collaboration with M.Sc. Trine Lomholt regarding the microstructural characterisation as well as PhD Kim Lau Nielsen for the very helpful sparring. Steffen Munch Jensen is thanked for his large help in teaching, preparing and helping with microscopy and hardness measurements. Assoc. Prof. Chresten Træholt is acknowledged for his help with the many electrical issues in the project. Furthermore, thanks to M.Sc. Peter Søe Nielsen and PhD Martin Skjødt for support and collegial advice during the project. The author has had a great collaboration with many students during the course of the project, and much of their work has been very useful for the project. Many thanks to Kim Richardt Pedersen, Anders Harthøj, Michael Kjeldal Jensen, Anders Madsen and especially to Søren Giversen for his large effort in the experimental work regarding measurements of electric resistance. Furthermore the expert help with hand polishing of mounted samples by Sui Kei Tang and Billy Tam is highly appreciated.

The companies SSAB (represented by Sven Erik Hörnström) and ThyssenKrupp are given many thanks for supplying the advanced high strength steels used in the project. Furthermore Swantec ApS (represented by Wenqi Zhang) is thanked for supplying the licens for the numerical welding software SORPAS and for useful input throughout the project. Regarding the financials the author would like to express his gratitude to the Danish Research Council for funding this PhD and to the Royal Danish Academy of Sciences and Letters for financial support to travel expenses during the project.

Nomenclature

α	The Holm radius	$[mm]$
$\bar{\epsilon}$	Equivalent strain	[−]
$\bar{\epsilon}_{\text{pre}}$	Material equivalent pre-strain	[−]
$\bar{\sigma}$	Equivalent stress	[MPa]
Δd	Incremental anvil displacement	[mm]
Δh	Increment in height	[mm]
Δh_{th}	Thermal expansion	[mm]
Δt	Incremental time step	[s]
$\dot{\epsilon}$	Strain rate	[−]
$\dot{h}$	Speed of change of height	[mm/s]
ϵ_h	Strain in height direction	[−]
ϵ_l	Strain in length direction	[−]
ϵ_t	Strain in thickness direction	[−]
ϵ_w	Strain in width direction	[−]
η	Contacting asperity density	$[\text{mm}^{-2}]$
$\frac{\mathrm{d}\rho}{\mathrm{d}T}$	Gradient of resistivity with respect to temperature	$[\mu\Omega\text{m}/^{\circ}\text{C}]$
$\frac{\mathrm{d}I}{\mathrm{d}t}$	Gradient of the current	[A/s]
κ	Thermal expansion coefficient	$[(^{\circ}\text{C})^{-1}]$
λL	Camera constant	$[\text{nm}^2]$
k	The shear flow stress	[MPa]
μ_0	The magnetic permeability of vacuum	[Tm/A]
Φ_B	Magnetic Flux	$[\text{Tm}^2]$
Φ_{BES}	Voltage drop from electrode interface to sheet measurement point	[V]
Φ_{BE}	Voltage drop across bulk of electrode	[V]
Φ_{BSS}	Voltage drop from sheet measurement point to sheet interface	[V]

Φ_{IES}	Voltage drop across electrode to sheet interface	[V]
Φ_{ISS}	Voltage drop across sheet to sheet interface	[V]
Φ_e	Offset error voltage	[V]
Φ_{ij}	Voltage drop from i to j	[V]
ρ	Resistivity	[$\mu\Omega$m]
ρ_1,ρ_2	Resistivity of contacting materials 1 and 2	[$\mu\Omega$m]
ρ_f	Film resistivity	[$\mu\Omega$m]
σ_1	First principal stress	[MPa]
σ_{s_soft}	Flow stress of the softest material in contact	[mm^2]
dQ	Generated heat	[J]
dt	Infinitesimal time increment	[s]
d$\mathbf{A}$	Infinitesimal area element of the open circuit	[m^2]
d$\mathbf{l}$	Infinitesimal length element of the conductor	[m]
ε_m	Electromotive force	[V]
$\mathbf{B}$	Magnetic field	Tesla [T]
$\mathbf{r}$	Vector from conductor to point P in space	[m]
A	Actual cross sectional area	[mm^2]
a	(Chapt. 7) Lattice parameter	[nm]
a	(Chapt. 4) Radius of contact spot	[mm]
A_0	Initial/nominal cross section area, or apparent area of contact	[mm^2]
A_b	Load bearing area or actual/real area of contact	[mm^2]
$Ac1$	Austenite initiation temperature	[°C]
$Ac3$	Austenite finish temperature	[°C]
$Au\%$	Percent austenization of microstructure	[−]
b	Width of open circuit	[m]
c	(Chapt. 7) Lattice parameter	[nm]
c	(Chapt. 3) Length of open circuit	[m]
d_0	Total displacement of anvils	[mm]
d_c	Sheet to sheet contact area diameter	[mm]

d_i	Lattice spacing of the atomic planes	[nm]
$d_m(F)$	Elastic compression of machine	[mm]
d_t	Initial electrode tip diameter	[mm]
D_w	Approximate diameter resulting in 10% increase in resistance	[mm]
F	(Chapt. 6) Force	[kp = 9.81N]
F	Force	[N]
f	(Chapt. 4) Fraction of real contact area	[−]
f	(Chapt. 3) Current frequency	[s^{-1}]
h	Actual height	[mm]
h_0	Initial height	[mm]
I	Electric current	[A = C/s]
$I_{\max}$	Peak current	[A]
K	Strength coefficient ($\sigma = K\epsilon^n$)	[MPa]
K_{err}	Standard error of model coefficient	[MPa]
L	(Chapt. 5) Induction coefficient	[V]
L	(Chapt. 3)Length of resistor	[m]
l	Actual length	[mm]
l_0	Initial length	[mm]
m	Strain rate exponent	[−]
M_e	Martensite finish temperature	[°C]
M_s	Martensite starting temperature	[°C]
m_X	The mass of element X	[kg]
n	(Chapt. 4)Exponent of Contact resistance decrease and number of contact spots	[−]
n	(Chapt. 2) Exponent of Hardening	[−]
N^2	Total number of possible contacts [76]	[−]
n_c	Number of clusters	[−]
N_X	Number of atoms of element X	[−]
n_X	The mol of an element X	[mol]

N_{A}	Avogadro's number	$[\mathrm{mol}^{-1}]$
n_{err}	Standard error of model coefficient	$[-]$
R	Electric resistance	$[\Omega = \mathrm{V/A}]$
r_0	Radius of conductor	[m]
R_1	Resistance component = R_{12}	$[\Omega]$
R_2	Resistance component = R_{23}	$[\Omega]$
R_3	Resistance component = R_{34}	$[\Omega]$
r_i	Spot radius	[nm]
R_0	Contact resistance fitting parameter	$[\Omega]$
R_{BS}	Sheet bulk resistance included in measurement	$[\Omega]$
R_{CR}	Contact resistance	$[\mu\Omega\mathrm{m}]$
R_{c}	Constriction resistance	$[\mu\Omega\mathrm{m}]$
R_{f}	Film resistance	$[\mu\Omega\mathrm{m}]$
s_{ij}	The distance between the i'th and j'th contact spot	mm
t	Actual thickness	[mm]
t_0	Initial thickness	[mm]
t_r	Cooling rate at 700°C	[°C/s]
t_{c}	Contact layer thickness	[mm]
U	Voltage drop	$[\mathrm{V = J/C}]$
$U_{I_{\max}}$	Voltage at peak current	[V]
V	Volume	$[\mathrm{mm}^3]$
w	Actual width	[mm]
w_0	Initial width	[mm]
W_c	Initial contact area width	[mm]
X_{C}^r	Atomic percent of C atoms	$[-]$
AHSS	Advanced High Strength Steels	$[-]$
Al6060	Aluminium 6060 T6 alloy	$[-]$
ANOVA	Analysis of Variance	$[-]$
B	Factor: Size of bottom electrode	$[-]$

BCC	Body Centered Cubic	[–]
BCT	Body Centered Tetragonal	[–]
BF	Factor interaction between B and F	[–]
BFI	Factor interaction between B, F and I	[–]
BFT	Factor interaction between B, F and T	[–]
BFTI	Factor interaction between B, F, T and I	[–]
BI	Factor interaction between B and I	[–]
BM	Base Metal	[–]
BT	Factor interaction between B and T	[–]
CE	Carbon Equivalent	[–]
CR	Contact Resistance (electrical)	[–]
DAQ	Data Acquisition	[–]
DC06	Low carbon DC06 steel	[–]
DF	Degree of Freedom	[–]
DP600	Dual Phase 600 steel	[–]
F	Factor: Weld Force	[–]
F_0	The test statistic	[–]
FCC	Face Centered Cubic	[–]
FI	Factor interaction between F and I	[–]
FT	Factor interaction between F and T	[–]
FTI	Factor interaction between F, T and I	[–]
FZ	Fusion Zone	[–]
HAZ	Heat Affected Zone	[–]
HFI	High Frequency Inverter	[–]
I	Factor: Weld Current	[–]
JBF	Joint Breaking Force	[–]
MS	Mean Sum of Squares	[–]
Ni200	Nickel 200 alloy	[–]
P	The power or probability that the null hypothesis is true	[–]

R	Correlation coefficient of model fitting	[−]
S235JR	Mild steel S235JR alloy	[−]
SS	Sum of Squares	[−]
SS316	Stainless Steel AISI 316 alloy	[−]
T	Factor: Number of weld cycles	[−]
TI	Factor interaction between T and I	[−]
TRIP700	Transformation Induced Plasticity (700) steel	[−]
WN	Weld Nugget	[−]

Chapter 1

Introduction

In this chapter the motivation for the project and the problem formulation is presented. Then the background of the project is presented by firstly giving an overview of resistance welding in general. Then modelling of resistance welding is discussed and put into context with current research in the field. Finally the actual focus of the project is detailed and argued.

1.1 Project Motivation

Resistance welding is a widely applied assembly process in industrial production. The process is more than 100 years old as some of the first patents were made around 1895-1900 by Elihu Thompson [1]. The process is used extensively in industry today, because it is extremely fast, cost-effective, and easy to automate, and it gives high strength joints with good reliability. The principle of resistance welding in its simplest form is to load the workpieces that are to be joined between two electrodes and to generate heat by passing electrical current through the workpieces. The heat softens and eventually melts the material at the interface between the workpieces subsequently forming a joint at the interface.

Today resistance welding, and especially spot welding, is used in a wide range of manufacturing companies. Especially the automotive and aviation industry make extensive use of the process to assemble cars and aeroplanes. Both industries have high safety requirements to their products and strict quality control procedures that put high demands on the quality and reliability of the welding process. These industries therefore have focus on the resistance welding process and how to optimise the use of it. Materials such as low carbon steels, high strength steels and aluminium alloys are joined by resistance welding in these industries.

Another growing area where resistance welding is finding application is in the micro manufacturing industry. This can partly be credited to the fact that the process equipment is easily downscaled for making micro joints. The heat input in resistance welding is generated internally in the materials, which is in contrast to many other welding processes where the heat is externally applied. In theory this makes it possible to weld joints designed with limited accessibility, which is often the case in compact micro components. Furthermore many bio-compatible materials such as titanium and nickel-free stainless steels are readily welded with resistance welding [2]. However, the downscaling does introduce new problems especially regarding control of tolerances in both equipment and workpieces, which can have very large influence on the outcome of the process.

Although in principle a relatively simple process, resistance welding is governed by a great number of variables such as geometry, material properties of parts and electrodes, as well as controllable and uncontrollable process parameters. Furthermore, innovative use of the resistance welding process for welding new and advanced materials as well as complex geometries and micro components is challenging and often involves new and unforeseen problems. This implies that the industrial use of resistance welding for complex joints relies on a great deal of experience and extensive empirical investigations which will often involve expensive and time consuming experimentation. Any knowledge concerning the robustness of a process is valuable to assure the quality of the production, but such knowledge can be costly to acquire by experimental investigations due to the large number of influencing parameters. This implies, that there is a large interest in investigating and to better understand the resistance welding process in general as well as in relation to its use with new and advanced materials and complex joints.

The resistance welding process has several aspects which makes it challenging to analyse scientifically, especially the interaction between the many different physical phenomena. It is of course possible to measure global process parameters such as electrode force and displacement as well as the electrical current and voltage signals during welding. Combined with metallurgical and mechanical studies of the final weld, these global measurements can be used to indirectly estimate local parameters such as current density, contact pressure and peak temperature, which are critical for a full understanding of the process. However, analytical analysis are restricted in the sense that they apply significant simplifications where critical parameters such as electrode and workpiece contact areas and/or electrical and thermal properties and boundary conditions are assumed constant. This then limits the accuracy of the results and the extent of the conclusions obtained in this way.

The use of the Finite Element Method (FEM) in computer software has opened up the possibility to analyse and better understand complex physical processes - as

resistance welding - using numerical simulation. By combining electrical, thermal, metallurgical and mechanical models in FEM-software, it is possible to predict and estimate the process parameters quite accurately saving comprehensive experimental tests and making it is possible to *see into* the weld during the process. This visually gives a better understanding of the weld development. Not only does numerical simulation allow us to estimate the distribution of temperature, current density, and stresses and strains throughout the weld development, it is also a quick and easy tool for optimisation and exploration of new weld configurations compared to costly experimental investigations. The effect of changing geometry and/or materials can be estimated quickly and easily and process parameters can be optimised off-line to provide the strongest weld, longest service life of the electrodes etc. Needless to say simulation has great potential for improving the understanding, as well as analysis and optimisation of resistance welding for research and industrial use [3].

As is the case with most FE-modelling, the simulation of resistance welding is by no means a trivial matter. The heat is generated by an electrical current and the electrodes both cool and mechanically deform the specimens. This dynamically changes especially the contact conditions during the process which implies, that in order to simulate resistance welding the FE-model should preferably couple the four models: an electrical, thermal, mechanical and metallurgical model [3–6]. This entails that the numerical software becomes complex, and both programming and building the model becomes time-consuming. Another big challenge in simulation of resistance welding is the contact problems arising in the contact areas between the electrode and the workpiece and between the workpieces themselves. Not only does mechanical contact pose strong challenges programming-wise, but the actual physical modelling of the dynamic electrical and thermal properties of contact pairs is a very complex area influenced by many variables and material specific parameters [3, 5, 7, 8]. Therefore, detailed knowledge of both the mechanical and electrical properties of the materials at a wide range of temperatures is necessary in order to simulate resistance welding with precise results. However, obtaining material data at elevated temperatures is often very troublesome as this data is not readily available - especially not for new and advanced materials - and because experimental measurements can be very costly and time-consuming. There are therefore several challenges, which are necessary to address in order to fully exploit the potentials in numerical simulation of resistance welding.

The framework program INNOJoint, which is funded by the Danish Research Council, was initiated in 2006 and is a larger research program with a total budget of more than 19 million DDK or €2.5 million euro. The program deals with the two welding processes: Friction Stir Welding and Resistance Welding. The overall aim of INNOJoint is, as stated in the application, to develop advanced numerical

models applicable for simulation of resistance welding (and friction stir welding) aiming at possible optimisation of the entire processes. Focus will be set on overall numerical modelling strategies specific for each of the two welding processes as well as detailed investigations of micro-structure, mechanical properties, strength and weld quality. The INNOJoint project is a cross-disciplinary project involving six different partners, five DTU research units and a private company. The project includes 6 PhD-projects and 4 Post.Docs. The current project is one of the PhD-projects within the frame of the INNOJoint program.

1.2 Problem Formulation

The overall objective of the present project is to investigate the characteristics and application of resistance welding for joining advanced materials and micro components. The research should be focused on the material aspects related to the size and geometry of parts and electrodes as well as the properties of materials before and after welding. The overall problem formulation of the project is as follows:

> How are material properties modelled in a process technological context during and after the resistance welding process for simulation of resistance welding of advanced materials and micro components?

The project therefore focus on combining process technological investigations with investigations of material characteristics and behaviour, aiming at developing models and strategies for numerical modelling of resistance welding. To answer the problem formulation the project has been divided into three main parts or themes. Under each theme the following working questions are formulated.

- **Part 1. Materials Mechanical and Electrical Properties**
  - How can the materials mechanical and electrical properties be experimentally measured and modelled?
  - What determines the electrical contact resistance of an interface and how can it be modelled?
- **Part 2. Micro Resistance Welding**
  - How can contact resistance be measured in micro resistance welding and what parameters influences, and is influenced by, the contact resistance?
  - What characterises micro resistance welding of the geometrically complex joint of a thin wire to a large block, and how is it numerically simulated?

- **Part 3. Advanced High Strength Steels**
  - What microstructural components does welds of AHSS comprise of and what methods can be used to characterise them?
  - What is the weldability of complex 3-sheet joints of AHSS and how can they be simulated?
  - How can post-weld properties of welds of AHSS be modelled?

In the following sections the background for the choice of problem formulation and working questions are clarified. First an introduction to resistance welding in general is given. Hereafter the modelling of resistance welding is presented and finally the project focus will be delimited based on a discussion of challenges in modelling of resistance welding as well as on previously published research in this area.

1.3 Resistance Welding

Resistance welding is a term covering the types of welding processes where the workpieces to be joined are heated by passing an electric current through them thereby using the electric resistance of the materials to generate heat. If a current $I(t)$ is running in an electric conductor having the total resistance $R(t)$ at time t then the current will cause the heat $\mathrm{d}Q(t)$ to be dissipated in the conductor according to Joules Laws [9] expressed on differential form in equation (1.1).

$$\mathrm{d}Q(t) = R(t)\, I^2(t)\, \mathrm{d}t \tag{1.1}$$

This is the governing equation for the heat generation in the resistance welding process.

The most common variant of the resistance welding processes is the spot welding process used to join sheet metal workpieces in a lap-joint, as illustrated in figure 1.1 on page 6, where two round copper electrodes clamp down on the two overlapping metal sheets to be joined. The electrodes have three primary functions: to conduct the current to the workpieces, to provide efficient cooling to the workpieces for better control of the heat development during the process, and finally to keep contact between the two metals during the welding process by pressing the workpieces together with a sufficient force. The applied current will heat up the specimens due to their electrical resistance following the relation given in equation (1.1). Besides the electric bulk resistance of the electrodes and workpieces the different *interfaces* restrict current flow and thereby create electrical contact resistance at the interfaces between electrodes and workpieces and between the two workpieces. Furthermore, many metal surfaces develop surface layers of oxides and contaminant

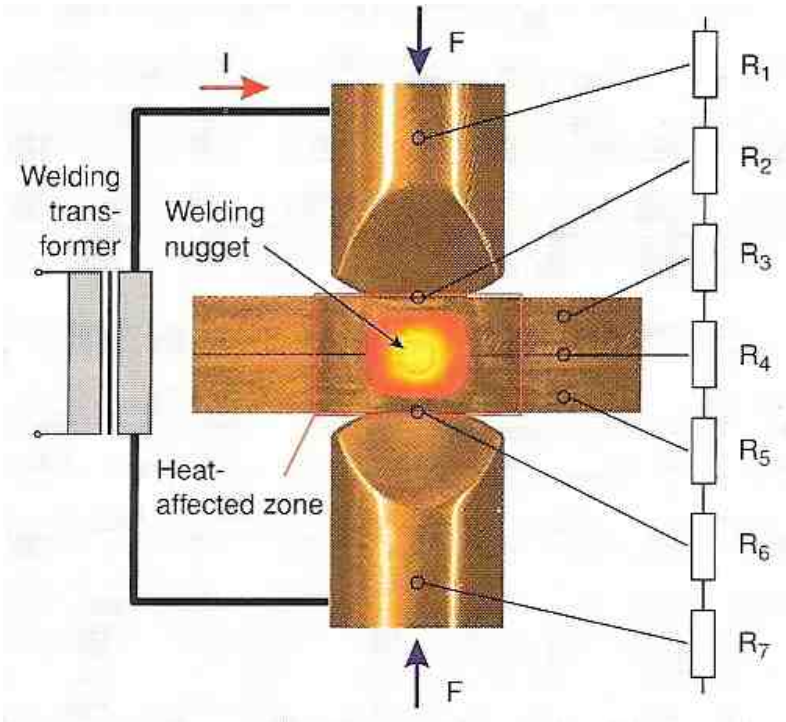

Figure 1.1: Resistance spot welding [10]

films on the free surfaces exposed to the atmosphere. Such surface layers often have a reduced conductivity compared to the base metal and the resistance of the film will add to the constriction resistance and help increase the total resistance of the interface. The contact resistance helps to concentrate heat generation at the interface where the joint is made. If the current is strong enough the dissipated heat will eventually melt the metal at the joint interface between the workpieces and produce a molten zone. The thermal expansion associated with the solid to liquid phase change would cause metal from the weld zone to be expelled from the molten zone if not for the compressive force from the electrodes that works to contain the weld-pool within the workpieces.

In figure 1.2 a cross section of a spot weld identifying the typical weld zones is shown. The centre of the weld is normally called the *fusion zone* (FZ) or simply the *weld nugget* (NG). The solidification structure of the dendrite grains in this area show that this area has been melted and subsequently re-solidified during the process creating a strong bond between the two specimens. Next to the FZ the heat affected zone or HAZ has experienced high temperatures during the process which both physically and visually affect the microstructure as seen on the figure. In the base metal (BM) outside the HAZ the temperature has not been high enough to initiate any changes in the material and the material in this area is thus unaffected by the welding process.

1.3.1 Welding Sequence

A weld sequence for a normal spot weld is schematically shown in figure 1.3. Firstly the specimens are inserted between the electrodes or the electrodes are moved and positioned on either side of the workpieces. In the squeeze stage the electrodes clamp down on the specimens building up the weld force improving the electrical connection to the workpieces. In the next stage - the welding stage - the welding current is turned on which results in electric heat generation and heating of the specimens. If the heat input is high enough the material melts at the interfaces. In the next stage the current is turned off but the electrode force is kept on, still holding the specimens and thereby increasing the cooling rate of the weld. The cooling rate can be an important factor in determining the resulting microstructure and implicitly the mechanical properties of the final weld. After the holding stage the workpieces are released and the weld is completed.

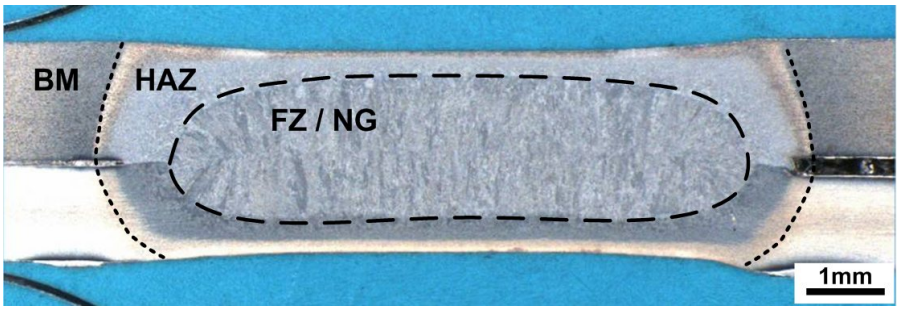

Figure 1.2: Resistance spot weld of Dual Phase steel (upper) to TRIP steel (lower) identifying zones of base metal (BM), heat affected zone (HAZ) and fusion zone / nugget (FZ/NG)

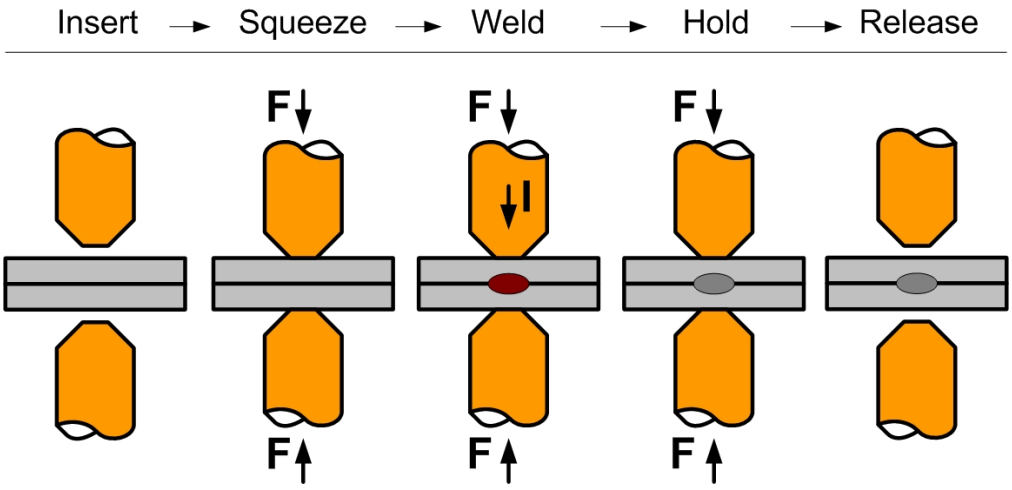

Figure 1.3: Welding sequence for a normal spot weld

1.3.2 Process Variants

The most common and well-known variant of the resistance welding processes is the already mentioned *spot* welding process, but another common and often used variant is the resistance *projection* welding process. In projection welding the current and hereby the heat generation is concentrated in the workpieces not by the shape and position of the electrodes, as is the case in spot welding, but by so-called projections in the geometry of the workpieces which confines the contact area between the specimens thereby significantly increasing the local current density and heat generation in these areas. Two examples of projection welds are shown in figure 1.4. Due to the localised contact area the surface layer in the contact region often experiences extremely fast heating and melting. The high electrode force then causes the softened projection to mechanically collapse. The molten surface layer will then be expelled from the contact region removing any oxides and surface contaminants at the interface. This results in almost pure metal to metal contact between the two specimens which greatly improves the bonding conditions at the interface. In fact, due to the removal of oxides and contaminants, it becomes possible to join materials which are otherwise very difficult to join by other welding methods, such as aluminium or CuSn to carbon rich steels [11].

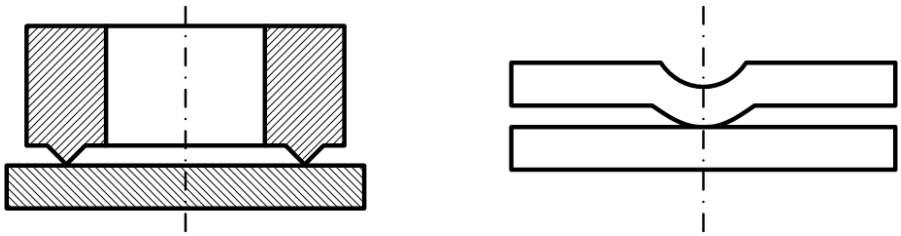

Figure 1.4: Examples on projection welding geometries

Besides spot and projection welding several other resistance welding processes exist, such as resistance butt welding, seam welding and percussion welding. Common for all these processes is that they utilise electrical resistance heating combined with high surface pressure as primary bonding mechanism. A description of these can be found in the Welding Handbook [12]

1.3.3 Factors Influencing the Resistance Welding Process

The most important factor influencing resistance welding is the welding current which influences the heat generation by the current squared, as can be seen from equation (1.1). Too low a current will not generate enough heat for bonding or melting of the materials while a too strong current will cause excessive heating resulting in metal expulsions and accelerated electrode wear. There are several

different types of power supplies available for resistance welding. In figure 1.5 is shown an overview of typical welding currents from some common types of power supplies for resistance welding (Alternating Current (AC), Direct Current (DC), Capacitor Discharge (CD) and High Frequency Inverter (HF-I)). The type of welding current can have large influence on the weld development and should therefore be considered with care [13].

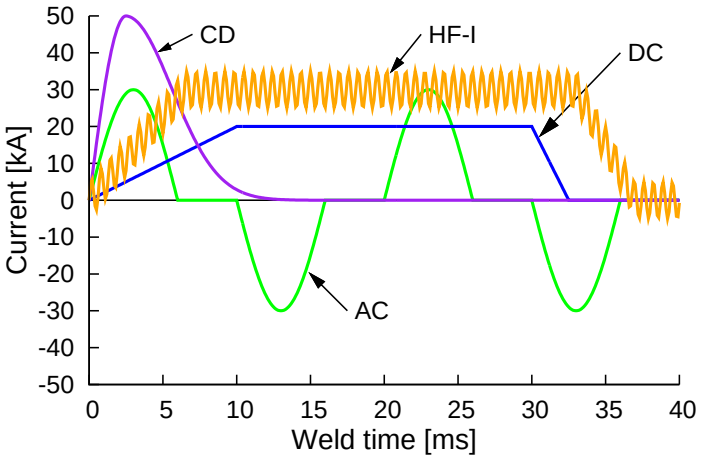

Figure 1.5: Different types of welding currents

The total heat generation governed by equation (1.1) is depending on the weld time. Although the weld current and the electrical resistance is varying with time, the total heat generation is approximately proportional to the weld time. Due to continuous cooling of the weld zone to the base metal and to the electrodes a certain minimum weld time is needed to produce a weld. After some weld time, if the current is not too high, the process will reach a close-to steady state situation where the internal heating of the weld equals the heat loss due to cooling. When reaching this steady state the weld zone will not expand further with time. Knowing this, it becomes clear, that if the welding current is too low to produce a weld, simply increasing weld time will have no effect.

The weld force affects the process by decreasing electric contact resistance at the interfaces, increasing contact area and increasing cooling by increased heat conduction through the electrodes. If the weld force is too low the contact resistance might be very high causing a rapid heat generation at the interfaces resulting in expulsion or splash, which can potentially decrease the quality of the weld. In projection welding the electrode force causes the projection to collapse and thereby forms the bond. The weld force is therefore crucial in determining the final weld result.

The electrical, thermal and mechanical properties of the materials are also highly influencing the outcome of the process. Especially the resistivity, heat conductivity, and the electrical and thermal contact resistance are to a large degree determining the heat generation and heat distribution in the weld. In projection welding the mechanical properties at a wide range of temperatures are determining the strength of the projections and when and how they collapse - thereby affecting the bond development. Surface coatings can greatly influence the electrical and thermal contact resistance and they can have a large negative effect on electrode life due to degradation of the electrode tip.

One of the final factors highly influencing the process, especially in projection welding, is the dynamic properties of the electrical and mechanical system of the welding machine. Thermal expansion and collapse of the projection requires dynamic movement of the electrodes. If there is a significant delay in the "follow-up" movement of the electrode system the force might increase or decrease unintentionally hereby changing the contact area and the contact resistance, which can affect the heat generation and the final weld result. Due to the fact that the machine dynamics are very difficult to measure and model, their influence is often disregarded.

1.4 Modelling of Resistance Welding

As mentioned earlier modelling of resistance welding is inherently a complex matter. During the process there is a strong interaction between mechanical, electrical, thermal and metallurgical effects. An overview of the different interactions is given in figure 1.6.

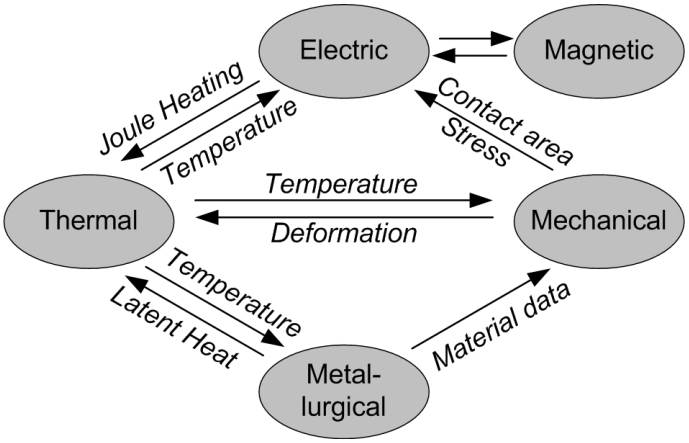

Figure 1.6: Overview of interactions of models in resistance welding (reproduced from Song [10])

As can be seen from the figure, the interactions are quite extensive when considering a complete description of the process. In an optimum model all these interactions would be included, but usually it is often necessary to disregard one or more interactions to simplify the problem.

Many authors have throughout the years made different attempts to model the resistance welding process almost entirely focusing on spot welding [4, 14–23]. As noticed by H.A. Nied [16] the modelling of resistance welding has primarily been concentrated on surface phenomena or heat transfer modelling. One of the earliest attempts to model resistance welding was made by Bentley et al. [14] who developed a heat conduction model of the spot welding process to predict the temperature distribution without considering the thermo-mechanical effects. His model was a linear axis-symmetric thermal model of the process and numerical results of the temperature distribution were obtained by solving the partial differential equation using the finite difference method [3]. The model gave some of the first approximations of the temperature distribution in spot welds, but as it neither considered thermo-mechanical effects, temperature-dependent thermal properties, nor contact resistance, the agreement with experimental results were not optimal. The effect of contact resistance was later included in the finite difference model by Rice and Funk [17] and Cho and Cho [15]. However, as augmented by H.A. Nied [16], one of the big shortcomings of the thermal finite difference model is that it does not consider the thermo-mechanical effects of electrode pressure on the size of the contact area at the faying surfaces. Nied was one of the first authors to propose a FE-model of the process using the commercial multipurpose FE-program ANSYS [1], which incorporated temperature dependent mechanical, thermal and electrical material properties in the model. The contact conditions were simulated using a boundary layer capable of simulating mechanical sliding of the surfaces as well as increased electrical and thermal contact resistance, however no exact details are given as to how this was achieved and which models were used. Nied [16] concluded that FE-modelling of resistance welding has great potential as an analytical tool to achieve a better understanding of the process.

Since the 1980's the use of the FE-method has been widely adopted in many scientific areas for analysing complex physical systems and processes. General purpose FE-software as ANSYS, ABAQUS and Comsol[2] has made finite element methods more readily available for researchers. However, although the mentioned commercial programs indeed are powerful tools for applying the finite element method, they are *multi-purpose* tools and are thus restricted by the fixed overall structure of the programs in this sense. As shown in figure 1.6 the large amount of interactions

[1] ANSYS, Ansys Inc. (http://www.ansys.com)

[2] ABAQUS, Dassault Systemes (http://www.simulia.com), COMSOL Multiphysics, COMSOL AB (http://www.comsol.com)

in resistance welding require a coupled electrical-thermal-mechanical-metallurgical model for optimal results, but this is often not possible in the general-purpose FE-packages [3]. Any process specific phenomena, such as the contact properties of the interfaces in resistance welding, are not standard options in multipurpose FE-software and therefore need to be added. The incorporation of such specific physical phenomena is then restricted to the structure and possibilities of the specific program used, but it could be done either by modifying user functions in the programs or by coupling external physical models to the simulation. In any case, modelling of resistance welding using commercial multipurpose FE-software can produce accurate simulations, but the procedure is time-consuming and restricted to specific weld problems.

In a response to the difficulties and shortcomings experienced in simulating resistance welding using general purpose FE-software, a few programs have been developed dedicated to simulating resistance welding. The best known and most widely used is the program SORPAS first developed at the Department of Mechanical Engineering, DTU and further developed and commercialised by the Danish company Swantec ApS[3]. The software is dedicated to and optimised for simulating resistance welding, and all essential physical models have been incorporated in the numerical code which is a coupled electrical-thermal-mechanical-metallurgical model. SORPAS is user-friendly and both modelling and the actual calculation can be done very fast and often more accurately compared to the general purpose FE-programs. Especially the contact modelling, which is a highly complex subject both modelling and programming-wise has been optimised in the dedicated software packages based on empirical data from research and industry. This helps to give software packages such as SORPAS clear advantages in modelling speed, simulation speed, and accuracy in simulation results which makes it an attractive tool for the resistance welding industry for development and optimisation. The main disadvantage of SORPAS is, that due to the build-in optimisation of the models in the program, the user has very limited possibilities to further change and optimise the models. Primarily the user has freedom to choose geometrical and material specific properties while the underlying physical models themselves are fixed in the program.

The frame of the present project dictates that an important task is to develop strategies for numerical simulation of the resistance welding process based on experimental investigations. The focus of the project is therefore not to develop and implement numerical code, but rather to use existing numerical software as a scientific tool in the project. For this reason SORPAS, the leading commercial FE-software for simulating resistance welding, will be the preferred choice when applying numerical procedures in the project. In the following sections specific

[3]Swantec ApS, http://www.swantec.com

topics regarding modelling of resistance welding will be presented and related to the aim and focus areas of the project.

1.4.1 Modelling Electrical Contact Conditions

One of the biggest challenges in resistance welding is the modelling of the electrical-thermal-mechanical contact conditions at the interface between the workpieces and between electrodes and workpieces. The contact conditions are essential in the resistance welding process as they are highly influencing the process dynamics. The contact area between workpieces and electrodes and at the faying surfaces between the workpieces are highly dependent on the load and the mechanical properties of the materials. The initial size and the development of the contact area has a large influence on the electrical and thermal properties of the interface during the process. Generally speaking, as the contact pressure increases the real contact area between the surfaces increases due to plastic deformation of the surface asperities resulting in the surfaces conforming to each other and breaking down thin surface films, thereby decreasing the electrical contact resistance. Greenwood [7] describes the, by now, classical theoretical contact theory originally developed by Holm [8] that correlates electric contact resistance to the size and number of micro contacts between surface asperities. Other authors have investigated the contact resistance with the purpose of modelling, and generally it is found that the contact resistance depends on the surface pressure p by either p^{-1} or $p^{-1/2}$ [24–26]. This will be explained in more detail in chapter 4 concerning modelling of contact resistance.

Mainly two methods for measuring contact resistance in resistance welding have been used in literature. One is the dynamic measurement of electrical contact resistance during spot welding of different materials, while the second method uses dedicated equipment that allows for a more controlled and static testing environment. As the resistance welding process is highly dynamic it is difficult to separate the effect of surface pressure and temperature on the measured contact resistance during the process itself. Therefore it becomes hard to model the contact resistance based on such dynamic measurement without making significant assumptions regarding temperature, temperature gradients and contact area. However, dynamic data can be valuable when verifying models and numerical simulations of the process.

Contact resistance measurements using dedicated equipment allow for individual control of the main factors influencing contact resistance: surface pressure, temperature and the condition of the surfaces in contact. This makes it possible to isolate the effect of these parameters and thereby to derive models suitable for the purpose of modelling of the entire process. Several authors (Sheppard [18], Vogler and Sheppard [25], Babu et al. [26], Rogeon et al. [27]) have constructed testing equip-

ment for measuring contact resistance. In all cases the pressure is applied using an axial loading system where the specimens can be heated by enclosing them, as well as part of the equipment, in an insulated heating furnace. The specimens are in this way heated to the desired temperature by heat conduction. Song [28] applies a different approach where a Gleeble-system is used to heat the specimens through resistance heating which allows for testing under very high temperature and load. Most commonly contact resistance measurements are done between two contacting specimens thereby measuring contact resistance across a single interface. Rogeon et al. [27] developed an alternative technique measuring across several identical interfaces in series by inserting a fixed number of specimens between the electrodes hereby amplifying the measurement signal. Attempts have been made to correlate the theoretical contact models described by Greenwood [7] to measured experimental data, unfortunately due to the complexity of the model limited success has been reported [25, 26, 28].

Despite attempts to describe the phenomenon of contact resistance theoretically and/or to derive empirical models based on various experimental methods, contact resistance in resistance welding remains an area which is not fully understood. Within the frame of this project it is desired to further investigate and model electrical contact resistance aimed for use in simulation of the entire process. Focus will initially be on developing and analysing the experimental method for measuring contact resistance which was initiated in a previous project at the department [10]. Furthermore, it will be investigated and discussed which approaches could be used for modelling of the contact resistance for simulation purposes.

1.4.2 Modelling of Bulk Material Properties

For the simulation of real processes, it is an almost self-evident fact that one should use realistic material properties. However, this fact is often neglected by researchers, because obtaining accurate and reliable material data can be time-consuming and troublesome. There is no guarantee that table values found in literature correspond to specific materials from other batches and possibly also different manufacturing plants. Especially the investigation of material data for elevated temperatures can be costly and sometimes very difficult. Applying accurate material data in any type of numerical simulation significantly increases the credibility of the simulation.

In resistance welding the material's electric, thermal, mechanical and metallurgical properties are all important for an accurate simulation of the process. Furthermore, the theoretical model by Greenwood [7] describing the electrical contact resistance of interfaces use the materials bulk electrical and mechanical properties as factors in the model. This implies, that not only does the knowledge of the material's elec-

trical and mechanical properties at a wide range of temperatures help to accurately describe electrical conductance and mechanical deformation of workpieces, it also allows for a much more accurate modelling of the electrical contact resistance at the faying surfaces.

Any experimental setup aimed at testing *mechanical* material properties must be able to heat the specimens to a desired temperature and keep them at that temperature during the test. The obvious way, but not necessarily the simplest way, is to encapsulate the test-specimens and the material testing equipment in a furnace, hereby heating the specimens by convection. This could be done with a standard tensile test or compression test where the specimens are closed inside a furnace allowing the anvils to move in the furnace hereby maintaining a constant temperature of the test-specimens during the test. In order not to damage the usually hardened anvils by the heat the maximum achievable temperature in this type of test setup is usually limited.

Another way of measuring mechanical strength at a wide range of temperatures is by the Gleeble system [29]. Usually the Gleeble system is used to perform standard tensile or compression tests while heating the specimens by resistance heating [28, 30, 31]. With this technique the heating can be concentrated in the specimens and not the tools. This type of heating is very fast and the maximum achievable temperatures are very high, often enough to actually melt the specimens. Using the Gleeble-compression test the stress-strain for a wide range of temperatures can be measured for a given material, provided that the material is available for making compression test samples. If the specific material only is available in sheet form other tests must be used, such as the tensile test. However, performing tensile tests on sheet samples at elevated temperatures necking initiates already at very low strains making it difficult to determine true values of the stress-strain relationship. Advanced techniques for performing tensile tests at elevated temperatures have been developed by Merklein et al. [30] and Turetta et al. [32], relying on optical measurements of the local strains during necking.

In order to have accurate electrical and mechanical materials data for simulation and modelling purposes, it is desired to measure the material properties of selected materials used in this project. The aim is to investigate different techniques for materials testing as well as the implementation of selected measuring techniques at the department.

1.4.3 Modelling of Micro Joining

The micro and small scale manufacturing industry is experiencing a large growth and the demand for reliable and effective joining processes for micro components

is increasing. Resistance welding has great potential to be used for micro joining purposes. It is obvious that precise tolerances are of increasing importance to the weld results, however the influence of downscaling on the process is still not fully understood, and the effect of the significant process parameters and their interaction with downscaling is crucial to know when simulating the process [2].

Some research has been carried out on investigating micro joining using resistance welding [2, 33–40]. Focus has been primarily on investigating the weldability of specific micro joints and/or materials and the effect of downscaling has been considered in relation to this. It is the aim of the present project to investigate the downscaling of the process in relation to the long-term goal to model the process on small scale. As the contact area and contact resistance are essential factors in modelling the process on small scale, the project will focus on the problems related to modelling contact area and contact resistance for micro resistance welding. Furthermore, in order to relate problems of micro welding to a practical example and to simulation of complex 3D problems, a more practical and industrial relevant problem of micro welding of fine wire to a block is addressed.

1.4.4 Strength of Welds

One of the obvious applications of modelling of resistance welding is the possibility to predict the actual strength of a weld based on especially the thermal history of the material in the weld zone and in the heat affected zone. Considering the strength of a resistance weld is often done by testing individual welds using standardised tests such as the peel or shear test [41, 42], or by fatigue testing one or several joints [43, 44]. The fracture mechanics and resulting strength of a resistance weld has been shown to be highly dependent on firstly the size and shape of the weld nugget and secondly on the hardness of the material in and around the nugget[45–51]. The hardness is of course highly dependent on the micro-structure which will be a product of the actual thermal history experienced by the material during the welding process. An important example of this is welding of Advanced High Strength Steels.

The ever rising demand for increasing fuel efficiency as well as increasing the safety requirements in the automotive industry has lead to the development of new materials such as the so-called Advanced High Strength Steels (AHSS). These steels offer an improved strength-to-weight ratio and their excellent mechanical formability makes them attractive in the manufacturing of cars. The AHSS-sheets are produced applying several heat treatments to custom-design the micro-structure of the steels, giving them their superior performance to regular steels. However, resistance welding of AHSS will affect the materials due to the elevated temperature and subsequent fast cooling, which will significantly alter the micro-structure of the

steels in and around the joint. Due to the usually relatively high carbon content of the AHSS the fusion and heat affected zone often experience a large increase in material hardness [45, 47, 48]. This can have consequences for the mechanical performance of the welds that might experience problems due to the high hardness of the weld nugget [45]. In the present project the aim is to investigate weldability and strength of selected AHSS and low carbon steels. Furthermore, the correlation between the alloy composition, the heat treatment of the steels during welding and the resulting micro-structure and hardness of the nugget is investigated for possibly modelling of the post weld hardness of the joints.

1.5 Delimitation

Only measurements of mechanical and electrical material properties are considered in the project. The thermal contact resistance and bulk thermal conductivities are also essential parameters in modelling of resistance welding, but they are not addressed in this work. The choice of materials used in the project is based on the following: For the welding of micro components were chosen stainless steel (AISI 316) and pure nickel (Nickel 200), which are both commonly applied in micro products [2]. The two materials are both readily available in different forms (foil, rod, wire) and sizes and they have significantly different material properties regarding electrical properties and weldability in resistance welding. For the bulk material properties testing and electric contact resistance measurements it is also chosen to use stainless steel 316 and Nickel 200 and to include aluminium 6060 T6 and mild steel S235JR. These four materials represent a wide range of common materials with significantly different combinations of material properties. For welding of advanced high strength steels TRIP700, DP600 and HSLA are chosen, because they represent three different types of high strength steels with different compositions and manufacturing procedures. The exact steel grades are chosen primarily based on availability from the suppliers.

1.6 Overview of Thesis

The thesis is subdivided into three main parts. The first part focuses on the experimental and theoretical investigation of how to model materials mechanical and electrical properties for use in simulation of resistance welding. This section is further divided into the investigations of bulk material properties and a chapter concerning contact resistance measurements. The second part deals with micro resistance welding and focus on two areas and their relation to modelling of the process: investigation of contact resistance in micro spot welding of foils and investigation of welding of thin stainless steel wire to a large block. The third part deals

with normal scale spot welding of high strength steels. Firstly the characterisation of the microstructure of welds in AHSS is described. Secondly an experimental and numerical investigation of the welding of complex three layer spot welding of AHSS is addressed, and finally an experimental and theoretical investigation of modelling of the post weld hardness based on thermal history and alloy composition is treated.

Chapter 2

Modelling of Material Rheology

In resistance welding the workpiece materials experience temperatures ranging from room temperature to above the liquidus temperature. Because the workpieces are pressed together with a considerable force from the electrodes the workpieces plastically deform during the process. In projection welding the deformation of the projection is governing the development of the contact area between the workpieces and thereby controlling the current density and heat generation. In spot welding the amount of electrode indentation is influencing the heat generation and is controlled by the plastic deformation of the workpieces during the process. Besides the macro scale deformations occurring in resistance welding the behaviour of the contact resistance is to a large degree depending on the micro scale plastic deformation of surface asperities at the interface. Hence, it is obvious that an accurate description of the plastic behaviour of the materials ranging from room temperature to the liquidus temperature is an important factor in simulation of resistance welding.

In this work the purpose has been to investigate the use of advanced techniques for measuring and modelling of the mechanical material properties at a wide range of temperatures and different strain rates for use in simulation of resistance welding. Furthermore the implementation of the measuring techniques at the Department of Mechanical Engineering at DTU is investigated and discussed.

2.1 Testing Material Rheology

Experimental material data at elevated temperatures is for most materials often not available. This applies especially for new and advanced materials, such as advanced high strength steels (AHSS) that are commonly resistance welded in the automotive industry. Due to the difficulties involved in obtaining accurate material data at elevated temperatures it is often necessary to extrapolate data based on

tests at room temperature and data for similar types of materials. The mechanical behaviour of advanced materials is often improved through complex heat treatments during production. This implies that the high temperatures experienced by the specimens during the resistance welding process might seriously affect the carefully engineered microstructure and thereby the mechanical properties. Because of this, the only way to get reliable mechanical properties of the materials for simulation of resistance welding is by determining them experimentally.

Another parameter known to influence the plastic deformation of metals is the strain rate of the deformation. The actual weld time in resistance welding is usually less than a second, and in resistance micro welding it can be less than 1/100th of a second. The strain rate in resistance welding can therefore have quite an influence on the deformation and outcome of the process. Knowledge about the influence of strain rate on plastic deformation of the materials can thus be of importance in simulating the process. However, hardly any specific material data exist on strain rate dependent material deformation and therefore needs to be measured.

In the field of rheology in solid mechanics there exist numerous different experimental methods for determining the plastic behaviour of materials under different states of stress. Two of the most utilised tests are the tensile test and the compression test used to determine the relationship between the equivalent strain and the yield stress of the material under uni-axial tension or compression, respectively. These tests are well documented and are normally performed at room temperature. At the DIMEG department at the University of Padova, Italy, methods for performing the two mentioned material tests at elevated temperatures have been investigated [30, 32]. The two tests are denominated as the *hot tensile test* and the *hot compression test*. In this chapter these two test methods are investigated and discussed in relation to modelling of material plastic behaviour for simulation of resistance welding.

In the present project a limited number of materials have been used in the experimental work. In order not only to investigate the usefulness of the testing methods, but also to have material data available for more accurate simulations throughout the project, it was chosen to test most of the materials used in the project. More precisely the mechanical behaviour of the three types of sheet material - Dual Phase 600, TRIP 700 and DC06[1] (low carbon steel) as well as the behaviour of four types of rod material - Nickel 200 ($\sim$ 99% Ni), AISI 316L stainless steel, Aluminium 6060 T6 and mild steel S235JR ($\sim$0.3% C) were investigated. The hot tensile test and most of the hot compression tests were performed mainly at the DIMEG department at the University of Padova, Italy. The mild steel S235JR and aluminium 6060 were tested at the Department of Mechanical Engineering at DTU.

[1]See chapter 7 for detailed description of these steels.

2.2 Hot Tensile Testing of Sheet Material

The hot tensile testing of sheet material is an advanced materials testing method developed at the DIMEG department at the University of Padova, Italy. Some of the main materials used in this project were tested at a wide range of temperatures for modelling of the materials in numerical simulations. Furthermore the tests were evaluated as testing method for acquiring material rheology data for the modelling of resistance welding.

2.2.1 Test Principle

Tensile testing is conventionally performed by tensile loading of a specimen of length l_0 and continuously measuring the required load F and the actual elongation l of the specimen (see figure 2.1). The elongation is usually measured using an extensiometer which is attached to and elongates together with the specimen. By assuming isotropic material behaviour, uniform deformation as well as constant volume ($A_0 l_0 = Al$) in the test specimen, the true equivalent strain $\bar{\epsilon}$ can be calculated from equation (2.1)

$$\bar{\epsilon} = \ln \frac{l}{l_0} \tag{2.1}$$

and the equivalent stress is calculated from equation (2.2).

$$\bar{\sigma} = \frac{F}{A} = \frac{F}{A_0 \frac{l_0}{l}} \tag{2.2}$$

At some point the deformation or strain hardening of the material reaches a critical value and the deformation concentrates locally in the necking-region. This is known as local instability [52]. All further deformation of the material now happens in this region and the equations (2.1) and (2.2) can no longer readily be used to describe

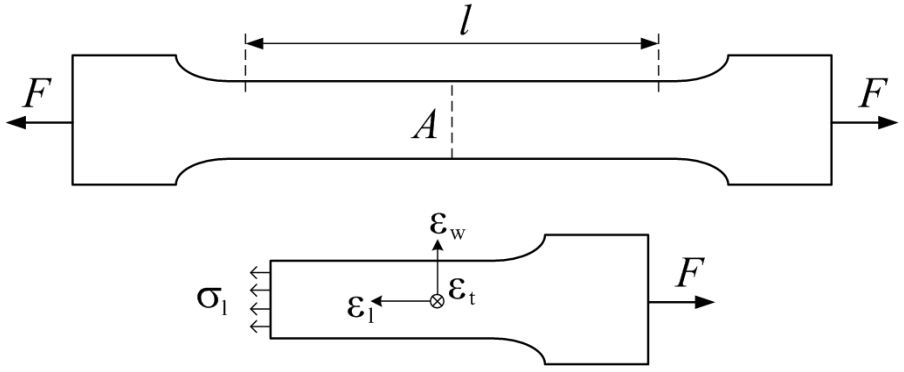

Figure 2.1: Schematic of tensile test principle

the stress-strain relationship. At room temperature necking usually initiates after a reasonable amount of uniform deformation, making the method described above fast and useful. However when performing tensile tests at elevated temperatures necking initiates almost immediately, which makes it more difficult to measure the stress-strain relationship by conventional methods.

In order to extract coherent values of equivalent stress and strain it is necessary to measure the strain locally in the necking region during the test. If we assume that the stress and strain are uniform in cross-sections with normal vectors parallel to the pulling direction, the strain in the thickness direction ϵ_t and the width direction ϵ_w is expressed as

$$\epsilon_t = \ln \frac{t}{t_0} \qquad \epsilon_w = \ln \frac{w}{w_0}$$

The actual cross-sectional area can then be found by assuming constant volume, i.e. $\epsilon_l + \epsilon_w + \epsilon_t = 0$

$$A = wt = (w_0 e^{\epsilon_w})(t_0 e^{\epsilon_t}) = w_0 t_0 e^{\epsilon_w + (-\epsilon_l - \epsilon_w)} = w_0 t_0 e^{-\epsilon_l} \tag{2.3}$$

The highest stresses and strains are found in the very centre of the necking region where the cross sectional area is smallest. By measuring the initial cross sectional area and the major and minor strain during the test, it is possible to calculate the stress in this region using equation (2.2) combined with equation (2.3). The stress and strain are assumed uniform in cross sections perpendicular to the pulling direction, but due to the necking mechanism it is not safe to consider the material deformation isotropic anymore and consequently equation (2.1) can not be used. If the in-plane strains (length and width strains, ϵ_l and ϵ_w) are measured in the necking region, the equivalent strain can be calculated from equation (2.4) according to Danckert [52].

$$\bar{\epsilon} = \frac{2}{\sqrt{3}} \sqrt{\epsilon_l^2 + \epsilon_w^2 + \epsilon_l \epsilon_w} \tag{2.4}$$

The calculation of the equivalent stress given by equation (2.2) is a simplification as it does not consider the three dimensional stress state which is acting in the necking region. By disregarding the stress contributions from the width and thickness directions the actual equivalent stress is underestimated, thereby underestimating the actual strength of the material. The calculated data can therefore be considered as a minimum estimate of the strength of the material.

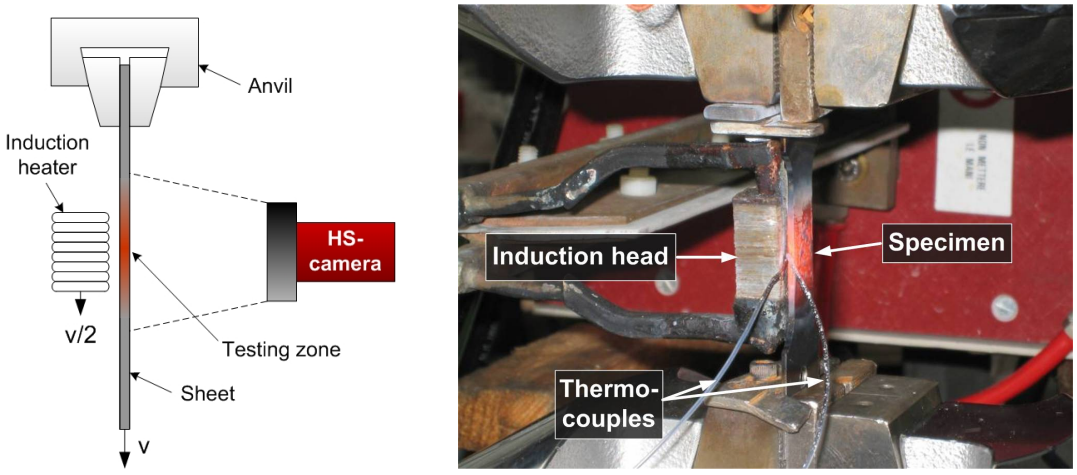

(a) (b)

Figure 2.2: Experimental setup for Hot Tensile Testing

2.2.2 Experimental Procedure

The experimental setup consist of a modified MTS[2] tensile-compression testing machine. In order to measure the strains locally during the test a high speed and high resolution camera has been installed to capture the deformation during testing. Furthermore the specimens are painted with a black and white randomly dotted pattern on the surface. Using the advanced image analysis software ARAMIS[3] the local in-plane strains (ϵ_l and ϵ_w) can be extracted from the deformed pattern on the test specimens. The heating of the specimen is achieved by local heating using a magnetic induction head positioned very close to the centre of the test specimen and controlled via temperature feedback through an attached thermocouple. The setup is shown in figure 2.2. The induction system is moved via a separate system and synchronised to the movement of the tensile testing machine through the controlling software. The induction head moves with half the testing speed, hereby staying in the centre of the test area during the entire test. The distance of the inductor from the sheet and the alignment with the sheet has significant influence on the heating of the specimen. A non parallel alignment results in a non uniform heat generation in the specimen. Placing the inductor too far from the specimen results in insufficient heat generation and it is not able reach the desired temperature, while a position too close to the specimen could produce an unstable testing temperature due to overshoot in the temperature feedback system caused by the rapid heat generation. The gap between the sheet and the inductor was approximately 1-1.5mm.

[2]MTS testing solutions, MN, USA, http://www.mts.com
[3]GOM Optical Measuring Techniques, Widen, Switzerland, https://www.gom.com

Table 2.1: Materials tested using hot tensile testing

			Composition [wt%]					
Steel	**Thk.**	**Coating**	**C**	**Mn**	**Cr**	**Si**	**P**	**Al**
DC06	1.5mm	-	0.002	0.15	-	-	0.01	0.04
DP600	1.5mm	-	0.11	0.9	0.5	0.4	0.015	0.04
TRIP700	1.2mm	Zinc 14μm	0.24	2	0.6	0.3	0.4	0.24

The test procedure consist of a heating period and a testing period. The heating time was between 90 and 120 seconds followed by a holding time of 60 seconds before the actual deformation was started. This allowed for a stable steady state temperature distribution in the test specimen prior to the actual deformation. During the heating time the controller of the tensile testing machine was set in zero force mode which allowed the material to thermally expand without restrictions. The tensile tests were all conducted with a deformation speed of 40mm/s. The images of the deformation as well as the displacement and force curves are captured with a LabView data acquisition system.

The investigation included three types of steel sheets - Dual Phase 600, TRIP 700 and DC06 low carbon steel with properties collected in table 2.1. The steels were tested at temperatures ranging from room temperature to 1200°C with suitable intervals. The dimensions - especially the length - of the test specimens were restricted due to the fact that all available sheet material had been cut into samples of 30x120mm - originally designed for samples for resistance welding. Due to this the samples were relatively short as compared to the normally desired size of tensile test specimens. This had implications for the tests with the TRIP steel, where the stress concentrations around the clamping resulted in a fracture at moderate temperatures. Unfortunately it was not possible to solve this problem during the testing period and therefore no results for the TRIP steel were obtained between room temperature and 600°C. Because the strains were measured optically the short length had no other implications for the stress/strain measurements.

The optical technique requires that an adequate pattern is visual during the entire test. This pattern is produced by spraying the specimen with a heat resistant black paint followed by a dotted pattern of white boron paint - producing a pattern of white dotted features on a black background. This pattern is useful up to temperatures around 600°C where the steels start to glow and the pattern is no longer useful for the vision system. It was learnt afterwards that applying only the white boron spray alone could have produced a stable pattern from 600°C up to

900°C, however this was not tried. The estimation of the strain at temperatures higher than 600°C was done by using the measured displacement as the elongation and then calculating the strain using equation (2.1). This is of course a rough simplification, which is further discussed in section 2.2.3.

2.2.3 Results

The results from the tensile tests consist of force displacement data from the press along with vision data from the camera. As explained in section 2.2.1 the resulting stress-strain relationship can be calculated based on these data. A model based on the Hollomon equation $\sigma = K\epsilon^n$ was fitted using a logarithmic transformation of the data. This is done by first transforming the data with the natural logarithm and then fitting a linear expression using linear regression analysis. The final part of the experimentally obtained stress-strain curves are influenced by the occurrence of fracture and usually shows a drop in the stress. This part of the curves was therefore not included in the regression analysis. In the case of the high temperature tests where the vision system did not give any useful results, the stresses and strains were estimated using the nominal values of the specimen dimensions as well as the force-displacement data from the press. In these cases only the very beginning of the tests was considered where the dimensions still can be assumed close to the nominal values. The results can be seen in figure 2.3 on page 26 and the estimated model coefficient are collected in table 2.2 (TRIP700 at 400°C is an estimate since no experimental values were obtained).

Table 2.2: Model coefficients obtained by the hot tensile test ($[K] = \text{MPa}$)

		Testing temperature [°C]								
		RT	200	400	600	700	800	900	1000	1200
DC06	K	523	395	292	188		61		51	
	n	0.28	0.29	0.27	0.24		0.1		0.096	
DP	K	1123	1028	873	319		88	67		29
	n	0.19	0.18	0.18	0.13		0.065	0.038		0.14
TRIP	K	1347	-	(1054)	428	220		146		41
	n	0.27	-	(0.26)	0.094	0.061		0.13		0.16

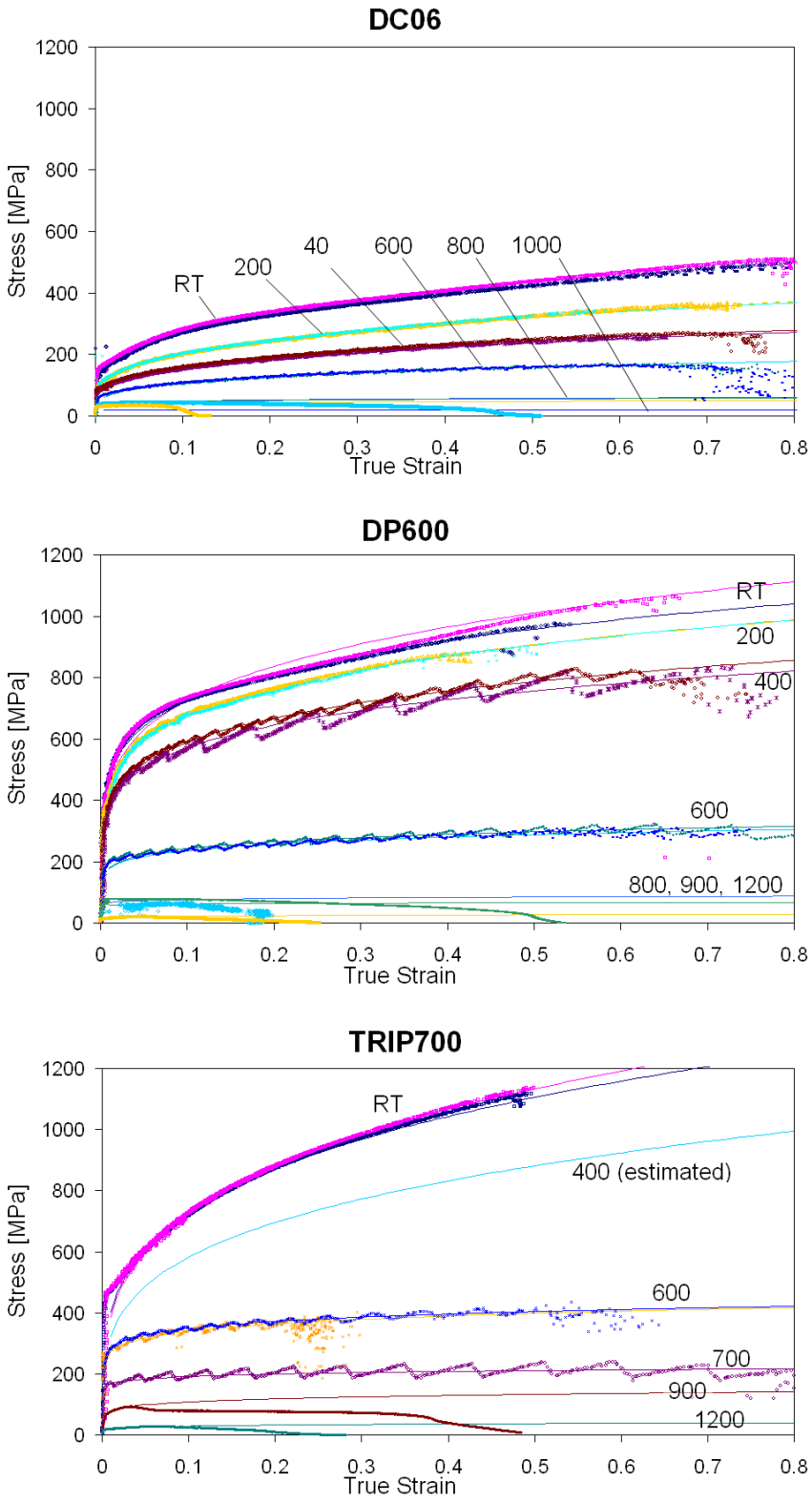

Figure 2.3: Results of the hot tensile test

As seen from figure 2.3 the Hollomon equation ($\sigma = K\epsilon^n$) is able to model the plastic behaviour of the tested steels with only minor discrepancies giving generally high correlation coefficients (R-values > 0.95). The results in figure 2.3 show that the low carbon steel DC06 has the lowest strength and that the strength gradually decreases with increasing temperature. For the the DP600 steel the strength from room temperature to 400°C decreases slightly and from 400°C to 600°C a large drop in strength is noticed. Above 600°C the DP600 becomes very soft and the strength decreases to around $\sigma_0 = 50$MPa. Comparing the two high strength steels it is noted that both steels start yielding around 500MPa, but the TRIP700 shows a larger work hardening and thereby higher strength at room temperature than the DP600. Otherwise the decrease in strength of the TRIP700 steel with increasing temperature show similar behaviour as the DP600 steel, although the TRIP700 is found to be stronger also at 600°C.

2.2.4 Discussion

As mentioned in section 2.2.3 the high strength steels show a significant decrease in strength when increasing the temperature from 400°C to 600°C. It is believed that this is partly due to phase transformations and partly due to annealing effects in the material microstructure. Advanced high strength steels undergo complex heat treatments during production which results in a specific microstructure increasing the strength of the material[4]. This microstructure is theoretically unstable at room temperature, but due to the low diffusion rate and phase-stabilising components the driving force for phase transformations is very small. However, increasing material temperature increases the mobility of the atoms which increases the phase-transformation rate, provided that it is diffusion controlled. This will influence the specially designed microstructure and decrease the strength of the material. Besides the actual transformation of the microstructure an elevated temperature decreases the strength of a material by thermal softening or annealing. During a tensile test the material work hardens, but due to the annealing effect at higher temperatures the increase in strength due to the work hardening is significantly decreased.

The hot tensile tests were only performed at one strain rate because the test is difficult to perform at high speeds. This is mainly due to the tensile testing machine which is not designed for high speed deformations. Furthermore, the occurrence of necking where deformation no longer is uniform makes the calculation of a constant strain rate very challenging. At high speeds there are also the difficulties of synchronising the different components of the test setup where the induction

[4]Microstructural investigations of the high strength steels are explained in more detail in chapter 7

system needs to follow the movement of the tensile test machine and the high speed camera should be able to capture sufficient frames to have enough data sets to work with. The strain-rate in resistance welding is mainly influencing material behaviour during the collapse of projections in projection welding and has only minor influence in spot welding. This implies that lack of material data regarding the influence of strain rate is less important for spot welding applications and the hot tensile test is therefore primarily suitable for testing of material properties of sheet metals for modelling of spot welding.

Another area where the hot tensile test has limitations is in the maximum achievable test temperature. Because of the glow of the metals at higher temperatures the painted pattern used for the strain analysis cannot be detected by the vision system. In this work the strength of the materials at temperatures higher than 600°C are calculated based on the nominal values of the cross section and a uniform deformation of the specimen. This is of course only a rough estimate of the actual strength. Due to necking the real cross sectional area decreases fast and because necking initiates practically immediately under these temperatures, the calculated stress-strain curves are assumed to underestimate the actual strength of the material. The absolute value of the strength of most materials that are resistance welded is lowered considerably at temperatures higher than 600°C compared to room temperature. This implies that the errors introduced when estimating the strength at higher temperatures are small on an absolute scale and the models are therefore adequate to be used as material parameters in numerical simulations.

The tensile test is measuring the strength of the materials under uni-axial tension. During resistance welding the workpieces are pressed together and are therefore in a state of compressive stress. Most materials show similar stress-strain behaviour in tension and compression which is also utilised in the Von Mises and Tresca yield criteria [53] and it is therefore reasonable to use the estimated yield strength in modelling of the plastic behaviour of materials in resistance welding.

In the present form the hot tensile test is restricted to testing sheet material due to the principle of one-sided induction heating. The strength of the induced magnetic field is highly dependent on the distance to the induction head. This implies that rod-shaped test specimens would experience asymmetric heating and it would be difficult to achieve a stable test temperature. The hot tensile test is on the other hand an excellent method for estimating the plastic behaviour of sheet material at a wide range of temperatures.

2.3 Hot Compression Testing

Compression testing of round cylindrical workpieces is often used for acquiring the stress-strain relationship of bulk material due to the simplicity of the test. The Gleeble system is a thermo-mechanical simulator that is able to carry out hot compression testing at a wide range of temperatures [29]. The DIMEG department at the University of Padova, Italy, has many years of experience in testing of material rheology and has a Gleeble 3500 system at their disposal. The Department of Mechanical Engineering at the Technical University of Denmark has an older Gleeble 1500 system, where material testing has been re-established and further developed in the present project based on experiences obtained at the University of Padova [10, 13].

2.3.1 Test Principle

Compression testing is performed by reducing a cylinder in height between two plain tools measuring corresponding values of force and displacement. If good lubrication is ensured friction can be neglected and the cylinder will deform in a uniform way. The true stress and strain throughout the deformation can then be calculated as below, where volume constancy is used to calculate the real contact area A during the compression [53].

$$\bar{\epsilon} = |\epsilon_h| = \ln\left(\frac{h_0}{h}\right) = \ln\left(\frac{h_0}{h_0 - \Delta h}\right) \tag{2.5}$$

$$\bar{\sigma} = \sigma_1 = \frac{F}{A} = \frac{F}{A_0\left(\frac{h_0}{h_0 - \Delta h}\right)} \tag{2.6}$$

The above equations are derived under the assumption of negligible friction between anvils and workpieces, which is why controlling friction becomes important for the validity of the test. Furthermore, it is important that the height-to-diameter ratio of the test specimens is not too large, in order to avoid buckling. Preferably the ratio should not exceed 1.5 for most materials.

The strain-rate $\dot{\epsilon}$ is known to have an influence on the rheological behaviour of materials [53]. An increase in strain rate will typically - especially at medium to high temperatures - decrease the plastic flow of the materials thereby increasing the strength. The strain rate is defined as the time-derivative of the strain and is for a simple compression test given as

$$\dot{\epsilon} = \frac{\mathrm{d}\bar{\epsilon}}{\mathrm{d}t} = \frac{\mathrm{d}}{\mathrm{d}t}\left(-\ln\frac{h}{h_0}\right) = -\frac{1}{\frac{h}{h_0}}\frac{\left(\frac{\mathrm{d}h}{\mathrm{d}t}\right)}{h_0} = -\frac{\dot{h}}{h} \tag{2.7}$$

where $\dot{h} < 0$ is the velocity with which the height of the specimen decreases and h is the momentary height of the specimen. The solution to equation (2.7) gives the height of the specimen at a given time as

$$h(t) = h_0(e^{-\dot{\epsilon}})^t \tag{2.8}$$

As can be seen from equation (2.8) the height and thereby also the velocity should decrease exponentially during the test in order to maintain a constant strain rate. The influence of strain rate on the stress-strain relationship of material can generally be expressed as given in equation (2.9) [53]

$$\sigma = K\epsilon^n \ \dot{\epsilon}^m \tag{2.9}$$

where $\sigma = K\epsilon^n$ is the standard Hollomon-equation, $\dot{\epsilon}$ is the strain rate and m is a temperature dependent exponent.

2.3.2 Experimental Setup

The test setup is shown schematically in figure 2.4. Due to their high hardness and high temperature stability anvils of Ø19mm of tungsten carbide are used for the tests. The specimens are round cylindrical workpieces with the dimensions given in table 2.3. Between the anvils and the specimens a 0.05mm graphite foil and a 0.1mm tantalum foil is inserted for the high temperature measurements. The graphite foil acts as a lubricant and keeps friction low and the tantalum foil insures a good heat distribution in the specimens by acting as high temperature insulation. Thermocouples type-k are welded to the specimen which is inserted in the machine insuring the thermocouple wires are free of the specimen holder. The

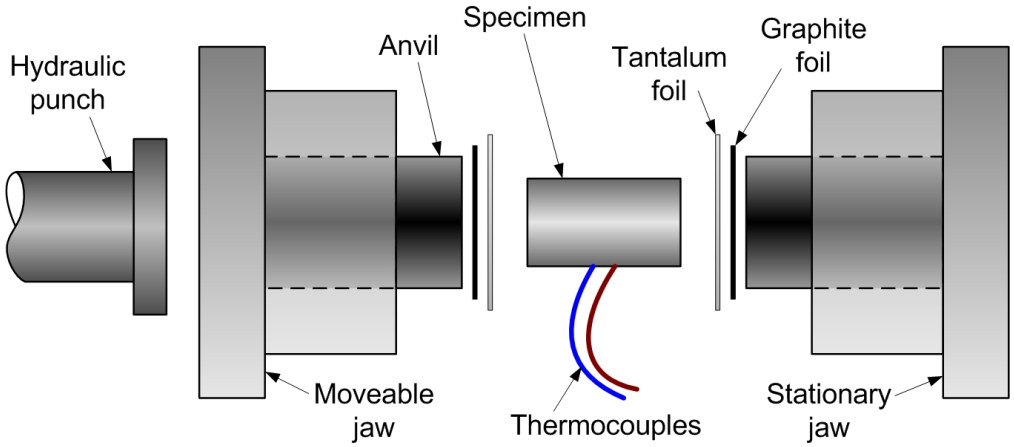

Figure 2.4: Experimental setup for hot compression testing

Table 2.3: Nominal specimen dimensions

Material	h_0	D_0	h_0/D_0
Stainless steel AISI 316L	10	8	1.25
Nickel 200	12	10	1.2
Aluminium 6060	10	8	1.25
Steel S235JR	10	8	1.25

thermocouples provide temperature feedback signals for accurate control of the temperature of the specimen. The heating system is based on electric resistance heating of the specimen. The jaws holding the anvils are water cooled which implies that the heat is concentrated in the specimen. By insulating the anvils with tantalum foil the heat flux to the tools is decreased even further. Measurements of specimen temperature across the length of the specimen reveal that by this procedure it is possible to obtain a very close to uniform temperature with only a few degrees difference from the centre to the end of the specimen. The mechanical system consist of two jaws where one is stationary while the other can be moved by the hydraulic punch as illustrated in figure 2.4. During a hot compression test the punch is displacement-controlled, meaning that the Gleeble is programmed to move the punch a certain distance during one or several specified time intervals.

Due to the fact that the test setup is not infinitely rigid the machine itself will elastically deform due to the forming load during a compression test. This implies that the total measured displacement d_0 by the Gleeble consists of two contributions namely the elastic compression of the machine $d_m(F)$ and the plastic deformation of the specimen $\Delta h = |h_1 - h_0|$. The actual deformation or height reduction of the specimen is thus given by equation (2.10).

$$\Delta h = d_0 - d_m(F) \tag{2.10}$$

As indicated in equation (2.10) the elastic deformation of the machine will in practise only depend on the load on the system. If the elastic behaviour $d_m(F)$ of the machine is known it is possible to calculate the real specimen deformation. The procedure is schematically illustrated in figure 2.5 where the correction in actual displacement is done by subtracting the stiffness of the machine $d_m(F_x)$ at a given load F_x from the measured displacement d_0 at that load. The compensation is applied to the measured data *after* the test.

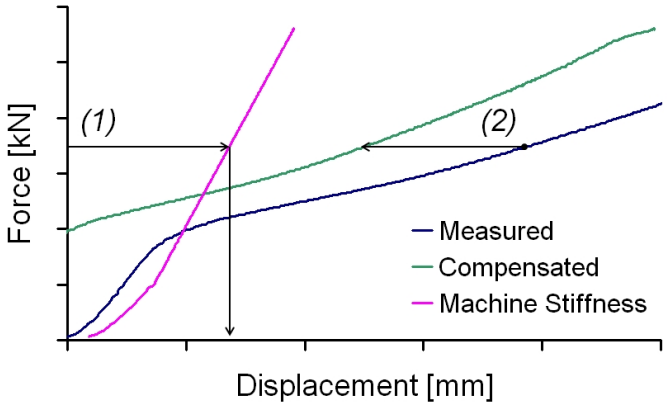

Figure 2.5: Machine stiffness correction - schematically

The hot compression test is performed in several stages. After having inserted the specimen in the machine as specified in figure 2.4 the specimen is heated to the specified testing temperature with approximately 10°C/s. It is then kept at the testing temperature for one minute before the actual compression is initiated. During the heating and holding stage the specimen expands due to thermal expansion. To avoid Prue-stressing of the specimens, the anvils are moved during heating to compensate for the thermal expansion Δh_{th} given by equation (2.11).

$$\Delta h_{\text{th}} = h_0 \kappa \Delta T \tag{2.11}$$

where h_0 is the specimen height at room temperature, κ is the thermal expansion coefficient of the specific material and ΔT is the increase in temperature calculated from room temperature. The compression consists of mainly two parts, an acceleration stage and the actual deformation stage. In the acceleration stage the punch is accelerated to the desired initial forming velocity corresponding to the chosen strain rate of the test. This stage is necessary mainly at high strain rates to ensure the correct velocity is achieved. In the deformation stage the punch makes contact to the anvils and compresses the specimen to the desired final height.

During the course of the project two experimental series were carried out. In the first series the two materials Nickel 200 and stainless steel 316 were tested at two different strain rates (1 and 10) and at varying temperature (RT, 100°C, 400°C, 700°C, 1000°C and 1300°C). The tests were set to a maximum strain of 0.8 which corresponds to a reduction in height of $1-e^{-0.8} \approx 55\%$. In the second experimental series the two materials Al6060 and mild steel S235JR were investigated at varying temperature but only at a single strain rate ($\dot{\epsilon} = 1$).

2.3.3 Implementation of Hot Compression Testing at DTU

The Gleeble 3500 system has an advanced control system capable of calculating the time-displacement program for the anvils when given the basic test properties such as specimen size, final strain, strain rate etc. The Gleeble 1500 system is an older system and programming is done manually. The implementation of hot compression testing on the Gleeble 1500 was done previously by Kristensen [13] who completed several measurements of material flow stress at elevated temperatures and different strain rates which he used for numerical simulation of resistance welding.

The procedures for hot compression testing as described by Kristensen [13] were tested during the course of this project and it was noted that the compliance of the Gleeble machine was not considered in the calculations. This introduces large errors in the results which were noted by Kristensen, but could not be explained. In order to account for machine stiffness, the compliance of the machine was measured by pressing the two anvils against each other without inserting a specimen. Corresponding values of applied force F and machine displacement d_0 were recorded and for a compression force higher than 1000kg the machine compliance was found to be linear. For a lower force the influence of the deformation of the graphite foil resulted in a slightly quadratic relationship. The following expressions were fitted to the data

$$d_m(F) = -1.92 \cdot 10^{-7} \cdot F^2 + 5.23 \cdot 10^{-4} \cdot F \qquad \text{for } F < 1000\text{kg} \tag{2.12a}$$

$$d_m(F) = 2.31 \cdot 10^{-4} \cdot F + 0.9 \qquad \text{for } F \geqq 1000\text{kg} \tag{2.12b}$$

As can be seen from equation (2.12b) the deformation of the machine is of considerable size ($d_m(1000\text{kg}) \approx 1.13\text{mm}$) and its influence can not be neglected in the evaluation of the results of the material rheology measurements on the Gleeble 1500.

The Gleeble 1500 is programmed by creating one or more movement-intervals specifying an anvil displacement Δd in a given time period Δt. Programming the Gleeble 1500 for hot compression testing as described by Kristensen [13] is done by defining an initial acceleration interval, a deformation interval and an over-travel interval. Based on the desired strain rate the intervals have constant anvil velocities corresponding to the initial velocity, an average velocity and the final velocity, respectively. This three-step velocity profile is illustrated in figure 2.6 on page 34 indicated by the label "Velocity - Kristensen (2000)". Calculations of the actual strain rate on the Gleeble 1500 using this "Three-step"-method revealed that the strain rate was not constant during the test but varied significantly. A detailed

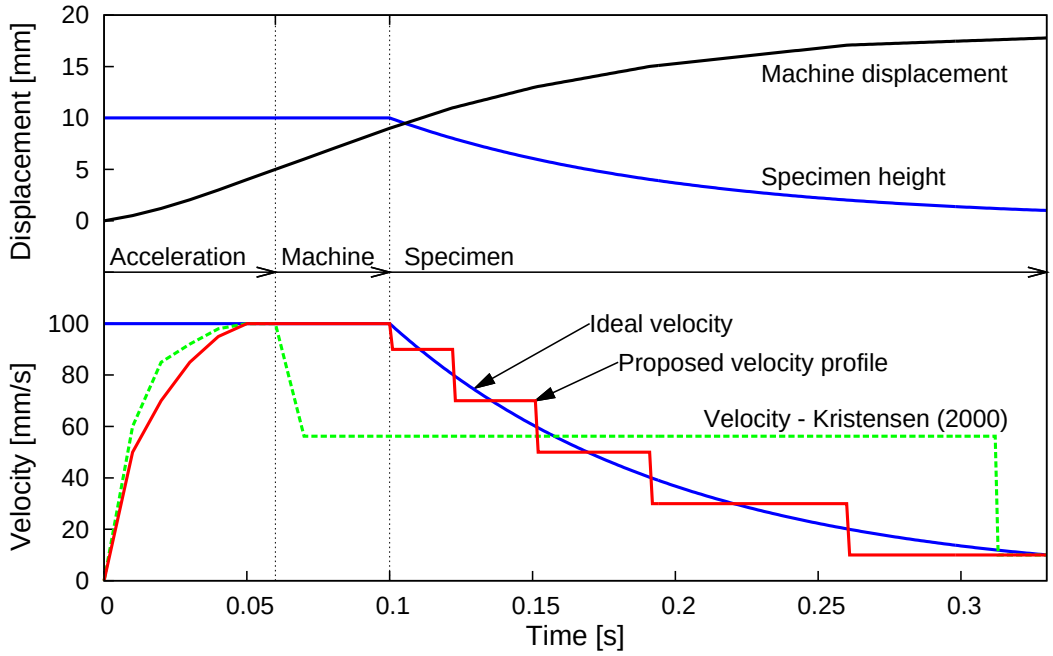

Figure 2.6: Displacement and velocities during hot compression testing

description of the discrepancy can be found in the work by Giversen [54]. The main reasons for the non-constant strain rate is the limited number of movement-intervals and the lack of compensation for the machine compliance. In order to improve the testing procedure to obtain a more constant strain rate during the experiments it is suggested to increase the number of movement-intervals to achieve a more steady decrease in velocity during the test. By combining equation (2.7) and equation (2.8) the ideal velocity of the anvil at a given time can be calculated and a suitable number of movement-intervals can be chosen as indicated in figure 2.6. Furthermore, it should be recognised that the initial part of the machine displacement will predominantly be taken up by the machine compliance and only when the contact pressure reaches the yield stress of the testing material the specimen will start to deform. As indicated in figure 2.6 this was not considered by Kristensen [13] which results in a too low initial deformation velocity. By estimating the initial deformation of the machine and adding it to the total acceleration distance, the velocity of the anvil will correspond to the desired strain rate velocity.

2.3.4 Results

Experimental Series no. 1

In the first series the Nickel 200 and the stainless steel were tested at varying temperatures and two strain rates. The output of the tests is a series of force, temperature and displacement data. The displacement is corrected for the machine stiffness and the resulting strains and stresses can be calculated using equation (2.5) and (2.6). As described in section 2.2.3 the curves are fitted to a model of the form $\sigma = K\epsilon^n \dot{\epsilon}^m$ using a log transformation of the data and a least square fitting procedure[5]. The resulting model parameters are collected in table 2.4.

Table 2.4: Model coefficients obtained by hot compression testing of Nickel 200 and stainless steel AISI 316L ($[K] = \text{MPa}$)

T [°C]	**K**	**n**	**m**	**R**
RT	1192	0.1	0.005	0.92
100	973	0.08	0.009	0.85
400	690	0.04	-0.003	0.56
700	516	0.09	0.025	0.69
1000	267	0.17	0.068	0.94
1300	57	0.02	0.187	0.76

(a) AISI 316L Stainless steel

T[°C]	**K**	**n**	**m**	**R**
RT	709	0.15	0.003	0.97
100	658	0.15	-0.005	0.93
400	503	0.12	-0.016	0.95
700	307	0.16	0.066	0.92
1000	151	0.22	0.12	0.96
1300	40	0.12	0.22	0.89

(b) Nickel 200

The stress-strain curves can be seen in figure 2.7 and figure 2.8 on page 36. The strength of the materials are seen to decrease as the temperature increases. As seen from table 2.4 the correlation coefficient R is large (close to 1.0) for most test temperatures, however for the stainless steel 316L the R-value is seen to drop for 400°C and 700°C. This indicates that the model in equation (2.9) in general is able to describe the material rheology behaviour with good accuracy. As can be seen from figure 2.8 the poor fit at medium temperatures for the stainless steel is due to the material behaviour at low strain rates where the increased temperature implies close to *ideal plastic* material. The influence of strain rate is measured by the m-coefficient in equation (2.9). From table 2.4 it is seen that the influence of the strain rate is very low at low temperatures and around 700°C the influence increase and become significant for the material behaviour. Normally the strain rate is known to increase the strength of a material and the negative values of m should therefore be regarded as an expression of the experimental variance when m is close to zero.

[5]JMP from SAS Inc. (http://www.sas.com) was used to perform the least square fitting

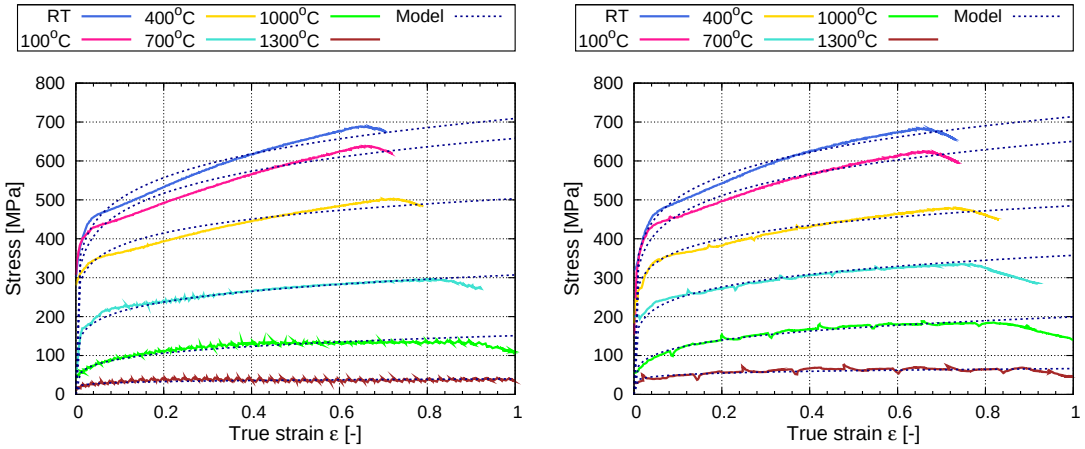

(a) Strain rate $\dot{\epsilon} = 1$ **(b)** Strain rate $\dot{\epsilon} = 10$

Figure 2.7: Hot compression test of Nickel 200

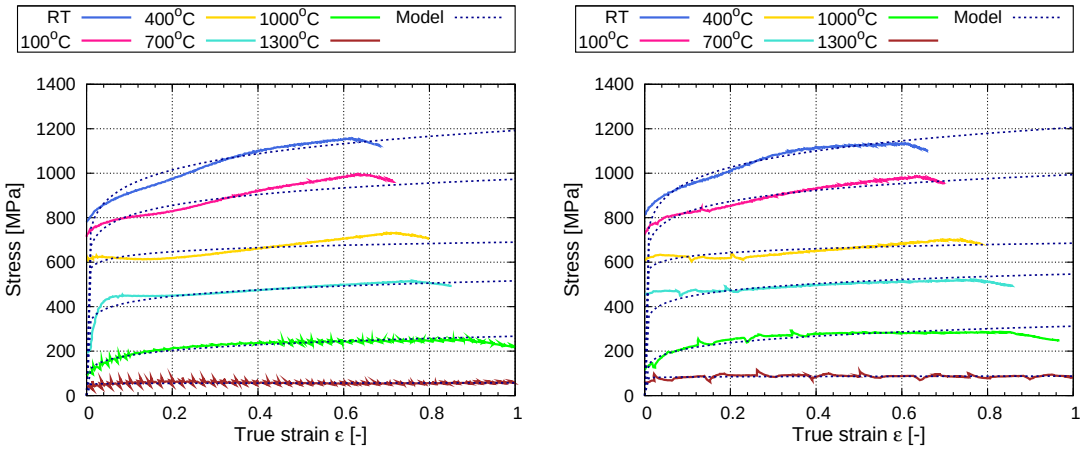

(a) Strain rate $\dot{\epsilon} = 1$ **(b)** Strain rate $\dot{\epsilon} = 10$

Figure 2.8: Hot compression test of Stainless AISI 316

Experimental series no. 2

In the second series the two materials Aluminium 6060 T6 and mild steel S235JR were tested at varying temperatures. The experimental data is fitted to the standard Hollomon equation of the form $\sigma = K\epsilon^n$ using a non-linear fitting procedure[6]. The model parameters can be found in table 2.5 and the models are plotted together with the experimental data in figure 2.9. The K_{err} and n_{err} are the standard error of the estimated model parameters. The results show that the strength

[6]The non-linear fitting procedure in Gnuplot release 4.2 (www.gnuplot.info) was used to estimate model parameters.

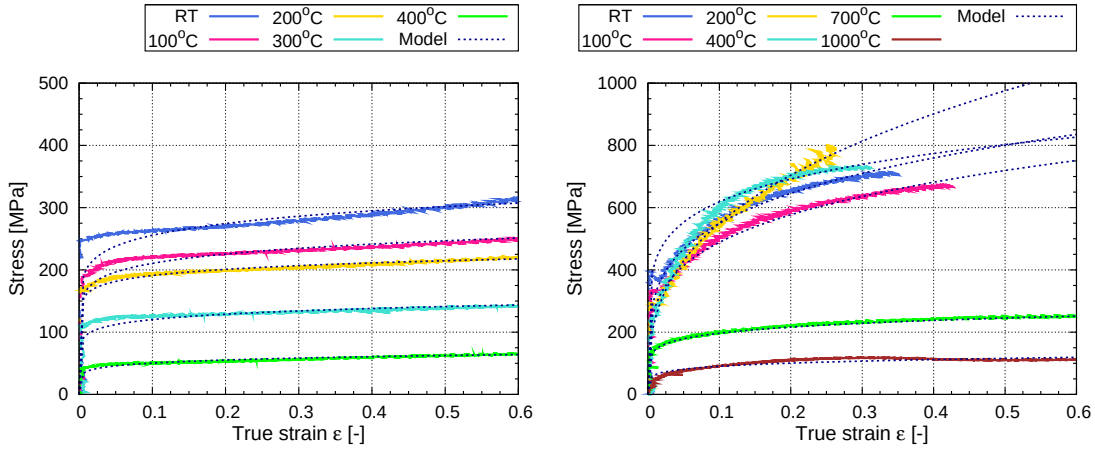

(a) Al6060 T6 **(b)** Mild steel S235JR

Figure 2.9: Hot compression test of Aluminium 6060 T6 and mild steel S235JR

Table 2.5: Model coefficients obtained by hot compression testing of Aluminium 6060 T6 and steel S235JR ($[K]$ = MPa)

T [°C]	**K**	**n**	$\mathbf{K}_{err}$	$\mathbf{n}_{err}$
RT	324	0.10	1.25	0.0022
100	264	0.10	0.87	0.0018
200	226	0.07	0.45	0.0011
300	151	0.10	0.50	0.0019
400	69	0.13	0.13	0.0013

(a) Aluminium 6060 T6

T[°C]	**K**	**n**	$\mathbf{K}_{err}$	$\mathbf{n}_{err}$
RT	941	0.23	5.30	0.0029
100	850	0.24	2.88	0.0020
200	1248	0.36	5.38	0.0022
400	897	0.16	1.92	0.0013
700	270	0.14	0.34	0.0010
1000	129	0.15	0.38	0.0021

(b) Steel S235JR

of the aluminium decreases steadily with temperature and the low values of the strain hardening exponent n show that the material only experiences little strain hardening. The standard errors are generally low indicating that the stress/strain behaviour of the aluminium is captured with good accuracy using the Hollomon equation.

The results for the mild steel S235JR show a more complex influence of temperature on the strength of the material. Increasing the temperature to 100°C decreases the strength. However, as the temperature reaches 200°C the material starts experiencing significantly more strain hardening which increases the strength of the material and it ends by having higher strength than at room temperature. At

400°C the material is still stronger than at room temperature, but a further increase in temperature results in a significantly decrease in temperature. It is noted how the measured stress/strain data especially at 200°C but also at 400°C show irregular jumps along the curve in figure 2.9b. This *jerky* behaviour and the increase in strength with temperature is typical for materials experiencing dynamic strain ageing, which is often seen for mild steels [55]. This is further discussed in the next section.

2.3.5 Discussion

The hot compression test is able to measure the rheological behaviour of the four tested materials. The test is fast, relatively simple and produces good repeatability also when comparing the two Gleeble systems 3500 and 1500 [54]. The stress state in the hot compression test is close to the stress state present in resistance welding, which makes the results suitable for use in modelling of the process.

The resulting stress-strain curve for Nickel 200 at room-temperature compares well with table values [56] while the obtained results for the stainless steel AISI 316 (W.no. 1.4401) are considerably higher than the table values [56]. The table data suggest that yielding should initiate between 400MPa and 500MPa while the experimental measurements show a yield stress close to 800MPa at room temperature. Furthermore the table data indicate that the steel should experience a higher degree of work hardening than found in the experiments. It is likely that the stainless steel AISI 316, which was tested in as-received condition, has not been annealed after the final drawing operation. This implies that the test specimens are pre-strained, which has increased the strength of the material. Comparing the stress levels, the table data suggest that the material has experienced an equivalent strain of $\bar{\epsilon}_{pre} = 0.4$ resulting in yield stress of approximately 800MPa. The fact that the test specimens have been pre-strained has impact on the resulting material models which should be remembered when using the models for numerical simulations. The material model should not only correspond to the actual material being welded, but should also consider potential pre-strain of the material. Furthermore in light of the results it could be argued that the chosen strain rate levels are not spaced far enough for a sound modelling of the effect of strain rate on the plastic behaviour of the materials resulting in negative values of the m-exponent. By choosing a larger interval between the strain rate levels the linear regression analysis will be more accurate as the effect will be more significant.

The result for the aluminium 6060 T6 material show a stress/strain behaviour showing only minor strain hardening. The T6 heat treatment involves heating the specimen to a high temperature and allow for the alloying elements to enter into a solid solution with the aluminium matrix. The specimen is then quenched creat-

ing a supersaturated solid solution and is subsequently age hardened at a suitable elevated temperature. From the experimental results is seen that the precipitates in this particular aluminium alloy increase the yield stress compared to pure aluminium and at the same time decrease the strain hardening of the material. As mentioned in the previous section the mild steel S235JR show significant signs of dynamic strain ageing. Strain ageing is the mechanism in which solute atoms such as carbon and nitrogen migrate to the "Cottrell atmosphere" of free dislocations and lock the dislocations [57]. The locking may result in the generation of new dislocations by the activation of dislocation sources, and, thus, cause an increase in the dislocation density and thereby the yield strength of the material. The jerky behaviour of the test curve is caused by the fact that when the force is high enough the dislocations are released from their locked state and become mobile. This then allows for plastic deformation at a lower stress level. Strain ageing is what causes mild steels to have an upper and lower yield point in the stress strain curve [57]. Dynamic strain ageing is caused by the interstitials being much more mobile. When the dislocations has been released from an area of increased nitrogen or carbon content, the interstitials will diffuse to free dislocations, that has been slowed down by the increasing dislocation density. At elevated temperatures this strain ageing mechanism happens rapidly and continuously why it is termed dynamic strain ageing [58]. The rheological behaviour of S235 is a result of this mechanism.

A restriction to the hot compression test in its present form is the requirement to the shape of the test specimens. Only round cylindrical specimens can be used in the test which implies that for spot welding purposes it is not possible to test the *actual* sheet material in the hot compression test. In this case it is necessary to perform the test on rod-shaped material of the same material type and grade and assume identical behaviour of the two materials. No validation of this sort was conducted during the course of this project. If the material is only available as sheet material - which is the case for most AHSS - then the test can not readily be used to test the material, and other tests such as the hot tensile test should be used.

The results of the hot compression test indicate that the Hollomon-equation given in equation (2.9) is able to describe the stress/strain behaviour of the tested materials for a wide range of temperatures and for the chosen strain rate interval with reasonably accuracy. However, the simple form of the Hollomon-equation does not directly include the temperature as a parameter, which limits its ability as a predictive model. To obtain a complete description of the yield behaviour it is necessary to measure yield curves at discrete temperature intervals hereby obtaining table values of the coefficients depending on temperature (c.f. table 2.2, 2.4 and 2.5). The Hollomon-equation could be further modified by estimating functions of the model parameters with respect to temperature. However the tested materials

show no common trend and the temperature dependent functions should therefore be estimated for each specific case. The use of table values is in this case just as applicable. More advanced models than the simple Hollomon-equation is available in the literature, however such models are often developed for a specific material or under specific conditions. For the purpose of modelling material rheology behaviour for a wide range of temperatures and strain rates in numerical simulation of resistance welding the Hollomon equation is thus adequate. One could argue that, in order to have a non-zero yield stress at zero strain, models including the initial yield stress should be used, such as the Swift or Ludwik equations [59]. However the numerical software SORPAS has routines for accounting for the initial elastic behaviour of the materials and the Hollomon equation is therefore adequate when using SORPAS for numerical simulation.

2.4 Conclusion

Different materials were tested using the hot tensile test and the hot compression test. No known commercial solutions exist for performing the hot tensile test and a custom-made and comprehensive experimental setup and instrumentation - as the one at DIMEG - is necessary. The hot compression test can with advantage be performed on the commercial Gleeble system. Both tests were found to be very effective in estimating the stress-strain behaviour of the test materials.

Due to the optical strain measurement method the hot tensile test is limited in the maximum achievable material test temperature, while it is possible to perform the hot compression test at temperatures close to the melting point of the materials. Both the mentioned material tests have restrictions on the type of materials that can be used in the test. Due to the induction heating system only sheet metal is suitable for the hot tensile test. For hot compression testing the specimens should be round cylindrical specimens to conform with the principles of the test. This implies that in many cases it is necessary to perform the hot compression test, not on the same material, but on material equivalent to the actual material being welded. This introduces some uncertainty, but the method is still considered to be valid for obtaining material data with relatively high accuracy.

The possibility of implementing the two tests were discussed. Hot compression testing on the existing Gleeble 1500 system was implemented and tested. The previously developed testing procedures [13] were investigated and based on the investigation significant improvements regarding compensation for machine compliance and more detailed velocity control were suggested. Implementation of the hot tensile test in the form, as it has been developed at DIMEG is discussed and it is found to involve comprehensive instrumentation.

The standard Hollomon-equation based on power-law hardening was found to be able to describe the rheological behaviour of the tested materials with good accuracy. By experimentally obtaining model coefficients at a wide range of temperatures and strain rates the model is hereby suitable for describing the material behaviour in numerical simulation of resistance welding.

Chapter 3

Measuring Material Electric Properties

This chapter focuses on measuring the electric bulk resistance of materials. Firstly basic concepts regarding electricity and electric resistance of materials are reviewed. Then an experimental method for measuring the electric resistivity of materials using a Gleeble 1500 system is presented. The electric resistivity of Nickel 200 (∼99% Ni), stainless steel AISI 316L, aluminium Al6060 and S235JR carbon steel (∼0.3% C) is tested and the results and the measuring technique is discussed.

3.1 Electromagnetism

When a current I is sent through a conductor a voltage U will develop which is directly proportional to the electric resistance R of the conductor. This relation is known as Ohms Law and is given in equation (3.1).

$$U = RI \tag{3.1}$$

The electric resistance is caused by the opposition towards the flow of charged particles through the conductor. The resistance depends on the material resistivity ρ, which is a material specific parameter. Assuming that the current is running *uniformly* through a conductor with cross section A and length L, then the resistance of the conductor is given by equation (3.2).

$$R = \rho\frac{L}{A} \tag{3.2}$$

Metals are in general extremely good electric conductors because they have a large number of free electrons for conducting current. The electric resistivity of metals is determined by the ease with which the electrons flow through the material. Factors

such as crystalline defects or imperfections as well as thermal vibrations lowers the mobility of the electrons thereby increasing the resistivity [55]. This implies that a higher alloying content, higher bulk temperature, and material strain hardening all work to increase the resistivity of metals. The resistivity of pure metals can often be approximated to increase linearly with temperature [55]. However, as material resistivity is caused by the movement of electrons it can only truly be understood by applying quantum mechanics theory. This is not inside the scope of this project and thus will not be further pursued.

The governing laws of electromagnetism predicts that when a current I is running in a conductor the moving electrons will generate a magnetic field $\mathbf{B}$ around the conductor as shown in figure 3.1. If we assume that the conductor with radius r_0 is narrow compared to the distance $\mathbf{r}$ from the wire to the point P in space where the magnetic field is evaluated (i.e. $r_0 << |\mathbf{r}|$), then the contribution to the magnetic field from the element d$\mathbf{l}$ can be calculated by the Biot-Savart law given in equation (3.3) [9]

$$\mathbf{B} = \int \frac{\mu_0}{4\pi} \frac{I \mathrm{d}\mathbf{l} \times \mathbf{r}}{|\mathbf{r}|^3} \tag{3.3}$$

where μ_0 is the magnetic permeability of vacuum. As can be seen from equation (3.5) the magnetic field generated by the current decays with the square to the distance to the conductor. The integral in equation (3.3) should be calculated for each case of a specific geometry of the conductor. If for example the conduc-

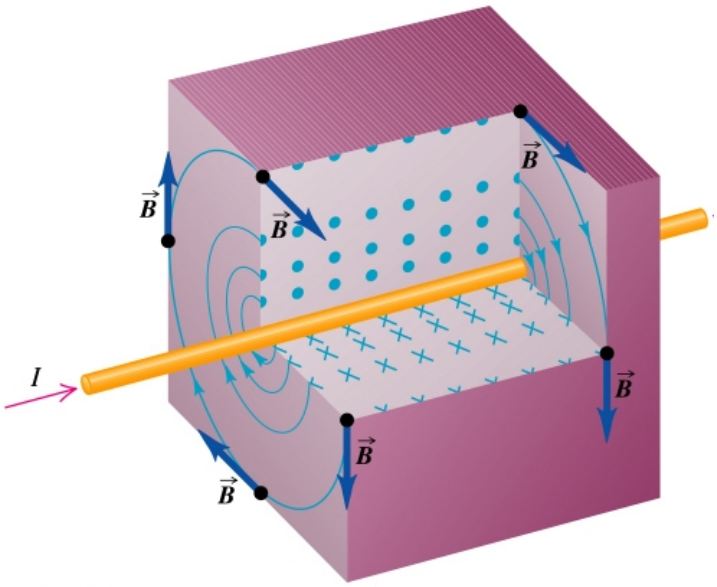

Figure 3.1: Magnetic field generated by a running current [60]

tor is infinitely long and linear, then the total contribution will be given by the following expression [60].

$$B = \frac{\mu_0 I}{4\pi r} \tag{3.4}$$

where r is the shortest (perpendicular) distance to the conductor. In many practical situations equation (3.4) will produce a fair approximation of the magnetic field from a simple conductor.

A varying magnetic field through a closed loop circuit will induce an electromotive force in the circuit. This phenomenon is expressed by Faraday's Law of induction presented in equation (3.5).

$$\varepsilon_m = -\frac{\mathrm{d}\Phi_B}{\mathrm{d}t} \tag{3.5}$$

The magnetic flux Φ_B is defined as:

$$\Phi_B = \int \mathbf{B} \cdot \mathrm{d}\mathbf{A} \tag{3.6}$$

where $\mathrm{d}\mathbf{A}$ is an infinitesimal area element in the closed loop circuit and $\mathbf{B}$ is the magnetic field running through that element. A relevant example is the calculation of the induced current in a closed circuit intended to measure the voltage drop through the linear conductor with radius r_0 between point D and E on figure 3.2.

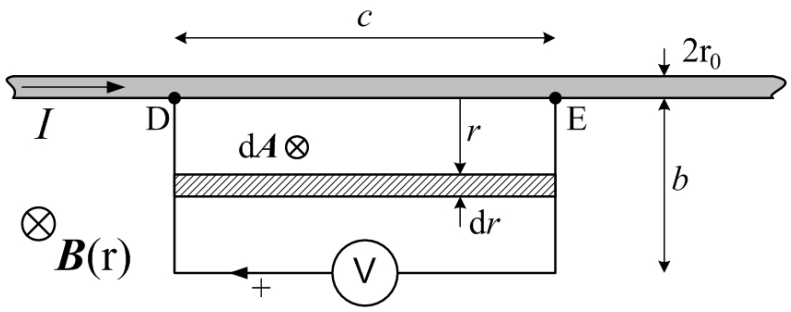

Figure 3.2: Calculation of the induced electromotive force in measurement wires.

Assuming the conductor is infinitely long, the magnetic field at the distance r from the wire is given by equation (3.4). By combining equation (3.5) with equation (3.6) and integrating the following result is obtained [11]:

$$\varepsilon_m = -\frac{\mathrm{d}}{\mathrm{d}t}\int_{r_0}^{r_0+b} \frac{\mu_0 I(t)}{2\pi r} c\,\mathrm{d}r = -\frac{c\mu_0}{2\pi} \ln\left(1 + \frac{b}{r_0}\right)\frac{\mathrm{d}I}{\mathrm{d}t} \tag{3.7}$$

The positive direction of the induced electromotive force is indicated on figure 3.2.

The result in equation (3.7) show that the induced electromotive force becomes negative and therefore increases the total measured voltage drop from D to E. As can be seen from equation (3.7) the electromotive force depends on the size of the loop (b and c) and the *change* in current with time. The electromotive force can therefore be decreased by minimising the size of the loop and the time derivative of the current.

A DC-current will typically distribute itself uniformly in a given conductor. If the current is alternating the current distributes itself so that the current near the surface of the conductor is greater than at its core [61]. In other words the current tends to flow at the "skin" of the conductor. This so-called skin effect originates from the presence of Eddy Currents [11] created by the oscillating mobile charges in the material. The skin effect increases with the frequency of the current and decreases with the resistivity of the material. The implications of the skin effect is that the effective resistance of the conductor increases with increasing current frequency. Terman [62] provides a formula for calculating the approximate diameter D_W of a conductor with a 10% resistance increase.

$$D_W = \frac{200\text{mm}}{\sqrt{f/\text{Hz}}} \tag{3.8}$$

Using equation (3.8) with the low power grid frequency of 50Hz the diameter $D_W \approx 28$mm is found. Normal size wires are practically unaffected by the skin-effect but if measuring on workpieces with considerably larger dimensions the skin effect might artificially increase the electric resistance of the material.

3.2 Experimental Method

In this section a method for measuring the electric resistance is developed. The procedure takes offset in the work by Song [10] using a Gleeble system for heating and applying pressure while an external system measures the electric resistance. This method is suitable as it can be used almost directly to measure the electric contact resistance. This is further investigated in chapter 4.

3.2.1 Experimental Procedure

The Gleeble 1500 system has been described in more detail in chapter 2 and therefore no general description is given here. The Gleeble heating system uses an A/C 60Hz current to resistance heat the specimens. The current profile is shown in figure 3.3 and it is noted how the current is applied in pulses with periods of zero current in between.

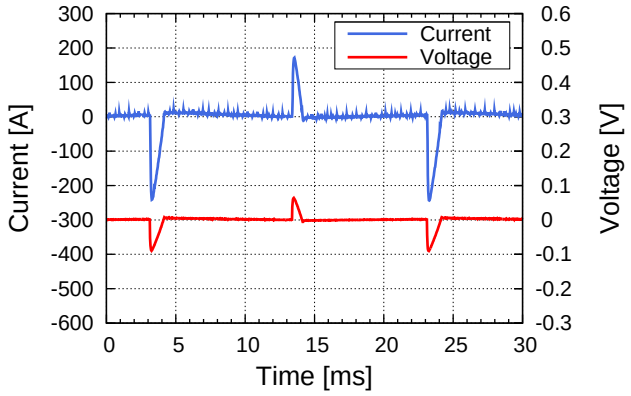

Figure 3.3: Example of current profile from the Gleeble

The principle of the experimental method for measuring the material electric resistance is to measure corresponding values of the current supplied by the Gleeble and the voltage through round cylindrical specimens of the test material. By using Ohm's Law the electric resistance can then be estimated. The Gleeble itself is not able to output neither current nor voltage through the specimen, and so this is measured with external equipment. The current is measured using a Rogowski coil (TECNA-1430) from the company TECNA SpA, Bologna, Italy. The coil is connected to a National Instrument BNC-2110 data acquisition board. The voltage is measured by micro resistance welding copper wires on the side of the specimen and measuring the voltage directly on the data acquisition board. The wires are placed approximately 3mm from the end of the specimens to avoid that any heat loss to the anvils might influence the temperature in the measuring zone. The distance between the wires is measured in order to be able calculate the material resistivity according to equation (3.2). The setup is schematically illustrated in figure 3.4.

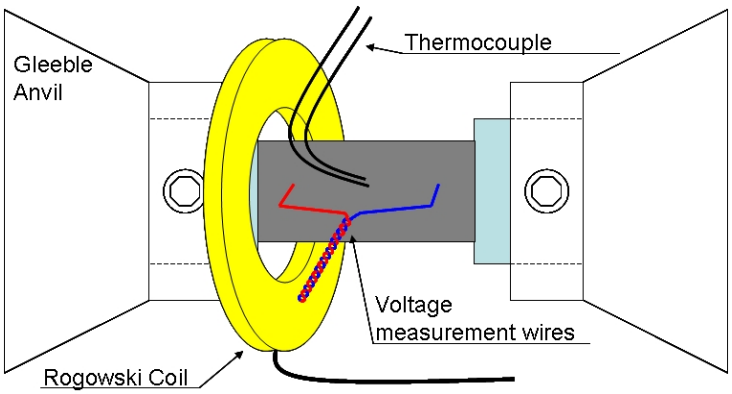

Figure 3.4: Schematic illustration of setup for resistance measurements [54]

The resistivity of the three materials, Nickel 200, stainless steel AISI 316L, Al6060 and S235JR carbon steel (∼0.3% C) is tested. The dimensions of the round cylindrical test specimens are given in table 3.1. The test is performed by:

- Heating the specimen to the specific measurement temperature and holding it at that temperature for 30 seconds to ensure a uniform temperature.
- Measure corresponding values of current and voltage for 30 seconds.
- Increase temperature to the next measurement temperature and repeat the measurement. The temperature is increased with intervals of 100°C.

The measurements are done with 3 repetitions, i.e. on three different specimens, in order to decrease the influence of experimental variation.

Table 3.1: Diameter and height of test specimens for resistivity test

	D [mm]	**h [mm]**	**h/D**
SS316	8	21	2.6
Ni200	10	26	2.6
Al6060	8	26	2.3
S235JR	8	26	2.3

3.2.2 Estimation of Electric Resistance

The resistance of the workpiece is calculated by Ohm's Law. However as indicated in section 3.1 the total measured voltage consist of the voltage drop due to the bulk electric resistance of the test specimen U as well as the induced electromotive force ε_m from the generated magnetic field.

$$R = \frac{U + \varepsilon_m}{I} \tag{3.9}$$

As also indicated in section 3.1 the induced error voltage can be decreased by 1. minimising the loop of the measurement wires and 2. minimise the gradient of the current. Regarding the first issue the loop is manually minimised by making the wires follow the side of the specimen and then twisting them as illustrated in figure 3.4. The second issue is considered by calculating the resistance at the peak of the current signal where $\frac{\mathrm{d}I}{\mathrm{d}t} \approx 0$. This is done automatically by programming the data acquisition programme to extract the peak current and the corresponding voltage drop through the specimen at that time. This is illustrated in figure 3.5.

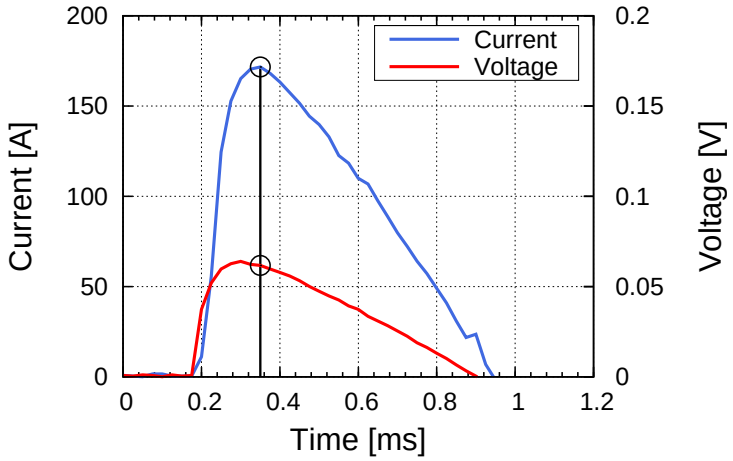

Figure 3.5: Procedure for extracting peak current and corresponding voltage value

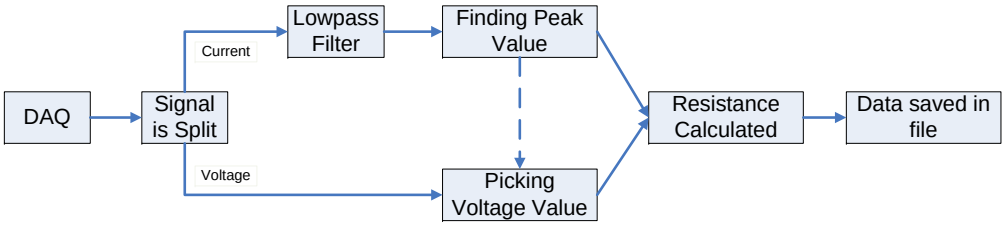

Figure 3.6: Flow diagram of data acquisition procedure [54]

The current frequency is 60Hz, and as the resistance is evaluated at every peak of the current the effective acquisition rate of the resistance measurements is thus restricted to 60Hz. Due to high frequency noise on the current signal it was further necessary to filter the current signal with a low-pass filter before extracting the peak current values. The final value of the material resistivity at a specific temperature is found by averaging the electric resistance measured during the 30 seconds measuring period. The complete data acquisition procedure is schematically illustrated in figure 3.6. To calculate the material resistivity equation (3.2) is applied together with the measured distance between the wires and the cross sectional area of the specimens as given in table 3.1.

3.3 Results

The estimated average resistivity as a function of temperature is plotted in figure 3.7 on page 51. The error bars on the plot represent ± the calculated standard deviation of the three repetitions. It is noted that the repeatability of the test in general is very good. Table values[1] are plotted together with the results [63–66]. The credibility of these table values cannot be verified elsewhere but they generally agree well with the results, although the results for the mild steel show an increase in resistivity at low temperatures which is an unexpected behaviour. The nickel show a similar tendency however on a much smaller scale. The resistivity of nickel is found to be considerably lower than the stainless steel while the mild steel increases steadily with temperature. The resistivity of the aluminium alloy is very low compared to the other material, but despite its absolute increase in resistivity with temperature is small the relative increase is substantial. Judging from the table values the resistivity of the mild steel was expected to be initially very low (close to the nickel) and then increase to a level close to that of the stainless steel. The discrepancy of the mild steel with the table values and the unexpected decrease in resistivity with temperature is discussed in the following section.

3.4 Discussion

Looking at the results, why does the stainless steel show such good agreement with tables values at room temperature while nickel and especially the mild steel show significantly and consistent deviation? The main explanation for this is believed to be the ferromagnetic properties of nickel and mild steel. This hypothesis is based on the fact that only the materials having ferromagnetic properties show deviation from the table values and that the temperature range showing deviation is related to the Curie temperature of the materials.[2] For mild steels this temperature is related to the austenization temperature ($\sim 700°C$) because austenite is paramagnetic while ferrite and martensite is ferromagnetic. For nickel the Curie temperature is approximately 350°C. From the results it is seen how both materials show much better correlation with table values after reaching these temperatures - and even somewhat before reaching them.

The explanation to the influence of the materials ferromagnetic properties is believed to be found in the inductive effect of the material. The magnetic properties

[1] As no exactly matching tables values for the S235JR mild steel was found the values on figure 3.7 is from hot rolled AISI 1023 steel ($\sim$ 0.25%C) which has close to the same alloy content [63].

[2] The Curie temperature is a material specific temperature above which a material losses its ferromagnetic properties and becomes paramagnetic [55].

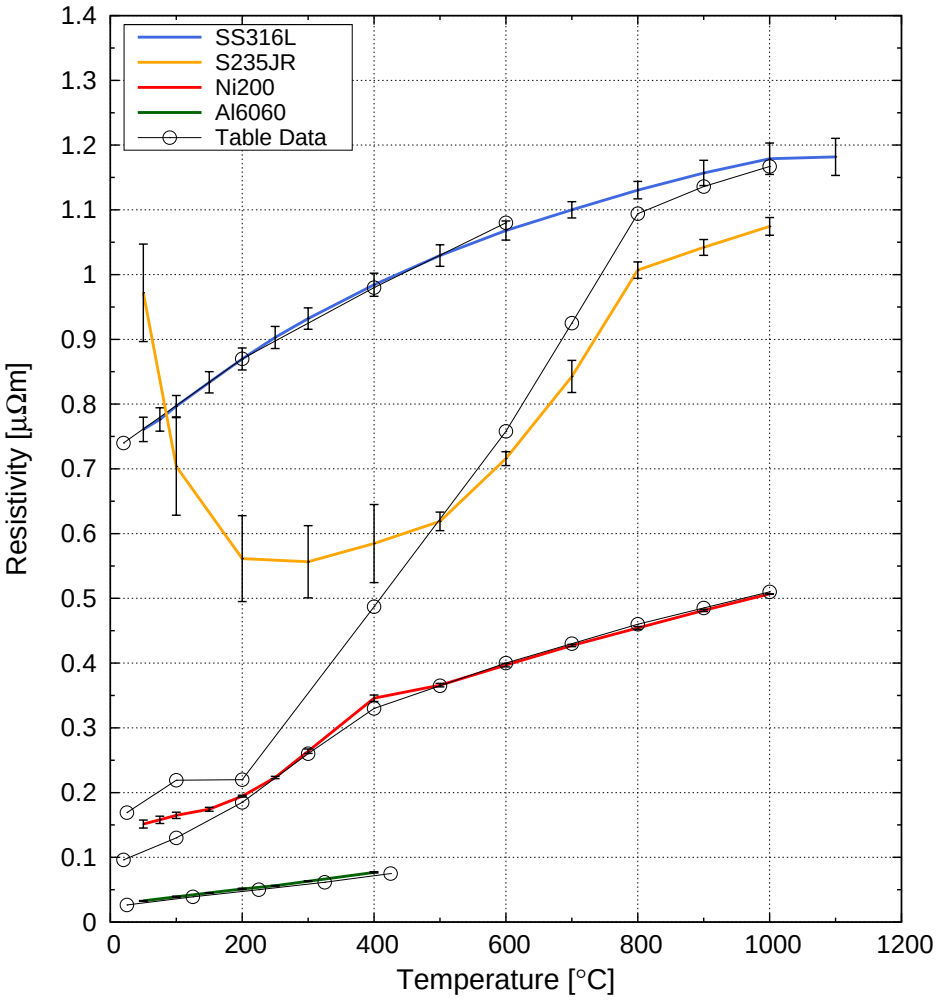

Figure 3.7: Measured material resistivity and table values [63–66]

of the specimen will work like an inductor in an electric circuit. The profile of the current signal provided by the Gleeble is illustrated in figure 3.3. As can be seen from the figure the current signal is not a standard A/C sine-curve but it consist of rather short current pulses. If an inductor is imposed a current pulse it will resist the flow of the imposed current resulting in an initial large increase in voltage through the inductor followed by an exponential decay. The magnitude of the voltage peak and the time needed for the voltage peak to settle depends on the inductance and the size of the current.

The permeability of ferromagnetic materials can be as high as $\sim 10^6$ which implies that the self induction of especially the mild steel specimens is high enough for them to function as inductors [55]. The influence of the self-inductance on the measurements is illustrated in figure 3.8 which show the voltage and current curves for the mild steel for three different measuring temperatures.

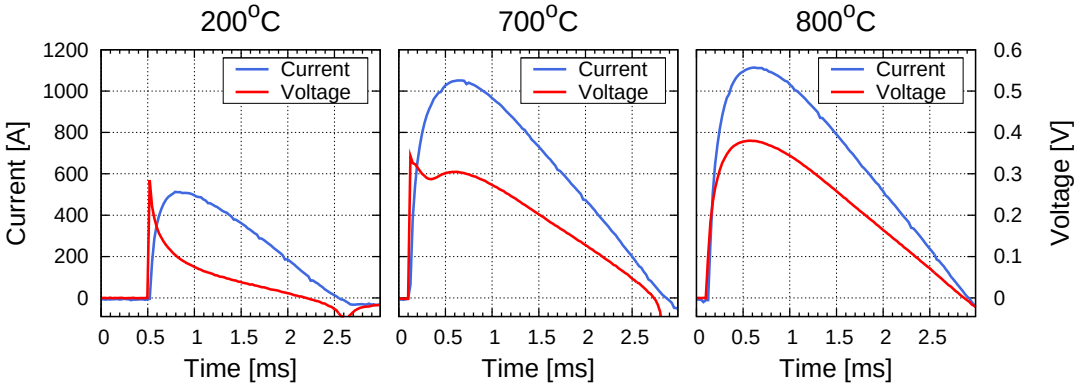

Figure 3.8: Influence of self induction on the measured voltage signal

For the low temperature measurement the material is still far from its Curie temperature and the material is therefore highly ferromagnetic and has a large self inductance. This results in the measured voltage response as seen on figure 3.8 (200°C) where the voltage initially peaks and then decays resulting in a too high resistance calculating. For higher temperatures closer to the Curie temperature of the material the measured voltage and current is illustrated in figure 3.8 (700°C). Here the influence of the self inductance is still visible in the beginning of the signal but it is no longer strong enough to influence the measurement at the peak current. This can be seen on figure 3.7 where the results conform much better with the table values. At even higher temperatures (800°C) the influence is not even visible on the measured voltage curve, and the resistivity increases with increasing temperature as expected for steels [55].

The experimental measurements suggest that the method applied in this study is not suitable for directly measuring the resistivity of materials showing ferromagnetic properties and having a high permeability - at least at temperatures below the Curie temperature of the material. However, this includes many types of normal steels that have either martensite or ferrite as its main microstructural constituent. At a first glance this significantly limits the use of the measuring method. By performing more advanced electrical analysis of the closed circuit in which the specimen is a part of and calibrating it with respect to the measured signals, it is most likely possible to compensate for the inductive response thereby getting better results at low temperatures. However such an analysis is not part

of the scope of the present study. Another initiative could be to decrease the cross section area of the specimen. In this way the ohmic resistance of the specimen is increased due to the smaller conducting area. This will increase the measured voltage contribution from the ohmic resistance of the specimen and thereby possibly exceed the voltage contribution from the inductive load, as it is illustrated on figure 3.8 for 700°C. Presumably the reduction of the area will either not affect or it might even reduce the inductive load due to a decrease in bulk volume of the specimen resulting in improved measurements. However this requires experimental confirmation.

As can be seen from the results in figure 3.7 the increase in the different materials resistivity with temperature all show different behaviour. The resistivity of nickel is seen to increase linearly with temperature but showing a sharp bend around 400°C. As Nickel 200 is almost pure nickel this bend is not a result of a phase transformation [67]. Rather it could be due to an annealing effect on the microstructure initiating around 400°C which will reduce the number of imperfections (dislocations) thereby decreasing the rate of resistivity increase with temperature ($\frac{\mathrm{d}\rho}{\mathrm{d}T}$). The stainless steel must be considered a relatively high alloyed steel which explains the high resistivity. A slight decrease in $\frac{\mathrm{d}\rho}{\mathrm{d}T}$ is observed but the overall behaviour is close to linear. Disregarding the erroneous measurement below 600-700°C the resistivity gradient $\frac{\mathrm{d}\rho}{\mathrm{d}T}$ of the mild steel is considerably higher than for the other materials. At 800°C a bend of the curve is observed. This might be due to the austenite transformation occurring around $700 - 800$°C and as can be seen the gradient $\frac{\mathrm{d}\rho}{\mathrm{d}T}$ of the austenitic mild steel is almost identical to the gradient of the austenitic stainless steel. This suggests that the crystal structure (BCC or FCC) for steels has a significant effect on the electrical resistivity and/or the rate of change with temperature $\frac{\mathrm{d}\rho}{\mathrm{d}T}$. Considering that the electric resistivity is caused by the number of free electrons and their mobility it is not unsupported that the crystal structure of the metal will have an influence on the electric resistivity. As expected the aluminium has a very low resistivity and a practically linear increase in resistivity with temperature. As long as the self-inductance of the specimens can be ignored the validity of the measuring technique developed in this chapter is good. This is mainly credited to the low experimental variation and the good agreement with relevant table values.

3.5 Conclusion

The experimental method developed in this study for measuring electrical resistivity of round cylindrical specimens at elevated temperatures is based on the Gleeble system. The test procedure is relatively simple and fast to perform. The experimental procedure compensates for the influence of the induced electromotive force

in the measurement wires by extracting corresponding values of current and voltage when $\mathrm{d}I/\mathrm{d}t = 0$. The method shows good repeatability, i.e. small experimental variation, and generally agrees well with comparable table values. However, it was found that the test produces unreliable results for materials with ferromagnetic properties. This is credited to the effect of the large self inductance of the specimen. It is suggested that decreasing the cross sectional area of the specimen might increase the voltage contribution from the ohmic resistance of the specimen and thereby decrease the influence from the inductive load. However this was not tested.

The resistivity of AISI 316L stainless steel, Nickel 200 ($\sim$99% Ni), aluminium Al6060 and mild steel S235JR was tested, the latter highly influenced by its ferromagnetic properties. The results show that the resistivity of the materials increase with temperature and that the (expected) rate of increase for the mild steel was considerably higher than for the other metals when below its austenization temperature. It was noted that stainless steel AISI 316L, Nickel 200 and the mild steel above 800°C all have a FCC crystal structure and that their gradients $\frac{\mathrm{d}\rho}{\mathrm{d}T}$ are almost identical. This suggest that the specific crystal structure influences the sensitivity of the resistivity of the materials with respect to the temperature.

Chapter 4

Electric Contact Resistance

The purpose of this chapter is to investigate the modelling of electrical contact resistance for use in numerical simulation of resistance welding. A literature study on contact resistance is presented introducing both experimental and theoretical results. By further modifying the experimental method for electric resistance measurements presented in chapter 3 the electric contact resistance is measured for the four different materials: Nickel 200 (∼99% Ni), stainless steel AISI 316L, aluminium Al6060, and S235JR mild steel (∼0.3%C). Based on the results and the theoretical foundation the contact resistance is discussed and related to the modelling of resistance welding.

4.1 Literature Study

The electrical resistance increases in an interface between two surfaces. This increase in resistance due to contact is called *electrical contact resistance*, or simply *contact resistance* R_{CR}. The increase in resistance generally arises from two physical phenomena, *constriction resistance* and *film resistance*. The constriction resistance R_c is caused by a non-perfect contact condition where the actual contact area or load-bearing area A_b is smaller than the apparent area of contact A_0. At the interface the flow of the current, which in the bulk material can be assumed uniform, is restricted to flow through the actual asperities in contact at the interface. This physical constriction of the current flow increases the electrical resistance, and this resistance increase is called constriction resistance (see figure 4.1 on page 56).

The other interface phenomena that increases the electrical resistance is the oxide films present on many metals as well as contaminants (oil, grease,...) which acts as insulation. The resistance of films and contaminants R_f is called film resistance. Assuming no interaction between the two types of resistance the total contact

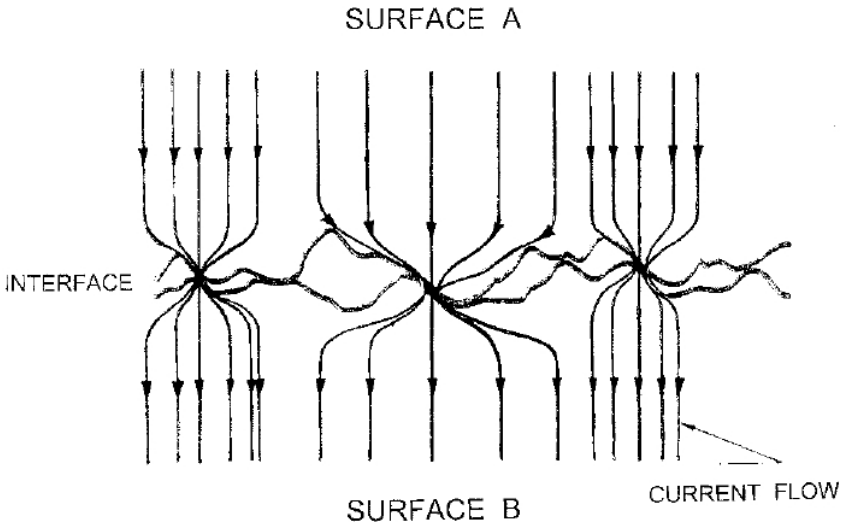

Figure 4.1: Current flow through a real interface [68]

resistance is simply given by:

$$R_{CR} = R_c + R_f \tag{4.1}$$

The constriction resistance is mainly affected by the actual load-bearing area which is highly dependent on the microscopic deformation of the surface asperities in contact. Increasing surface pressure will increase the load-bearing area which will decrease the current constriction and thereby the constriction resistance. Increasing material temperature softens the asperities which also allows for greater deformation of the asperities and less constriction resistance. The film resistance is often rather complicated to predict. The film resistance generally depends on the resistivity of the film, the thickness of the film, the amount of mechanical rupture of the film induced by the surfaces coming into contact, and metallurgical and thermal breakdown of the film. Many metal oxides form electric insulating films that greatly increase the contact resistance in the initial stages of the resistance welding process.

In the following sections a literature review on contact resistance is presented and the main conclusions are discussed in relation to the aims of the current project.

4.1.1 Empirical Investigations

The importance of the effect of the electric contact resistance on the resistance welding process is widely recognised and is specifically discussed by Kaiser et al. [69]. There have been several attempts by researchers to experimentally measure electric contact resistance at conditions similar to those found in resistance welding

- more specifically at high temperatures and high loads. Studer [24] uses a simple lever loading system together with a furnace to measure contact resistance between different types of steels and aluminium. He reports that the variation of contact resistance with load F is most often found to follow a simple power-law relation of the form

$$R_{\mathrm{CR}} = C \cdot F^n \tag{4.2}$$

where C is a temperature dependent constant and n is in the range $[-1; -1/2]$ depending on temperature and material. For increasing temperature Studer [24] also finds that the contact resistance decreases. This is mainly explained by a lowering of the yields strength of the material and by a likely cleaning mechanism that burns off oil and other contaminants, which help to increase contact resistance at lower temperatures. Furthermore, he states that for all practical purposes the contact resistance is found to be independent of the nominal area in contact. Several other researchers [25–27] have measured the contact resistance using equipment of the similar form as Studer [24] and find a relation similar to equation (4.2). Song [28] applies a slightly different approach for measuring contact resistance using a Gleeble system [29]. In this way heating is done by internal resistance heating which is precisely controlled by a feedback system and which allows for very high temperatures and loads. His results are comparable to the previously reported measurements. Weimin [70] measured contact resistance of mild steel (0.45wt%C) also utilizing a Gleeble system. The initial experiments suggested that the loading speed had a significant effect on the behaviour of the contact resistance, however, no detailed experimental investigation was presented to support these observations.

In general experimental measurements of contact resistance show varying results depending on the exact experimental method and the applied materials and type of specimens, and the experimental variation is often reported to be substantial. For these reasons authors are often cautious about making general conclusions regarding the behaviour of the contact resistance for specific materials.

4.1.2 The Load-bearing Area

The load-bearing area or true area of contact A_b is often used in relation to modelling of friction or electrical conductance across an interface and is therefore addressed here. The actual contact between two surfaces consists of several contacting asperities. As the pressure increases the asperities are plastically deformed. This increases the contact areas of the single asperities and allows for more asperities to come into contact which effectively increases the true area of contact. It is shown by Bowden and Tabor [71] that the load-bearing area is independent of the nominal contact area and that it only depends on the load and the strength of the materials in contact. They found that the true contact area A_b can be expressed

as a function of the load F and the yield stress σ_{s_soft} of the softer material in contact.

$$A_b = \frac{F}{3\sigma_{s\_soft}} \tag{4.3}$$

This relation has been shown by Wanheim et al. [72] to hold only as long as the plastic fields of the deforming asperities do not interact. If the surfaces are assumed stationary, e.g. no friction stresses act on the asperities, and the bulk of the material does not plastically deform, equation (4.3) applies until the normal pressure p exceeds approximately 1.5 times the yield stress 2k of the bulk material.

$$\frac{p}{2\mathrm{k}} < 1.5 \tag{4.4}$$

The interaction between neighbouring asperities restrict their plastic deformation which decreases the growth rate of the load bearing area with respect to the load. The load-bearing area will then develop asymptotic towards the nominal contact area. In resistance welding the contact pressure is often not higher than the limit in equation (4.4) which is why equation (4.3) is often used to describe the development of the real contact area in models of contact resistance. However, it has been shown by Wilson and Sheu [73] using an upper-bound analysis, that if the bulk material experience simultaneous sub-surface deformation, then the limit given in equation (4.4) is considerably lower. Sutcliffe [74] confirms this by a slip-line analysis with consideration to sub-surface deformation. Their conclusion is that when sub-surface deformation is present the real contact area develops faster than predicted in equation (4.3) and there is no longer a linear relationship between load and real contact area. The yield strength of the materials in resistance welding is often lowered considerably due to heating of the specimens and it is not unlikely that in many cases - especially in projection welding - sub-surface deformation will occur. This implies that the relation in equation (4.3) might not be adequate to describe the development of the real area of contact in resistance welding.

4.1.3 Mathematical Analysis

Some of the first attempts to model electrical constriction resistance between contacting metallic surfaces was done by Holm [8]. Greenwood [7] later presented the theory by Holm and further validated it by a thorough investigation which is often cited in literature. Holm states that when two large conductors with radius $D/2$ touch over a small circular area with radius a, it can be shown that there is a constriction resistance R_c between them given by

$$R_c = \frac{\rho}{2a} \tag{4.5}$$

whenever $D/2 >> a$ (cf. [8]). However, when two metals touch the actual contact is formed between *several* contacting asperities of the two surfaces - not a single uniform spot. Depending on the large scale waviness of the surfaces the contact is formed by a number of clusters of micro-contacts. The constriction resistance will then depend partly on the number and size of micro contacts and partly on their grouping into clusters. Greenwood [7] analyses the most simple case where two semi-infinite bodies make contact through a single cluster of micro-contacts. Greenwood assumes that all the micro-contacts in the cluster are uniformly distributed and share the same equipotential and he uses electrostatic theory to derive the following expression of the electric constriction resistance between the two contacting bodies.

$$R_c = \rho \left(\frac{1}{2na} + \frac{1}{2\alpha} \right) \tag{4.6}$$

where ρ is the electric resistivity of the metals, n is the number of micro-contacts, a is the (average) radius of the micro-contacts, and α is the Holm radius [7]. The analysis by Greenwood shows a geometrical interpretation of the two terms in equation (4.6). The first term is denoted the *self-resistance* of the micro-contacts. This term only depends on the number n and average radius a of the contacts - not their relative positions inside the cluster. It is obvious that if contact is made between only a few small micro-contacts, then the self-resistance is large. On the other hand, if there are many large contact spots the self resistance becomes small. The second term is related to the electric *interaction* between contact spots. This term depends not on the size but on the number and the positions of the contacts. Greenwood [7] estimated the following mathematical expression of the Holm-radius

$$\alpha^{-1} = \frac{3\pi}{16n^2} \sum \sum \frac{1}{s_{ij}} \tag{4.7}$$

where s_{ij} is the distance between the i'th and j'th contact spot and $i \neq j$. Greenwood shows that for a small number n of contact spots the interaction-term will be small compared to the self resistance, which will dominate the constriction resistance. When the number and size of contact spots increase the self resistance decreases and as the average spot-to-spot distance decreases the interaction between contact spots becomes significant. This is illustrated in figure 4.2a on page 60 showing a random cluster of micro-contacts and in figure 4.2b showing the corresponding constriction resistance calculated using equation (4.6). As seen from the figure the total constriction resistance decreases as the number and size of micro-contacts increases. In theory, as the number of micro-contacts increases and fills up the cluster, the total resistance should approach the constriction resistance of a single contact spot with a radius equal to the cluster radius. Greenwood [7] shows that the interaction term approaches a constant value with increasing n implying that the Holm-radius in equation (4.7) becomes constant for a large n.

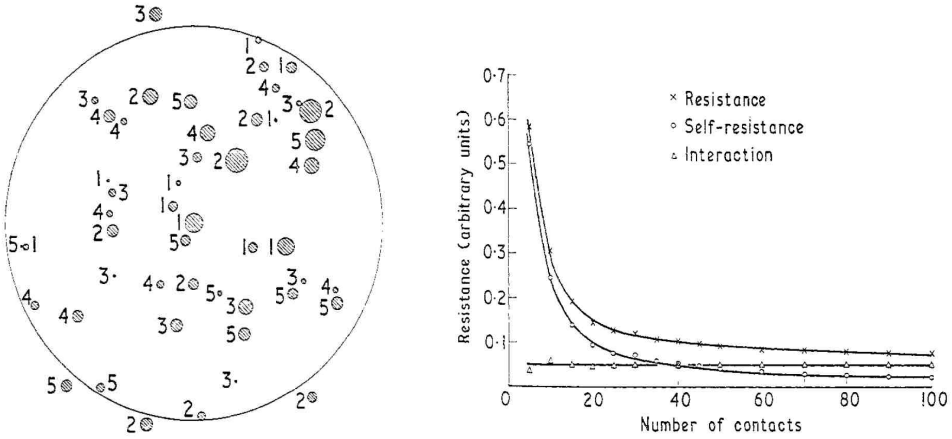

(a) **(b)**

Figure 4.2: Example from Greenwood [7] showing (a): Example of cluster, (b): Calculated constriction resistance of cluster

Greenwood explains that for a cluster of linear dimension l the mean spot-to-spot distance is approximately $l/2$ and the doubled summation in equation (4.7) can be approximated by $n(n-1)2/l$. For a large n this approximately equals $2n^2/l$ and implies that the Holm-radius can be expressed as the following constant value independent on the number and size of micro contacts and only depending on the size of the cluster.

$$\alpha^{-1} = \frac{6\pi}{16l} \tag{4.8}$$

It is noted that equation (4.8) according to Greenwood [7] applies for a large number of contact spots n and for a well-defined cluster with linear dimension l.

Although the work by Greenwood [7] is often cited in literature it is difficult to use equation (4.6) directly to calculate the constriction resistance as it requires knowledge of the number and size of the micro-contacts as well as the size of the cluster. The entire analysis by Greenwood [7] assumes that two semi-infinite bodies contact through a single cluster of micro-contacts. This implies that boundary effects from the edges of the real conductors as well as interactions between individual *clusters* of micro contacts, which are present in a real contact situation, are ignored. The analysis by Greenwood [7] can therefore not directly be used to calculate constriction resistance in an arbitrary contact situation.

Braunovic et al. [75] extend the result by Greenwood by introducing a "cluster" term in equation (4.6). They do this by using the same technique as Greenwood but replaces the distance between contact spots with the mean distance between clusters. The Holm radius is replaced by a radius r that encompasses all contact

clusters and the upper limit for r is therefore equal to the radius of the apparent area of contact. Based on this Braunovic et al. [75] suggest the following expression for describing the contact resistance of an interface, where n_c is the number of clusters.

$$R_{CR} = \rho \left(\frac{1}{2na} + \frac{1}{2n_c\alpha} + \frac{1}{2r} \right) \tag{4.9}$$

Just as the original expression by Greenwood the expression in equation (4.9) is not very applicable for practical calculations of the resistance as the size and number of both contact spots and clusters are very difficult to estimate in practise.

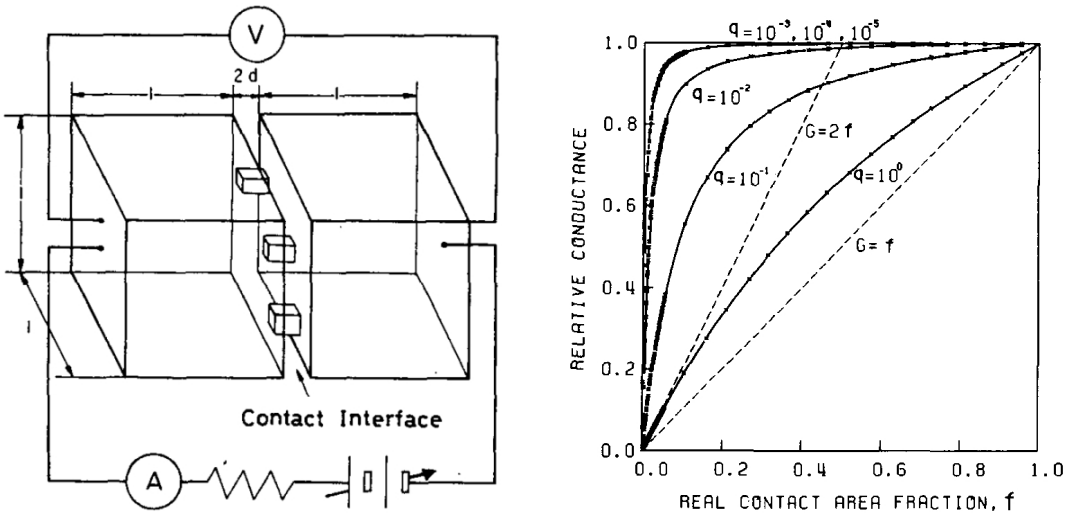

(a) Schematic FE-model [76] **(b)** Calculated relative conductance [77]

Figure 4.3: Example from Nakamura and Minowa [76, 77]

Nakamura and Minowa [76, 78, 79] apply the FE-method and build a "global" model of a contact interface. The model is schematically shown in figure 4.3a and consists of two conducting blocks connected by n number of square contact spots with thickness $2d$. The resolution of the contact interface, or the nominal area of contact, is given by N^2, where N is the number of contact spots along one side of the blocks. By varying the number of contact spots they estimate the relative conductance (i.e. the conductance of the interface to the conductance of a perfect interface) as a function of the contact area fraction f (i.e. the real area of contact to the nominal contact area). In figure 4.3b the results of the investigation are shown indicating the effect of relative film resistance q[1]. They are able to reproduce the theoretical formulae by Holm [8] and Greenwood [7] for a single contact spot and a cluster of contacts (equation (4.5) and (4.6)) from

[1] A small q corresponds to a low film resistance and vice versa

their numerical results. Nakamura and Minowa [76] conclude that the relative conductance is highly sensitive to the number as well as the distribution of contact spots for low contact area fraction $f < 20\%$ and that the relative conduction for a larger f is very close to unity - implying zero contact resistance. In a later work they investigate the effect of surface film on the contact resistance using the same numerical model [77]. As can be seen from figure 4.3b their results suggest that a higher film resistance (increasing value of q on figure 4.3b) will decrease the rate of increase of the relative conductance of the contact-pair with increasing load-bearing area [77]. This suggests that there is an interaction between surface film resistivity and the influence of the real contact area on the conductivity.

4.1.4 Single Contact Spot Approximation

Timsit [68] appreciates the conclusion by Greenwood and uses his results to estimate the constriction resistance as a function of the load-bearing area A_b. Timsit [68] suggests that the constriction resistance can be estimated purely through knowledge of the Holm-radius. More precisely Timsit assumes that the self resistance in equation (4.6) can be ignored assuming n is always large for any practical surface. This implies that the constriction resistance R_c can be estimated by the Holm-radius α as

$$R_c = \frac{\rho}{2\alpha} \tag{4.10}$$

This expression equals the classical expression for constriction resistance through a single contact spot given by equation (4.5) but here the spot radius equals the Holm-radius. He assumes next, without any reference to literature or explanations, that the Holm-radius and the load-bearing area are directly dependent via the following relation

$$A_b = \xi \pi \alpha^2 \tag{4.11}$$

where ξ is an empirical coefficient of the order unity. Equation (4.11) expresses that the Holm-radius approximately equals the radius of a circle with an area equal to the total load-bearing area. In other words the theory presented by Timsit [68] suggests that the constriction resistance can be calculated by assuming that contact occurs through a single contact spot with an area equal to the total load-bearing area of the actual asperities in contact.

Although the theoretical derivation by Timsit [68], which are later adopted by Song [10], involves considerable simplifications, the final *form* of the model for the constriction resistance is found to agree reasonably well with empirical results in literature [68]. The final model is derived by combining equation (4.10) and (4.11) and inserting the expression in equation (4.3) for the load-bearing area, which

yields

$$R_c = \frac{\rho}{2}\sqrt{\frac{3\xi\pi\sigma_{s\_soft}}{F}} \tag{4.12}$$

It is noted that the model in equation (4.12) is proportional to the square root of the yields stress of the softest material in contact σ_{s_soft} divided by the load F. Equation (4.12) models constriction resistance of an interface between two conductors of similar resistivity. In order to model constriction resistance between conductors of dissimilar materials Song [10] modifies the model by using the average resistivity of the interface $\rho = (\rho_1+\rho_2)/2$. Furthermore, he implements the effect of surface film resistance by adding a material specific resistivity coefficient ρ_f which is a function of temperature. This results in the following expression for the total contact resistance across an interface

$$R_c = \left(\frac{\rho_1+\rho_2}{2} + \rho_f\right)\sqrt{\frac{3}{4}\frac{\xi\pi\sigma_{s\_soft}}{F}} \tag{4.13}$$

Song [10] estimates the film resistance ρ_f by using empirical data. He reports only limited agreement with his experimental measurements of contact resistance for stainless steel, mild steel, and aluminium.

4.1.5 Asperity Density Model

Babu et al. [26] also derive a theoretical expression for the contact resistance of metals based on the work by Greenwood [7]. Contrary to Timsit, Babu et al. include both terms in equation (4.6). They estimate the Holm radius by the following expression

$$\alpha^{-1} = \frac{6\pi}{16nl} \tag{4.14}$$

Except from the n factor, this expression is identical to the approximate expression in equation (4.8) of the Holm radius for large values of n derived by Greenwood. This results in the model given in equation (4.15).

$$R_{CA} = R_c A_0 = \frac{\rho_1+\rho_2}{2}\left[\left(\frac{\pi\sigma_{s\_soft}}{4\eta F}\right)^{1/2} + \frac{3\pi}{8\eta^{1/2}}\right] \tag{4.15}$$

R_{CA} is defined as the *unit area contact resistance* equal to the measured resistance multiplied by the nominal area $R_c A_0$ and is introduced by Babu et al. to: *"...facilitate comparison of resistance measurements..."*. In this way the nominal contact area A_0 will have an effect on the result which is contradictory to the observations by Studer [24]. Equation (4.15) is of similar form as equation (4.12) having a square root dependency of the force F and the yield stress σ_{s_soft}. However, the model by Babu et al. also depends on the number of micro-contacts via the *con-*

tacting asperity density η defined as the number of micro-contacts divided by the nominal area of contact n/A_0. The contacting asperity density is found empirically as a function of temperature, load, and yield strength by fitting equation (4.15) to experimental determined values of R_{CA}. Despite the fitting procedure Babu et al. found that the model had problems conforming to experiments for high surface pressure underestimating the contact resistance. They suggest that this might be due to material strain hardening and the effect of deformation rate, which is not accounted for in the model.

4.1.6 Contact Layer Model

A fundamentally different approach to modelling of contact resistance is used by Zhang et al. [4]. This approach does not use equation (4.6) but builds on the assumption that the constriction resistance can be modelled as a resistor, where the total resistance is proportional to the resistivity of the material ρ and the length of the resistor L and inversely proportional to the conducting area A_c. It is assumed that the constriction resistance of a material is associated with a certain depth t of a *contact layer* on the surface contributing to the increased resistance. Hence the contact resistance is modelled as the bulk resistance of an interface layer with the assumed thickness $t_c = t_1 + t_2$, where t_1 and t_2 are the two contributions to the contact layer originating from the two materials in contact. The conducting area A_c equals the load-bearing area A_b of the contact. Assuming $t_1 = t_2 = \frac{t_c}{2}$, the constriction resistance R_c between two materials can be written as the sum of the constriction resistance of the two contact layers

$$R_c = R_1 + R_2 = \rho_1 \frac{t_1}{A_b} + \rho_2 \frac{t_2}{A_b} = \frac{(\rho_1 + \rho_2)}{2} \frac{t_c}{A_b} \tag{4.16}$$

By inserting the expression for the load-bearing area found in equation (4.3) we get the following expression for the constriction resistance between two contacting surfaces:

$$R_s = \frac{3t_c}{2}(\rho_1 + \rho_2)\frac{\sigma_{s\_soft}}{F} \tag{4.17}$$

The contact resistance due to surface film, contaminants, and oxides are added as an extra resistivity term ρ_f to the resistivity of the two materials. This term is a material specific function depending on temperature.

$$R_c = 3t_c\big(\frac{\sigma_{s\_soft}}{F}\big)\big(\frac{\rho_1 + \rho_2}{2} + \rho_f\big) \tag{4.18}$$

The relation above builds on the assumption that a part of the surfaces in contact with depth t_c have the total (bulk) resistance R_c as in equation (4.18). The assumptions regarding the presence of a contact layer is not supported elsewhere

in literature, but despite this reasonable agreement with experiments have been reported [10]. In fact, the model has been implemented and is currently used as the generic model for determining contact resistance in the commercial software SORPAS for simulation of resistance welding.

4.1.7 Discussion of Literature Study

As mentioned in section 4.1.3 the fundamental equation (equation (4.6)) by Greenwood [7] does not describe the behaviour of an entire interface but rather the theoretical contact resistance of a single cluster of contacts. This implies that the contact resistance of the cluster does not approach zero for large n, rather it approaches the expression of the contact resistance of a single contact spot (equation (4.5)) with radius $a \approx \alpha$. The models derived by Timsit [68] and Babu et al. [26] use equation (4.6) as an offset to derive a *general* expression for the contact resistance of an interface. It is not examined how the interaction of clusters affect the electrical contact resistance and its effect is therefore unknown. In the following the models presented in the previous sections are shortly critically addressed.

Theoretical Models

The derivation of equation (4.12) by Timsit assumes that the contact resistance of an interface can be assumed to consist of a single circular contact spot with an area equal to the total load-bearing area. This implies that the Holm radius increases with an increasing number of contacts. This does not comply with theory by Greenwood [7]. According to Greenwood the Holm-radius is not equal to the equivalent single contact spot radius but rather equal to the radius of the cluster as n increases. In his discussion Greenwood argues that it is *not* correct simply to estimate the real area of contact from the constriction resistance using the hypothesis of a single circular contact given by equation (4.5) as this gives erroneous estimates of the contact resistance [7, page 1630].

The model by Babu et al. [26] (equation (4.15)) is also claimed to be based on Greenwood [7]. However, the expression for the Holm radius in equation (4.14) does not agree with the expression developed by Greenwood. Because the factor n now conveniently occurs in both terms in the equation it is possible to continue the derivation by dividing with the nominal area [26, page 127]. By introducing the factor n in the term for interaction between contact spots the Holm radius becomes dependent on the number of contact spots for large values of n. Again this is contradictory to the results presented by Greenwood [7] who argues that for a large number of contact spots the cluster resistance approaches the resistance of a single contact spot having the cluster radius equal the Holm radius.

The theoretical basis of the *contact layer model* presented in equation (4.18) does not take offset in the theory by Greenwood. The model does not consider aspects of the electric flow through single contact spots or asperities. Rather it takes on a more "engineering approach" to modelling of the contact resistance by defining a contact zone/volume that behaves like a simple resistor. This is especially appropriate for using the model in FE-software as the contact layer can be directly simulated by special interface elements incorporating the electrical behaviour of the model.

Although the described models show a power-law relation similar to the empirical investigations (cf. section 4.1.1), it can be argued that the theoretical foundation of the models is questionable. This is probably also why the models often do not directly fit to experimental values, and typically it is necessary to include a fitting parameter in the model that accounts for surface films, contaminants etc. However, despite the dubious theoretical description of the underlying phenomena determining the contact resistance, the models *do* describe the general influence of the main large-scale parameters such as contact pressure, material yield stress, and resistivity.

Influence of Main Parameters

The theoretical models presented in the previous sections all utilise the load-bearing area as a parameter in the model and relates this to the force and strength of the materials in contact as given in equation (4.3). In this way the effect of the load on the contact resistance is introduced and can in all cases be simplified to the form given in equation (4.2). This is of course only true until the deformation fields of the asperities start to interact which depends on the contact pressure and, as explained in section 4.1.2, the amount of sub-surface deformation in the material [74]. If in fact the relation given in equation (4.3) underestimates the load-bearing area due to a lowering of the yield stress caused by material heating and due to subsurface deformation, the models presented previously overestimate the actual constriction resistance.

So far in this discussion the effect of surfaces films on contact resistance has only slightly been addressed. In practical terms it is difficult to experimentally evaluate the effect of surfaces films on the contact resistance. Theoretically film resistance is generally considered to be proportional to the thickness of the film and inversely proportional to the area of the contact spot [24, 25]. One of the main problems in relation to modelling of surface films is to be able to describe the mechanical and metallurgical rupture of the film during loading. Especially mechanical rupture of the film is extremely difficult to model as it depends on the shape and deformation of the individual asperities in contact. For this reason the contact resistance of

surface films is often either ignored or assumed as a constant contribution to the resistance, as is the case in the single contact spot- and contact layer model in equation (4.13) and (4.18), respectively. Due to the high degree of complexity involved in modelling of surface films in relation to resistance welding, it will in most cases be practically impossible to separate the film resistance from the constriction resistance in any experimental measurements of contact resistance. For this reason surface film resistance will not individually be addressed or specifically sought measured in the further investigation.

Modelling

The theoretical basis for the models for calculation of the contact resistance [4, 10, 68] is in general found to be too simple to function as a general purpose model for contact resistance. The physical phenomena of contact resistance is an extremely complex matter having many influencing parameters as well as interactions among these parameters. The most obvious parameters are pressure, temperature, bulk resistivity, bulk yield stress, surface film resistance and rupture, load-bearing area, the formation and interaction between clusters of micro-contacts, as well as mechanism of asperity deformation. The development of a theoretical model that incorporates the main significant parameters and their interactions must therefore be based on an extensive and systematic experimental investigation. Empirical data should be used as the basis for developing the theoretical knowledge necessary for understanding and modelling of the actual physical phenomena involved. However, such investigations demand large amounts of resources due to the large amount of parameters that possibly influences the contact resistance.

Despite the lack of detailed understanding of the contact resistance, the models so far have proved to be adequate to understand and to model the entire process. In resistance welding the influence of contact resistance is important but because of the relatively large bulk volumes involved in normal scale resistance welding it is possible to achieve even very accurate results for predictions of the final weld result while still using the approximated models presented above. However, in micro resistance welding the effect of downscaling means that much lower currents and less force is used in the process. It is known from the downscaling of cold forming of micro components that the so-called size effect influences friction conditions due to the decrease in surface area combined with unaltered surface roughness [80]. This implies that the understanding of the governing physical mechanisms in contact resistance models become increasingly important in relation to modelling of resistance welding on small- and micro-scale. The current study aims at partly investigating the proposed method for measuring contact resistance and partly it is sought to highlight and identify discrepancies and areas of improvement of the governing theoretical models for contact resistance in resistance welding.

4.2 Measuring Contact Resistance

In this section the experimental investigation of the contact resistance between round cylindrical test specimens is presented. The experimental method and the obtained results are discussed in relation to possible sources of error and variation. Based on the experimental observations the modelling of contact resistance is discussed.

4.2.1 Experimental Procedure

The experimental procedure is to a large degree based on the method presented in chapter 3 for measuring bulk electric properties. For measuring the contact resistance two round cylindrical specimens are placed end to end between the Gleeble anvils as seen in figure 4.4. The wires for measuring the voltage drop across the

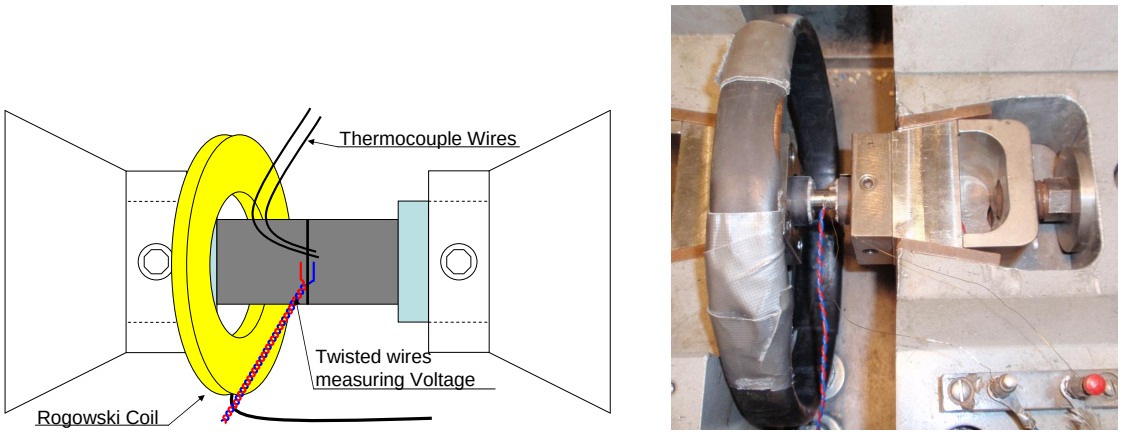

Figure 4.4: Experimental setup of contact resistance measurements

interface are welded to the specimens close to the interface to minimise the induced electromotive force in the wires, as explained in section 3.2.2 on page 48. For each test the distance between the wires is measured with a calibre in order to be able to compensate for the bulk resistance of the specimens in the calculation of the contact resistance. On average the distance is 1.3mm implying that the contribution from the bulk resistance is expected to be small. Careful alignment of the specimens is necessary before the anvils are slightly moved just enough to keep the specimens in place. Due to the rather rough resolution of the control of the anvil displacement a minimum force of approximately 400N was on average applied as the initial contact pressure. The experiments are performed at constant temperatures by steadily heating the specimens to the desired measuring temperature and keeping them at that temperature to ensure a uniform temperature at the

interface. Based on approximate values of the thermal expansion of the specimens the anvils are moved during heating to compensate for the calculated increase in length. Following the heating stage the actual measurements are performed by step-wise increasing the contact pressure while measuring corresponding values of heating current and voltage drop. The procedure is schematically illustrated in the flow diagram in figure 4.5.

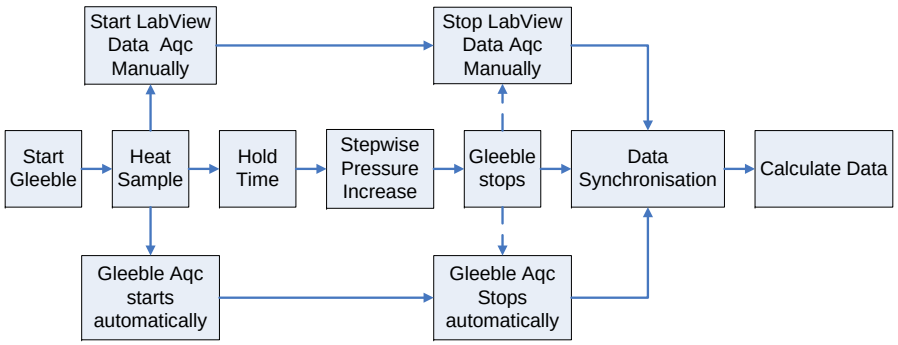

Figure 4.5: Flow diagram of procedure for contact resistance measurements [54]

At each pressure level corresponding values of force, temperature, current, and voltage is measured in a $t = 5\text{s}$ period. Corresponding values of peak current $I_{\max}$ and voltage $U_{I_{\max}}$ are extracted from the measurements resulting in a total of $n = 5s \cdot 60\text{Hz} = 300$ values. The contact resistance $R(p_0, T_0)$ for pressure level p_0 and temperature T_0 is then calculated by

$$R(p_0, T_0) = \frac{1}{n} \sum_{i=1}^{n} \frac{U_{I_{\max},i}}{I_{\max,i}} = \frac{1}{n} \sum_{i=1}^{n} R_i \tag{4.19}$$

The pressure and temperature is calculated in a similar way.

4.2.2 Preparation of Test Specimens

In order to test the applicability of the measuring method as well as getting a varied picture of the behaviour of the contact resistance, four different materials were tested: Nickel 200 (∼99% Ni), stainless steel AISI 316L, aluminium Al6060, and S235JR carbon steel (∼0.3% C). The dimensions of the round cylindrical test specimens are given in table 4.1.

Table 4.1: Diameter and height of test specimens for contact resistance test

	D [mm]	**h [mm]**
SS316	8	6
Ni200	10	6
Al6060	8	6
S235JR	8	6

The test specimens are made from rod material. The actual surfaces being used for testing contact resistance are therefore determined by the way the samples are cut from the rods. The influence and magnitude of this parameter, the preparation method of the test specimens, is unknown, and it is therefore desirable to include it in the experimental investigation. Because of this two different methods were used for preparing the test specimens: Turning and EDM[2]. The two processes produce two distinctively different surfaces. In figure 4.6 are shown close-up pictures of the two surfaces for specimens in stainless steel AISI 316L. Just from visual appearance the surfaces are distinctively different. Surface profiles of nickel and stainless steel specimens are measured using a Taylor Hobson FTS 50mm Stage stylus profilometer. By measuring parallel profiles on a 2×0.5mm area and combining them the surface profiles in figure 4.7 is obtained. Although the scales on the z-axis (the height) is not completely the same on the profiles, the figure clearly show that the turned surface has a regular pattern of groves originating from the cutting tool geometry and the cutting speed, while the EDM wire cut surface is totally arbitrary and does not have any periodic or directional pattern.

[2]Electric Discharge Machining [81]

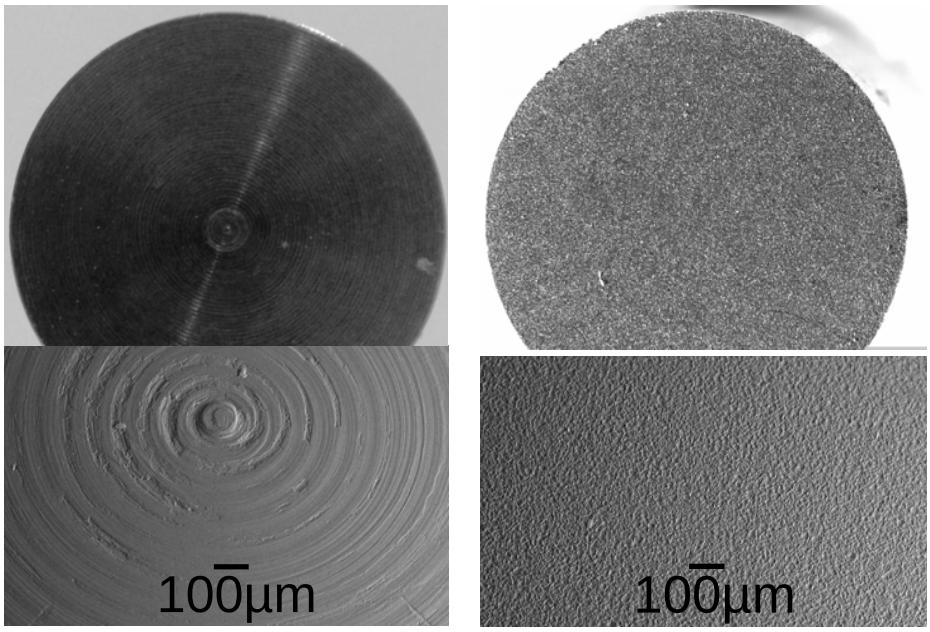

(a) Turning **(b)** EDM wire cutting

Figure 4.6: Close-up of surfaces for contact resistance measurements

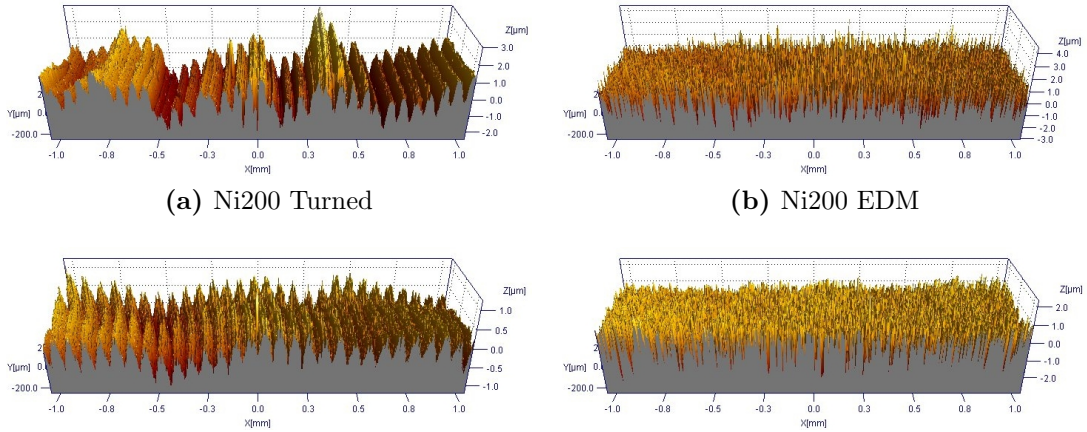

(a) Ni200 Turned **(b)** Ni200 EDM

(c) SS316 Turned **(d)** SS316 EDM

Figure 4.7: Measured surface profiles of turned and wire EDM surfaces

Calculation of mean roughness parameters of the surfaces in figure 4.7 as well as the standard deviations are plotted in figure 4.8. As can be seen the average roughness values of the two surfaces are rather similar while the standard deviations of the means differ depending on the surface type. The variation in the roughness parameters is larger for the turned surface indicating that the turned surfaces are significantly less uniform than the EDM wire cut surfaces.

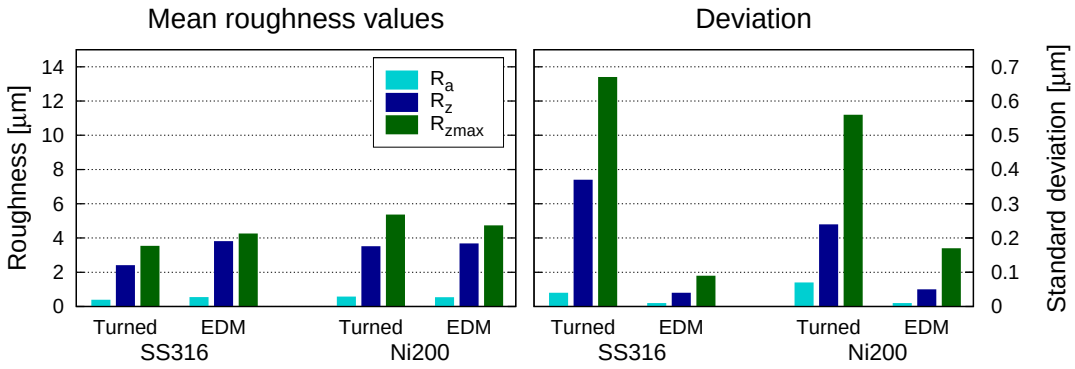

Figure 4.8: Calculated roughness values and coefficients of variation for the surfaces in figure 4.7.

Prior to testing all samples were cleaned in ethanol using an ultrasonic bath. Furthermore, the stainless steel samples were all passivated in nitric acid to ensure a uniform oxide layer on all specimens instead of the more random layer that naturally develops over time and that might be of varying thickness.

4.2.3 Results

In the following sections the measured contact resistance for the different test specimens is presented. For each material data points of the measured contact resistance vs. pressure are plotted with the testing temperature indicated by the point style. A plot for each surface type is made and a calculated average resistance curve for each temperature is plotted. This curve is calculated by averaging the data points falling inside a certain pressure interval and for a given temperature, and it illustrates the general tendency of the contact resistance behaviour. In section *4.2.4 Data Analysis* the data is analysed by fitting it to appropriate models. On the following pages the results will be presented for the four materials.

Nickel 200

Measurements on the Nickel 200 generally show some of the lowest measured values of the contact resistance. As seen from figures 4.9 and 4.10 the contact resistance decreases rapidly with increasing pressure and for medium to high contact pressure the contact resistance is practically zero. For high pressures neither the surface type nor the temperature is seen to have any significant effect on the contact resistance behaviour, but at small contact pressures a small decrease in resistance can be identified as the temperature is increased.

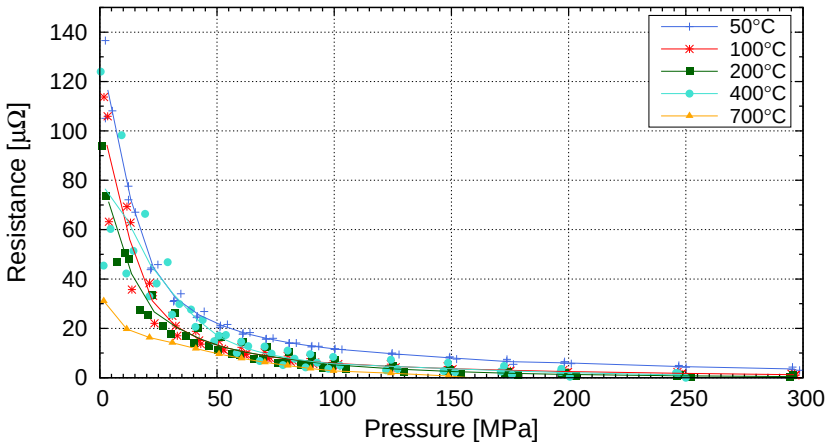

Figure 4.9: Measured contact resistance for turned Nickel 200 specimens

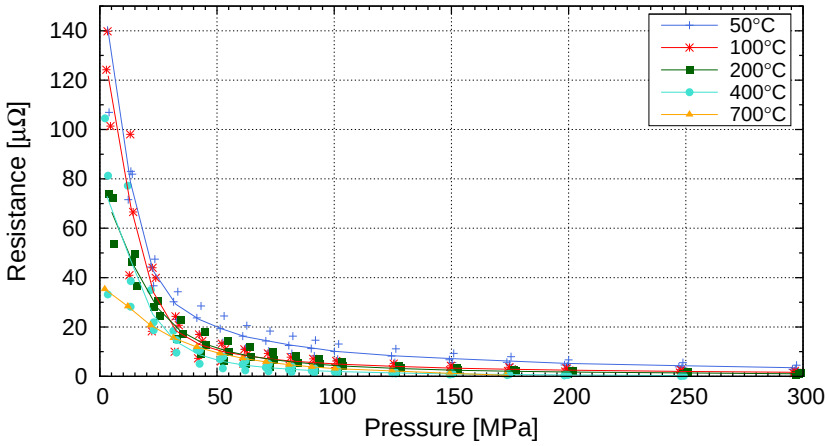

Figure 4.10: Measured contact resistance for EDM cut Nickel 200 specimens

Stainless Steel AISI 316L

For the stainless steel measurements a clear difference in contact resistance behaviour is observed for the turned (figure 4.11) and the EDM cut specimens (figure 4.12). For the turned specimens the contact resistance is generally higher and its decrease with increasing pressure is less than for the EDM cut specimens. Furthermore, there is a clear effect of the temperature on the contact resistance across the entire pressure range for the turned specimens while the EDM specimens only show significant influence from temperature at low pressures (i.e. $p < 100$MPa). It is noted that at 1000°C the contact resistance is still present at low pressures despite the high temperature.

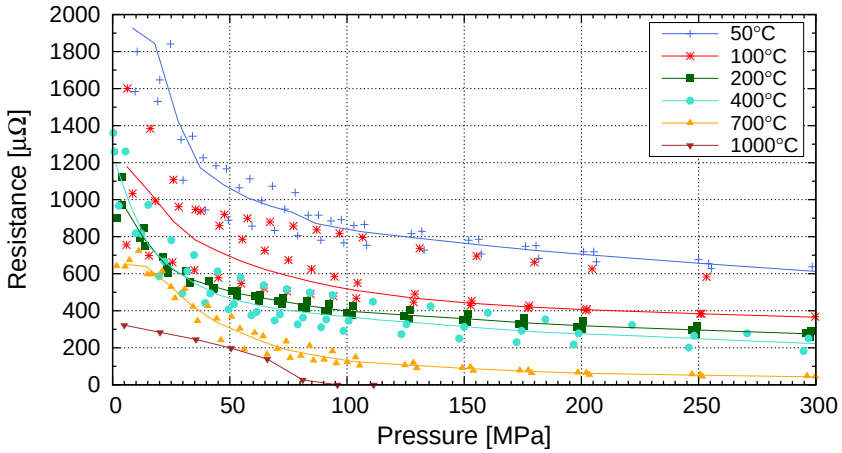

Figure 4.11: Measured contact resistance for turned stainless steel 316 specimens

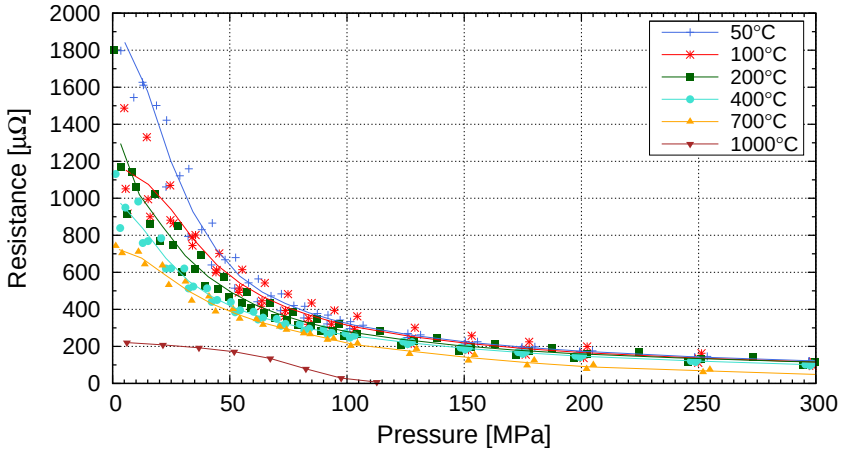

Figure 4.12: Measured contact resistance for EDM cut stainless steel 316 specimens

Aluminium 6060 T6

Due to limited resources only two temperatures, 50°C and 200°C, were tested for the turned surfaces while also 100°C and 400°C were tested for the EDM surfaces. The aluminium specimens show considerably different behaviour depending on the surface type. The EDM surfaces have high contact resistance for low temperatures which drops when increasing temperature. Furthermore, the EDM surfaces produce relatively high variation indicated by the scatter in the data points in figure 4.14. The contact resistance of the turned surface for 50°C is low compared to the EDM surface. The increase in temperature to 200°C actually increases the average contact resistance showing consistent results in all three repetitions. This is the only tested material and surface combination that show this behaviour.

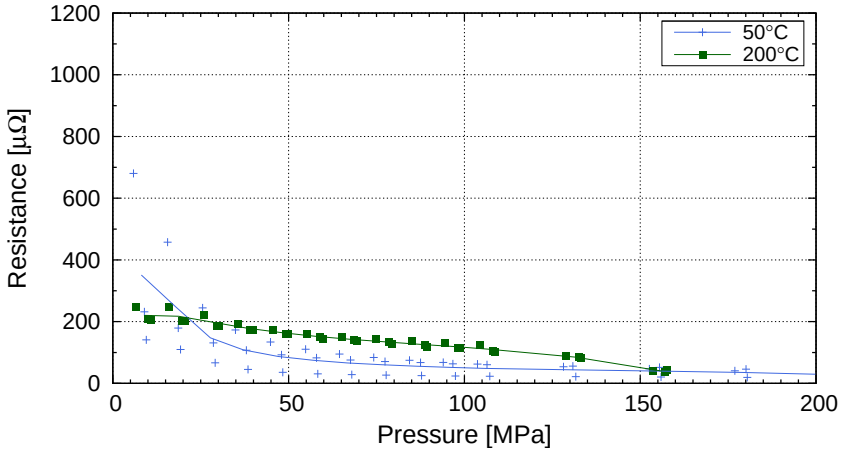

Figure 4.13: Measured contact resistance for turned aluminium 6060 specimens

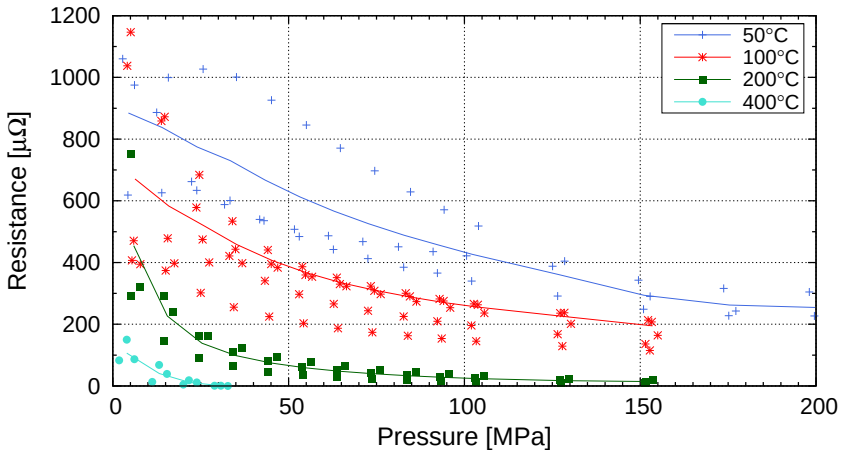

Figure 4.14: Measured contact resistance for EDM cut aluminium 6060 specimens

Mild Steel S235JR

Good repeatability is observed for the mild steel experiments and the results show a similar behaviour of the contact resistance as the stainless steel. The most significant differences are that the absolute values of the contact resistance are lower and that the temperature dependency is observed for the EDM surfaces - not the turned surface, which was the case for the stainless steel. It therefore appears that there might be a strong interaction effect between material, surface type and the testing temperature on the contact resistance for the tested materials.

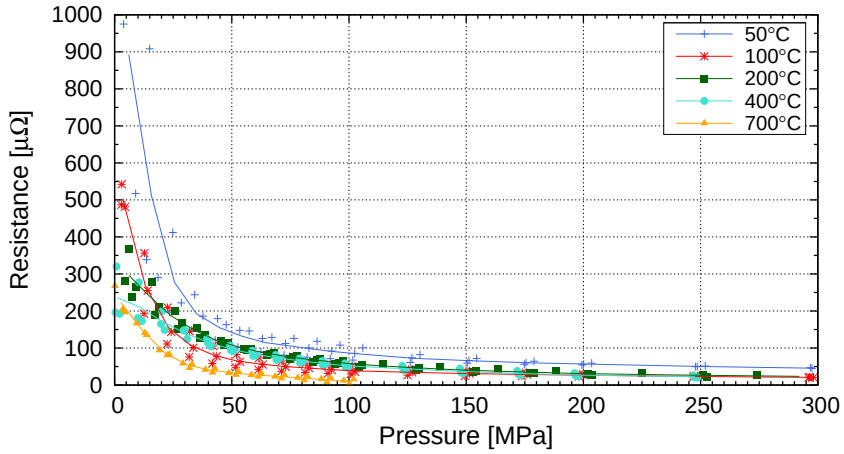

Figure 4.15: Measured contact resistance for turned S235 steel specimens

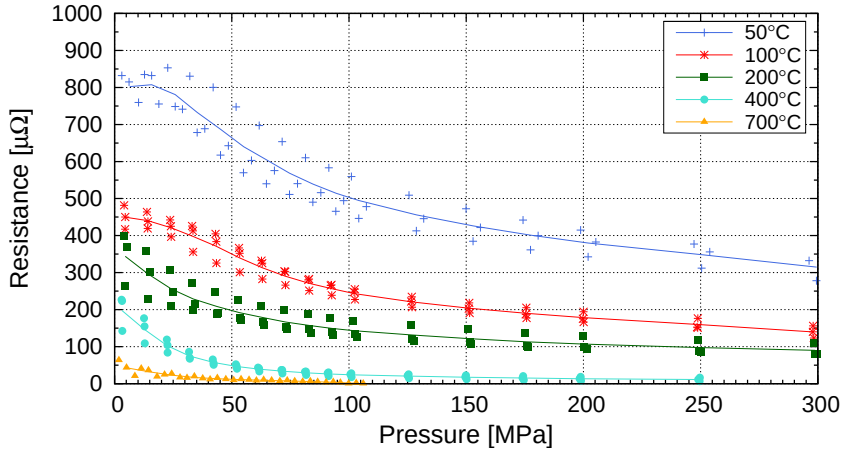

Figure 4.16: Measured contact resistance for EDM cut S235 steel specimens

4.2.4 Data Analysis

In order to be able to further analyse the results presented in section 4.2.3 a mathematical function capable of describing the data is determined. As discussed in section 4.1 the contact resistance as a function of pressure can often be described by an inverse power-law relationship of the form

$$R_{\mathrm{CR}} = R_0 p^n \tag{4.20}$$

where most often $-1 < n < -0.5$ and R_0 is the contact resistance for $p = 1\mathrm{MPa}$. The relation predicts that the contact resistance asymptotically approaches infinitely as the pressure approaches zero. This can be argued to be true based on the assumption that the real area of contact approaches zero for a diminishing pressure. However, in a curve fitting context this implies that data points for low pressures will often dominate the fitting procedure, because the residuals (the calculated difference between fitted model and data points) are more sensitive to variations in the fitting parameters due to the singularity at $p = 0$. This implies that the data points for low values of p are unintentionally given more weight resulting in an unbalanced fit.

Equation (4.20) will follow a straight line on a plot with log-scale. To investigate this further the experimental data for the stainless steel specimens are used as an example and plotted using log-scale in figure 4.17 and 4.18 on the next page. From the figures it can be seen how the data overall resembles a straight line in a log-plot, indicating that the power function in equation (4.20) could be used to describe the data. However, it is noted that the data points for the low pressures ($p < 10\mathrm{MPa}$) have a tendency not to follow the same slope (i.e. not have the same n exponent) as for the data at high pressures. The same tendency is observed for the other materials where the measured contact resistance at low pressures is generally to low to match the slope of the data at high pressures. This could be due to the following two primary reasons:

- It might not be possible to describe the contact resistance at low pressure using a simple power-law function because the underlying physics results in a different behaviour. For a very low pressure the actual contact area is only a very small fraction of the apparent area. According to Greenwood [7] if the number of micro contacts is small, then the actual number will have an influence on the contact resistance. This could imply that the contact resistance follows a different behaviour at a small pressure compared to the situation at a higher pressure.

- Another plausible reason is that the measuring technique is not fine enough to perform measurements at a too low pressure. The force transducer of the

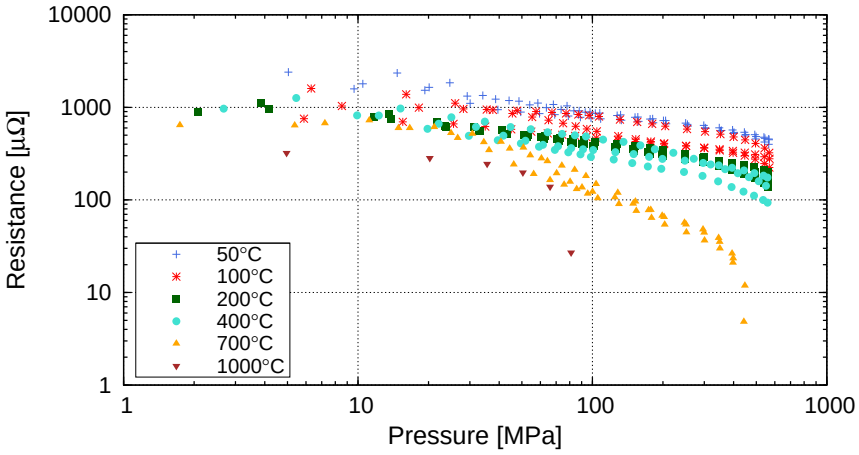

Figure 4.17: Contact resistance for turned stainless steel 316 specimens (log-scale).

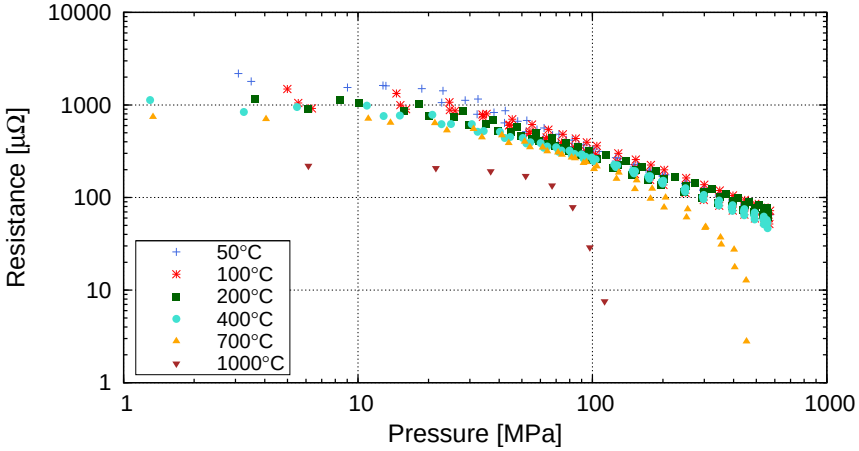

Figure 4.18: Contact resistance for EDM cut stainless steel 316 specimens (log-scale).

Gleeble can measure up to 8000kg and the resolution at a pressure close to zero will therefore increase the uncertainty in the measurements. Furthermore, when the specimens are inserted in the Gleeble a minimum force is need to keep the specimens from sliding out of the anvils. The initial pressure is typically 2-3MPa and it was therefore not possible to perform measurements below this pressure.

Based on the described uncertainty regarding the measurements at low pressure their validity is questionable. Trying to fit equation (4.20) to the data will result in an average fit having a slope n not able to describe the data for both high and low pressure. One of the aims of fitting a function to the experimental data is to be able to compare the data in a more quantitative way. For this reason the function needs to describe the data accurately and as there is some uncertainty regarding the measurements at low pressure the further analysis will focus on the data for

pressures higher than p_0. Based on a subjective estimate the value of p_0 is chosen to 10MPa. By disregarding the values at pressures close to zero the fitting procedure will also not be dominated by the experimental values at low pressure due to the singularity at $p = 0$, as described in the beginning of this section. However, the obtained conclusions will only be valid for $p > 10$MPa.

In the following sections equation (4.20) is fitted to the individual data set and the results are plotted and commented. The resulting fitted curves as well as the resulting fitted parameters can be seen in appendix A. When evaluating the quality of the fit it should be remembered that the plots are on a log-scale. This can result in a visually poor fit for the high pressure data points as even a small variation from the fitted function will be clearly visible.

Nickel 200

The fitted functions for the nickel specimens are shown in figure 4.20 and 4.21 for the turned and EDM cut specimens, respectively. The resulting temperature dependent fitting parameters (c.f. equation (4.20)) are shown in figure 4.19 and their standard error is indicated on the plot. As can be seen from the log-plots only little difference in contact resistance is seen for the two surface types and also only limited temperature dependence is visible. However, when studying the fitting parameters in figure 4.19 it is possible to see a small difference between the two surface types at temperatures higher than 50°C. The turned surfaces show almost constant parameter values of $R_0 \approx 1000$ and $n \approx -1$ although they start deviating at 700°C. The results for the EDM surfaces show higher R_0-values and lower n-values in the entire measured pressure range. At 400°C the EDM parameters show a rather large increase in R_0 and decrease in n, but as the standard error of the estimate is relatively large this somewhat discontinuous behaviour with respect to temperature might be due to experimental variation in the results. A higher numerical value of the n parameter indicates that the pressure has a larger influence on the contact resistance, i.e. rate of decrease in contact resistance with increasing pressure is larger. The R_0 parameter can be thought of as a measure of the initial magnitude of the contact resistance. Based on this it is seen from figure 4.19 that the initial contact resistance (R_0) for the turned surfaces is lower than for the EDM surfaces, but the rate of decrease ($|n|$) is slightly smaller for the turned surfaces. Effectively the contact resistance for the nickel specimens is close to constant regardless of temperature and surface type.

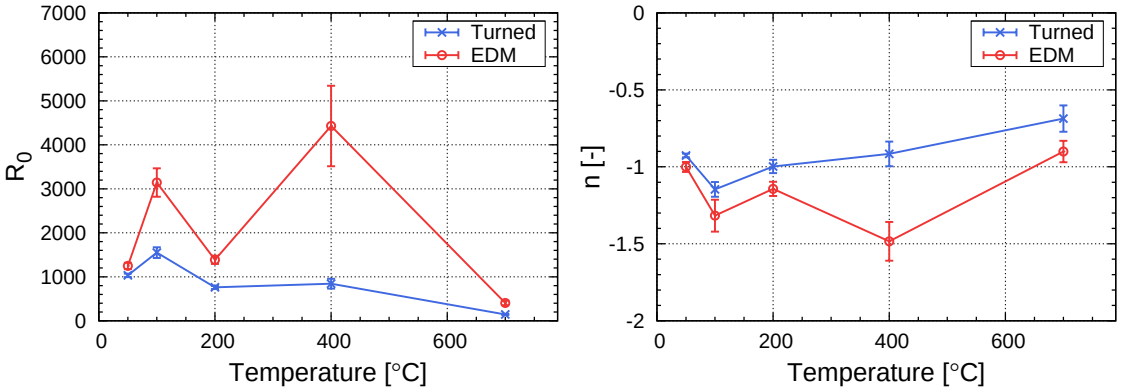

Figure 4.19: Fit-parameters as a function of temperature for Nickel 200

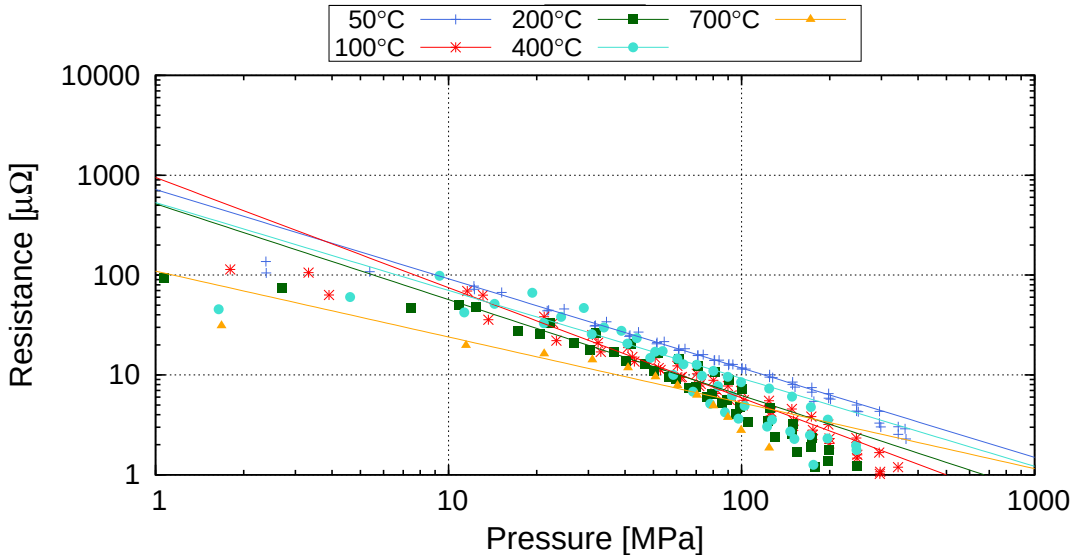

Figure 4.20: Measured contact resistance for turned Nickel 200 specimens and fit

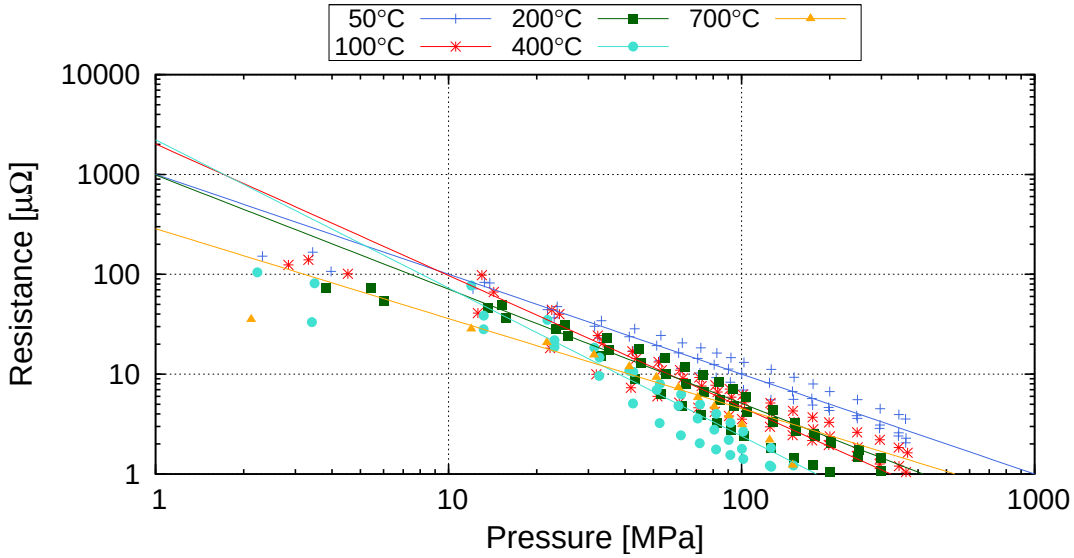

Figure 4.21: Measured contact resistance for EDM cut Nickel 200 specimens and fit

Stainless Steel 316

In general the contact resistance is much higher for the stainless steel specimens which was also noted in section 4.2.3. Contrary to the nickel specimens the stainless steel show significant variation with temperature and surface type (the results for 1000°C can not be fitted to equation (4.20) with any reasonable result and are therefore left out). Figure 4.23 and 4.24 can be seen to differ and this is also found in the fitting parameters in figure 4.22. At low temperatures the turned surface have a lower numerical value of n and the initial resistance R_0 is smaller than the EDM surface, which have a very high R_0 at 50°C. This results in the contact resistance of the turned specimens to decrease at a considerable lower rate than the EDM specimens. Furthermore, the temperature is clearly affecting the contact resistance for the turned specimens by increasing the absolute value of n while the effect of the temperature on the EDM specimens is considerable smaller as the n is close to constant. At 700°C the absolute value of n of the turned specimens have actually decreased below the parameter from the EDM surfaces. Overall it is seen that there is a strong interaction effect between specimen surface type and the testing temperature.

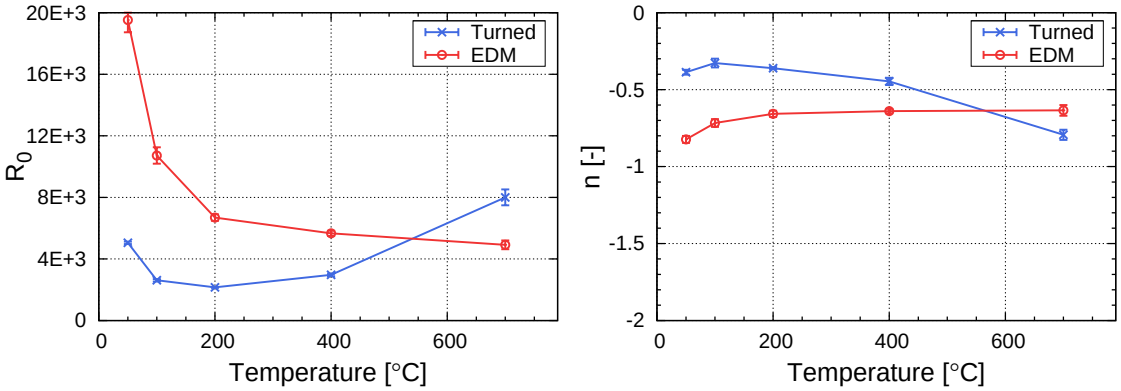

Figure 4.22: Fit-parameters as a function of temperature for stainless steel 316

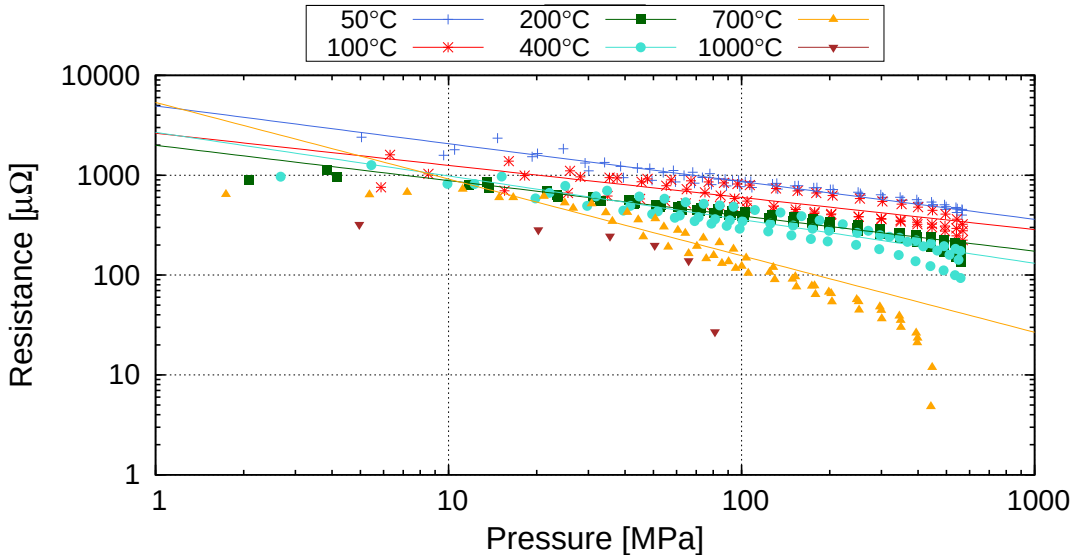

Figure 4.23: Contact resistance for turned stainless steel 316 specimens and fit

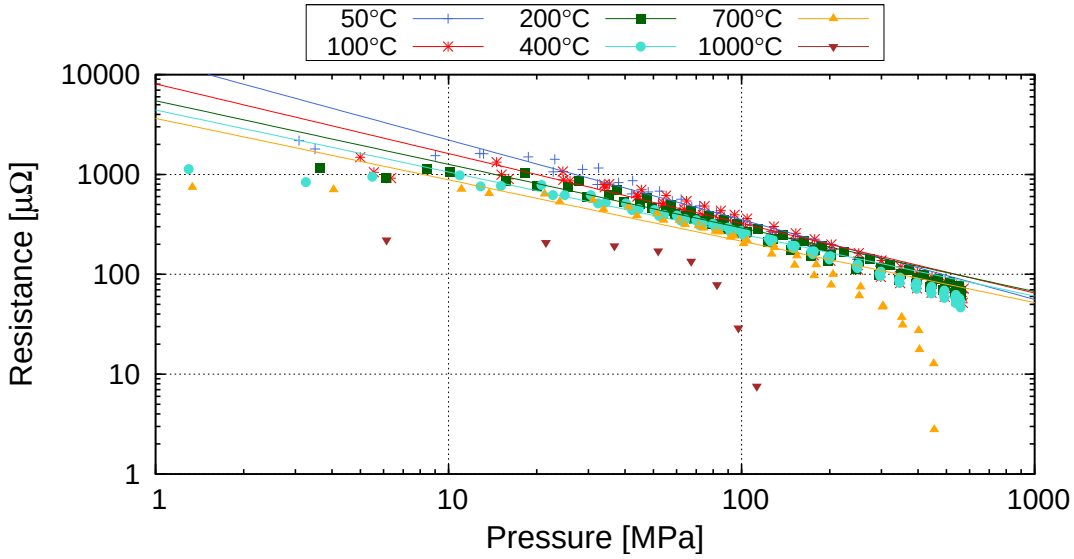

Figure 4.24: Contact resistance for EDM cut stainless steel 316 specimens and fit

Aluminium 6060

The interaction between surface type and temperature is very strong for the aluminium specimens. As can be seen from figure 4.25 the slope of the change in parameters values with temperature have different signs depending on the surface type (The fitted parameters for the EDM surfaces at 400°C have a very large variation and should not be given that much weight when looking at the results). For the EDM surfaces the absolute value of both n and R_0 increase with temperature while they decrease for the turned surfaces. Compared to the measurements of the other materials the aluminium, especially at low temperatures, show large scatter in the data. This is visible in figure 4.27 but maybe even more clear in figure A.6 in appendix A.3 on page 247.

The turned surfaces show a high rate of decrease in contact resistance with increasing pressure at 50°C, but at 200°C the rate of decrease has dropped considerably and the contact resistance only show a slight decrease with increasing pressure. The EDM surfaces show a more typical behaviour of decreasing contact resistance with increasing temperature. Furthermore, it is noted that the absolute values of the contact resistance are of considerable size compared to the nickel - considering the low resistivity of aluminium compared to nickel (c.f. chapter 3).

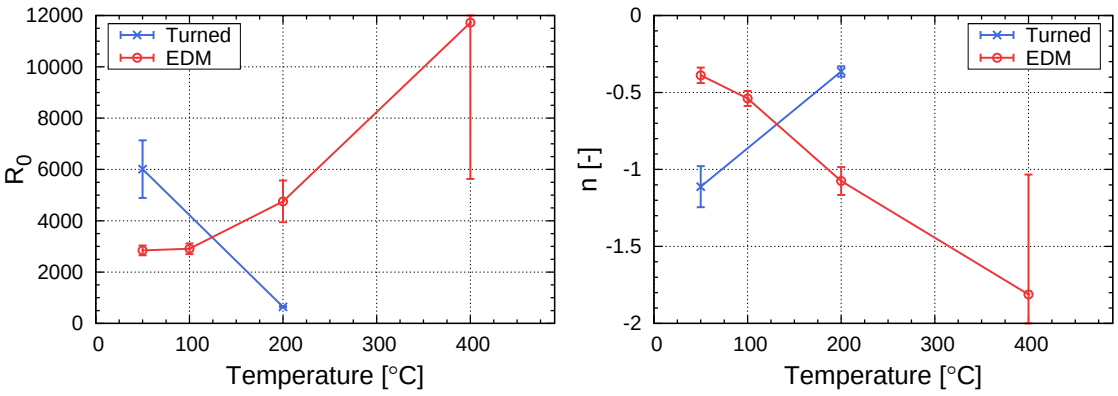

Figure 4.25: Fit-parameters as a function of temperature for aluminium 6060

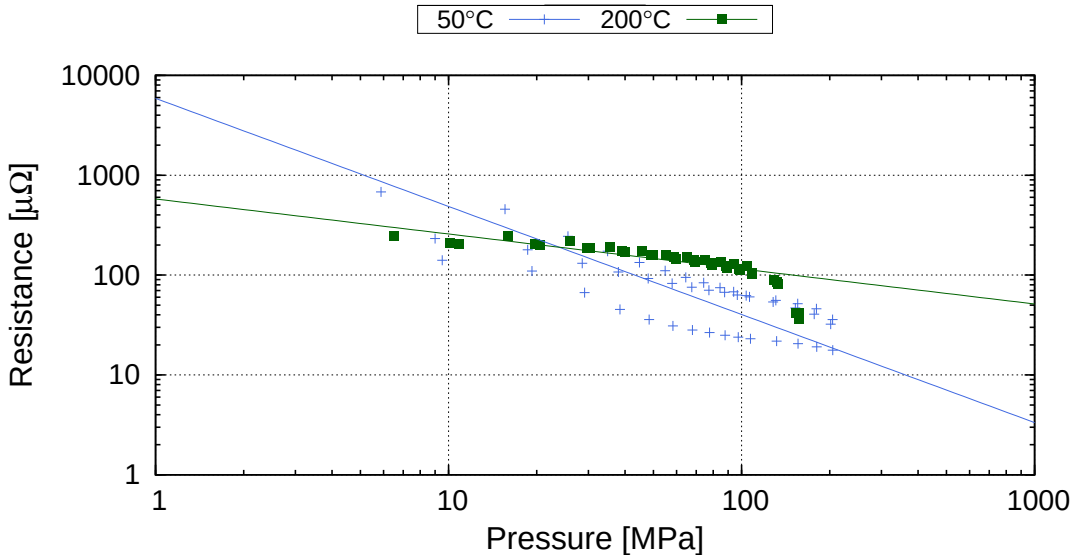

Figure 4.26: Contact resistance for turned aluminium 6060 specimens and fit

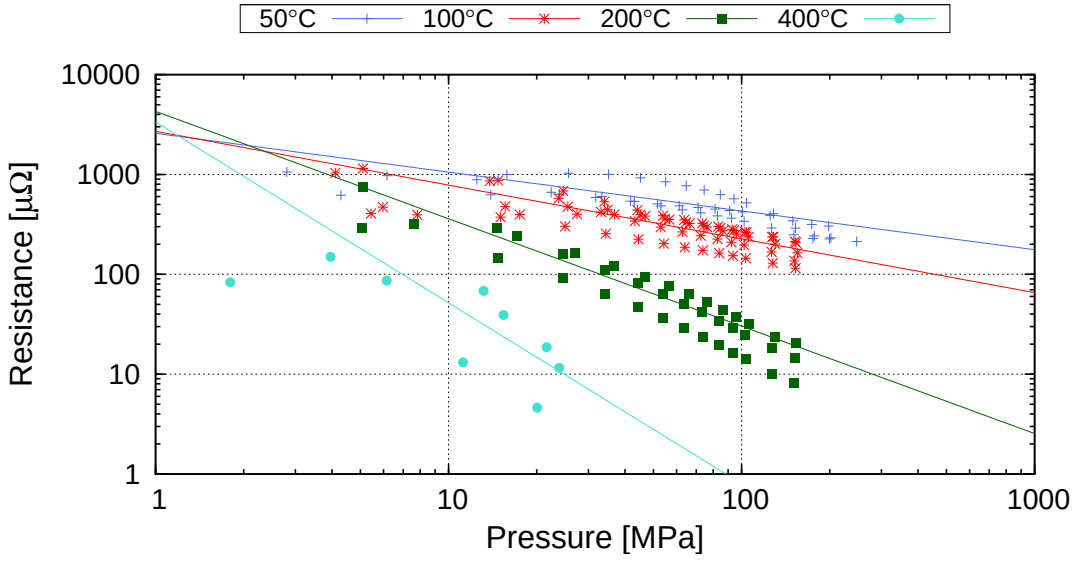

Figure 4.27: Contact resistance for EDM cut aluminium 6060 specimens and fit

Mild steel S235JR

The fitted curves for the mild steel S235JR is seen in figure 4.29 and 4.30 and the model parameters are plotted in figure 4.28. As can be seen from the result there is again a large difference between the two surface types. The EDM surfaces show a very low rate of decrease $|n|$ at 50°C that steadily increases with temperature. The turned surface show a more constant value for n with some variation. The turned surface at 400°C show a large drop in R_0 value. This is mainly due to the three measurements around $p = 10$MPa, which can be seen on figure 4.29, that influences the fit by decreasing $|n|$ and R_0. This results in the fit to overshoot the data points for high p indicating that the proposed function in equation (4.20) in this case might not be adequate for describing the data for $p > 10$MPa. It is noted that even though the numerical value of the n parameter for the EDM surfaces is small for low temperatures it increases with increasing temperature and it ends up being larger than that for the turned surface, which was relatively high also at low temperatures. The same behaviour is seen for the stainless steel specimens, with the only difference being that the effect is opposite for the two surfaces.

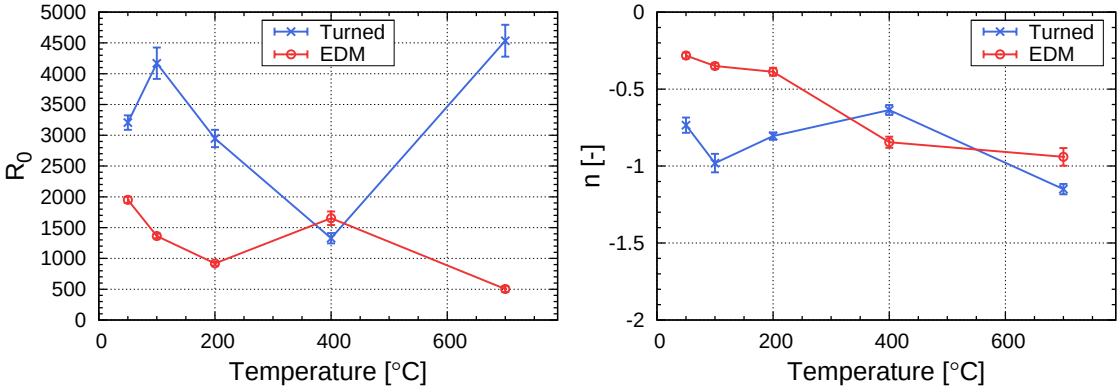

Figure 4.28: Fit-parameters as a function of temperature for steel S235JR

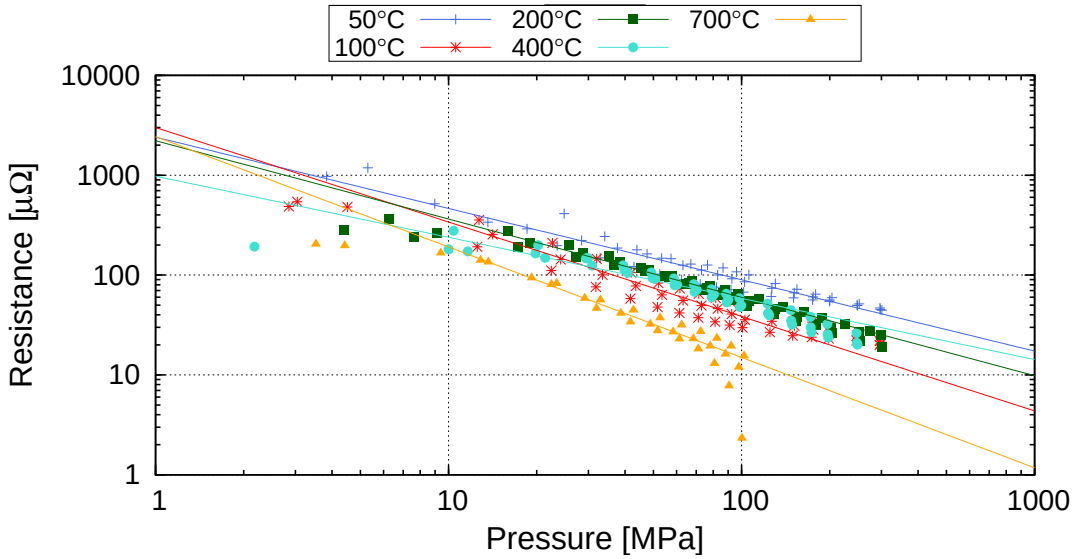

Figure 4.29: Contact resistance for turned steel S235JR specimens and fit

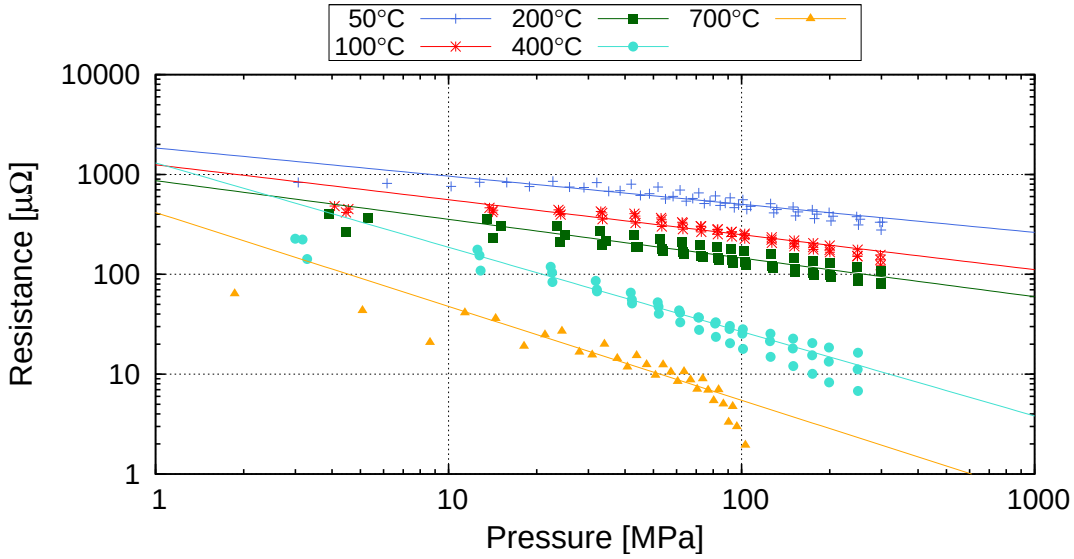

Figure 4.30: Contact resistance for EDM cut steel S235JR specimens and fit

4.3 Discussion

Experimental Investigation

The experimental method for measuring contact resistance was primarily developed in chapter 3 for measuring material resistivity. The method was readily applied for measuring contact resistance by synchronising the data acquisition of the contact pressure applied by the Gleeble system. The main source of error observed in chapter 3 was introduced by the self-induction caused by of the ferromagnetic properties of the specimens. Investigation of the measured current and voltage curves from the measurements of the contact resistance did not show any influence of the self-induction of the specimens. The reason for this is believed to be due to the difference in total ohmic resistance in the primary circuit. Compared to the resistivity measurements the total ohmic resistance is significantly increased during contact resistance measurements - due to the relatively high contact resistance compared to the bulk resistivity. This implies that the inductive load becomes negligible compared to the ohmic resistance which eliminates its influence on the voltage signal.

The experiments indicate that the material, the pressure, the surface type, and the temperature all have significant effect on contact resistance. Furthermore, the result show significant interaction between the surface type, the temperature, and the pressure for a given material. It is well known that contact resistance generally decreases with increasing temperature. However, it was shown that, depending on the surface type, temperature affected not only the absolute value of contact resistance but also the *rate of decrease* (expressed by the n parameter) with increasing pressure.

The interaction between the surface preparation method and resulting contact resistance is significant. Examining the two steels, stainless steel 316 and mild steel S235, it is seen how the surface type significantly affects the rate of decrease with pressure. For the stainless steel specimens the turned surfaces are influenced by the test temperature while the effect on the EDM surfaces is much smaller. This is in contrast to the mild steel, where the contact resistance of the *turned* surfaces is practically unaffected by temperature, while the EDM surfaces show significant interaction with the test temperature.

One of the main differences between the two materials is the effect of temperature on the hardness of the materials. The stainless steel is austenitic at room temperature which implies that it cannot be hardened to any major degree by a heat treatment and subsequent quenching. Exposing the stainless steel to high temperatures will more likely initiate relaxation and recrystallisation of the mi-

crostructure thereby decreasing any initial hardness induced in the material. By contrast the mild steel is a typical low carbon steel which is hardenable due to martensite formation caused by heating and subsequent quenching.

The principle of the EDM wire cutting process is based on spark erosion where the material is melted and expelled. During the process the specimens are flushed with a cutting fluid that aids spark production and removal of eroded material, as well as cools the specimens. The sparks create a heat affected zone (HAZ) as well as a so-called "white layer" of recast material on the surface. The depth of the HAZ and the thickness of the white layer depends on the power, type of power supply, and the number of skim cuts [81]. Based on this it can be assumed that the surface of low carbon steel cut using wire EDM is hardened due to the heat treatment. The stainless steel will not harden due to heat treatment, however, as measured in chapter 2 the stainless steel 316 has been severely work hardened and it is reasonable to assume that the EDM process therefore will result in softening of the recast material on the surface of the specimens.

The turning process will not produce enough heat to thermally affect the specimens and so no thermal hardening or softening is expected. The mechanical deformation of the surfaces associated with the turning process might produce strain hardening of the surface material. This applies for both steel grades. However, compared to the thermal effect of the EDM process the influence of the turning process on the mechanical properties of the surfaces is expected to be minor. As seen in chapter 2 the low carbon steel did not show any sign of pre-straining to higher hardness. It is therefore assumed that the surface of the turned stainless steel specimens has a higher hardness compared to the EDM surfaces, and the turned low carbon steel specimens are expected to have a lower hardness compared to the thermally hardened surfaces of the EDM specimens. Unfortunately the surface hardness could not be experimentally verified due to the visual appearance of the EDM surfaces where micro hardness measurements could not be distinguished from the surface roughness.

The experiments suggest that there is a correlation between the surface hardness of the specimens and the resulting contact resistance of the steel specimens. The specimens having high hardness experiences a higher initial contact resistance as well as a lower rate decrease of the contact resistance. Furthermore, the hardened specimens show a clear effect of increasing test temperature which significantly decreases contact resistance. One of the main factors influencing contact resistance and which is identified in literature is the hardness or yield stress of the softest material in contact [18, 24–26, 82]. The influence of hardness is explained by the increased resistance to plastic deformation of the surface asperities, thereby requiring a higher pressure to obtain the same real area of contact. From the experiments

it is seen how the fitting parameter n numerically is smaller for the hardened surfaces resulting in lower rate of decrease of the contact resistance with increasing pressure. However, the experiments also suggest, that for materials, which have not been hardened, or which have been softened, prior to testing, the effect of increasing temperature show only a minor decrease in contact resistance and rate of decrease. This implies that the "normal" decrease in flow stress associated with increasing temperature (c.f. chapter 2) only affects the contact resistance slightly while the increased strength due to hardening can have a high impact in materials contact resistance. Only when reaching 700°C the two surface types start showing similar behaviour indicating that the initially hardened material has experienced relaxation and softening due to the heat treatment.

The nickel specimens show only a very small influence of surface type. This can be explained by the fact that the material had not been previously work hardened and that pure nickel does not harden due to heat treatment. This implies that there are only minor differences between the two surface types which results in the same behaviour of the contact resistance. However, also nickel show a slight decrease in contact resistance with increasing temperature, indicating that the yield stress of the material also affect the contact resistance in this case.

Aluminium 6060 is the softest of the test materials and it has the lowest resistivity - both factors working to decrease contact resistance. Despite of this the experiments show that the aluminium 6060 contact show a considerable contact resistance, especially for the EDM surfaces. The reason for this behaviour is believed to be found in the aluminium oxide layer which is known to greatly influence the contact resistance of aluminium [83]. Especially the wire EDM specimens show a considerable contact resistance at low temperatures which might be due to the EDM process promoting the formation of a thick oxide layer. The fact that the aluminium specimens are flushed with a cutting fluid while relatively high currents are being send through the specimens to create sparks might help building a thick and electric insulating surface oxide [84]. The reason why the average resistance actually increases for the turned aluminium surfaces when increasing the temperature to 200°C is not clear (cf. figure 4.13). All three repetitions show the same trend with only minor scatter. When comparing the two surface types it is clear that part of the explanation should be found in the specific differences between the two surface types, as there is a clear difference in contact resistance behaviour.

Modelling

The results obtained by Nakamura and Minowa [76] are interesting because the proposed FE-model is simulating a "global" contact interface - not just a single cluster as the analysis by Greenwood [7] is restricted to. The result of the sim-

ulations, which are indicated in figure 4.3b, show several important observations regarding the relation between the contact resistance and the true area of contact. In the simplest case the resistivity of the contact spots are the same as the base material. In this situation they show that with a random pattern of contact spots the contact resistance has decreased to practically zero already at the fraction of the true area of contact $f = 0.2$. By using the results by Bowden and Tabor [71] from equation (4.3) it is possible to calculate at which pressure p the contact resistance has reduced to zero depending on the yield stress σ_0

$$p = 3f\sigma_0 \tag{4.21}$$

The experimental measurements on the nickel specimens showed no effect of the surface type on the results. Furthermore, nickel is not expected to form any type of strong oxide on the surface and it can therefore be assumed that the resistivity at the single contact spots is not increased due to films or material hardening. In chapter 2 the yield stress of the nickel was estimated to approximately 400MPa at low temperatures. Inserting this in equation (4.21) and assuming that the contact resistance has reduced to zero at a true contact area fraction of $f = 0.2$ yields

$$p = 0.6\sigma_0 = 0.6 \cdot 400\text{MPa} = 240\text{MPa} \tag{4.22}$$

As can be seen from the results on figure 4.9 and figure 4.10 the contact resistance has dropped to a very low value around 240MPa, although this normal pressure corresponds to a fraction of true contact area of only 0.2. When evaluating contact resistance of "clean" surfaces the decrease in contact resistance progresses with a much higher rate than the increase in real contact area, and this is due to the mechanisms of self- resistance and contact spot interactions as described in section 4.1.

The limit above applies for contact pairs where the resistance of the contact spots are not increased due to film resistance or, as has been indicated by the experimental study, high surface hardness. Nakamura and Minowa [77] show that by increasing the material resistance of the contact spots, corresponding to for example the presence of an insulating oxide layer, the decrease in contact resistance with increasing fraction of true contact is less steep. This implies that a higher true area of contact is needed before the resistance is reduced to a level corresponding to the resistance at 100% true contact area. These results obtained by FEM can be recognised in the experimental results of the wire EDM manufactured aluminium specimens from the present study. The specimens are expected to have a thick oxide layer due to the anodising effect of the EDM process and the yield strength is either unaffected by the white layer formation or it will soften the originally heat treated aluminium. The log plot in figure 4.27 on page 85 show that the contact

resistance at low temperatures is high, compared to its resistivity, and that the rate of decrease is low with increasing pressure. The oxide layer of the turned surfaces has not been exposed to accelerated film growth through anodising and the film thickness and electric resistance is therefore less as well as having a faster rate of decrease with pressure.

The above analysis challenges the existing governing description of the contact resistance - that the total contact resistance R_{CR} is composed of the *sum* of the contributions from the constriction resistance R_c and the film resistance R_f as given in equation (4.23) [8, 35, 85].

$$R_{\mathrm{CR}} = R_c + R_f \tag{4.23}$$

Rather the results by Nakamura and Minowa [77] and the experimental observations in this study suggest that there is a significant influence of the film resistance on the constriction resistance. This implies that the two effects can *not* simply be separated as in equation (4.23) but should be considered as interacting with each other.

As seen in section 4.1 the influence of material hardness is introduced in the theoretical models by relating the true area of contact with the yield strength of the materials in contact. This implies that the simple inverse power relation given in equation 4.20 on page 77 can be used to describe the overall form of all the theoretical models presented in section 4.1 by setting n constant to $n = -1$ or $n = -1/2$. The model parameter R_0 primarily becomes a function of the resistivity, the yield stress and a fitting variable λ depending on the specific model. The fitting variable is then justified by attributing it to either the unknown influence of the surface film (as in the *single contact spot* and *contact layer* models [4, 10]) or to the unknown asperity density (as in the *asperity density* model [26]). The influence of temperature on contact resistance is included indirectly in the models by considering the influence of temperature on the mentioned variables (including λ). The variable R_0 from equation 4.20 can therefore be described as in equation (4.24), where the variables themselves are functions of temperature.

$$R_0 = R_0\left(\rho, \sigma_0, \lambda\right) \tag{4.24}$$

In a log-plot the fitting function in equation 4.20 will resemble a straight line with the slope n. This implies that for n constant the value of R_0 will solely parallel shift the line in the cartesian y-direction. However, as can be seen from the results in section 4.2.3 the slope n of the data can not be considered constant, but rather it depends on the specific material properties (ρ,σ_0) as well as on the average resistance of the surface oxides, here described again by the function λ.

The observed effect of temperature on the contact resistance is mainly credited to the indirect effect on the material properties. This implies that the n factor should be described as a function given in equation (4.25).

$$n = n\left(\sigma_0, \lambda\right) \tag{4.25}$$

The results therefore suggest that it is not enough only to introduce the influence of material yield strength through its effect on the true area of contact, as this will only affect R_0 and not n.

The above analysis assumes that the simple inverse power-law function given in equation 4.20 is adequate for describing the physical nature of the contact resistance in resistance welding. However, although the validity of the results for low values of p was questionable, they still indicated that the inverse power law might not describe the data for small values of p. This could imply that n itself is a function of p or that the contact resistance should be described by a function with two terms each with weighting functions depending on the pressure level. An exact description of R_{CR} at low values of p is of increasing importance when the resistance welding process is downscaled to micro size, as the pressure levels are often lower for micro welding applications [2]. This is illustrated in table 4.2 where typical pressure values, which are used in the project, are calculated for large scale and micro resistance welding. Table 4.2 clearly indicate that the contact pressure in micro welding is close to or even lower than $p = 10\mathrm{MPa}$, emphasising that exact description of contact resistance at low pressure levels is of large importance for modelling of micro resistance welding.

Table 4.2: Example of typical pressure values in large scale and micro welding

Scale	**Electrode tip D [mm]**	**Force [kN]**	**Pressure [MPa]**
Large scale	6	2 - 3	71 - 106
Micro	3.5	0.05 - 0.15	5 - 16

4.4 Conclusion

Several models for describing contact resistance was presented in the literature study in section 4.1. The results by Greenwood [7] are often used as theoretical basis for deriving more practically applicable models of contact resistance. However, it was argued that the theoretical foundation of these models often is based on extensive assumptions and simplifications.

The electric contact resistance of contact pairs of round cylindrical specimens of Nickel 200, Stainless steel 316, Aluminium 6060, and mild steel S235JR was measured employing the Gleeble system. The technique for measuring resistivity as explained in chapter 2 was extended to measure contact resistance by synchronising data acquisition of applied force with the resistance measurements. The method generally proved good repeatability.

Test specimens were made from rod material using wire EDM and conventional turning, producing two distinctively different surfaces. It was shown how material, surface type, temperature, and pressure all influenced the contact resistance. The wire EDM affect the surface layer with high temperatures that hardens the mild steel and softens the previously strain hardened stainless steel. The experiments indicate that the surface hardness has a large influence on the contact resistance and also on the rate of decrease of contact resistance with increasing pressure. The nickel showed no influence of surface type as nickel is neither hardened nor softened by heat treatment. The aluminium was highly influenced by surface type as the EDM process was suspected of accelerating the growth of a strong oxide due to an anodising effect.

Based on previous investigations in literature the experimental measurements were fitted to an inverse power-law function. The theoretical models in the literature applied constant values of the power-exponent, but the experiments indicate that the exponent is a function of material yield stress, the oxide layer, and temperature and therefore is not constant.

A FEM investigation was presented that showed how the contact resistance is decreasing rapidly with increasing true area of contact and that almost zero contact resistance remains for surfaces free of oxide and contaminant film at a true contact area fraction of 20%. The introduction of surface films, that locally increase the resistance of the contact spots, resulted in a slower rate of decrease. This implies that the constriction resistance and its development with pressure is influenced by surface films. This questions the otherwise widely accepted assumption that the effects of constriction resistance and the surface film resistance are separated terms and that they therefore can be modelled separately.

Chapter 5

Contact Resistance in Micro Spot Welding of Foils

The physical interactions involved in electrical contact resistance and the understanding of its influence on the outcome of the resistance welding process is a complex matter. Knowledge of the nature of contact resistance is important to understand and model the process. Especially on small-scale contact resistance and its interaction with other process parameters is believed to have a great influence on the process due to the downscaling of the process parameters.

The purpose of this chapter is to investigate an often applied methodology for measuring electrical contact resistance during micro resistance spot welding of foils as well as measuring the behaviour of the contact resistance of stainless steel AISI 316 and Nickel 200 and the influence of the main process parameters. Numerical simulation of the process is used in the analysis and the numerical methodology is discussed in relation with potential challenges for simulation of the spot welding process on micro-scale.

5.1 Experimental Method

The contact resistance during micro spot welding of nickel foils has previously been investigated by Tan et al. [35] applying the same method as investigated in this work. Tan et al. have proposed a schematic of a typical contact resistance curve identifying several stages (1,2,3 and 4) and the three components (film-, constriction- and bulk resistance) of the measured contact resistance. The schematic is shown in figure 5.1. As can be seen from the figure the film resistance (R_F) is initially very high (stage 1) but drops rapidly as the film is ruptured both electrically and mechanically in the beginning of stage 2. The contribution of the

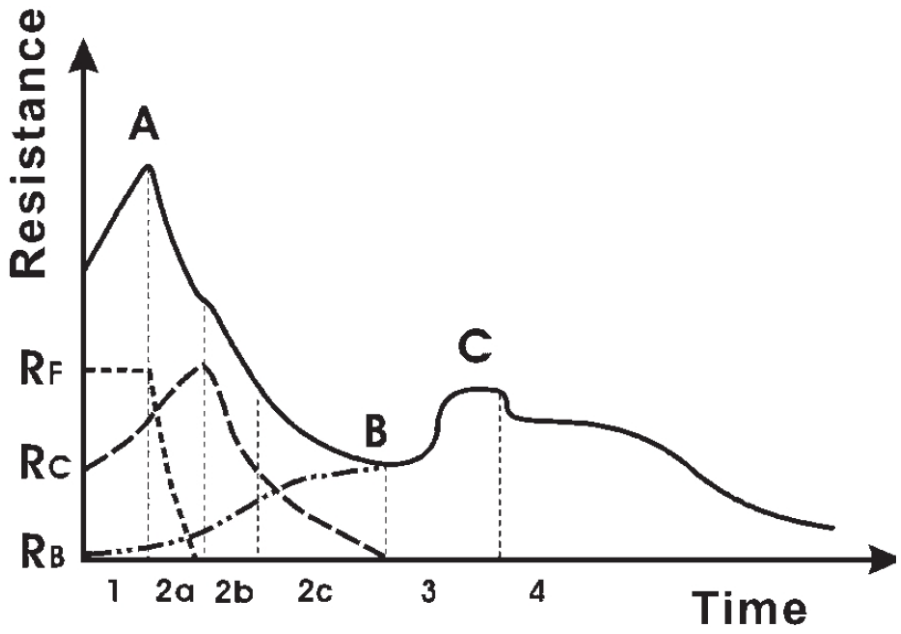

Figure 5.1: Schematic of a typically measured contact resistance curve of spot welding of Ni-sheets and its components [35]

bulk resistance (R_B) to the measured contact resistance is initially very small but increases as the temperature increases. The constriction resistance (R_C) decreases as the interface is softened and eventually disappears as the interface starts to melt forming a nugget in stage 3. In this stage Tan et al. [35] suggest that all contact resistance disappears and only the bulk resistance remains.

The applied experimental method is based on measurements of the electric potential between the two workpieces in micro resistance spot welding of foils. Similar methods have been applied by Luo et al. [86], but a thorough investigation of the approach has not been found. The following section investigates and justifies this method in relation to measuring contact resistance during micro resistance spot welding.

5.1.1 Experimental Setup

The experimental setup consists of a pneumatic controlled spring-loaded DK250 weld head from Resistronic[1] capable of delivering between 30N and 500N. The power supply for the static contact resistance measurements is a standard laboratory DC-power supply delivering from 0V to 20V while for the actual welding and dynamic measurements an Akzent-5000 high frequency inverter (HFI) from

[1]Resistronic AG, Turgi, Schwiterland

Resistronic is used. The HFI can deliver currents up to 5kA with current profile resolutions down to 1ms. The welding current is measured with a LEM LT1005-S closed loop Hall Effect current transducer and the force is measured using a Kistler 9001A piezoelectric force transducer installed under the bottom electrode. The electrodes used are Class 2 RWMA CuCrZr alloy having an outer diameter of 6mm and varying tip diameters. The experimental setup is shown in figure 5.2.

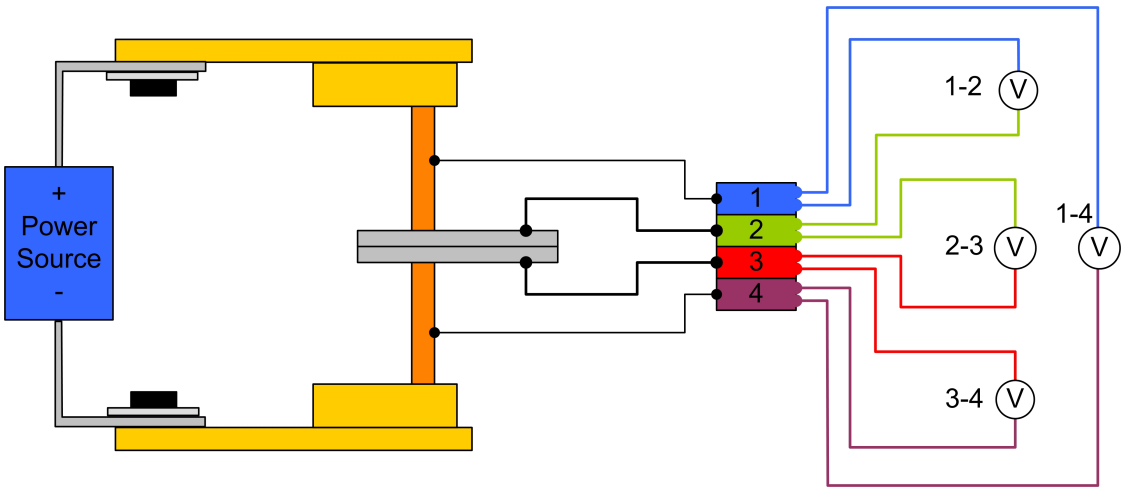

Figure 5.2: Experimental setup - schematically

The figure illustrates the weld head clamping down on two sheets in between the two electrodes. The upper and lower part of the weld head is connected to the poles of the power source. This forms a closed circuit consisting of a power source, weld head, electrodes and the specimens to be welded. To measure the voltage drops through this closed circuit four connections (1,2,3 and 4) are made as illustrated on the figure. Connections 1 and 4 are connected to the electrodes and connection 2 and 3 are connected to the upper and lower specimen, respectively. These four wires are collected in a wire connector box and four potentials can be measured.

5.1.2 Testing of Experimental Setup

Connections are made as illustrated on figure 5.2. The measured voltage drop from i to j is written as Φ_{ij}. With perfect connections and zero loss in the wires it is expected that

$$\Phi_{14} = \Phi_{12} + \Phi_{23} + \Phi_{34} \tag{5.1}$$

Simple tests measurements show that equation (5.1) is not satisfied when inserting the acquired values, but instead

$$\Phi_{14} < \Phi_{12} + \Phi_{23} + \Phi_{34} \tag{5.2}$$

The condition is not heavily violated but is still clearly not satisfied. Through experimentation it was found that each measuring channel has an offset error voltage Φ_e on it. Inserting in equation (5.1) yields:

$$\begin{aligned} \Phi_{14} + \Phi_e &= (\Phi_{12} + \Phi_e) + (\Phi_{23} + \Phi_e) + (\Phi_{34} + \Phi_e) \Leftrightarrow \\ \Phi_e &= \frac{\Phi_{14} - (\Phi_{12} + \Phi_{23} + \Phi_{34})}{2} \end{aligned} \tag{5.3}$$

The offset was measured to be close to 0.3mV by using the relation in equation (5.3) and it was found to be independent of the actual measurements Φ_{ij}. The individual channels are calibrated with this offset during measurements.

Measuring Voltage

A voltage drop across an unknown resistance R_x is normally measured by inserting a voltmeter having a known resistance R_m in parallel with the voltage drop to be measured. By measuring the current passing through the known resistance the voltage can be calculated using Ohm's Law. The idea is that the impedance of the inserted resistance should be large compared to the measured resistance so the current running through the voltmeter will be small compared to the current between the measuring points. If for example the connection of the voltage measurement equipment is imperfect an additional error resistance R_e will be inserted in the circuit as seen on figure 5.3.

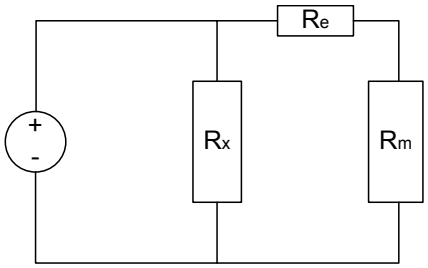

Figure 5.3: Simple Circuit

This could come from a bad contact in the connection zone and/or resistance in the wires. The measured voltage on the voltmeter U_m can now be expressed as

$$U_x = U_e + U_m \qquad \Leftrightarrow \qquad U_m = U_x - U_e \tag{5.4}$$

where U_x is the desired voltage drop across the resistance R_x and U_e is the potential drop due to the error resistance R_e. However, in practically all situations, even

when relatively poor contacts are made between measuring equipment and the measurand, the impedance of the voltmeter is very large compared to the impedance of any error resistances introduced in series with the voltmeter itself (as seen on figure 5.3) implying that $R_m + R_e \approx R_m$. Therefore even poor connections between the specimens and measuring equipment are not expected to influence the measurements.

Induced Error in Voltage Measurements

When performing measurements of static contact resistance where a small and constant current is used to generate the voltage drop in the system, it is safe to disregard any induced electromotive force in the measurement wires. However, when performing dynamic measurements of contact resistance implying high currents and large gradients of the current, the induced potential in the measuring wires need to be considered. In general the measured voltage U_m consists of two contributions: the potential drop U_{sys} due to the electric resistance of the system R_{sys}, and the induced electromotive force ε_m. The electromotive force is proportional to the negative value of the change in magnetic flux through the closed circuit and hence the potential drop due to the resistance in the system can expressed as

$$U_{\text{sys}} = U_{\text{m}} - \varepsilon_m = U_{\text{m}} + L\frac{dI(t)}{dt} \tag{5.5}$$

The resistance of the system can then be calculated using ohm's law

$$R_{\text{sys}} = \frac{U_{\text{m}} + L\frac{dI(t)}{dt}}{I(t)} \tag{5.6}$$

The induction coefficient L is depending on the geometry/position of the wires that forms the closed circuit which determines the magnitude of the magnetic flux through the circuit (cf. section 3.1). The induced electromotive force is difficult to estimate and the most practical solution is often to try and minimise it rather than estimate it. To avoid inducing an electromotive force in the measurement signals, the area spanned by the measurement wires should be as small as possible and perpendicular to the generated magnetic field during the welding process. This implies that keeping the wires approximately in the same plane as the horizontal sheets will minimise the magnetic flux in the circuit.

5.1.3 Measuring Contact Resistance

It is desired to measure the actual electrical contact resistance between the sheets during the welding process. It is however, not possible to access the contact zone

with measurement equipment/wires without affecting the same contact conditions which are measured. The most common way of measuring contact resistance is by attaching wires to the electrodes close to the welding zone and attaching wires to the edges of the sheets/components which are welded (see figure 5.2). Hereby, not only the contact resistance between the specimens and electrodes are measured, but also some of the bulk resistance between the connected wires. The amount of bulk resistance in the electrodes is only depending on the vertical distance between electrode tip and the position of the measurement wire. The wires attached to the end of the sheets will measure a potential depending on the current flow through the specimens and the resistivity of the specimens. Simple calculations with a sheet having uniform resistivity reveals that the measured potential at the ends of the sheet equals the potential at a point P in the middle of the sheet as seen in figure 5.4.

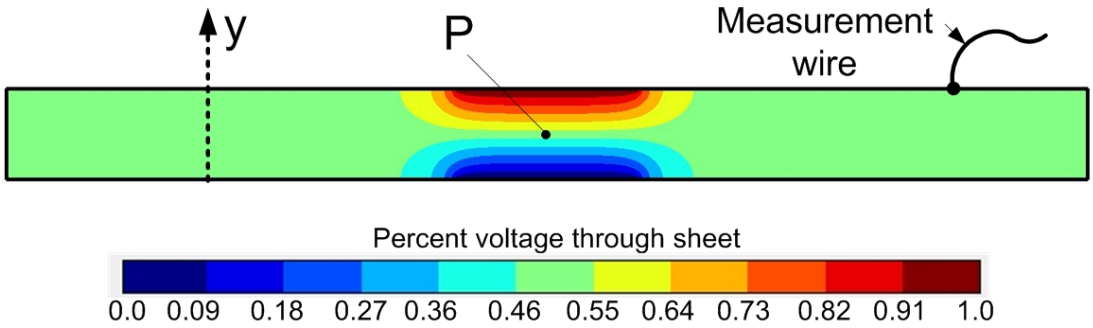

Figure 5.4: Contour plot of voltage potential in sheet with constant ρ

The figure shows the upper sheet in a lap spot welding of two 0.1mm stainless steel sheets. The current flow is restricted to the contact area of the electrode and sheet interface and the interface between the two sheets ($y = 0$). In this situation it is obvious that when measuring the contact resistance - either between electrode and sheet (E/S) or between the two sheets (S/S) - a bulk resistance R_{BS} is included in the measurements. For a uniform current flow through material with uniform resistivity it is clear that the measurement point P is located exactly in the centre of the sheet. If however the resistivity is non-uniform throughout the sheet thickness - which would be the case in a normal welding situation where a significant temperature gradient is present - the measurement point P is expected to move.

A small parametric study has been conducted of the effect of varying the resistivity on the position Y_P of the measurement point P, and the percentage potential drop V_P from the S/S interface at $y = 0$ to P with respect to the total voltage drop through the sheet. The resistivity is approximated to be a function of y and

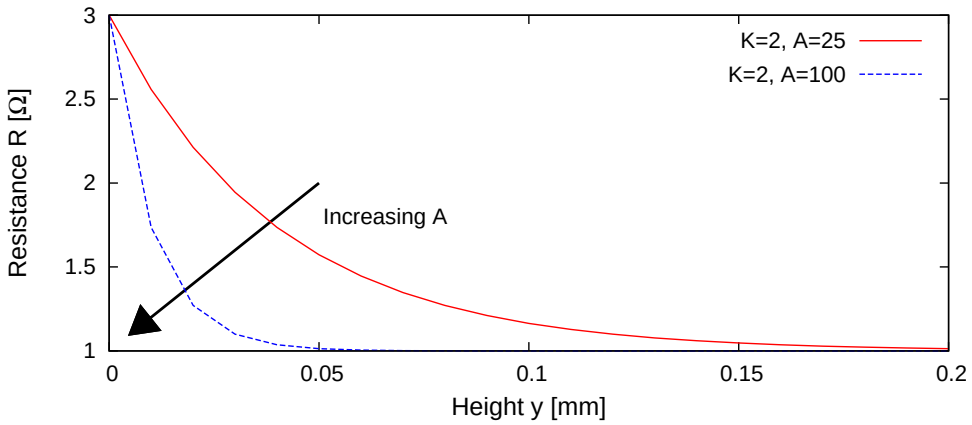

Figure 5.5: Resistivity function for parametric study

following an exponential relation

$$\rho(y) = \rho_0(1 + Ke^{-|y|\cdot A}) \tag{5.7}$$

ρ_0 is the resistivity at room temperature, K is a measure of the maximum value of ρ at the S/S interface at $\rho(0) = (K+1)\rho_0$ and A controls how fast $\rho(y)$ decreases toward ρ_0 when y increases. The actual value of ρ_0 and the current density is proportional to the potential drop and will therefore only affect the absolute values of the potential in this example. The function is shown in figure 5.5 for $K = 2$ and $A = 25$ and $A = 100$. A small study of the effects of the levels of A and K on the potential lines through the sheets has been performed. The K value is varied between 2 and 10 corresponding to a resistivity increase through the sheet of 2 and 10 times the resistivity at $y = 0.1$. As seen from chapter 2 the increase in resistivity with temperature is between 2 and 7 times the value at room temperature, and the choice of $K = 10$ therefore represents an aggressive choice. The levels of A parameters are chosen as 25 and 100 representing a low and high rate of decrease, respectively. Two parameters were investigated: the position Y_P of the point P measured from the bottom of the top sheet ($y = 0$) and the fraction of the measured voltage drop compared to the total voltage drop through the sheet. The effects are plotted in figure 5.6 on page 102.

The study shows that even for relatively large values K and small values of A - corresponding to a big difference in resistivity between the S/S interface and the E/S interface - the position Y_P of the measuring point moves no further away from the S/S interface than 0.02mm (The right graph). This suggests that the position of the measuring point P can be assumed constant throughout the measurements.

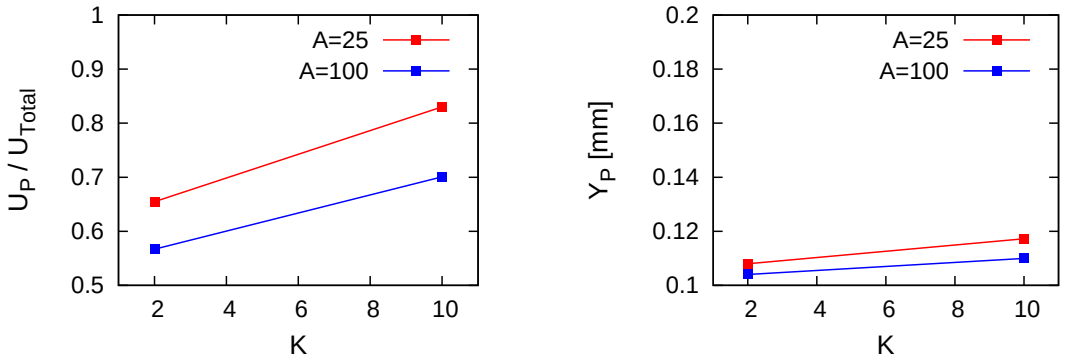

Figure 5.6: The effect of A and K on measured voltage fraction (left) and position of P (right)

The results also show that though the point P is close to stationary the fraction of the total voltage drop measured from P to the S/S interface is highly dependent on the actual resistivity profile through the sheet. Referring to figure 5.2 in section 5.1.1 the measured potentials Φ_{ij} can be split into potential drops across sub-components of: bulk of electrodes Φ_{BE}, bulk of sheets from electrode interface to measurement point Φ_{BES}, bulk of sheets from measurement point to S/S interface Φ_{BSS}, the E/S interfaces itself Φ_{IES} and the S/S interface Φ_{ISS}. Assuming symmetry around the S/S interface we get:

$$\Phi_{12} = \Phi_{\mathrm{BE}} + \Phi_{\mathrm{IES}_1} + \Phi_{\mathrm{BSE}} \tag{5.8}$$

$$\Phi_{23} = \Phi_{\mathrm{ISS}} + 2\Phi_{\mathrm{BSS}} \tag{5.9}$$

$$\Phi_{23} = \Phi_{\mathrm{BSE}} + \Phi_{\mathrm{IES}_2} + \Phi_{\mathrm{BE}} \tag{5.10}$$

When performing measurements of the static contact resistance the resistivity of the bulk material is primarily assumed constant due to low currents and Joule heating. The typical values of the conductivity σ of copper at room temperature is around $6.0 \cdot 10^7 \Omega^{-1}\mathrm{m}^{-1}$ [87, page 620]. If the diameter D_0 of the electrode is 6mm and the vertical distance l_0 of the position of the measurement wire to the tip of the electrode is 20mm the total bulk resistance $\mathrm{R_{BE}}$ of the electrode is roughly estimated to be

$$R_{\mathrm{BE}} = \rho \frac{l_0}{\frac{\pi}{4}{D_0}^2} = \frac{1}{6.0 \cdot 10^7 \Omega^{-1}\mathrm{m}^{-1}} \cdot \frac{20\mathrm{mm}}{\frac{\pi}{4}(6\mathrm{mm})^2} = 12\mu\Omega \tag{5.11}$$

If disregarding the edge effects the bulk resistance of the sheet can be estimated as a cylinder with a diameter d_0 equal to the tip diameter/contact area. The height h of the cylinder equals the distance from the point P to the contact interface being measured. The height of the cylinder will equal approximately half the thickness of the sheet. Assuming a stainless steel sheet at room temperature (i.e. constant

resistivity) with a thickness of 0.2mm, a resistivity of $7.4 \cdot 10^{-7}\Omega$m and an electrode tip diameter of 3.5mm the measured bulk resistance equals

$$R_{\mathrm{BES}} = R_{\mathrm{BSS}} = 7.4 \cdot 10^{-7}\Omega\mathrm{m}\frac{0.1\mathrm{mm}}{\frac{\pi}{4}(3.5\mathrm{mm})^2} = 7.7\mu\Omega \tag{5.12}$$

This implies that using the estimates of the bulk resistance of sheet and electrodes at room temperature and with the dimensions and material properties specified the actual contact resistances can be estimated to be

$$R_{\mathrm{IES}_1} = R_{12} - 12\mu\Omega - 7.7\mu\Omega = R_{12} - 20\mu\Omega \tag{5.13}$$

$$R_{\mathrm{ISS}} = R_{23} - 2 \cdot 7.7\mu\Omega = R_{23} - 15\mu\Omega \tag{5.14}$$

$$R_{\mathrm{IES}_2} = R_{34} - 12\mu\Omega - 7.7\mu\Omega = R_{34} - 20\mu\Omega \tag{5.15}$$

This only applies at room temperature. During welding the bulk temperature of the sheets and electrodes increases and the estimates in equation (5.13-5.15) no longer applies. If the sheet material had been pure nickel (Nickel 200) the resistivity had been approximately ten times smaller [55]. As will be shown in section 5.2 the contribution of bulk resistance as estimated in equation (5.13) to (5.15) is negligible compared to the constriction resistance in the static contact resistance measurements. In the dynamic measurements the bulk resistance can no longer be ignored as described by Tan et al. [35]. However in the initial part of the process the bulk contribution is still small and the measurements are expected to give good estimates of the contact resistance.

5.2 Static Contact Resistance

5.2.1 Experimental Plan

An investigation of the static contact resistance in micro resistance welding was conducted in order to test the experimental setup and discover any problems associated with the measurements. A 2^5 factorial experimental design with n=3 (no. of repetitions) was chosen to investigate overall effects of changing parameters on the contact resistance. The chosen parameters and their levels is shown in table 5.1.

Factor		**Levels** Low (-)	High (+)
F	Force [N]	30	100
I	Current [A]	1	4
D	Electrode tip diameter [mm]	3.5	4.5
Thk	Sheet thickness [mm]	0.1	0.2
M	Material	Ni200	SS316

Table 5.1: Experimental factors and levels

In total $2^5 \cdot 3 = 96$ measurements were taken. Referring to figure 5.2 on page 96 the three potential drops Φ_{12}, Φ_{23} and Φ_{34} were measured after inserting the specimens and applying force and current. Using Ohm's law the total electrical resistances R_{12}, R_{23} and R_{34} of each measurement can be calculated. The numerical value of these factors are very large compared to the bulk resistances prescribed in equation (5.13-5.15). This implies that the bulk resistance of sheets and electrodes are negligible compared to the static contact resistances of the interfaces and the measured resistances R_{12}, R_{23} and R_{34} can directly be regarded as the static contact resistances of the interfaces E/S, S/S and S/E, respectively. In the following the three resistance components are named R_1, R_2, and R_3, respectively.

5.2.2 Experimental Procedure

Samples of approximately 10x60mm are cut from larger sheets of material. A normal copper-wire is projection welded to the one end of every sheet sample and wires are attached to the electrodes as shown in figure 5.2. The faying surfaces of the sheets were cleaned with ethanol to remove dirt and to get surfaces of similar quality and cleanliness. When changing the factor levels between experiments a "dummy" sheet was used to set the force and current levels before the actual measurement sheets were inserted and the measurement taken. From the recorded data the contact resistance is calculated using Ohm's Law. Due to the fact that the

changing of electrodes was somewhat time consuming this factor restricted the experimental plan and experiments were randomised *within* the electrode factor [88]. The actual order of the experiments is not expected to influence the measurements but the electrode itself could vary in geometry and influence measurements. Because of this, the electrode pair was changed between repetition runs but the final analysis of the data showed no clear block-effect of the individual electrodes (not to be confused with the electrode diameters which are actual factors in the analysis).

5.2.3 Results

The results are plotted in a box plot in figure 5.7 showing the measured resistances for stainless 316 (left) and nickel 200 (right) with the holding force as a factor. The box plot is a common way of getting an overview of a data set and easily spot

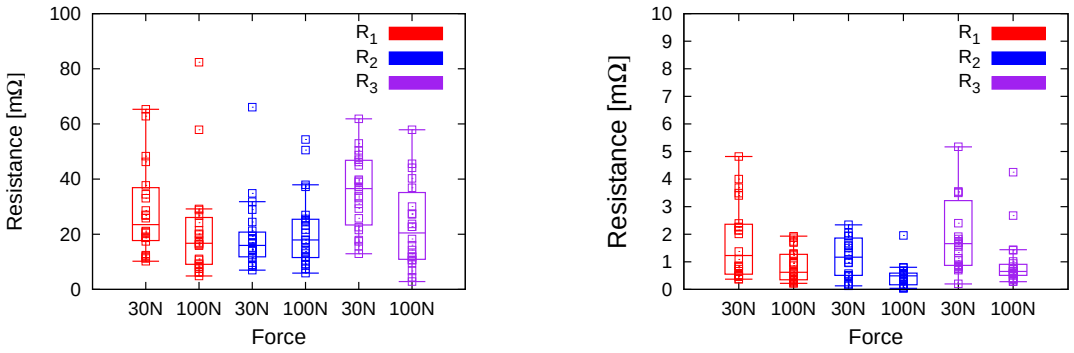

Figure 5.7: Box plot of measured static contact resistance with force as factor showing stainless steel 316 (left) and nickel 200 (right)

possible outliers. The plot shows the single measured values (points) and a box from the 25% quartile to the 75% quartile. The median is marked inside the box as a horizontal line. The *whiskers* extending from the ends of the box mark the last measurement which is within 1.5 times the length of the box's distance from either the 25% or the 75% quartile. Based on the majority of the experimental values the values which are outside the range of the whiskers are likely to be outliers and if not removing them could give erroneous conclusions.

Looking at the data in figure 5.7 it is first of all clear that the static contact resistance is more than 10 times smaller for the nickel sheets compared to the stainless steel (note the scales on the y-axis). Furthermore the data set has several values which are likely to be outliers. Because of the stochastic nature of true surfaces any measurements of contact resistance is always influenced by a high degree of variability [24]. Measurements falling outside of the whiskers in the box plot are disregarded in the analysis in order not to be influenced by single measurements that are statistically abnormal.

Looking at the contact resistance using nickel sheets it can be seen how the spread (e.i. the size of the box) decreases when increasing the force. The median values are also seen to decrease when the force increases. This is as expected because a higher contact pressure increases the actual contact area and the electrical contact resistance hereby decreases. The results for the stainless steel sheets does not show the same apparent trend. Increasing the force does not seem to decrease the variability of the measurements and only the interface resistance between the electrodes and sheets seems to decrease with increasing force whereas the contact resistance between the sheets seems more or less unaffected by the force.

A standard ANOVA (**AN**alysis **O**f **Va**riance) [88] analysis was performed on the results testing only for main effects and first order interactions and removing the outliers found from the box-plot in figure 5.7. An ANOVA table of the factors and their effects is collected in table 5.2 on page 107 and the factor notation is shown in table 5.1. Table 5.2 show the estimated effects (*Estimate*) and the probability (*Prob*) in percentage that the variability of the response *only* is due to experimental error. This means that a probability less than 1% implies that their is more than 99% propability that the factor has an significant effect on the response. In the table all values less than 1% are enclosed in () and marked with a *. As the influence of the current level A was not significant the factor was dropped from the model implying that the number of repetitions effectively increased in the analysis improving its accuracy. As suspected from the box plot the ANOVA concludes that the force indeed has a significant effect on the contact resistance - except for the S/S interface using stainless steel. Furthermore also the thickness of the nickel sheets are seen to have an significant effect on the static resistance in the E/S and S/E interfaces (R_1 and R_3) and the electrode diameter has an effect on R_3. In general however, it was found that the experiments suffered from a large experimental error and/or uncontrollable factors influencing the measurements and so the overall fit of the model estimated by the ANOVA analysis is fairly poor. It is therefore suspected that the apparent effect of the diameter and sheet thickness is due to variations in the surfaces of the nickel sheets and the electrodes and not the factors themselves.

5.2.4 Discussion

The experimental series of measuring static contact resistance generally showed large variations in the measured responses. Uncontrollable factors greatly influenced the measurements and caused the large variability. One of the main uncontrollable factors are believed to be surface film thickness and mechanical rupture of surface films prior to measuring. When inserting the sheets between the electrodes and during the loading the sheets are able to move, bend and slide a little in response to any initial misalignments of the sheets. Because of this relative motion

Stainless steel AISI 316

	R_1		R_2		R_3	
Factor	**Estimate**	**Prob**	**Estimate**	**Prob**	**Estimate**	**Prob**
D	-1.89	0.279	1.71	0.17	-2.55	0.2869
Thk	-1.76	0.315	0.35	0.7756	-2.67	0.2643
F	4.78	(0.008)*	-0.61	0.6181	6.90	(0.0055)*
D·Thk	-3.21	0.071	-1.00	0.415	-0.44	0.8537
D·F	-1.54	0.372	0.76	0.5322	1.11	0.6365
Thk·F	0.51	0.77	0.90	0.4642	-1.28	0.588

Nickel 200

	R_1		R_2		R_3	
Factor	**Estimate**	**Prob**	**Estimate**	**Prob**	**Estimate**	**Prob**
D	0.046	0.7483	-0.11	0.1849	-0.25	(0.0095)*
Thk	-0.49	(0.0014)*	-0.17	0.0317	-0.48	(< 0.0001)*
F	0.48	(0.0016)*	0.32	(0.0002)*	0.53	(< 0.0001)*
D·Thk	0.25	0.0892	0.080	0.3111	0.12	0.0344
D·F	0.057	0.6903	-0.025	0.7481	-0.10	0.2723
Thk·F	-0.19	0.1878	-0.063	0.4246	-0.23	(0.0022)*

Table 5.2: Effect estimates and significance

between sheets and electrodes the typically brittle surface films on the surfaces of the specimens can rupture. Depending on the amount of relative motion and variation in film thickness across the specimens the film will rupture in an uncontrollable manner. As the repeatability of both the manual inserting of specimens and the film thickness across the specimens are practically impossible to control, the experiments consequently suffer from large variations in measured static contact resistance. Besides influence from surface films the asperities of two surfaces that are in sliding contact will deform plastically and/or slide to a better fit in such a way that the real area of contact increases whereby decreasing the local pressure on the asperities. A larger true area of contact decreases contact resistance.

Despite the large variation in the measured static contact resistance the results of welding nickel and stainless steel foils do not show large variation in the outcome of the process, i.e. the repeatability of joint breaking force and nugget size is not influenced by large variation. This indicates that the specific value of the static contact resistance is less important in determining the outcome of the process. Measurements of the static contact resistance is therefore not suited as a process control parameter or for quality control.

5.3 Measuring Dynamic Contact Resistance

5.3.1 Experimental Plan

The effect of the main parameters on the dynamic contact resistance is investigated through a 2^k factorial experimental plan intending to give an overview of the influencing factors. Due to the expected high degree of experimental variation three repetitions (n=3) are made of the plan. Disregarding any material related issues, the main process parameters that are likely to affect the contact resistance and the final strength of the weld is the weld force F, the weld current I, and the current ramp-up rate A. The factors and factor levels for each material is seen in table 5.3 and a graph showing the current versus time curve for the experiments is shown in figure 5.8. The weld time excluding the current ramp-up time is set constant for all the experiments.

		Levels		Levels	
Factors		**Low (-)**	**High (+)**	**Low (-)**	**High (+)**
F	Electrode Force [N]	50	75	50	150
I	Current [% (of max)]	35	45	15	25
A	Current Ramp-up [A/ms]	50	100	50	100
M	Workpiece Material	Ni200		SS316	

Table 5.3: Experimental factors and levels - Dynamic contact resistance measurements

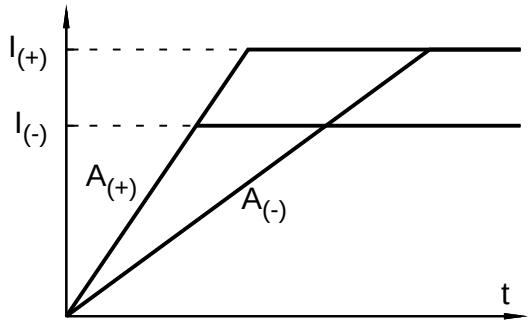

Figure 5.8: The current vs time curve for the factorial experiments

In the experiments with Ni200 material the electrode-pair was changed for each repetition, implying that the experiments have restrictions on the randomisation and the experimental order is randomised only within each repetition. As described

in section 5.1.3 the measured potential drop across the S/S interface include the potential drop across approximately half the thickness of the bulk of two sheets, which effectively is the bulk of a single sheet. At room temperature this potential drop is negligible compared to the actual contact resistance between the sheets. However, as the welding process progresses the interface is broken down and a bond is created. This implies that the contact resistance starts to diminish while the bulk resistance increases due to higher temperatures in the material. The potential drop across the bulk material will no longer be negligible which should be remembered when analysing the results and estimating actual dynamic contact resistance.

5.3.2 Experimental Procedure

Samples with 0.2mm thickness of approximately 15x60mm of the two sheet materials are cut and a copper-wire is welded to the one end of the sheets using a capacitor discharge power supply. Before welding the samples are wiped with a cloth with ethanol to remove the worst contaminants from the surfaces and to ensure that the surfaces are as equal as possible. When inserted between the electrodes and just before the weld current is initiated the data acquisition (DAQ) wires connected to the sheets are bend and positioned manually to reduce the area of the closed circuit as well as positioning the circuit perpendicular to the direction of the current through the electrodes. This is done to minimise the amount of magnetic flux that passes through the closed circuit formed by the sheets and measurement wires and thereby minimising the induced electromotive force in the measurements.

The current is measured with a LEM LT-1000 closed loop hall-effect current transducer with a $< 1\mu s$ response time and capable of measuring frequencies up to 150kHz with peak currents of 2kA. A High Frequency Inverter (HFI) from Resistronic, Switzerland is used as power supply. The HFI is capable of delivering a stable RMS current of up to 5kA. The frequency of the HFI is approximately 10kHz and according to the Nyquist-Shannon theorem the minimum sampling rate of the DAQ-system in order to avoid aliasing should be more than 20kHz [89]. In order to get a reasonably resolution of the acquired data the sampling rate of the DAQ-equipment is therefore set to 48kHz.

After lap welding the specimens, the welds are tensile shear tested in an Insitron tensile testing machine measuring the maximum tension force and the extension at the max force. After testing, the diameter of the nugget is estimated using light optical microscopy and evaluating the size of the failure surface of the weld. It should be noted that the optical technique for this purpose is associated with a high degree of uncertainty, as the exact dimensions of the failure surfaces are difficult to estimate precisely.

Analysis of Acquired Data

During welding the current and the voltage drops are measured. Due to the high frequency of the welding current the voltage measurements are influenced by an induced electromotive force. Although steps are taken to minimise the induced voltage by reducing the area of the measurement wires contributing to the magnetic flux the voltage error is still non-negligible. On figure 5.9 an example of the collected data is shown. It can be seen how both the current and voltage fluctuates with the frequency (approx. 10kHz) from the high frequency inverter power supply. If simply calculating the resistance by $R = U/I$ it can be seen (on the top graph) how the error affects the calculation and the resistance varies a lot. To compensate for this a simple RC low-pass filter is applied to the measured data. As can be

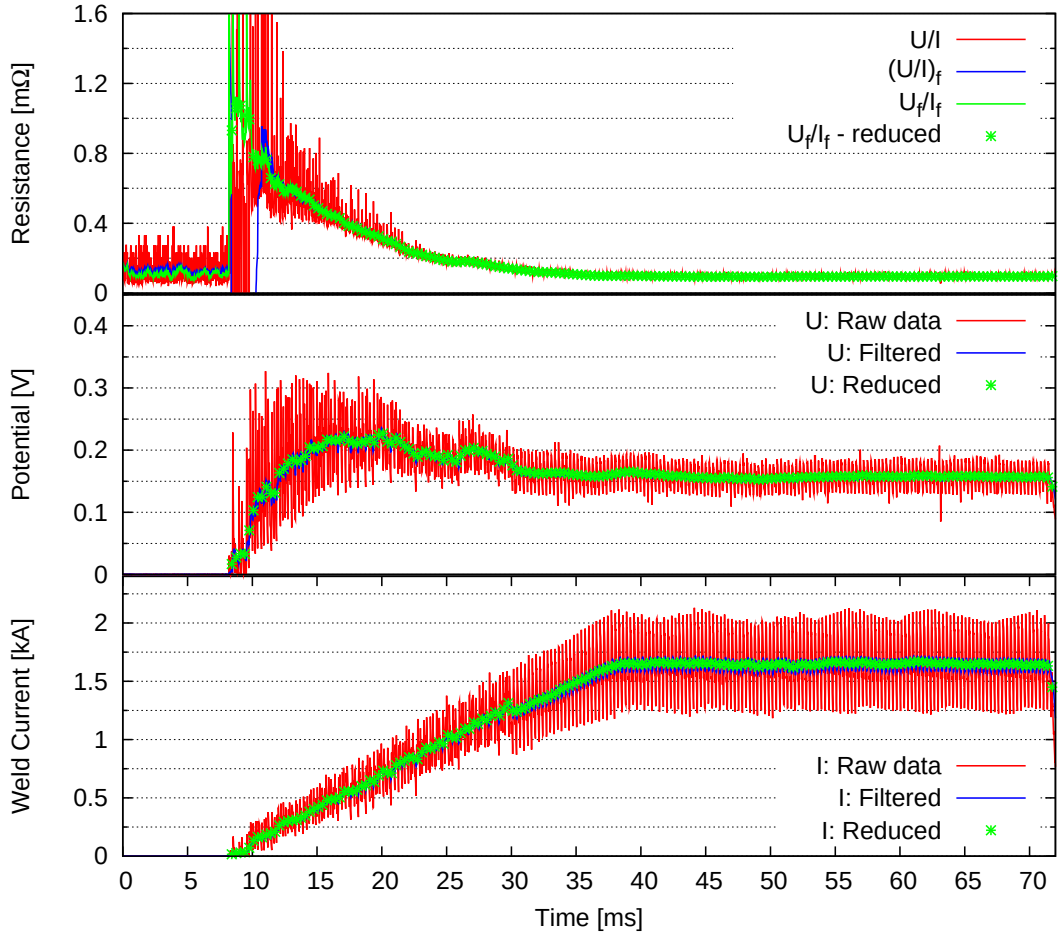

Figure 5.9: Example on measured and filtered current and voltage signals and calculated contact resistance for micro spot welding of nickel

seen from figure 5.9 this greatly decreases the amplitude of the current and voltage signals (I_f and U_f) as the filter functions as an exponentially weighted moving average. To calculate the resistance two methods are shown. The first method applies the filter to the calculated resistance $(U/I)_f$ and the second method calculates the resistance using the filtered signals (U_f/I_f). From figure 5.9 is can be seen that the first method applying the filter to the U-I ratio gives an erroneous result in the initial part of the curve where the values for the resistance becomes negative due to the large fluctuations in the original data. The second method calculating resistance from the filtered signals yields a much smoother curve during the entire range. When using filtered signals to calculate a value it is important to remember that this has an averaging effect on the result removing most of the fine details and the calculated resistance must therefore be regarded as an average signal value. However, due to the relatively high acquisition rate of 48kHz the averaging effect is still small when considering the total acquisition time. In order to properly plot the contact resistance curves in the results section it was furthermore necessary to reduce the resolution of the data. The reduced signals are plotted on top of the data in figure 5.9.

5.3.3 Results

ANOVA of Maximum Joint Strength

The maximum joint breaking force (JBF) measured by tensile shear testing of the welded specimens are found in appendix B.1 and is analysed by the Analysis of Variance method (ANOVA) [88]. In table 5.4 is shown the results of the analysis for the SS316 material. The **SS** is the sum of squares, **DOF** is the degree of freedom, **MS** is the mean sum of squares (**SS**/**DOF**), **F0** is the test statistic ($\mathbf{MS}_{factor}/\mathbf{MS}_{error}$), and **P** is the power indicating the probability that the factor has *no* effect on the response. Significant factors therefore have a low P-value and

Factor	**SS**	**DOF**	**MS**	**F0**	**P**	
Model	216585.1	7	30940.7	14.32	0.00%	*
F	4279.5	1	4279.5	1.98	17.84%	
I	199734.8	1	199734.8	92.47	0.00%	*
FI	7544.9	1	7544.9	3.49	8.00%	
A	1955.8	1	1955.8	0.91	35.55%	
FA	2850.7	1	2850.7	1.32	26.75%	
IA	54.7	1	54.7	0.03	87.55%	
FIA	164.8	1	164.8	0.08	78.59%	
Error	34560.4	16	2160.022			

Table 5.4: ANOVA table of maximum joint tensile force for the SS316 material

is marked by a star *. As can be seen from the table, the only factor showing a significant effect on the JBF is the weld current. Neither the force nor the current ramp-up rate has significant influence on the JBF compared to the experimental error in the investigated range of the factors. For sure, if the levels of the electrode force or the current ramp-up rate had been chosen even more aggressively, at some point we would start to see an effect of these factors. However for the factor range specified in table 5.3 the only significant effect is the current. Based on the analysis a linear response curve is fitted to the data which models the response of the factors. The fitting is based on the least square approach, and the calculated response model is shown in equation (5.16). The unit for JBF is [N] and I is inserted as [%] of max current capacity of the power supply.

$$JBF_{SS316}(I) = -110.2 + 18.2I \tag{5.16}$$

Calculating the adjusted R^2 statistics for the reduced model (only I is included) yields

$$R^2_{Adj,SS316} = 1 - \frac{SS_{Error}/DOF_{error}}{SS_{Total}/DOF_{Total}} = 0.79 \tag{5.17}$$

This indicates that the model is able to explain close to 80% of the variability in the measured JBF. This means that 20% of the variability in the data can not be attributed to any factor and must therefore be contributed to experimental variability which includes variability in the tensile shear tests. Although care was taken to align the specimens during tensile testing small variations in the alignment will influence the maximum JBF thereby introducing variability.

The ANOVA analysis on the Ni200 material is shown in table 5.5. Besides the weld current the electrode force is now having a significant effect on the JBF of the Ni200 joints. This is addressed later in section 5.3.4. Fitting a response curve

Factor	**SS**	**DOF**	**MS**	**F0**	**P**	
Model	152733.2	7	21819.0	26.35	0.00%	*
F	44396.6	1	44396.6	53.61	0.00%	*
I	85954.8	1	85954.8	103.79	0.00%	*
FI	3757.9	1	3757.9	4.54	5.14%	
A	3716.6	1	3716.6	4.49	5.25%	
FA	60.3	1	60.3	0.07	79.11%	
IA	3526.3	1	3526.3	4.26	5.81%	
FIA	1916.8	1	1916.8	2.31	15.04%	
Block	563.0	2	281.5			
Error	11594.1	14	828.2			

Table 5.5: ANOVA table of maximum joint tensile force for the Ni200 material

to the model yields

$$JBF_{Ni200}(I, F) = -158.65 - 3.5F + 12.4I \tag{5.18}$$

Again the units of JBF, I and F is [N], [%] of max current and [N], respectively. The adjusted R^2 statistics of the model is calculated to be

$$R^2_{Adj,Ni200} = 0.84 \tag{5.19}$$

Again most of the variability is explained by the model, but there is still a non-neglectable part (16%) which is not explained and is due to experimental variation and uncertainties in process output and testing methods. The ANOVA analysis of the two experimental series both suggest that the JBF is not influenced by the current-ramp up rate.

Contact Resistance Curves

The measured contact resistance R_2 during welding of the Ni200 samples can be seen on figure 5.10 and for the SS316 material on figure 5.11 on page 114. The graphs on the left show curves for the low level of the force and the curves on the right show curves for the high level of the force. No clear visual effect of the current level on the resistance curves could be identified and to simplify the plots no distinction is made between the levels of the current. There is a significant difference between the two materials. First of all the size and range of the contact resistance of the two materials differ a lot - note the scales on the graphs. Furthermore the actual development of the contact resistance differs mainly in the beginning of the process. The contact resistance of the stainless steel (figure 5.11) is initially very high. The actual value of the initial contact resistance is not very accurately estimated as there is a lot of scatter in the data just when the current is initiated. The value however is expected to lie in the range measured in section 5.2. The resistance drops very fast during the first 4-6ms of the process and settles around 0.2-0.4$m\Omega$. The contact resistance curves for the Ni200 material (figure 5.10) shows a small increase in the beginning of the process and then drops to settle around 0.1$m\Omega$. The same initial peak in contact resistance has been measured by Tan et al. [35]. He concludes that the peak is caused by the surface oxide-layer that breaks down when exposed to a certain critical potential drop depending on the thickness of the oxide layer. This critical potential drop was shown to be fairly consistent through several repetitions and for the lap-joints of 0.2mm Ni200 sheets it was found that critical breakdown voltage was around 0.16V-0.23V depending on the thickness of the oxide-layer [35].

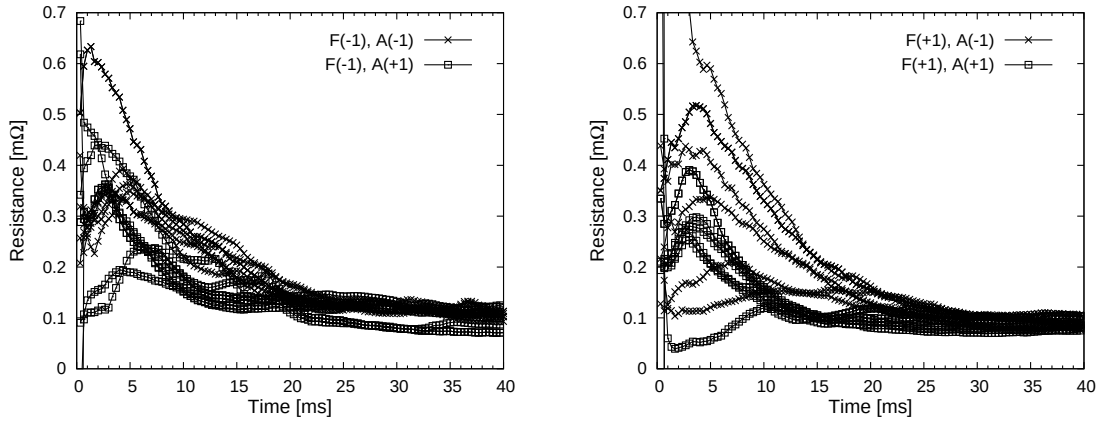

Figure 5.10: Measured contact resistance curves for Ni200 showing effect of current ramp rate.

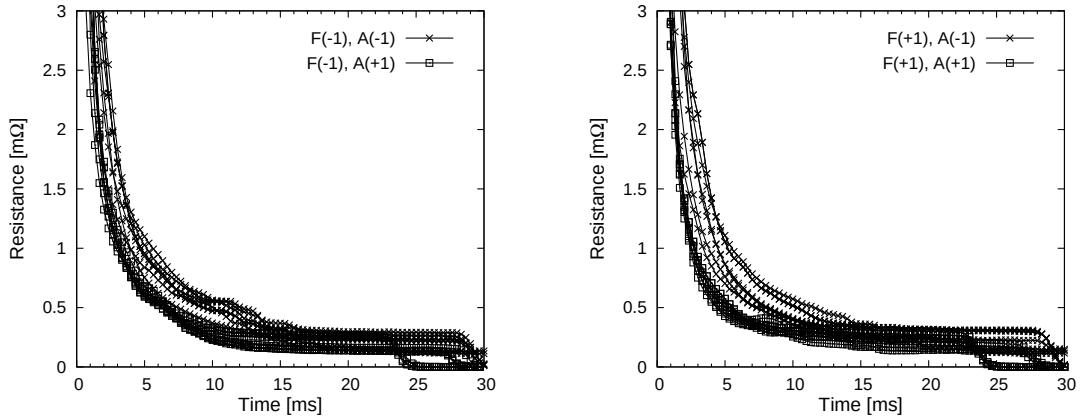

Figure 5.11: Measured contact resistance curves for SS316 showing effect of current ramp rate.

Figure 5.12 and 5.13 shows the measured interface voltage drops U_2 during welding of Ni200 and SS316, respectively. For the nickel welds it is seen how the potential increases at a close to constant rate in the beginning of the weld. This is most obvious for the low electrode force settings (left graph) while the voltage curves for the high electrode force settings (right graph) seems to have larger variation in the rate of increase. This could most likely be due to variations in the mechanical rupture of the surface oxide-film prior to welding which is intensified due to the larger pressure. After approximately 5ms the increase in voltage starts to level out around 0.18-0.2V, which agrees well with the measurements in [35]. Looking at figure 5.10 it can be seen that the resistance curves peaks approximately after 5ms, which is exactly where the voltage levels out. The appearance of the potential curves for the SS316 material seen on figure 5.13 has a somewhat different appearance than the Ni200. The voltage drop is right from the initiation of the current at a relatively high level (0.3V) and then decreases steadily throughout the process.

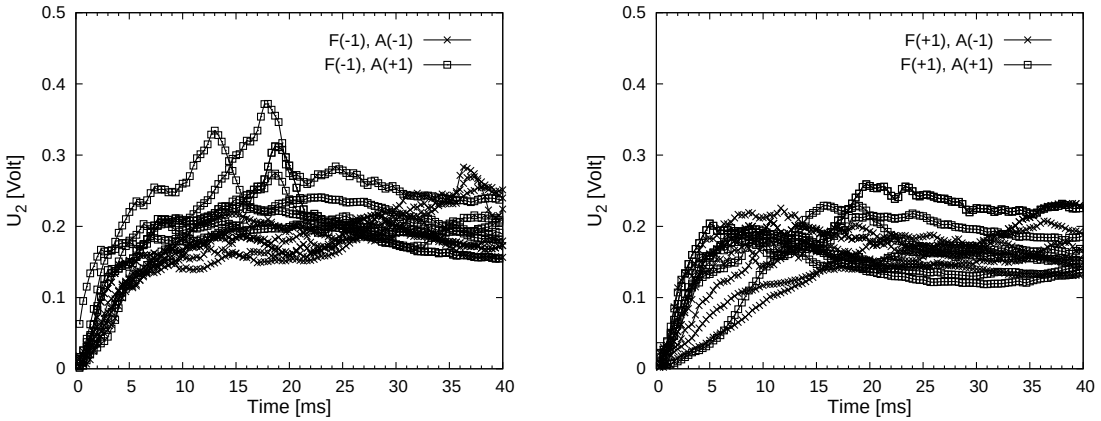

Figure 5.12: Measured voltage drop U_2 of Ni200 showing effect of current ramp rate.

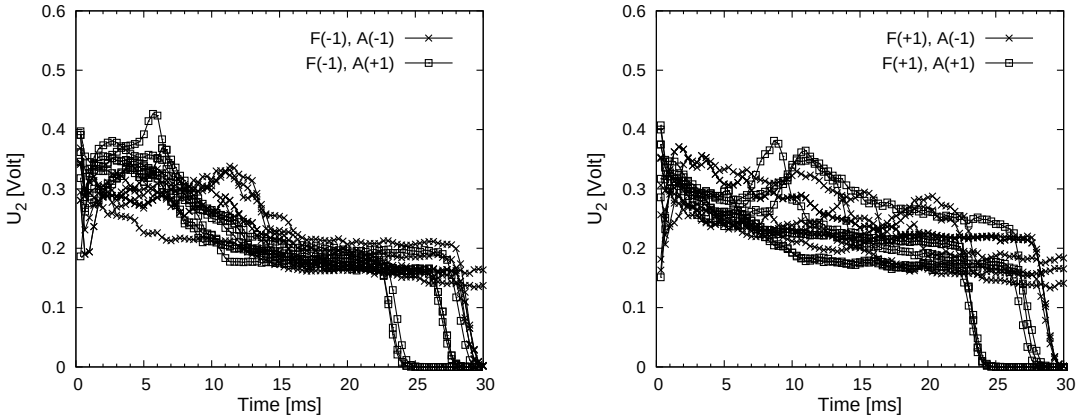

Figure 5.13: Measured voltage drop U_2 of SS316 showing effect of current ramp rate.

5.3.4 Discussion of Results

The effect of the current ramp-up rate on the development of the contact resistance can be seen on figure 5.10 and 5.11. Going from low to high current-ramp rate doubling the value from 50 to 100A/ms the contact resistance is significantly lowered. In fact, until the curves level out at the steady state contact resistance, the resistance for the low ramp-rate is approximately twice the value of the high ramp-rate at the same process time-step. This corresponds well with the fact that the current, at any given time-step during the ramp-up phase is, twice as high for high ramp-rate than for the low. The dependency is further explored by plotting the contact resistance as a function of the current as seen on figure 5.14 and figure 5.15[2] on page 116. Here it can be seen, that especially for the SS316 material

[2]The group of low resistance data points approaching zero current are due to the downslope of the current and should be disregarded

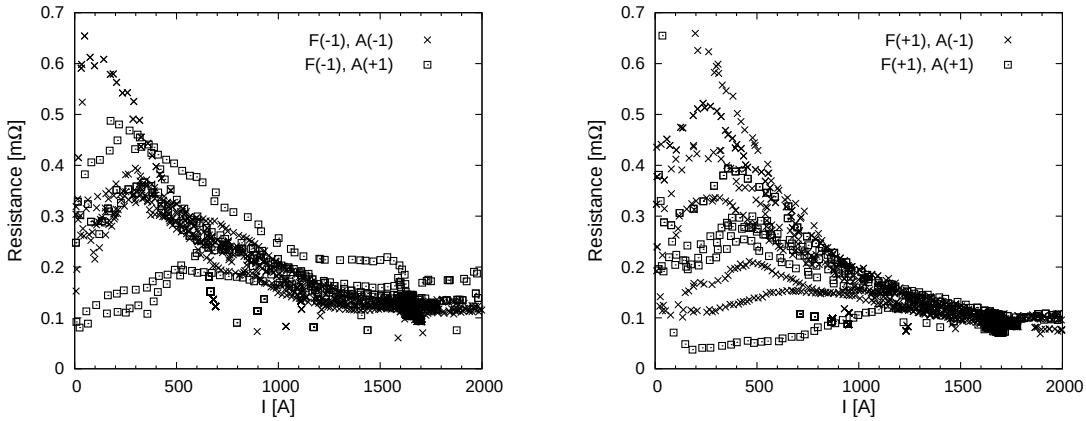

Figure 5.14: Measured contact resistance of Ni200 as a function of welding current showing effect of current ramp rate.

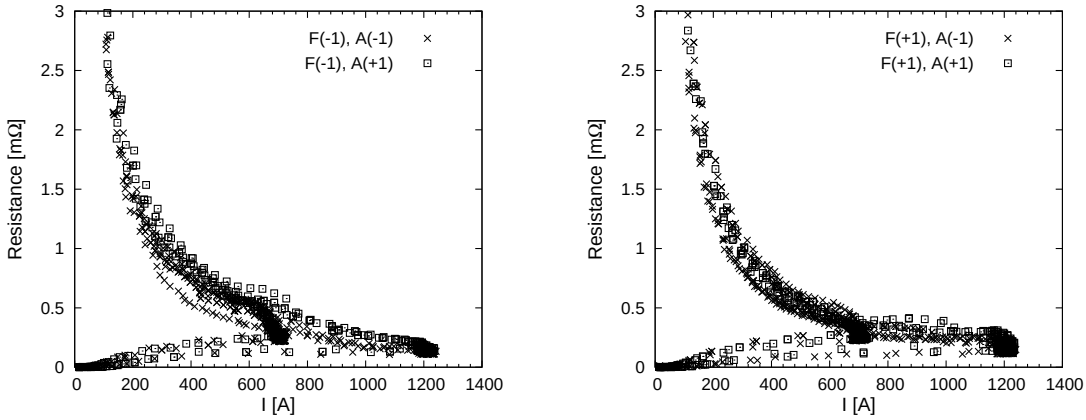

Figure 5.15: Measured contact resistance of SS316 as a function of welding current showing effect of current ramp rate.

the interface resistance is to a high degree controlled by the actual level of the weld current. For Ni200 this is seen to hold primarily for the experiments with the low electrode force (left graph) while the experiments with high electrode force (right graph) does not follow the current level until after it reaches 1000A.

Figures 5.10 and 5.11 show how the measured contact resistance during welding decreases and reaches a close to steady state after a certain time. Practically all the dynamic changes in the contact resistance happens during the ramp-up period of the current. This could imply, as also suggested by Tan et al. [35], that the contact resistance during micro spot welding is only significant in the very beginning of the process. However, as the ANOVA analysis suggest, the primary factor affecting weld strength is the final weld current, which have no effect on the process in the

beginning of the process during the ramp. This could imply that for the range of parameters investigated in this study the initial contact resistance should not have large importance on the final result when modelling the process. This will be investigated further by numerical simulation of the process.

5.4 Numerical Modelling of Micro Resistance Spot Welding

In this section numerical modelling of micro resistance spot welding of stainless steel AISI 316L and Nickel 200 foils is investigated using the commercial FE-program SORPAS[3]. Focus will be on contact problems in relation to the experimental results presented in section 5.3.

5.4.1 Numerical Procedure

The resistance spot welding process can be modelled by a 2D axis symmetric model. The elements used are 2D solid quadrilateral elements. To simulate a sheet using solid elements a certain minimum number of elements should be used in order to be able to adequately capture the deformation and the thermal and electrical field in the simulation. In this work four elements were used because the plastic deformations are limited in spot welding. The contact layer defining the contact resistance, which has to be defined in SORPAS, should have an appropriate thickness compared to the sheet thickness. The standard settings in SORPAS are not suited for small scale welding and needs to be adjusted. In this work a contact layer thickness of $20\mu m$ was used, corresponding to 5% of the foil thickness. Element size should be optimized in such a way that areas exposed to large deformations and/or non-uniform and complex thermal and electrical fields should have a fine mesh. Therefore the mesh was refined in the foils and in the tip of the electrodes. The model is shown in figure 5.16 on page 118.

In the study in section 5.3 a High Frequency inverter was used as the power supply. The actual profile of the weld current consist of a high frequency (5kHz) current. In SORPAS it is not possible to select an HF-power supply and so it is necessary to approximate the signal with a DC-power supply, setting the weld current to the RMS value of the actual high frequency signal. The electrode force is set as a constant value and machine dynamics is not considered in this study.

[3]Simulation Of Resistance Projection And Spot welding, version 9.83 - SWANTEC ApS, http://www.swantec.com

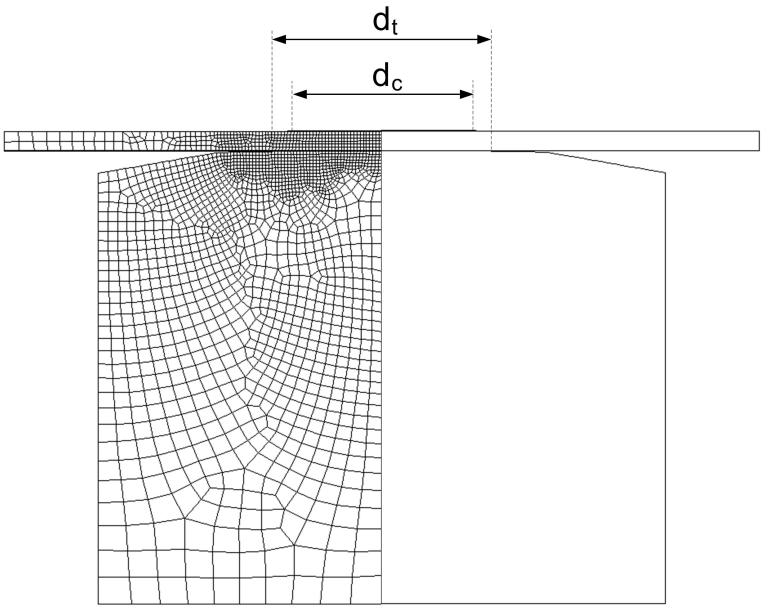

Figure 5.16: FE-model of micro resistance spot welding of foils.

The Electrode to Sheet Contact Area

In spot welding the actual contact area is defined by the shape of the tip of the electrode and the weld force that presses the electrodes into the workpieces. Alignment issues in the experimental setup implies that it has not been possible to use flat-ended electrodes, because the contact becomes highly irregular and only occur on the edge of the electrodes. By using electrodes which have a slightly domed-shaped curvature on the tip (R=80mm), the contact zone will now be more independent of the non perfect alignment of the electrodes and result in a circular contact area [90]. This greatly improves the consistency of experimental results, however, the numerical procedure becomes more complicated. Compared to a flat ended electrode where the contact area in theory is defined by the electrode tip radius, the contact area is now mainly controlled by the actual tip curvature, the electrode force and the deformation of the sheets. This implies that the numerical simulations become highly dependent on the simulation of the electrode indentation and the applied numerical algorithm for determining whether contact has occurred or not. In large scale resistance spot welding the contact area is typically well-defined because of the relatively high forces involved. In micro resistance spot welding the typical contact pressure is smaller than in large scale. This has the effect that the dimensional tolerances has more influence on small scale both experimentally and numerically. It was found that even small variations in the geometry of the models would significantly influence the heat generation in the simulation due to a change in contact area. Inserting the nominal values of the electrode tip radius of

curvature resulted in a clear underestimate of the actual contact area and therefore a too high heat generation. In order to come about this problem it was necessary to manually define the initial contact tip diameter of the electrode defined as d_t on figure 5.16. Based on the experimental results found in appendix B.1 the maximum achieved nugget diameter and the maximum diameter of the solid state bond area was estimated to be 1.15mm. It is often assumed that the nugget diameter approximately equals the diameter of electrode to sheet contact area [3, 91]. Based on this d_t was set to 1.2mm in the numerical simulations. The validity of this assumption is questionable, but considering the close to plane electrode face and low electrode force the contact area is not expected to vary significantly from this value.

The Sheet to Sheet Contact Area

As with the electrode to sheet contact area the actual contact zone between the workpieces is defined by the size of the electrodes and the applied force. In large scale resistance spot welding the sheets being welded will most often bend due to the electrode pressure thereby clearly defining the contact area. An example of sheets separation during welding is shown in figure 5.17 and in simulation of large scale resistance welding some separation will almost always occur thereby clearly defining the contact area.

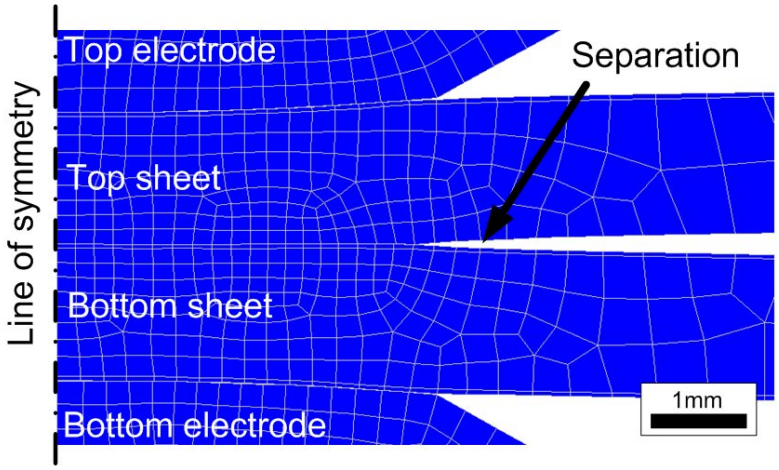

Figure 5.17: Example of sheet separation in simulation of large scale resistance welding of soft deep drawing steel ($F = 4.5$kN

The downscaling of the sheet thickness is often not proportional to the downscaling of the electrode size resulting in a lower contact pressure in micro welding compared to normal size welding. Therefore the contact pressure in micro welding is low enough to prevent the mechanical bending and separation of the sheets. In the simulations of micro spot welding of foils the results show that in fact there is

tension stresses normal to the surface acting on the sheet-to-sheet interface on the periphery of the electrode contact area. An example hereof is seen in figure 5.18, which shows the results of a numerical simulation of resistance welding of Nickel 200 foil.

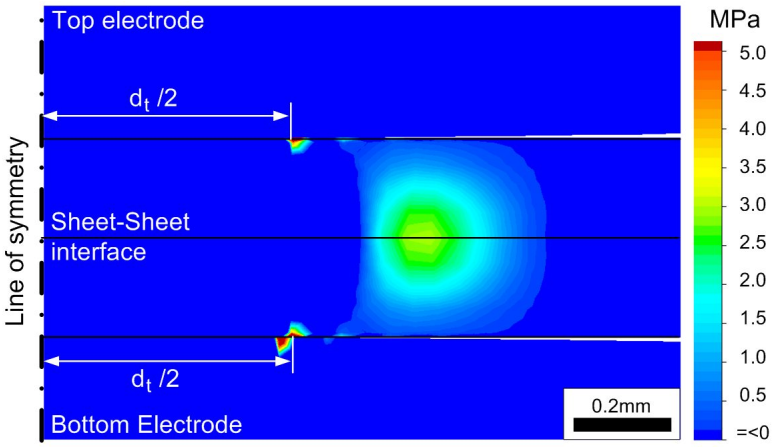

Figure 5.18: Example of vertical tension stresses on sheet-to-sheet interface in micro spot welding of Ni200 foil ($F = 50$N, $I = 2.25$kA)

Despite that the actual electrode to sheet contact, and thereby also the compressive force, is limited to the area marked by the contact radius $d_t/2$ the sheets does not separate *numerically* but remain in contact. This can probably be contributed to an assigned threshold value of the separation criteria in the numerical contact algorithm in the software. As can be seen from figure 5.18 the stresses are only a few MPa which most likely fall under the threshold value for separation in order to stabilise the convergence of the numerical implicit solver.

In numerical simulation of the process the actual sheet-to-sheet contact area can have a significant impact on the outcome of the simulation, because the size of the contact area is crucial in determining the current density and thereby the heat generation at the interface. This is illustrated in figure 5.19a, showing the simulated maximum temperature in resistance micro spot welding of $0.2mm$ Ni200 foils as a function of d_t and d_c (c.f. figure 5.16), where d_c is controlled by manually defining the diameter of the contact layer. It is noted how the maximum temperature asymptotically is approaching a constant value for increasing sheet-to-sheet contact diameter d_c as the effect on the current flow becomes negligible at a certain distance from the weld zone. Figure 5.19a illustrates that if the sheets *do* separate during the actual welding process, thereby decreasing the sheet-to-sheet contact area, this has impact on the outcome of the process which should be included in the numerical analysis.

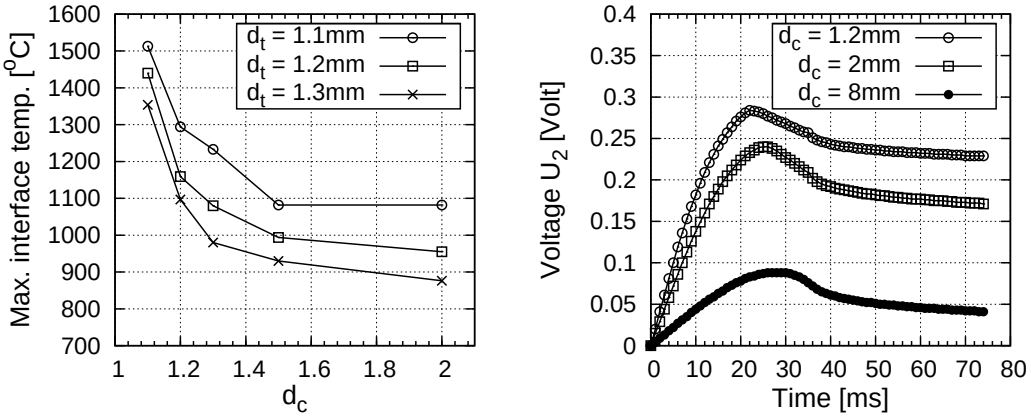

Figure 5.19: Influence of electrode-to-sheet contact diameter d_t and sheet-to-sheet (Ni200) contact diameter d_c on a) maximum interface temperature and b) ($d_t = 1.2mm$) interface voltage ($F = 50$N, $I = 2.25$kA)

It is difficult to give an accurate estimate of how the actual contact conditions develop during welding and thereby estimate the effect of any restrictions on the contact area. The measurement technique described in section 5.1 for measuring contact resistance relies on voltage measurements on the end of the sheets assuming contact is established under the electrode contact area. On figure 5.19b is shown the effect of the change in sheet-to-sheet contact area on the simulated voltage drop. The default simulation setting produces a contact area covering the entire sheet-to-sheet overlap ($d_c = 8mm$) resulting in a decreased voltage and thereby contact resistance measurement. However this measurement does not represent the experimentally measured values (c.f. figure 5.12). By manually decreasing the interface d_c it is observed how the measured voltage drop increases to values corresponding to the experimentally measured values.

The numerical simulations suggest that the positive normal stress in the sheet-to-sheet contact area is limited to an area approximately equal to the electrode-to-sheet contact area. Because of this, it is suggested that the diameter of the contact layer at the sheet to sheet interface d_c is manually reduced to approximately the size of the electrode to sheet contact area d_t in simulation of micro resistance spot welding. Alternatively the electrode to electrode contact area is evaluated in each case by estimating the location of the tension stresses and then manually decreasing the contact area to the width of the zone experiencing compression stresses.

Material Properties

One of the features of the numerical software SORPAS is its comprehensive materials database. In the simulations the default electrical, thermal and electrical properties for Nickel 200 and Stainless steel AISI 316 is used from the SORPAS database. The electrical contact resistance is modelled by the contact layer model described in section 4.1 on page 64. The model is shown again below in equation (5.20).

$$R_{\mathrm{CR}} = 3t_c\left(\frac{\sigma_{s\_soft}}{F}\right)\left(\frac{\rho_1+\rho_2}{2}+\rho_f\right) \tag{5.20}$$

For Nickel 200 it was found that using the default values of the contaminant resistance ρ_f resulted in generally poor correlation between the experimental and simulated voltage drop across the sheet-to-sheet interface. The contaminant function ρ_f was therefore fitted by trial and error until a better agreement with experimentally measured values of the voltage drop and contact resistance were found. For the Nickel 200 the contact resistance was increased and the default values for the stainless steel was not changed. The new and old values are found in figure 5.20.

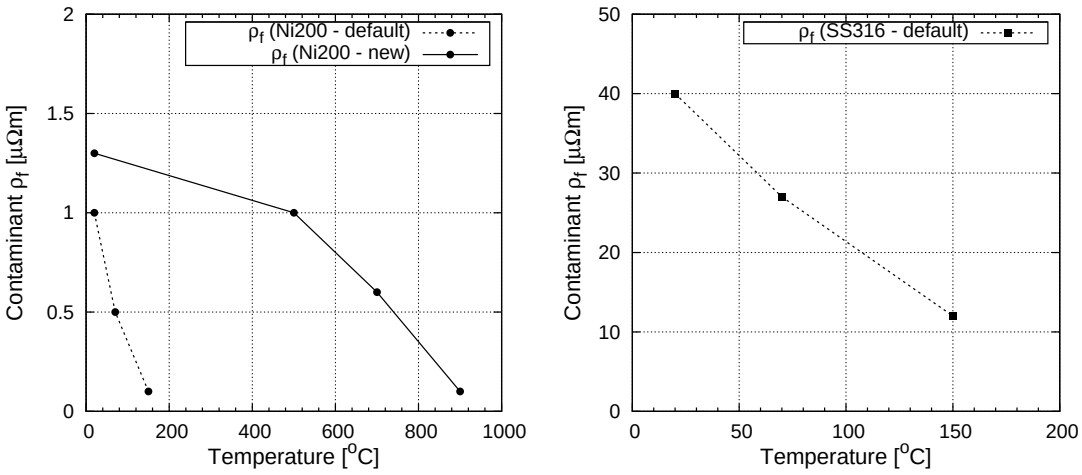

(a) Nickel 200 **(b)** Stainless steel 316

Figure 5.20: Original and fitted values of contact resistivity due to contamination ρ_f.

5.4.2 Numerical Results

Simulations of the factorial plan of Nickel 200 and Stainless steel AISI 316 has been conducted using SORPAS v9.83. From the simulations are extracted the maximum interface temperature for the different factor level combinations, and the results are plotted in figure 5.21a and 5.21b on page 124. The graph labels indicate the factor combinations in relation to table 5.3. The label (-) indicate that all factors where at the low level, while for example IF indicate that current and force is on the high level and ramp rate is on the low level.

The simulations suggest the following:

- The change in current ramp rate (A) has an effect on the rate of temperature increase ΔT in the interface zone and for a given time and a given level of the force (F) it approximately holds that $\Delta T_{A,high} \approx 2\Delta T_{A,low}$ during the current ramp up.
- For a given level of the force (F) the maximum temperature achieved is independent of the current ramp-up rate (A) but only depends on the final level of the current (I).
- Increasing the level of the force (F) lowers the maximum temperature achieved in the weld.
- For Nickel 200 non of the simulated weld schedules result in melting of the interface and nugget formation. The simulations suggest that only solid state bonds are formed during the welding of Ni200 using the parameter range seen in table 5.3. For Stainless steel AISI 316 the welds at high current level I_{high} result in melting and nugget formation.
- The maximum temperature for the stainless steel AISI 316 saturates around 1430°C which is the melting temperature of the material.

The observations presented above suggests that the maximum interface temperatures are not affected by the shape of the welding current signal but rather by the maximum welding current, the electrode force and the contact resistance. This is consistent with the experimental results from section 5.3.

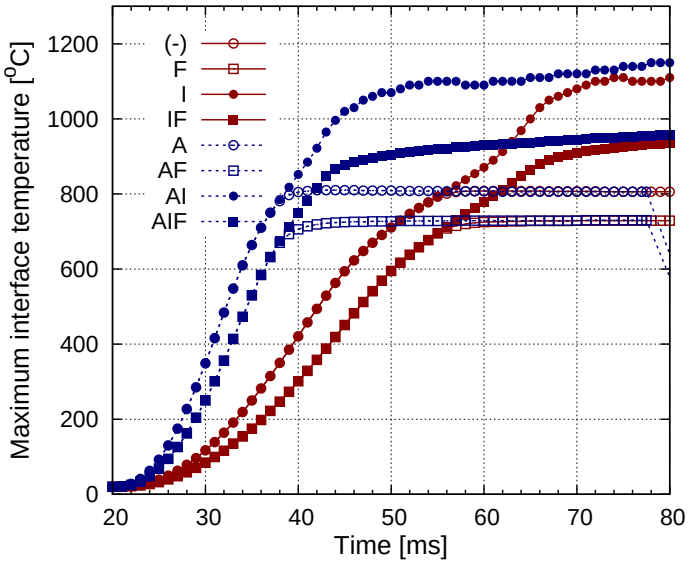

(a) Nickel 200

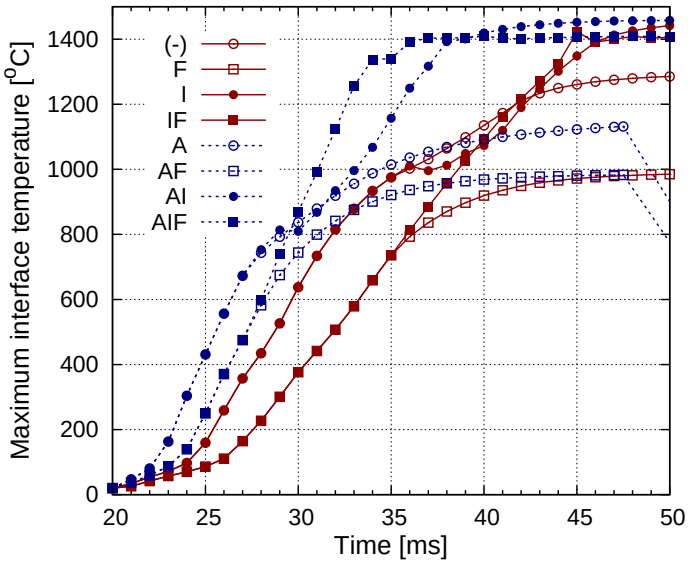

(b) Stainless Steel AISI 316

Figure 5.21: Simulated maximum interface temperatures for the factorial combinations

5.5 Discussion

The experimentally measured contact resistance is found to be influenced by a relatively large degree of experimental variability. Especially the static contact resistance varies a lot. However, compared to the variability of the measured dynamic contact resistance and the variability of the measured JBF of the welds the static contact resistance does not directly influence the welding process significantly. It was difficult to associate any distinct patterns of the development of the contact resistance with the different factor combinations. Most distinct however, was the influence of the current ramp-rate A on the contact resistance R_{CR} of both materials. During the ramp phase of the current the following relation, which is schematically shown in figure 5.22, was shown to approximately hold for a given ramp-rate A_0 and current I_0 profile.

$$R_{CR}(A_0) = \frac{1}{2} R_{RC}(A_0/2) \quad \Leftrightarrow \quad R_{CR}(I_0/2) = 2R_{CR}(I_0) \tag{5.21}$$

The results of numerical simulations suggest that the temperature of the interface share this proportional relationship with the current $T \propto I$. This indicates that the contact resistance to a good approximation is inversely proportional to the temperature of the interface. This agrees with the findings in chapter 3 where temperature was seen to mainly influence material yield strength thereby increasing true contact area and decreasing contact resistance. Furthermore the results suggest that there is little influence from the dynamics in the resistance welding process on the contact resistance. This is beneficial seen from a modelling point of view as it simplifies the model describing the contact resistance during resistance welding. The indications of JBF mainly being influenced by the maximum interface temperature could be attributed to the interface bonding mechanism being controlled mainly by the maximum temperature.

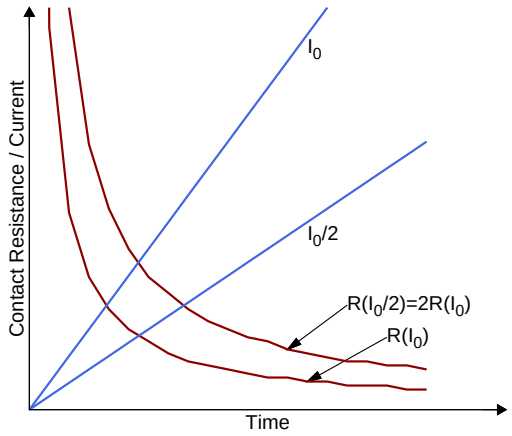

Figure 5.22: Schematic illustration of the relation between weld current and contact resistance

It is shown how the measured contact resistance progresses differently for the two different materials and that the level of the contact resistance is much higher for the stainless steel than for the Nickel. The majority of the contact resistance measurement of the Nickel 200 welds show a characteristic initial increase in contact resistance during the first few milliseconds. This small peak was also observed by Tan et al. [35] who relates it to the electrical breakdown of the insulating oxide layer on the nickel surface. After this initial peak the contact resistance steadily decreases to a steady state around $0.1\mu\Omega$. Tan et al. [35] furthermore observes a second peak on the resistance curve which he relates to the forming of a weld nugget. No such "second peaks" were observed in the present study which could be due to the absence of weld nugget formation in the experiments. The contact resistance of the stainless steel is initially relatively high and comparable to the values estimated by the static contact resistance measurements in section 5.2. The exact values are however, hard to estimate as there is large variation in the measured response during the first couple of milliseconds where the current builds up. Then the contact resistance drops rapidly as the current increases and levels off at a value around $0.25\mu\Omega$. The initial high value of the contact resistance and the rapid drop in contact resistance could be attributed to a breakdown of the passivated chromium-oxide layer in the beginning of the process which is known to increase the electrical contact resistance of stainless steels [91], though this is not further investigated. No obvious characteristic of the resistance welding curves could be related to the formation of a weld nugget. The measured contact resistance curve in resistance micro spot welding of stainless steel foils is therefore not directly suitable for monitoring or suitable as a quality control parameter.

The factor levels collected in table 5.3 have been chosen so the total heat generation during welding would not become too large. This was necessary in order to be able to observe a change in the response due to a change in factor combinations. The response, i.e. the JBF or nugget size, is not a linear function of the process parameters. If the heat input is too large, the response saturates producing close to the same nugget size and JBF, independent of the specific factor levels. Had this been the case the ANOVA analysis would not be able to identify any significant factors or interactions. This however had the result that many of the welds did not produce a weld nugget, which is often regarded as a quality parameter in spot welding, but instead they bonded by solid state bonds. Despite of this the high strength bonds resulted in large bonding zones and nugget pull-out failure types indicating bond strengths comparable to fusion bonds of same size.

The results of the ANOVA analysis in section 5.3 suggest that the only factors significantly affecting the weld size/weld strength is the current I and the force F for the Ni200 material while only current affects the SS316 welds. The reason for this difference is most likely due to firstly: the chosen factor level range, and secondly:

that the Ni200 bonds are solid state bonds while the SS316 welds are more likely to form fusion welds due to the higher electrical resistance of the stainless steel compared to nickel [92][93][34]. Solid state bonds are facilitated by the grain growth and metallic bonding across the interface to create strong bonds. This process is highly affected by temperature and time, but as the weld time is held constant the main parameter is the temperature. As can be seen from the simulations, only the current and force affect the final welding temperature, which is why they significantly affect the weld strength. In fusion welds the parent weld interface is consumed by the liquid weld nugget which implies that the effect of the force on the contact resistance (and thereby the heat generation) disappears. But as long as the interface has not melted the amount of surface pressure influences the contact resistance and heat generation. Looking at the ANOVA table 5.4 for the SS316 welds the interaction between force and current (FI) has a relatively high probability ($100-8 = 92\%$) and is close to have a significant effect on weld strength. This can be explained by the fusion/solid state bond differences as described above. For low current levels solid state bonding is dominating and the force is affecting the contact resistance and thereby the interface temperature and weld strength. For high current levels the welds form fusion bonds and the effect of the force on the weld strength is no longer present. This results in an interaction effect between F and I.

5.6 Conclusion

The most widely applied experimental method for estimating contact resistance during resistance spot welding is based on measurements of the potential difference between the two workpieces. Although often used in literature no theoretical justification or validation of the method is readily available and the experimental method has therefore been investigated and discussed in relation to micro resistance spot welding of foils. It was found that the method is able to provide accurate estimates of the dynamic contact resistance, but it is not possible experimentally to separate the electric bulk resistance of the foils from the results. However, it was shown that this contribution is small in the beginning of the process but is expected to have larger influence on the measurements in the last part of the process where the size of the contact resistance becomes comparable to the bulk resistance of the heated workpieces.

Experimental investigations revealed that electrical contact resistance in micro spot welding of foils is subjected to a relatively large degree of experimental variation. It is likely that this is due to the relatively low electrode force applied in micro resistance spot welding, because the true area of contact and the effect of surface films is more sensitive to experimental variations. Despite the relatively large

variations it was possible to distinguish between groups of measurements that on average showed different levels of the contact resistance.

To investigate the effect of some of the main process parameters on the contact resistance *and* the resulting joint breaking force a factorial investigation was performed. Stainless steel AISI 316 and Nickel 200 foil was spot welded and the effect of the welding current, the electrode force, and current ramp-up rate was investigated. The two materials showed significant difference in the level of the electrical contact resistance which can be attributed to the difference in bulk material properties and surface oxide formation. A standard ANOVA analysis revealed that increasing welding current and decreasing electrode force had significant influence on the strength of the welds but no obvious influence by theses parameters on the shape of the contact resistance curves could be found.

The current ramp-rate did not show any significant effect on the bond strength however, the measured contact resistance was influenced by the progression of the current. Decreasing current ramp-up rate by a factor 2 increased the measured contact resistance during the ramping stage by approximately the same factor. This indicates that the contact resistance during the initial heating stage to a large degree is depending almost solely on the actual value of the welding current. It was then shown by numerical simulation that the interface temperature was approximately proportional to the welding current. This suggests that the contact resistance of the interface during the initial part of the process to a high degree is depending on the actual interface temperature, rather than on factors such as electrode force and heating time.

The numerical simulation of micro resistance spot welding of foils with special consideration to contact conditions were investigated using the commercial program SORPAS. Potential problems in connection with the down-scaling of the process in a numerical context was identified. Due to the relatively low electrode forces applied in small scale resistance welding the modelling of the formation of the actual contact area represents a possible problem. Furthermore it has been shown that the simulation of the small deformations involved in determining initial electrode-to-sheet contact area is very sensitive to actual electrode dimensions and tolerances. Experimental estimation and numerical simulation of the contact area in micro resistance welding should be further investigated to better understand its influence on the process and the simulation hereof.

Chapter 6

Micro Resistance Welding of Thin Wire to Block

Stainless steel is ideal for use in many types of implantable medical devices due to its high corrosion resistance and non-magnetic properties. Although a widely applied joining process, only limited literature on resistance micro welding (RMW) for medical devices exist. In micro size medical or electronic devices joints are often made between components of considerably different geometries and sizes. A common example is the joining of a fine wire to a larger block or connector. Due to the fact that the workpieces themselves generate and conduct both heat and current in RMW the relative size and geometry of the workpieces can severely affect the outcome of the process. Current research has focused primarily on symmetrical weld configurations such as cross-wire and resistance spot micro welding of identical workpieces [33, 35, 37, 38, 40, 94, 95].

RWM of Ni and Au-plated Ni sheets and wire has previously been investigated [35–38] and it is shown that the low resistivity of Ni compared to stainless steel impedes the creation of a fusion joint due to less joule heating and a large heat conduction from the weld zone. Fusion bonding requires that the interface temperature exceed the melting temperature of the workpieces. Khan et al. [40] presented a detailed study of resistance crosswire welding of fine 316 LVM stainless steel wire. They showed a transition from solid state to fusion bonding with increasing current and lowering electrode force and thereby increasing heat generation in the weld. Optimal weld configuration was found to create sound joints with smooth surfaces and high strength (8kp) suitable for bio-medical applications.

To study the effect of welding non-identical workpieces the purpose of the present study is to investigate RMW of D=0.4mm stainless steel 316 LVM fine wire to a block of the same material and to compare the bonding mechanism to that of

cross-wire welding. Focus will be on determining and characterising the welding and bonding mechanism as well as the final strength and microstructure of the bonds.

6.1 Experimental Investigation

6.1.1 Experimental Procedure

The bond is made by projection welding a stainless steel wire (0.4mm) to the surface of a block using round RWMA class 2 (Cu-Cr) flat ended electrodes with a 3.2mm face diameter. The welding setup is schematically shown in figure 6.1a. A MacGregor DC400P direct current controller and Unitek 80A/115V weld head (Miyachi Unitek Corporation, Monrovia, CA) were used. The welding current was varied with 100A interval ranging from the initiation of a bond to over-welding resulting in severe deformation of the joint. Two levels of the weld force (2.5kp and 5kp) were used. The weld schedule was comprised of 1ms current upslope, 50ms weld time and 3ms downslope. The joint breaking force was determined using an Instron 5548 micro tensile tester with a test-setup shown in figure 6.1b. A 500N load cell with ±0.4% accuracy was used to measure the breaking force at a pull speed of 10mm/min. Cross sections of the welds were observed using optical microscopy and the specimens were prepared by etching with a solution of 5ml HNO_3, 25ml HCl and 30ml H_2O at an elevated temperature of 80°C for 3-5

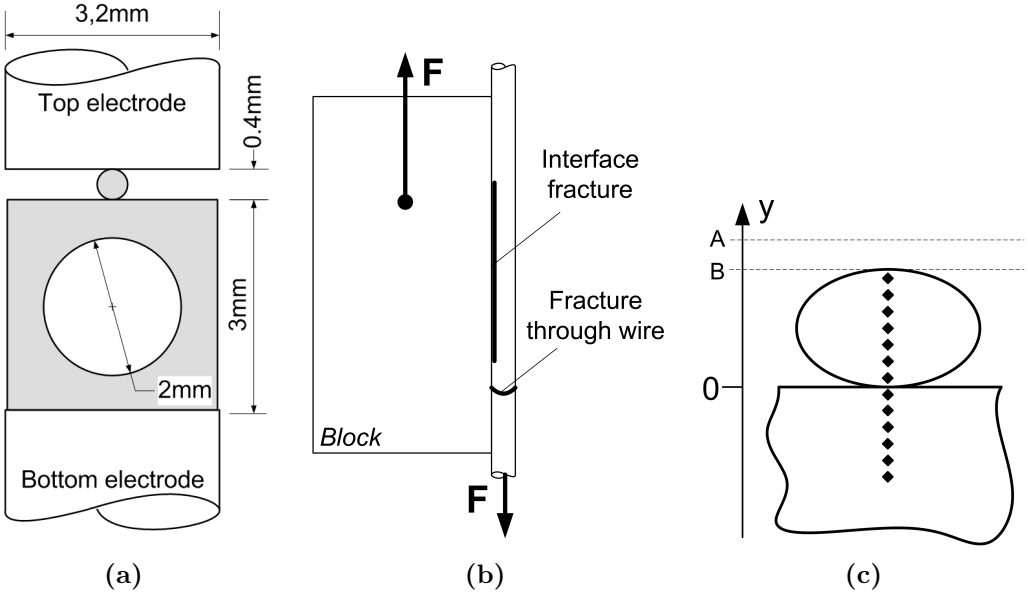

Figure 6.1: Experimental setup of wire to block micro welding

seconds. Fracture surfaces were investigated using scanning electron microscopy. As illustrated on figure 6.1c the collapsed height B of the wire with original height A was quantified by the measured setdown A-B of the top electrode during the weld. Hardness testing was conducted on a Shimadzu micro hardness tester (Shimadzu Corporation, Kyoto, Japan) with a 10g load held for 15 seconds. The hardness profiles were made through the wire and interface region as illustrated in figure 6.1c.

6.1.2 Experimental Results

Tensile Shear Testing of Joint Strength

The measured electrode setdown for 2.5kp and 5kp weld force as a function of weld current are shown in figure 6.2. For the 5kp weld force bonding was found to initiate after 200A and increase in strength up to 600A. Welding currents above 800A caused overwelding where high energy inputs induce weld defect (i.e. excessive melting and expulsion), resulting in a reduction in strength.

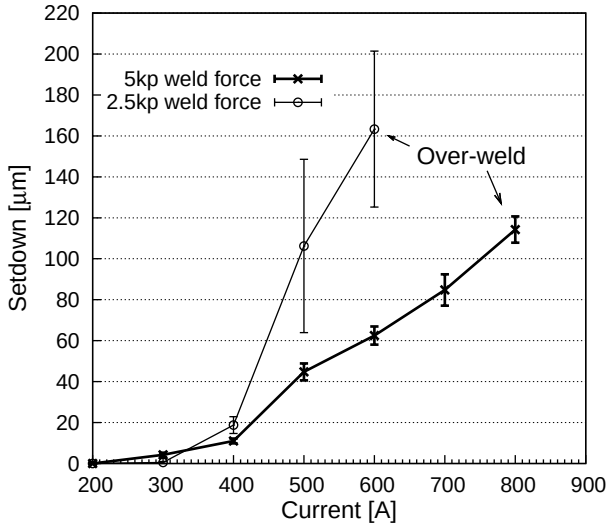

Figure 6.2: Measured electrode setdown

Similar results were observed for the 2.5kp weld force, however, overwelding initiated at 600A. The maximum JBF achieved was 60N and 70N for the 2.5kp and 5kp weld force, respectively. Measured electrode setdown increased with increasing welding current (c.f. figure 6.2). At 500A and 600A the setdown was considerably higher for the 2.5kp weld force. The experiments with 5kp weld force therefore show better process robustness with regard to the weld current.

The joint breaking force (JBF) for 2.5kp and 5kp weld force as a function of weld current is shown in figure 6.3. The JBF for joints welded at 200A could not be

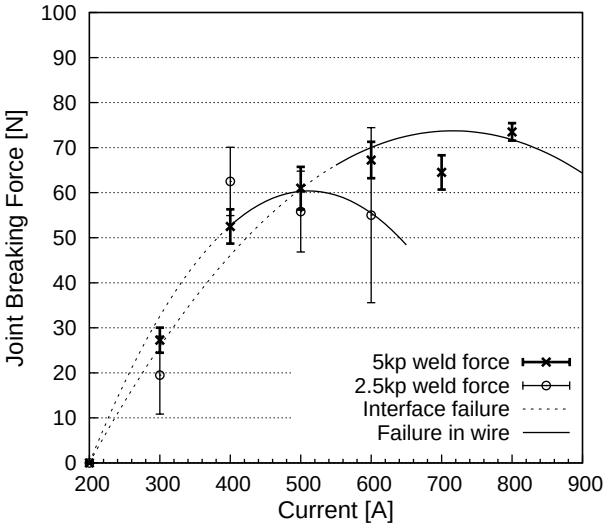

Figure 6.3: Measured Joint Breaking Force (JBF)

tested because the bonds were so weak that they fractured upon clamping in the tensile testing machine and their JBF is therefore set to zero in figure 6.3. The joint fracture mode observed during testing is indicated by the line-type of the curves fitted to the data in figure 6.3 using a polynomial function. Two types of failure mode was observed in experiments. "Interface fracture" indicates that the joint fracture through the interface completely separating the wire from the block while "Failure in wire" implies that the fracture occurs through the heat affected and softened zone in the wire thereby leaving the bonded wire attached to the block. The two types of bond failure are shown schematically in figure 6.1b. Generally a failure through the wire indicates that the bond itself was adequately strong and the process window is normally thought of as initiating here. It was found that the transition from interface failure to failure through the wire occurred around 400A and 600A for a weld force setting of 2.5kp and 5kp, respectively.

Khan et al. [40] tested the JBF for crosswire welding of 316 LVM stainless steel wire of the same dimensions as in this study. The type of fracture and the maximum JBF agree well with the results in this work, however, the maximum JBF was found at lower currents than was necessary in the present study.

Weld Microstructure

Weld cross sections made with weld currents ranging from 200A to 500A for both 2.5kp and 5kp weld force are shown in figures 6.4 to 6.7 on page 134-135. At 200A the heat input was too low to initiate bonding (cf. figure 6.3); however, recrystallisation and grain growth was observed primarily in the wire near the interface, as shown in figure 6.8. As in the case of micro cross-wire welding [36] cold collapse of the wire during the initial stage of the bond process was observed, resulting in an increase in contact area at the faying surfaces (figure 6.4).

The 300A weld cross section in figure 6.5 reveals a zone in the lower part of the wire where the microstructure morphology has changed. Upon closer examination, shown in figure 6.9, it is seen that the original material has been partly melted indicating that the wire in this zone has experienced the highest temperatures during welding. Melting and subsequent squeeze out of partly molten material at the interface during cross-wire welding of 316L wire has been reported by Khan et al. [40]. Figure 6.5a suggest that material might have been squeezed out and re-solidified on the edge of the interface. Figure 6.10 show a close-up of the flash material microstructure marked in figure 6.5a, which reveals that the material originates from the free surface of the wire and *not* the interface, as a coherent grain structure was found. Little difference in setdown or JBF was observed for the two weld force settings at 300A.

Increasing welding current to 400A (figure 6.6) resulted in the onset of significant melting for both 2.5kp and 5kp. Using 2.5kp weld force the entire wire except a small area just at the wire to block interface clearly shows dendritic grains. At the higher 5kp weld force there was a smaller melted volume which was confined near the centre and bottom part of the wire. In the upper part of the wire the grain size is considerably smaller and identical to the as-received microstructure indicating that the temperature close to the top electrode did not reach the recrystallisation temperature, likely due to its contact with the cold copper electrode. Detailed interface microstructure for welds created using 400A, 5kp is shown in figure 6.11.

The picture clearly shows the transition from the solidified region (A) in the centre of the wire to the relatively large-grained recrystallised zone (B) on both sides of the wire to block interface. Prior to etching there was no visible interface indicating bond formation across the interface, while after etching the interface appeared. Similarly, Fukumoto and Zhou [36] observed a clear interface (i.e. no visible bonded areas) for high strength bonds of Ni crosswire welding which was attributed to the etching process which preferentially attacked the joint interface.

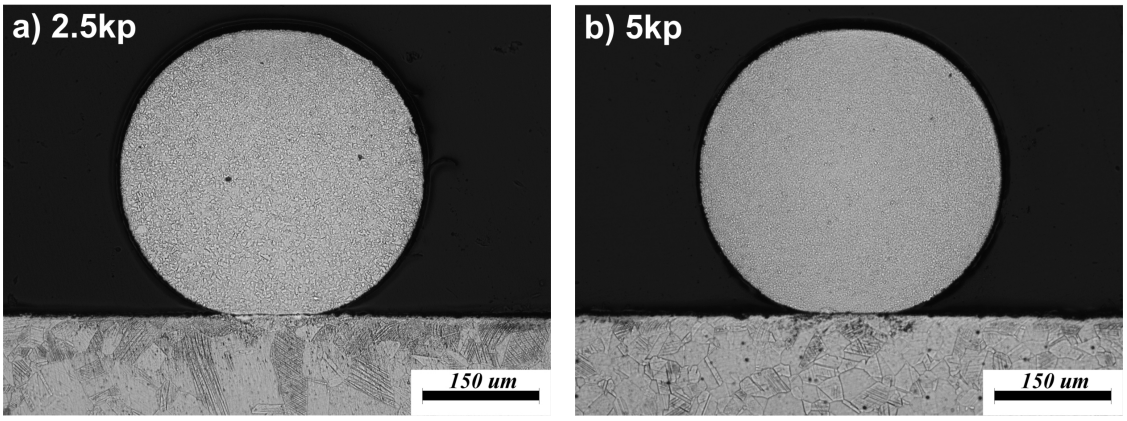

Figure 6.4: Weld cross section for 200A, a) 2.5kp, b) 5kp

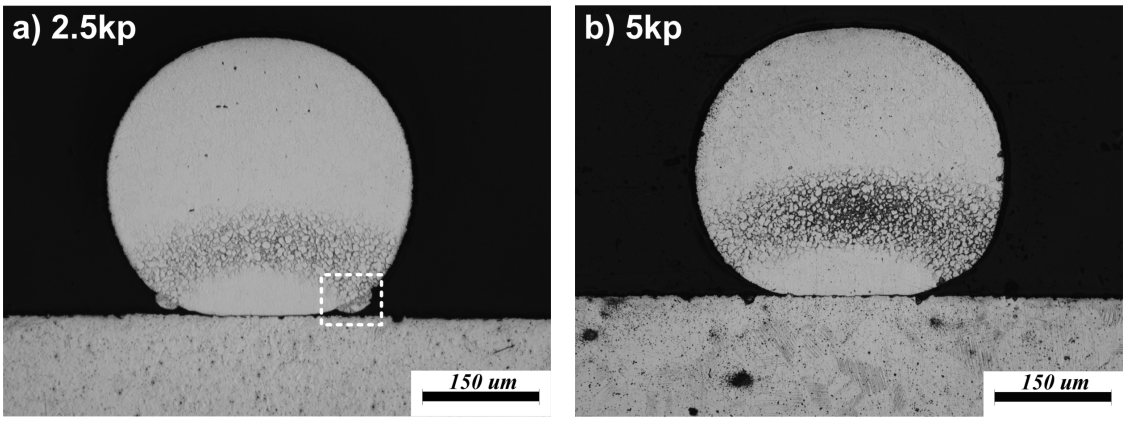

Figure 6.5: Weld cross section for 300A, a) 2.5kp, b) 5kp

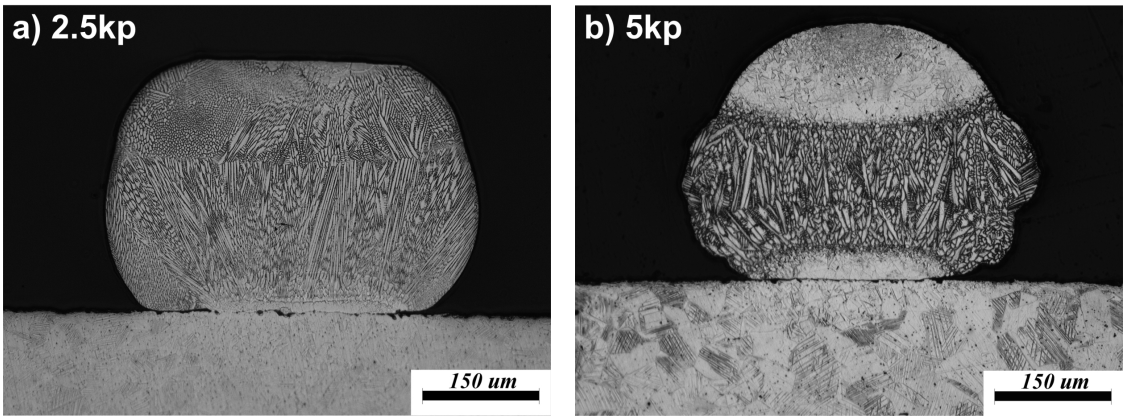

Figure 6.6: Weld cross section for 400A, a) 2.5kp, b) 5kp

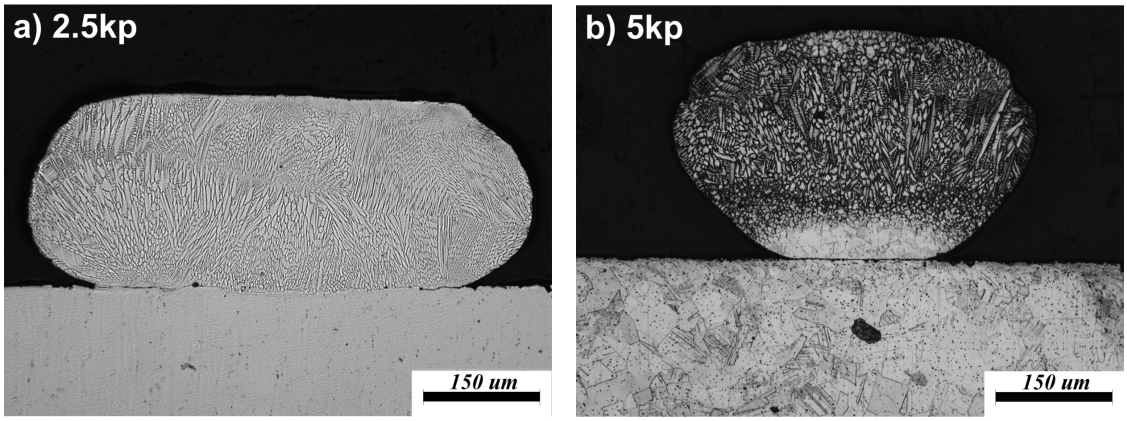

Figure 6.7: Weld cross section for 500A, a) 2.5kp, b) 5kp

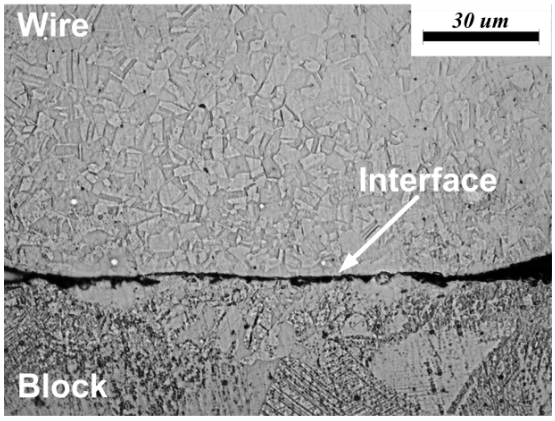

Figure 6.8: Interface of 200A, 2.5kp force

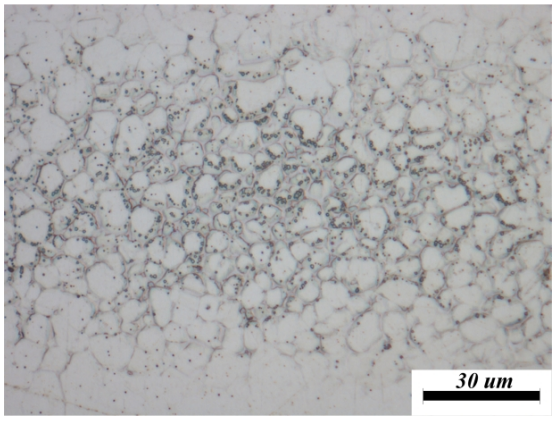

Figure 6.9: Bulk wire of 300A, 2.5kp force

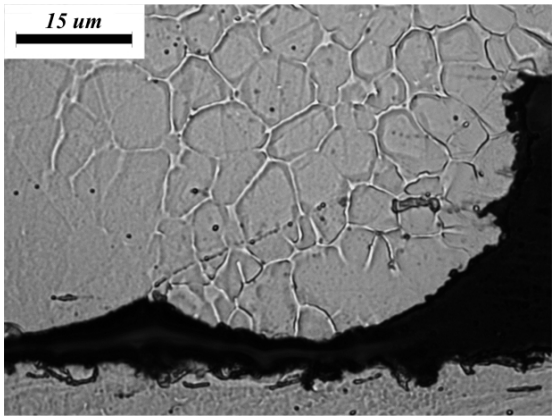

Figure 6.10: Close-up of figure 6.5a

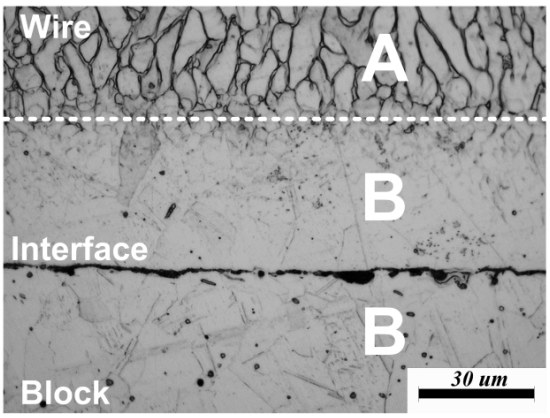

Figure 6.11: Interface of 400A, 5kp force

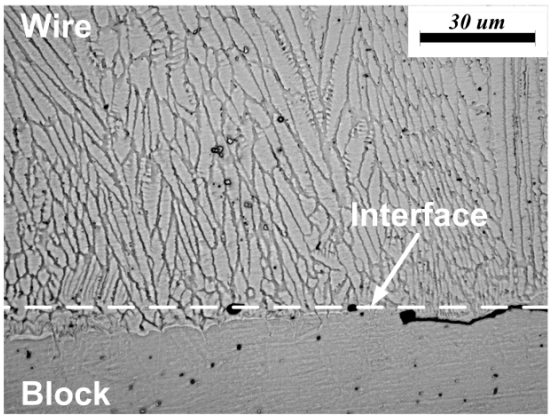

Figure 6.12: Interface of 500A, 2.5kp force

Increasing welding current to 500A increases heat generation and leads to a higher volume fraction of molten material. At 500A the wire was heavily deformed and completely melted with 2.5kp weld force while the 5kp weld force still has no melting at the interface (figure 6.7). Investigating the bond interface for 2.5kp weld force (figure 6.12) show that the interface has been melted and the dendritic structure grow across the wire-block interface producing a fusion bond. Increasing the weld force decreases the temperature at the interface and only the upper part of the wire show solidification structure. Although it appears as if the molten metal is in direct contact with the upper electrode during welding, no bonding or electrode sticking to the wire was observed during the experiments.

As can be seen from figure 6.4 to 6.7 there is a clear effect on the welding mechanism when increasing the weld force from 2.5kp to 5kp. A higher weld force provides a more intimate contact at the contacting surfaces which reduces the electric contact resistance and increases the thermal conduction across the interfaces. Furthermore the higher force results in larger plastic deformations of the natural projection of the wire which results in a significantly larger initial contact area between wire and block. All these effects decrease heat generation at the interfaces and increases cooling which results in lower temperatures in the workpieces, especially in the wire that has the smallest bulk material volume and heat capacity.

Hardness of Weld Zone

The measured hardness across the weld zone is shown in figure 6.13a for 2.5kp weld force and in figure 6.13b for 5kp. For the high weld force setting (figure 6.13b) the hardness profiles are rather un-affected by changes in the weld current. The hardness decreases when approaching the interface from the block-side and reaches a minimum of approximately 200HV around 100μm into the wire. When approaching the top of the wire the hardness increases for 300A and 400A while it remains low for 500A. The same trend for the hardness profiles is seen for the lower weld force on figure 6.13a although here the profile for 500A show a lower hardness across the interface and in the block compared to the other current settings.

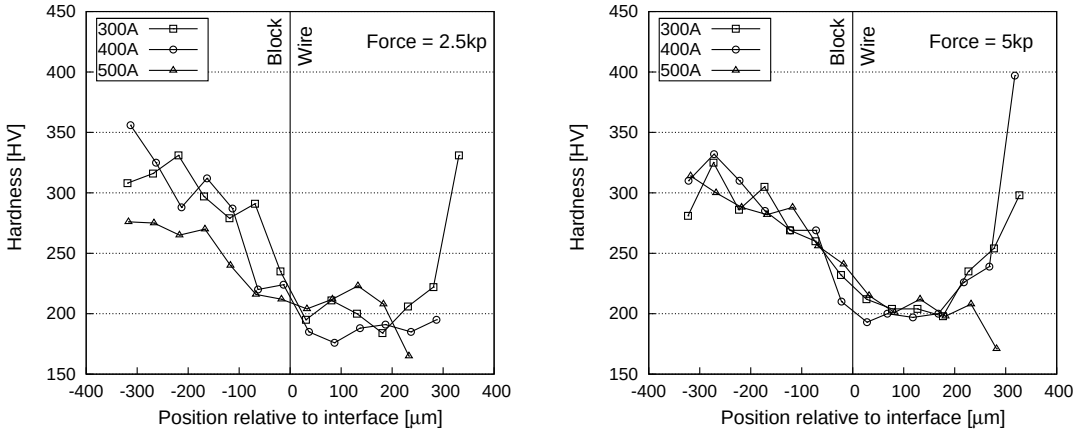

(a) 2.5kp weld force

(b) 5kp weld force

Figure 6.13: Hardness profiles

The base metal of the SS316 LVM wire has been cold worked during production and therefore has a fine uni-directional grain structure with high hardness, which was measured by Khan et al. [40] to be in the range 480-500HV. Due to the thermal cycle of the welding process both wire and block softens due to recrystallisation or melting and re-solidification of the material. The amount of softening can roughly be related to the peak temperature of the materials [40, 93, 96]. The hardness profiles on figure 6.13 clearly show that the wire material has experienced the highest degree of softening and hence the highest temperature during welding. This is supported by the cross sections of the welds on figure 6.5 to 6.7 showing that melting and softening concentrates in the wire.

Comparing the observed microstructure of the welds at 400A shown in figure 6.6 with the hardness profiles in figure 6.13 good agreement is found. The hardness

profiles show that an increased electrode force from 2.5kp to 5kp results in an increase in hardness in the top part of the wire indicating that the temperature in the top part of the wire is lower than in the centre. The cross sections of the welds in figure 6.6 support this as the molten region decreases and concentrates in the centre of the wire. This is most likely caused by a decrease in electric contact resistance and by increased cooling through the electrode facilitated by the improved contact due to the higher force.

The transition in bond failure type from interface failure to fracture through the wire for the 2.5kp weld force setting can be seen from the hardness measurements on figure 6.13a. At 500A it is seen how the soft region in the wire extends more than 75μm into the block before the hardness starts to increase. This indicates that the interface region for this weld configuration has experienced a higher temperature compared with lower currents and the higher weld force. The higher temperature has facilitated a fusion bond as seen on figure 6.12 which results in the non interface failure.

Fracture Mechanism

Figure 6.14 show overviews (seen from above) of pre- and post tensile tested specimens for a weld force of 5kp using 600A and 800A, respectively. Both settings result in fracture occurring through the HAZ in the wire where the material has been softened. However, while the weld at 600A show a smooth and uniform geometry the weld at 800A has experienced over-welding, resulting in local thinning of the wire.

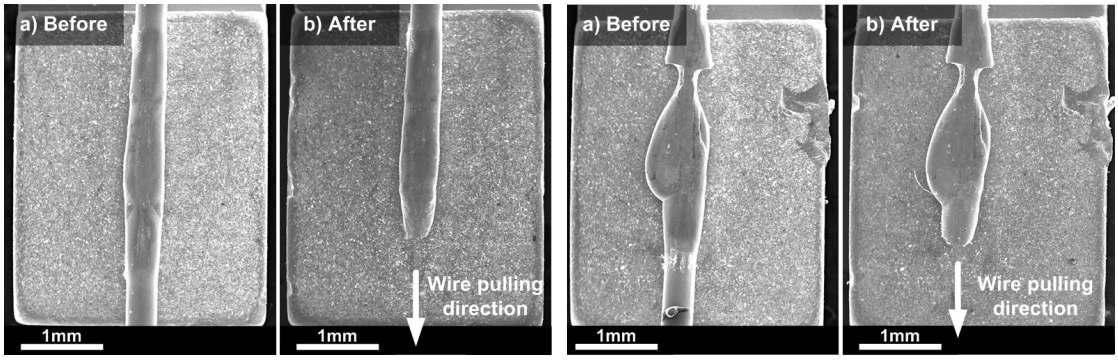

(a) 5kp, 600A **(b)** 5kp, 800A

Figure 6.14: SEM images of wire and block seen from above

In the present situation the wire is pulled from the direction illustrated on figure 6.14. If the pulling direction had been from the other end of the wire the thinning would most likely significantly decrease the JBF due to the much smaller

cross sectional area of the wire. In order to maintain consistency in the experimental work all welded specimens are inserted the same way between the electrodes and tested from the same direction. This implies that the observed thinning associated with over-welding always occur on the side of the joint opposite of the tensile testing direction, hereby not influencing the measured JBF as seen on figure 6.3. However, thinning is still a weld defect and over-welding is not accepted when evaluating the weld quality. The weld current is therefore not increased further after reaching the over-welding stage.

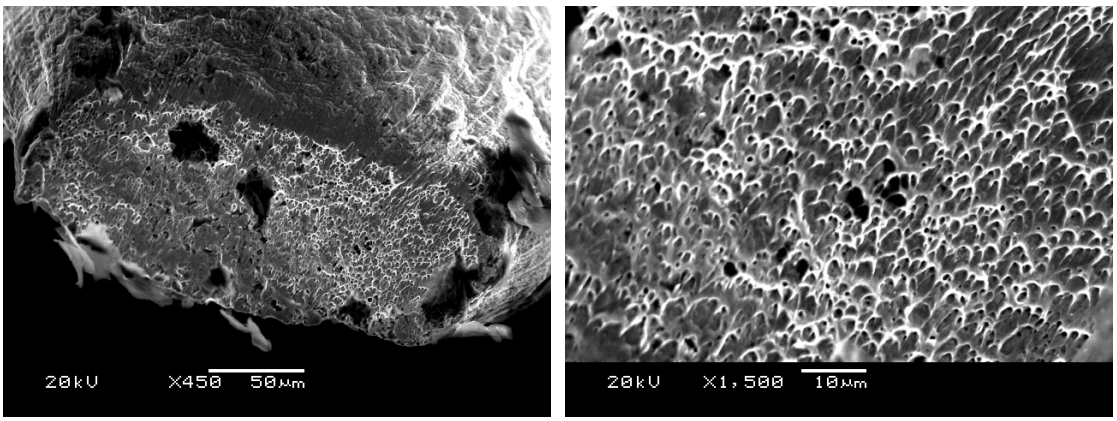

(a) Fractured wire **(b)** Dimple structure

Figure 6.15: SEM images of fracture surface

During tensile testing it is found that the joints failing at the wire to block interface all exhibit a brittle fracture. On the other hand, the specimens fracturing through the wire all show ductile behaviour. The ductile fracture mechanism through the wire is confirmed by investigating the fracture surface of the wire as shown in figure 6.15 where a clear dimple structure at the fracture surface indicate failure by void growth and coalescence during severe plastic deformation of the wire material. This was also the case for crosswire welding as observed by Khan et al. [40].

6.2 Numerical Simulation of Wire to Block

6.2.1 FEM-Modelling

The following section investigates the possibility of simulating the wire to block weld using SORPAS ver. 9.83. The problem of welding a wire to a block is a 3D case. In order to simulate the problem in SORPAS it has to be simplified into an equivalent 2D problem. This is done by approximating the problem with an in-plane/plane strain analysis, which in principle only simulates the volume under the electrodes where the un-welded geometry is not accounted for. The meshed model (2000 elements) is shown in figure 6.16. However, due to the very short process time the thermal energy generated in the block will not have time to travel very far. Comparisons between simulations of the entire block and only half of the block (as shown in figure 6.16) produce close to identical thermal energy in the wire and in the block during the actual welding. During the cooling time the temperature curves start to differ showing temperatures which are too high for the half-block model. This however, is mostly visible in the block, but far away from the weld while the difference in simulated temperatures in the weld itself is negligible.

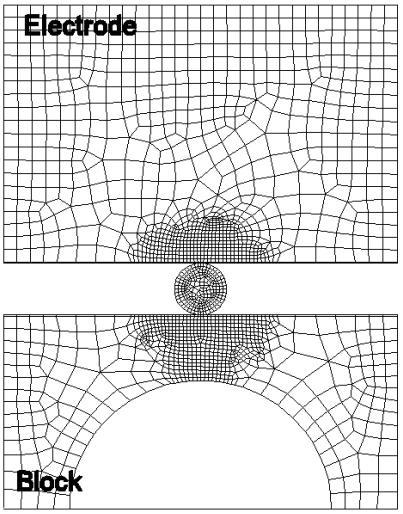

Figure 6.16: Numerical model - half block

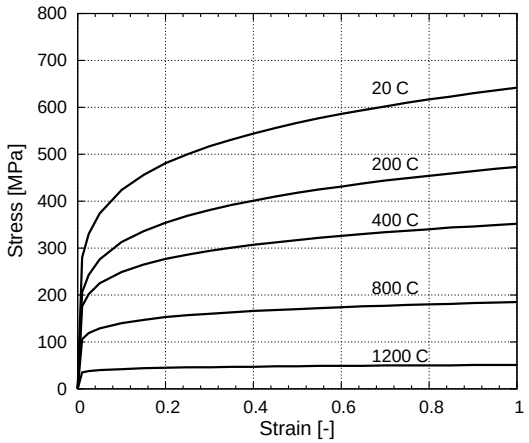

Figure 6.17: Mechanical properties of AISI 316 Stainless Steel used in numerical simulation

In the actual welding process the un-welded parts of the wire and the block work as thermal heat sinks and increase the cooling of the weld during the process. By simulating the process as a plane-strain problem the electrode is simulated as a rectangular block. This increases the total volume of the simulated electrode compared to the real cylindrical round electrodes and will effectively increase the

cooling effect of the electrodes. In the real experiment the part of the wire not being compressed by the electrode will work as structural support for the wire in contact with the electrode and thereby decrease the deformation of the wire. In the simulation it is not possible to directly account for neither of these boundary effects and it is expected that the mechanical collapse of the wire is more severe in the simulation. The standard values from the SORPAS database is used to describe the material properties of the stainless steel 316 used in the study. The mechanical properties are plotted in figure 6.17.

Contact Area

In the experiments the initial contact area between the round electrode and the flat surfaces of the wire and the block depends on the elastic and plastic deformation of the wire. In the simulations however, this area needs to be manually defined because the software requires that the initial contact should be a finite area. To investigate the effect of the collapse of the wire as observed in the experiments in section 6.1 on the resulting temperature distribution in the weld, the contact area is manually varied. This is done by manually flattening the wire while keeping the cross-sectional area constant. The contact width W_c between wire and block is shown in figure 6.18. The electrode to wire contact area is kept constant at 0.01mm which is close to the minimum contact area due to a limitation in element size. The initial contact area between block and wire is varied between $W_c = 0.01$mm, $W_c = 0.07$mm and $W_c = 0.15$mm.

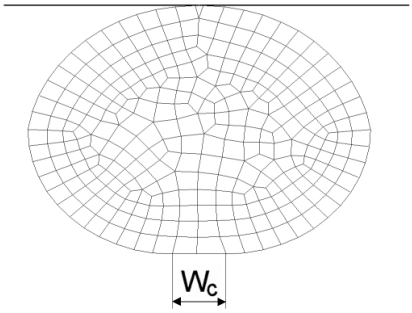

Figure 6.18: Contact Area

Electrode Force and Welding Current

The electrode force is varied between $F = 1.5$kp and $F = 5$kp. The 1.5kp setting is chosen to ensure observation of the effect of changing electrode force on simulation results although the lowest force setting in the experiments were 2.5kp. The welding current was varied between 300A to 600A with intervals of 100A.

6.2.2 Numerical Results

The results of the numerical simulations are described in the following. An example of the result of a simulation showing the peak temperature in the material during welding is shown in figure 6.19.

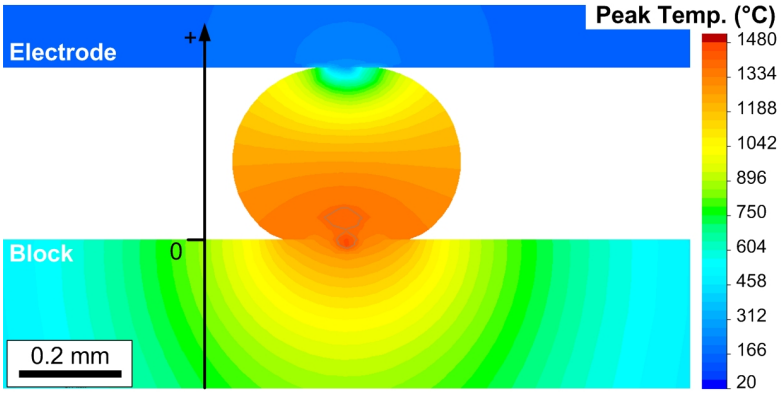

Figure 6.19: Simulated temperature profiles in block and wire for $W_c = 0.01mm$, $F = 5$kp and $I = 600$A.

As can be seen from the figure the simulations suggest that the wire in general experiences the highest temperatures, but that the block also heats up considerably. Peak temperature profiles similar to the hardness profiles from section 6.1.2 are estimated from the simulations and collected in appendix C.1. The profiles generally suggest that the heating rate is largest at the wire to block interface. The collapse and setdown of the wire onto the block is, however, not experienced in the simulation in the same degree as observed in the experiments. The simulated wire setdown is illustrated in figure 6.20 for varying the initial contact width W_c.

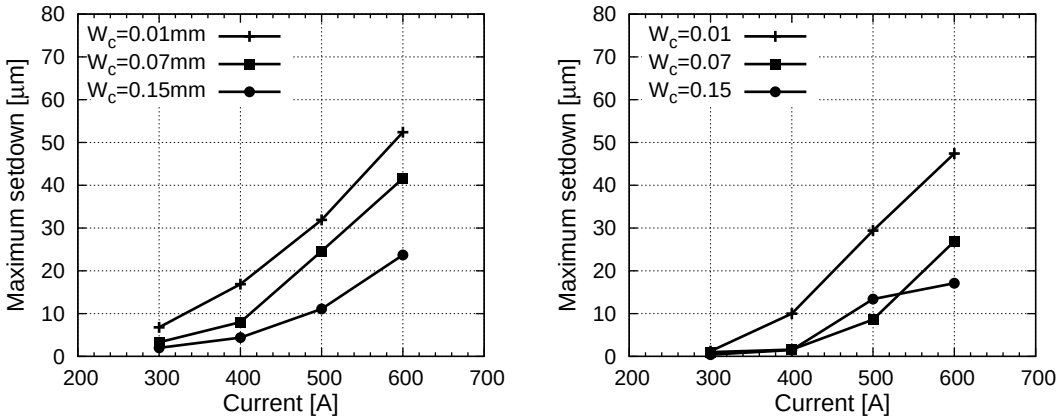

(a) $F = 1.5$kp **(b)** $F = 5$kp

Figure 6.20: Simulated setdown of wire during welding.

Compared to figure 6.2 the simulated setdown is significantly less than the experimental measured for the low weld force while only slightly lower for the high weld force setting (It is most reasonable to compare the $W_c = 0.01$mm with experiments as this corresponds best with the actual situation). Furthermore it is noted that setdown is close to independent of the weld force while the experimental data show a clear effect increasing setdown with decreasing force.

In figure 6.21 is plotted the simulated maximum temperature in the wire and block cross-section showing the effect of varying the initial contact area width W_c from 0.07mm to 0.15mm. The profiles for $W_c = 0.01$mm can be seen in appendix C.1 and are not plotted in this figure in order to avoid corrupting the graph.

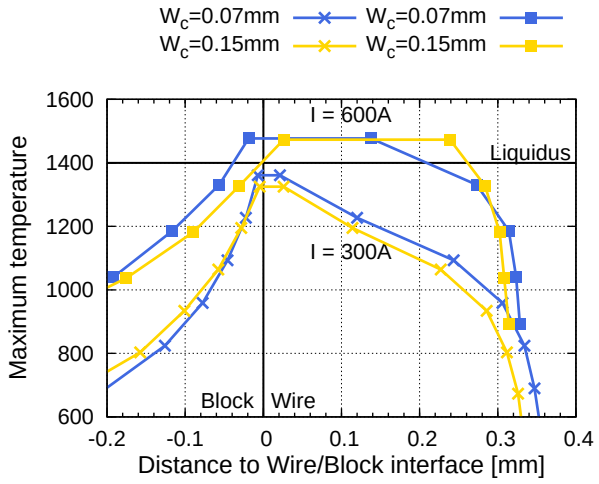

(a) $F = 1.5$kp

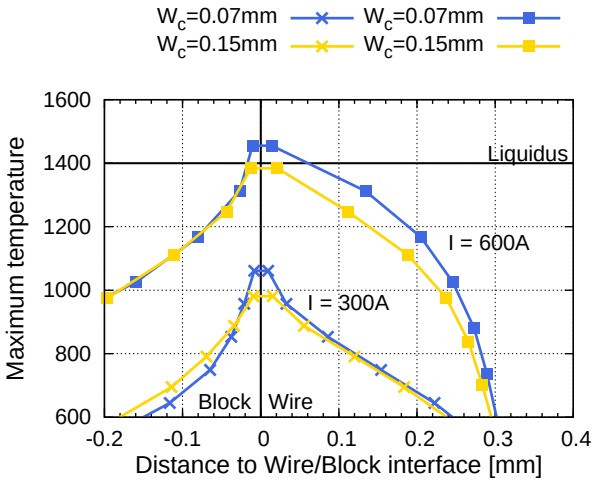

(b) $F = 5$kp

Figure 6.21: Simulated temperature profiles in block and wire comparing contact width W_c.

The following observations in figure 6.21 are emphasised:

1. Increasing electrode force significantly decreases heat generation and the maximum temperature in the materials.

2. The temperature in the wire decreases very rapidly when reaching the electrode to wire interface giving rise to very high temperatures in the majority of the wire while the electrode is significantly cooler (c.f. figure 6.19).

3. For the 5kp electrode force (figure 6.21b) the maximum temperatures are found at the wire to block interface.

4. For the 1.5kp electrode force (figure 6.21a) and low welding current (300A) the maximum temperature is reached at the interface.

5. For the 1.5kp electrode force and high welding current (600A) the area reaching temperatures above the liquidus temperature (marked on the figures) is moved towards the bulk area of the wire when increasing the contact area width W_c.

The results of the numerical simulations are further discussed in section 6.3.2 and compared with the experimental observations.

6.3 Discussion

6.3.1 Mechanism of Joint Formation

The mechanism of joint formation in cross-wire welding of Ni and Au-plated Ni has been investigated by Fukumoto et al. [37] and Fukumoto and Zhou [36] and cross-wire welding of SS316 by Khan et al. [40]. For Ni-wires the primary bonding mechanism was found to be a strong solid state bond due to the creation of advantageous bonding conditions at the interface. Because of the localised heating at the interface the surface films and contaminants are melted and squeezed out during the initial stages of the bonding process hereby promoting direct metal to metal contact resulting in a strong solid state bond at the interface. The primary bonding mechanism in cross-wire welding of SS316 wires was found to be fusion bonding initiating at the interface between the two wires.

In the present study the bonding mechanism is different from micro resistance spot welding and micro resistance cross-wire welding. From figures 6.4 to 6.7 it is seen how the maximum temperatures are not concentrated around the bond interface in the case of wire to block welding. Rather the observed bonding mechanism is based on melting of the wire and creating a fusion zone in the bulk of the wire. With

increasing current this fusion zone expands to the entire cross-section of the wire eventually penetrating into the interface between block and wire hereby creating a fusion bond. Before the interface is actually engulfed in the weld pool the contact pressure and elevated temperatures at the interface result in solid state bonds with reasonable strength (cf. figure 6.3).

It is believed that the reason why the fusion bond does not initiate at the interface between wire and block is partly due to the large difference in size between the workpieces and partly because the natural projection of the wire collapses before bonding can occur. In figure 6.22 is presented a proposed bonding mechanism of RMW of fine SS316 wire to a block consisting of 4 stages in time of the fusion weld formation. At lower welding currents the heat input might not be high enough for the material to go through all 4 stages.

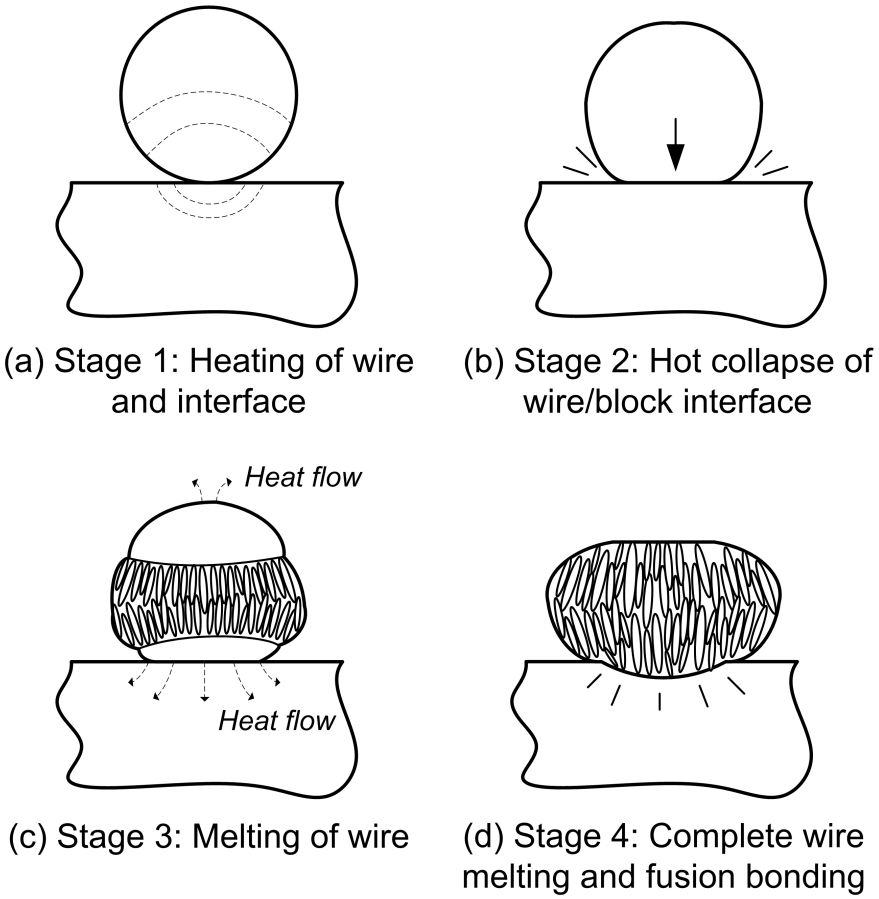

Figure 6.22: Schematic proposed RMW bonding mechanism for stainless steel 316 LVM wire to block

In the first stage (figure 6.22(a)) resistance heating increases the temperature in the bulk of the materials and at the interfaces due to contact resistance and the restriction of current flow due to the natural projection of the wire. As a consequence of the relatively smaller bulk volume of the wire it heats up especially in the bottom part of the wire close to the wire-block interface because the top electrode cools the top part of the wire. Due to the increased temperature of the wire the material becomes softer which leads to plastic deformation of the wire caused by the compressive electrode force.

In this second stage (figure 6.22(b)) the wire projection at the wire-block interface collapses in a hot collapse, while due to the cooling of the electrodes the top part of the wire is still strong enough to support the load and therefore remains undeformed. The collapse of the wire increases the contact area between wire and block hereby significantly reducing the stresses and slowing down further collapse of the wire. After the collapse the larger contact area greatly increases the heat transfer at the wire-block interface and reduces the current density across the interface. This effectively cools the interface as well as reduces the heat generation.

It is in the third stage (figure 6.22(c)) that melting initiates in the bulk of the wire, because this is where most heat is build up. Because the top electrode is so effective in conducting heat away from the wire the volume just around the electrode-to-wire interface does not soften much and does therefore not plastically deform to increase the contact area. This can be seen from the hardness measurements on figures 6.13 where the hardness increases very fast at the top part of the wire indicating that the wire has experienced a very high temperature gradient in this area because of the effective cooling. It is possible for the entire cross section of the wire to melt in the centre of the weld area while the edges of the wire closer to the periphery of the electrode remains below the liquidus temperature and thereby helps support the electrode so it does not totally squeeze out the molten wire.

If the heat input is high enough the molten area will eventually melt the wire-to-block interface and propagate into the block producing a fusion bond between wire and block (figure 6.22(d)). If the current is increased too much the heat generation might happen too fast and the wire will deform locally due to uneven thermal expansion of the wire. This results in locally very high stresses that squeeze out the molten material thereby thinning or totally separating the wire. This over-welding results in uncontrollable weld formation and final joint strength and is therefore not desirable. Furthermore, for medical applications smooth surfaces are desirable to avoid damaging the prepared surfaces of the base material.

The described mechanism of joint formation is mainly applicable to micro resistance welding of vacuum melted stainless steel 316LVM with the specimen dimensions

applied in this work. It is indicated that the process is dependent on the actual heat distribution due to size and geometry of the workpieces. It is believed that changing geometry and/or material type of electrodes and workpieces could result in a completely different joint formation mechanism in micro resistance welding of wire to block than the one described here.

6.3.2 Numerical Simulation of Wire to Block Welding

The numerical results generally show that the peak temperature in the weld is concentrated at the interface (c.f. figure 6.21 and appendix C.1). The experimental results on the other hand clearly show that melting initiates in the wire and therefore that the peak temperatures are not expected to be found at the interface. The main reasons for this discrepancy is believed to be due to:

1. Inadequate simulation of mechanical collapse of the wire.
2. Insufficient cooling of the interface in the simulation.
3. Too high electrical and thermal contact resistance at interface.

The simulated setdown and mechanical collapse of the wire during welding is significantly smaller than the experimentally observed values resulting in a smaller wire to block contact area. Especially the heat generation at the interface is highly influenced by the current density and thereby also the conducting area at the interface. By manually increasing the contact area (the width W_c) it is seen in figure 6.21 that the peak temperature show a tendency to move into bulk of the wire - although still largely concentrated at the interface.

The experimental data suggest that nugget formation initiates in the bulk of the wire and not the interface. This supports the idea that the deformation and collapse of the wire has a large impact on the weld mechanism and that exact modelling of the collapse has significant influence on the result of the simulation. The reason why the mechanical collapse is not simulated correctly is not clear. As the simulation is not able to account for the cooling boundary effect from the un-welded material adjacent to the welding zone the heat generation and softening of the material is expected to be higher in the simulation. This should in theory result in a larger collapse of the wire, however, the opposite is seen to be the case. This could be due to discrepancy in the mechanical material data in the simulation or problems related to the mechanical model in the numerical software.

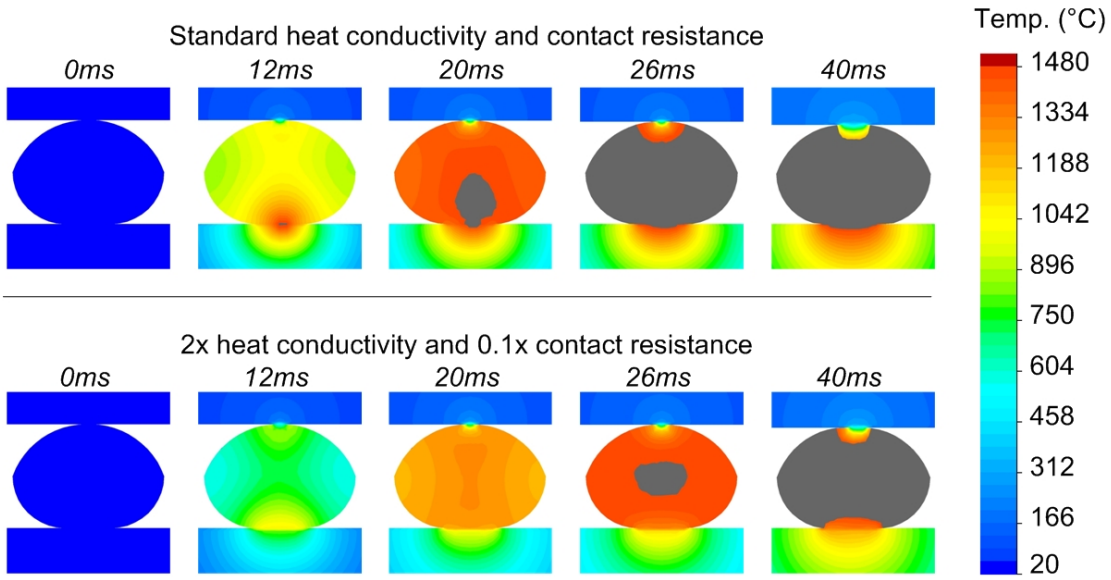

Figure 6.23: Comparison of simulated weld developement

In the top part of figure 6.23 is shown an example of a simulation using the standard material data of AISI 316L stainless steel and applying 600A welding current and 5kp weld force. The initial contact width W_c is set to 0.15mm to account for the lack of mechanical collapse in the simulation. The five pictures show screen-shots of the simulation at times 0ms, 12ms, 20ms, 26ms and 40ms. Furthermore, as noted from the numerical results in section 6.2.2, the peak temperature is reached at the interface and the nugget develops from the interface and into the wire. Compared to experimental data the heat generation at the wire/block interface is too high. This could be due to insufficient cooling of the interface or too high thermal and electrical contact resistance at the interface.

In the bottom part of figure 6.23 is shown a simulation of the same model but with double the thermal conductivity of the material and decreasing the electrical and thermal contact resistance by a factor 0.1, compared to the standard settings. As can be seen from the figure the heat generation at the wire to block interface is still significant in the beginning of the process, but due to the increased cooling at the wire to block interface the peak temperature is moved into the bulk of the wire. After 26ms it is seen how the nugget formation initiates in the bulk of the wire and expands to melt most of the wire. The modified simulation illustrated in figure 6.23 corresponds better with the experimentally observed welding mechanism in figure 6.6 and 6.7. This could suggest that the downscaling has a significant influence on the behaviour of the contact resistance. In this type of welds it results in an overestimate of the contact resistance and due to the lack of boundary conditions of the 2D approximation of the geometry the cooling of the interface is underestimated.

6.4 Conclusion

The present study has examined resistance micro welding (RMW) of stainless steel 316L fine wire to a block of the same material both experimentally and numerically. Experimentally the joint breaking force (JBF), weld zone hardness, fracture surfaces and weld development was investigated for 2.5kp and 5kp weld force and for varying weld currents. Based on this the weld mechanism for welding of fine wire to a block was detailed and compared to resistance micro cross-wire welding. The main conclusions of the experimental results are summarised in the following:

1. The proposed bonding process in time is (1) Initial heating of wire and wire-to-block interface, (2) Hot collapse of wire interface increasing contact area, (3) Melting of the bulk of the wire and solid state bonding at the wire-to-block interface, (4) Complete melting of wire and penetration of fusion zone across bond interface, (5) Possible over-heating and local thinning of wire.

2. The observed dominating fracture mechanism for low heat input settings was a brittle interface failure totally separating the wire from the block. For higher heat inputs the failure changed to a ductile fracture through the softened heat affected zone of the wire.

3. The maximum JBF was just below 7kp for weld force settings of 2.5kp and 5kp. The experimental variation in measured setdown and JBF was significantly higher for the lower weld force and the most robust process settings is therefore a weld force of 5kp. However, this setting required a higher current of 600A to produce a fusion bond with smooth surfaces and optimal JBF.

The numerical investigation showed that the simulation of the mechanical collapse of the wire was insufficient thereby causing discrepancy between the numerical and experimental results due to excessive heat generation at the interface. Furthermore it was shown that the standard settings of thermal and electrical contact resistance between wire and block might be too high also contributing to increase heat development at the interface. By manually increasing the wire to block contact area, decreasing contact resistance and increasing the cooling effect from the block the weld mechanism was found to correspond better with the experimental observations.

Chapter 7

Microstructure Characterisation of AHSS

The strength of a resistance weld is closely related to its microstructure. In order to be able to predict the mechanical properties of the final weld it is essential to know what microstructure is present. Determining the microstructure of welds of high strength steels is not a trivial matter due to the complexity of the steels, however, establishing reliable methods for doing so is crucial for a better understanding of these steels and the transformations occurring during welding.

TRIP and DP steel both have complex multi-phase microstructure containing several phases. TRIP steel has the most complex microstructure containing ferrite, retained austenite, bainite and martensite whereas DP steel contains only ferrite and martensite [97]. The presence of the many microstructural phases in the same material leads to difficulties with identification of the different phases. It is unclear which phases are present in the material before and after welding, and the goal of the present study is to determine this using different microstructural characterisation techniques. To reveal the microstructure for microscope examination the surface of the as-polished specimen is etched. In this work it is desired to investigate several etching methods and find out which methods are suitable for this application.

7.1 Theoretical Background

Martensite

Martensite transformation can occur due to mechanical deformation as well as by rapid cooling of the material. The martensite transformation induced by deformation is the mechanism leading to the properties of TRIP steels where austenite is

transformed to martensite under applied stress or deformation [98]. The temperature dependent martensite formation in iron-based alloys begins spontaneously after cooling below the martensite starting temperature (M_s). The M_s depends upon the concentration of austenite-stabilising elements, on prior thermal and mechanical treatment, and on grain size. As the temperature is lowered below M_s further transformation occurs until the reaction ceases at the martensite finishing temperature (M_f). The amount of formed martensite after cooling depends purely on the temperature to which the steel is cooled and is independent of holding time at that temperature. This is due to the fact that the cooling induced martensite is formed by the formation of new martensite plates rather than by the growth of pre-existing plates [98].

In practise, the martensite reaction can never be completed and some retained austenite will always remain. The amount of retained austenite can be controlled by alloying elements, e.g. increased amount of carbon will lower the M_s and M_f and thereby lower the transformation of austenite into martensite. This is the fundamental in TRIP steels where carbon together with other alloying elements will stabilise retained austenite at room temperature. Retained austenite can also be mechanically stabilised which is described in other studies [98]. The morphology of martensite is strongly related to the various martensitic phase transformations that occur in the alloy depending on the composition and conditions during transformation. First of all, there are two main structures of martensite; lath and plate martensite. Plate martensite is mainly found in high-carbon steels whereas lath martensite typically is found in low-carbon steel (< 0.6wt%C) [98]. The most common martensite transformations in steel are

$$\begin{array}{llll} \gamma & \text{austenite (FCC)} & \rightarrow & \alpha' \quad \text{martensite (BCC or BCT)} \\ \gamma & \text{austenite (FCC)} & \rightarrow & \epsilon \quad \text{martensite (HCP)} \end{array}$$

Of these two the most common martensite is the α' martensite with BCC or BCT lattice whereas the ϵ martensite forms only in ferrous alloys with a low stacking fault energy of the austenite. In plain carbon steels martensite is a supersaturated solid solution of carbon in iron which has the BCT crystal structure [98]. The tetragonality of the lattice is strongly related to the carbon content and in pure iron or in very low-carbon steel the lattice would be close to BCC. Electron diffraction patterns of martensite will approach the BCC pattern, but slightly distorted due to the tetragonality of the lattice. The crystal structure of BCT martensite is shown in figure 7.1.

As the c-parameter increases with increasing carbon content, the a-parameter will decrease. Empirical studies have shown that that the lattice parameters in marten-

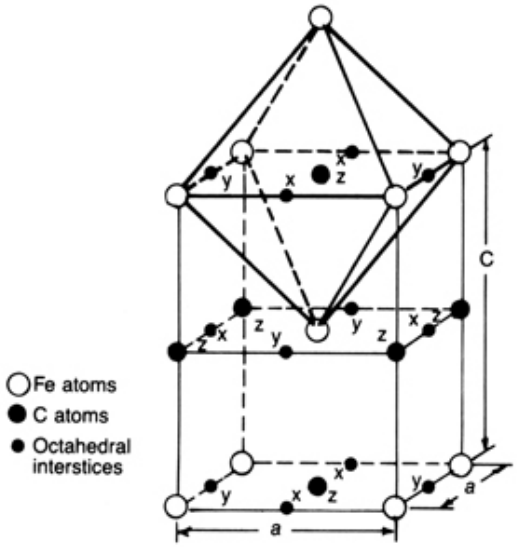

Figure 7.1: Crystal structure of martensite [98]

site can be described by the following equations [99]

$$a = 0.28664 - 0.00028 \cdot X_{\mathrm{C}}^{r} \tag{7.1a}$$

$$c = 0.28664 + 0.00247 \cdot X_{\mathrm{C}}^{r} \tag{7.1b}$$

where X_{C}^{r} is the atomic percent of C atoms in the material defined by equation (7.2) where N is "number of atoms"

$$X_{\mathrm{C}}^{r} = \frac{N_{\mathrm{C}}}{N_{\mathrm{total}}} \tag{7.2}$$

For pure iron the crystal system becomes cubic BCC ferrite with the lattice parameter $a = c = 0.28664$. X_{C}^{r} can be estimated from knowledge of the weight percent of carbon in the alloy by assuming that the alloy consists purely of iron and carbon, i.e. $N_{\mathrm{total}} = N_{\mathrm{C}} + N_{\mathrm{Fe}}$. The total mass of an alloying element m_{X} is related to the number of atoms N_{X} of the element by the following relationship

$$N_{\mathrm{X}} = n_{\mathrm{X}}\mathrm{N_A} = m_{\mathrm{X}}\frac{\mathrm{N_A}}{A_{\mathrm{X}}} \tag{7.3}$$

where A_{X} is the atomic weight of the element, n_{X} is the mol of the element and $\mathrm{N_A}$ is Avogadro's number. The weight percent of an element X (wt%X) is calculated from the following formula where m_{total} is the total weight of the alloy

$$\mathrm{wt\%}X = \frac{m_X}{m_{\mathrm{total}}} \tag{7.4}$$

If we assume that the alloy solely consists of iron and carbon (i.e. wt%Fe = 1 − wt%C) we can calculate the atomic weight percent of carbon in the alloy by combining equation (7.2), (7.3) and (7.4)

$$X_{\mathrm{C}}^{r} = \frac{N_{\mathrm{C}}}{N_{\mathrm{Fe}} + N_{\mathrm{C}}} = \frac{m_{\mathrm{C}}/A_{\mathrm{C}}}{m_{\mathrm{Fe}}/A_{\mathrm{Fe}} + m_{\mathrm{C}}/A_{\mathrm{C}}} = \frac{\mathrm{wt\%C}}{(1 - \mathrm{wt\%C})\frac{A_{\mathrm{C}}}{A_{\mathrm{Fe}}} + \mathrm{wt\%C}} \tag{7.5}$$

Bainite

Bainite is formed from austenite when cooled below the nose of the pearlite transformation curve but still above the M_s temperature. Similar to pearlite bainite is not a phase but a mixture of the two phases; ferrite and cementite. However, the microstructure of bainite is quite distinct from pearlite. Bainite is in general terms described as a non-lamella ledge-wise formation of ferrite and cementite, growing in a non-cooperative process. In pearlite the growth of cementite and ferrite is cooperative. The ferrite laths are nucleated due to undercooling of austenite and as ferrite laths are growing in thickness the carbon content in the intermediate austenite is increased. At a certain carbon level cementite is nucleated and the ferrite-cementite layered structure is formed. At the highest temperatures of the bainite transformation, pearlite and bainite occurs simultaneously and competitively. It can be difficult to separate the two structures since the morphology becomes very similar. The only difference is the crystallography where in pearlite the growth of ferrite and cementite has no particular orientation relationship to the original austenite grain whereas the bainite is strongly related to the original austenite grain [67, 98]. The morphology of bainite is mainly controlled by the temperature at which it is formed. Bainite can attain mainly two morphologies; upper and lower bainite. The name refers to the temperature at which they are formed [67, 98]. In figure 7.2 a schematic illustration of upper and lower bainite is shown.

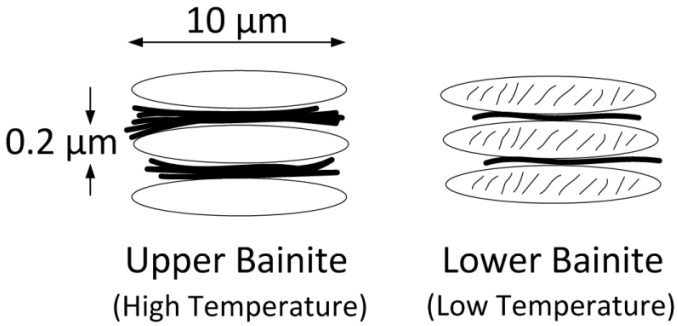

Figure 7.2: Schematic illustration of upper and lower bainite (reproduced from [100])

Upper bainite consists of ferrite laths with cementite precipitates in between the laths. Lower bainite is formed at lower temperatures where the carbon diffusion is very poor. The ferrite laths become much finer and so does the cementite precipitates between the ferrite laths. Furthermore, carbides precipitate inside the ferrite laths [67, 98]. Bainite is not a particular phase but rather a mixture of ferrite and cementite lattice. Therefore, the crystal lattice of bainite is a combination of the ferrite and cementite. There is a special orientation relationship between the two phases and normally there is no distortion of the ferrite lattice. In figure 7.3 are shown diffraction patterns of bainite as reported in literature [101–103]. It is clear from the diffraction patterns that two phases are present.

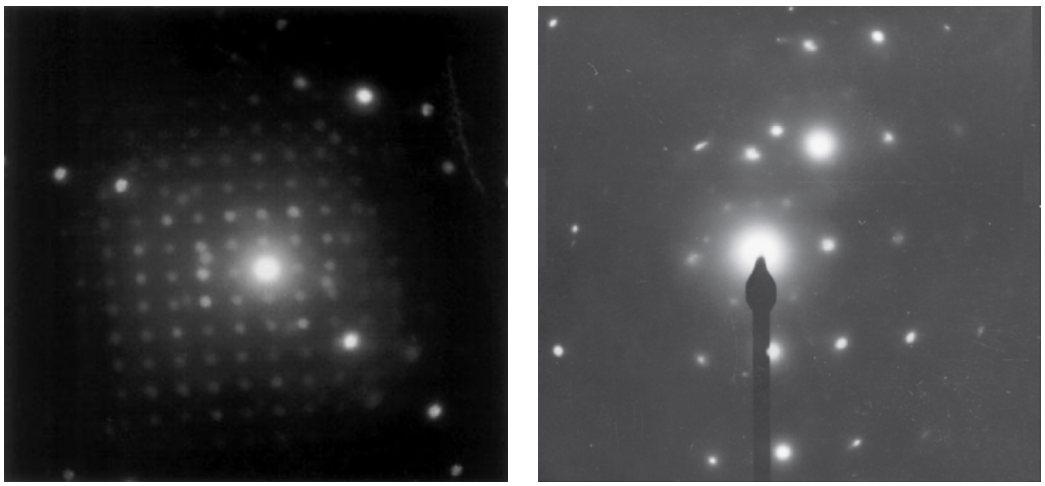

(a) Madariaga et al. [102] **(b)** Das et al. [103]

Figure 7.3: TEM diffraction patterns of bainite showing two distinct overlapping patterns; ferrite and cementite

Electron Diffraction Theory

In the following is described the essential considerations in the applied experimental procedure for determining the lattice parameters of the crystal structure from the obtained diffraction patterns. The diffraction patterns are mainly used to distinguish the ferrite BCC lattice from the BCT martensite lattice, but they are also used to estimate the carbon content in the observed martensite from the tetragonality of the crystal lattice. A more comprehensive description of the theory involved in electron diffraction measurements and diffraction patterns is made by Goodhew [104].

From a diffraction pattern it is possible to obtain the different spot radii r_i by manual measurements of the distance between spots. The diffraction of the electrons

is controlled by the lattice spacing d_i of the atomic planes in the crystal structure. The following relationship applies between the measured radius and lattice spacing [104]

$$d = \frac{\lambda L}{r} \tag{7.6}$$

In equation (7.6) λ is the wavelength of the electrons and L is the applied camera length. The product λL is called the camera constant and is a constant for a specific setting of the microscope. In order to relate the parameter d with the actual crystal structure it is necessary to know the zone axis of the diffraction pattern and the corresponding spot indices (h, k, l). For a pure BCC crystal structure the following relation exist between indices (h, k, l), lattice parameter a and atomic plane spacing d_{hkl} [104]

$$\frac{1}{d_{hkl}^2} = \frac{h^2 + k^2 + l^2}{a^2} \tag{7.7}$$

If the microstructure is martensitic and the crystal structure is BCT the structure is described as having two similar lattice parameters a and an additional lattice parameter c. In this case the following relation exists between indices, lattice parameters and atomic plane spacing

$$\frac{1}{d_{hkl}^2} = \frac{h^2 + k^2}{a^2} + \frac{l^2}{c^2} \tag{7.8}$$

If the crystal structure is BCC and a therefore is equal to c we see that equation (7.8) is similar to (7.7). Now we utilise the fact that the lattice parameter a is only slightly affected by the presence of carbon in the Fe matrix (cf. equation (7.1)). Especially with low amounts of carbon the lattice parameter a is almost constant while c is almost ten times more sensitive. Using this fact we can assume a to be constant and equal to 0.28664nm which is its value in a normal Fe-BCC structure. In order to find the camera constant λL and the lattice parameter c we need two dissimilar spot vectors r_1 and r_2 where the one vector r_1 has no coordinate in the c-direction in the lattice. The c-direction is in the following chosen as the one being represented by the l-coordinate. It is possible to choose one of the other coordinates as being the one representing the c-direction but it is important that all coordinates are held constant for all planes in that particular pattern. In the following derivations the l-coordinate represents the c-direction but could in theory be substituted by one of the other coordinates. By combining equation (7.6) and (7.8) an expression for the camera constant can be isolated

$$\frac{r_1^2}{(\lambda L)^2} = \frac{h_1^2 + k_1^2}{a^2} \quad \Leftrightarrow \quad (\lambda L)^2 = r_1^2 \frac{h_1^2 + k_1^2}{a^2} \tag{7.9}$$

The second spot vector r_2 should have an l-coordinate in the c-direction and in-

serting the values and combining with equation (7.9) yields

$$\frac{r_2^2}{(\lambda L)^2} = \frac{h_2^2 + k_2^2}{a^2} + \frac{l_2^2}{c^2} \quad \Rightarrow \quad c = a|l_2| \left(\frac{r_2^2}{r_1^2}(h_1^2 + k_1^2) - (h_2^2 + k_2^2) \right)^{-\frac{1}{2}} \tag{7.10}$$

Equation (7.10) can now be used to calculate the lattice c-parameter.

The estimation of the exact lattice parameter c involves a great amount of uncertainty which is due to the small difference between a and c. As can be seen from equation (7.10) the measured spot radii r_i are squared inflating the measurement uncertainty. An example on how much the measurement uncertainty can influence the results is calculated. If we assume the crystal structure to be BCC with $a = c = 0.28664nm$ and the zone axis (h, k, l) is 111 then the measured spot radii are expected to be equal. We assume that the uncertainty on the measurements is 1% which corresponds to approximately 3 pixels with a spot radius of 300 pixels. Worst case scenario a measure of $r_2 - 1\%$ and $r_1 + 1\%$ is made, which gives us the following value of c using equation (7.10)

$$c = 0.28664\text{nm} \cdot 1 \cdot \left(\left(\frac{0.99}{1.01} \right)^2 (1 + 1) - (1 + 0) \right)^{-\frac{1}{2}} = 0.2974\text{nm} \tag{7.11}$$

The example illustrates how even small errors in the measurements can have large impact on the results. This is even more the case in the example above because the 111 zone axis is so simple and the c-direction coordinate l is equal to 1. In diffraction patterns with zone axis with numerically larger spot indices the influence of the measurement error is decreased. This can be seen by doing the same calculation as above on the 313 zone axis where the calculated c then becomes 0.2931nm, however, the error is still significant and care should be taken when measuring the different spot radii.

7.2 Experimental Method

7.2.1 Materials

In this study two different steel types has been investigated: Dual-phase (DP) steel and Transformation Induced Plasticity (TRIP) steel. The DP steel has a two-phase microstructure containing ferrite and martensite whereas the TRIP-steel has a multiphase microstructure containing ferrite, martensite, retained austenite and bainite. In the following a short description of the two steel types will be given.

DP Steel

Dual-phase steel is produced from low-carbon steels typically containing a ferrite-pearlite microstructure. The ferrite-martensite microstructure of dual-phase steels are produced by annealing the ferrite-pearlite steel in the intercritical temperature range (ferrite + austenite equilibrium region) to produce a ferrite-austenite mixture. This is followed by accelerated cooling to transform all austenite into martensite. The amount of martensite and ferrite in the final dual-phase steel is strongly dependent on annealing temperature and duration. If the annealing time is too short and the temperature too low the pearlite cannot be completely dissolved into austenite and the resulting microstructure will contain ferrite, martensite, and pearlite. If the annealing time is longer than necessary for dissolution of the pearlite, the austenite grains will grow and the resulting microstructure will contain more martensite. This is of course only valid for samples quenched after annealing [105].

TRIP Steel

The microstructure in TRIP steels are usually obtained by a two-step heat treatment procedure [106]. First, the material is annealed at an intercritical temperature (ferrite + austenite equilibrium region) at which austenite and ferrite coexists. It is then rapidly cooled and held at an intermediate ageing temperature at which some bainite can form and thus contribute to the stabilisation of the retained austenite. The steel is finally cooled down to room temperature [106]. The stabilisation and retention of austenite at room temperature is the main challenge in TRIP steels. Carbon enrichment of austenite during annealing and bainite transformation is found to be very effective in retaining the austenite at room temperature [107, 108].

Composition

The DP steel is manufactured by SSAB and the commercial name is DP600. The TRIP steel is manufactured by ThyssenKrupp under the commercial name TRIP700. The numbers refer to the yield strength of the material. In table 7.1 is given the composition of the two steel grades as given by the manufacturers.

Table 7.1: Composition of the two steel grades as defined by the manufacturers. Compositions are given in wt%

Alloy	C	Mn	Cr	B	Si	P	S	Al	Fe
DP600	0.11	0.9	0.5	-	0.4	0.015	0.002	0.04	97.88
TRIP700	0.24	2	0.6	0.005	0.3	0.4	0.01	0.24	96.21

Harthoej and Pedersen [109] measured the alloy composition with GDS giving a composition somewhat different from what was predicted by the manufacturer. Since the carbon content is most essential, only the difference in carbon content will be given. The predicted and measured carbon contents are listed in table 7.2.

Table 7.2: Carbon content of the steel grades as predicted by the manufacturer and measured values by Harthoej and Pedersen [109]

Alloy	Nominal	Measured
DP600	0.11	0.083
TRIP700	0.24	0.294

It is seen that there is a significant difference between the nominal carbon content and the measured carbon content, in both steel grades. The carbon content in DP is measured lower than the nominal content and in TRIP the measured content is higher than the nominal content. Overall, this implies that the difference in carbon content between the two steel grades is expected to be larger than the nominal content predicts.

7.2.2 Welding

The compositions of the two steel grades are collected in table 7.1. DP600 sheets have a thickness of 1.5mm and are uncoated. TRIP steel sheet has a thickness of 1.2mm and is provided with a hot-dipped galvanised Zn-coating ($14\mu m$). For the experiments the sheets were cut in samples of 100x25mm and welded as a lap joint. The welding was done on a TECNA 8105 AC welding machine with a TE-180 weld controller. The electrical system can deliver up to 85kA with 50Hz. The actual current was measured using a Rogowski coil together with a pre-calibrated TECNA-1430 conditioner. The mechanical system is pneumatically driven and can deliver up to 20kN weld force. The actual load during the welding process was measured using a piezo electric force transducer. The electrodes used were of material CuCrZr and 20mm diameter ISO 5821-1979 type B with a tip diameter of 8mm and a 50mm tip rounding radius. The actual welding parameters are given in table 7.3.

Table 7.3: Overview of welding parameters (cycles of 50Hz)

Material combination	Current [kA]	Force [kN]	Weld Cycles
DP – DP	9.8	6	17
TRIP – TRIP	9.5	4.5	17
DP – TRIP	9.8	5.2	17

7.2.3 Preparation of Samples

In this study the microstructure of TRIP and DP steel is examined in the as-received conditions and after being joined by resistance welding. Samples of sheets were prepared for microstructure analysis by casting en resin, grinding and polishing. After welding the microstructure of the weld nugget and the heat affected zone (HAZ) is heavily affected by the process and new phases are formed. These alterations in microstructure require sophisticated etching techniques to identify all microstructural constituents. In table 7.4 on page 161 is shown an overview of etching methods considered suitable for TRIP and DP steel.

Three methods are chosen for this study: Nital, SMB[1], and the modified LePera method. Nital is chosen mainly because of the DP steel where the method is highly suitable. SMB is chosen because of the ability to distinguish between many phases due to its colourfulness depending on small microstructural differences. Finally, the modified LePera method has many recommendations in literature for etching TRIP steel [97, 110].

It is desired that the three etching methods will complement each other well in identifying all microstructural constituents in the two steels and their respective welded and temperature affected regions. The recipes of the used etchants are shown in appendix D.1.

Nital

Nital is the most common etchant used to reveal the microstructure in common steel grades. Nitric acid is the base content in Nital. The etchant has been used in many years to reveal ferrite grains and highlighting the features in martensitic microstructure [111]. However, in multiphase steel grades like TRIP steel Nital is insufficient to reveal all microstructural constituents [110] which is why alternative etching methods are explored.

SMB

SMB etching is a tint etching technique. Tint etchants do not really etch the sample because they do not attack the surface by removal of material but instead chemical films are deposited selectively on the constituents on the surface. The result is coloured microstructure images from where phases can be distinguished [111]. One significant drawback of the tint etching technique is the variation of the colours with composition of the alloy. What may appear blue in one alloy can in another alloy appear brown and the consistency of the method will thereby be lost.

[1]SMB = Sodium Meta Bisulphate

Table 7.4: Overview of etching methods suitable for TRIP and DP steels[97, 106, 110–112]

Method	Contains	Application	Drawbacks	Appearance of phases
Nital [110, 111]	HNO_3	Determination of ferrite and martensite by grain etching	Do not colour the phases but only etches the grain boundaries	Reveals ferrite grains and grain boundaries and features in martensite. Shows also prior-austenite grain boundaries.
SMB [111]	SMB	Darkening the martensite	Only martensite is revealed. Grain boundaries are not clearly seen.	Ferrite: untouched Austenite: clear Martensite: brown/dark
Nital, SMB [97]	HNO_3, SMB	Determination of phases in TRIP (unless bainite and martensite)	Carbon containing phases such as bainite, martensite and carbides appear dark.	Ferrite: off-white Bainite, martensite: dark Austenite: white
Marshall's [110, 111]	H_2SO_4, H_2O_2	Displays grain boundaries	Do not distinguish between phases but only shows grain boundaries.	Only ferrite grains are revealed
Vilella's [111]	HCl, SMB	Good for ferrite-carbide structures such as bainite. Also determination of prior-austenite grain size.	Best on tempered martensite	Bainite appears darker than martensite
LePera [97, 106, 112]	Picric acid, SMB	Distinguish between austenite/martensite, bainite and ferrite	Difficult to distinguish between martensite and austenite	Ferrite: yellow/blue Bainite: brown Austenite, martensite: white
Modified LePera [97, 110]	Picric acid, HCl, SMB	Determination of all phases in TRIP steel		Ferrite: slightly discoloured Bainite: dark blue/brown Austenite: white Martensite: straw coloured

Modified LePera

The many microstructural phases in TRIP steel are difficult to etch with standard etching techniques. SMB alone fails to differentiate martensite from bainite, and martensite and ferrite can also be difficult to differentiate [112]. An improved etching technique was developed in 1980 to overcome this problem; the LePera etchant. LePera etchant is a combination of tint etching with SMB and attack etching with picral acid. Picral attacks interfaces between ferrite and carbide phases e.g. in bainite and martensite. With the LePera etchant it is possible to obtain a microstructure where martensite appears white, bainite appears black, ferrite appears tan, and, in most cases, grain boundaries are not strongly etched [112]. However, many studies have refused LePera because it is not always possible to distinguish austenite and martensite. Then a modified LePera was developed [97]. The modified LePera etchant is slightly revised with a minor addition of HCl which according to literature gives an improved result compared to the regular LePera technique. Many studies have described the examination of the microstructure in TRIP and DP steels, in both as-received and welded conditions, but no one describes the microstructure of TRIP and DP welded together as in this study. The challenge in this study is therefore to use techniques which can reveal all microstructural constituents in both base materials and in the welded region. This is the motivation for testing many etching methods. If no single method can accomplish this demand, then two methods must be adopted for one sample to reveal each region.

Microhardness Measurements

Microhardness measurements are performed on a microhardness tester FM-700 supplied by Future Tech. In order to ensure alignment of the specimen orthogonal to the positioning plate, the specimens are aligned using wax and an optical plate.

7.2.4 Microscope Examination

Reflective light microscopy or light optical microscopy (LOM) was performed on a Neophot 30 microscope. For scanning electron microscopy (SEM) a JEOL JSM-5900 with LaB6 filament was used for microstructure investigation applying secondary electron (SE) and EDS (Oxford Instruments) for quantitative chemical analysis. For transmission electron microscopy (TEM) samples were prepared by electropolishing of thin film. TEM was carried out on a Technai T20 with tungsten filament, operated at 200 kV accelerating voltage. Diffraction, bright field and dark field imaging was used during TEM examination. Determination of crystal structure from diffraction analysis will be given in the following section.

7.2.5 Crystal Structure from Diffraction

Due to limited resources only one weld was subjected to diffraction analysis in TEM. The chosen specimens were taken from the weld nugget in the TRIP-DP weld. The experimental procedure used to estimate the crystal structure from the diffraction patterns is described in the following. The procedure consists of three steps: 1. Manual measurement of diffraction patterns, 2. Estimating zone axis and spot indices and, 3. Calculating lattice parameters.

1. **Manual measurement of diffraction patterns**
   The diffraction patterns are measured manually using the program ImagePro Plus. The measurements are done in pixels directly from the digital images of the diffraction patterns. Several measurements of the same spot radius are made and measurements are made across several spots to decrease measurement uncertainty. Same procedure is used to measure the angles between the spots. It is assumed that an uncertainty of 1% is associated with the manual measurements of diffraction patterns.

2. **Estimating zone axis and spot indices**
   In order to identify the zone axis of the measured diffraction patterns the web application EMS-online [113] is used. The application works by choosing a specific crystal structure and compare the measured results against it. Because we know that the crystal structure is either martensite or bainite BCC is chosen to find possible combinations of zone axis and camera constant which results in the measured diffraction pattern. It is also possible to vary the lattice parameters to approach a BCT martensite structure. The application will then suggest one or several solutions of which the one with the simplest or most likely combination of zone axis and camera constant is chosen. This is done by using another web application: WEB-EMAPS [114] that draws the specific diffraction pattern and which is then compared to the measured pattern for verification. From the computer generated pattern it is possible to identify the specific spot indices for the different patterns.

3. **Calculating lattice parameters**
   In order to calculate the distorted lattice parameter c in the BCT crystal structure the relevant spot radii and coherent spot indices needs to be chosen. The use of equation (7.10) requires that one of the three measured spots have a zero-indice in the distorted c-direction in the lattice. Some of the zone axis give some freedom in choosing the correct spot as representing the one with zero-indices in the c-direction. For example a 111 zone axis have spot indices of 110, 101 and 011. If the crystal is BCT, equation (7.8) dictates that two of the measured spot radii (the ones with non-zero indices in the c-direction)

should be of equal length and smaller than the third (with zero indices in the c-direction). With patterns of other zone axes it is typically not that simple to identify the correct indices corresponding to the c-direction. In this case a trial and error approach is applied until the spot chosen for calculating the camera constant from equation (7.9) yields a reasonable c-lattice parameter. Theoretically the two estimates of c should be equal but due to uncertainty in measuring the spot radii some variation will occur.

7.3 Estimation of Phases from Diffraction Patterns

Diffraction patterns obtained from the weld nugget of the TRIP-DP weld is used to estimate the crystal structure of the phases present. The applied experimental procedure is described in section 7.2.5.

7.3.1 Diffraction Patterns

Diffraction was performed in areas with different morphology and all patterns were identified as slightly distorted BCC patterns. In figure 7.4 is shown a measured (111)-zone axis diffraction pattern and pixel measurements of the three lengths confirms that one length is different from the two others (e.g. $r_1 \neq r_2 = r_3$).

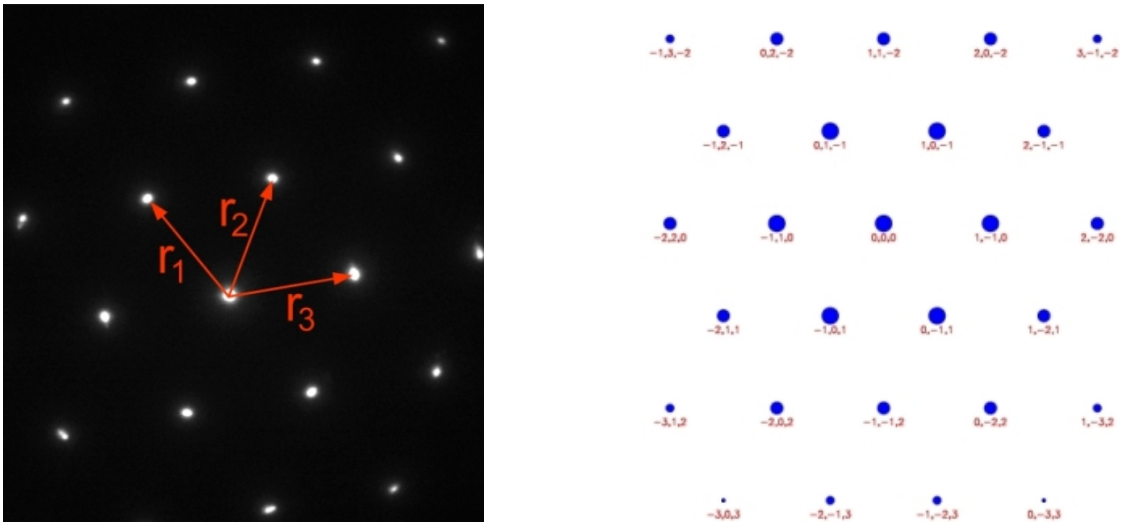

(a) Measured pattern

(b) Calculated pattern using BCC crystal [114]

Figure 7.4: Diffraction patterns from a (111)-zone axis

The distortion of the BCC lattice is caused by tetragonality of the cubic lattice which corresponds to BCT martensite. All diffraction patterns indicate a distortion of the lattice, even when taking uncertainty of the measurement into account. Diffraction are performed in many areas in the weld nugget of TRIP-DP and all patterns indicate that martensite is the only phase present in the weld nugget. If bainite was present, two diffraction patterns would have been expected in one pattern due to the presence of both ferrite and cementite in bainite as illustrated in figure 7.3 in section 7.1.

7.3.2 Estimation of Carbon Content from Diffraction Patterns

The carbon content of the steels investigated in this project is listed in table 7.1 with the corrected measured values of the AHSS steels in table 7.2. When welding two dissimilar materials together the melt in the weld nugget becomes a mixture of the alloying elements in the two materials. From the nominal carbon content in the materials an approximate estimate of the lattice parameters a and c is calculated in the following. It is assumed that the melted zone will have an average composition of the content in the two original alloys although this is not completely true because the sheet thickness is different for the two alloys. With the original carbon content of 0.08 and 0.29wt% in DP and TRIP, respectively, the carbon content in the weld nugget is approximately 0.18wt%. Using equation (7.5) the atomic weight percent of carbon can be calculated and inserted in equation (7.1) which gives the theoretical lattice parameters of the martensite formed in the weld nugget. This is collected in table 7.5.

Table 7.5: Calculated lattice parameters from carbon content

	wt%			**Lattice parameters**	
Material	**C**	**Fe**	**X [at%]**	a	c
DP600	0.08	99.92	0.509	0.2865	0.2879
TRIP700	0.29	99.71	1.106	0.2863	0.2894
TRIP-DP	0.18	99.83	0.809	0.2864	0.2886

From the calculated lattice parameters of martensite in table 7.5 it can be seen that the relatively low amount of carbon is expected to cause only a small distortion of the crystal structure. Changes in the lattice parameters are expected to be approximately 0.0002nm for a and 0.003nm for c which is considered to be very small and thereby challenging to measure experimentally.

To estimate the carbon content from the experimentally obtained lattice parameters calculated from diffraction patterns, the procedure in section 7.2.5 is applied. The results from the measurements are collected in appendix D.2 and the following points are emphasised regarding the results.

- The average estimate of c from all the measurements is 0.2916nm.
- The camera constant which is specified in EMS-online is close to constant throughout the measurements which gives us confidence that the found zone axis is correct.
- All the measurements except the ones from 111 zone axis (see the next point) estimates a value of the c-parameter which is larger than the a-parameter. This indicates that the lattice in fact is distorted and the microstructure therefore can be assumed to consist of BCT martensite.
- In the 111 zone axis measurements the measured spot radii are found to have unequal lengths indicating the distortion of the lattice as in martensite. If it was BCC (bainite or ferrite) the lengths would have been expected to be similar.

The preliminary result is based on the assumption that the a-parameter equals the BCC lattice parameter of 0.28664nm. This is only approximately true because the a-parameter decreases slightly as the c-parameter and the carbon content increases. By using the empirical formulae presented in equation (7.1) an iteration scheme can now be used to estimate coherent values of the two lattice parameters a and c. From the calculated c-value using the initial guess of $a = 0.28664$ the corresponding atomic carbon content can be calculated from equation (7.1a). Inserting this carbon content in equation (7.1b) a new estimate of the lattice parameter a is found. By using this value as the a-estimate in equation (7.5) it is possible to calculate a new average value of c - and so on. The iteration scheme is collected in table 7.6 and the values are seen to converge to a final estimate of 0.2916nm and 0.2861nm of c and a, respectively.

Table 7.6: Iteration scheme for estimating lattice parameters a and c

Iteration	a **(guess)**	c **(average)**	**X [at% C]**	a **(calc.)**
1	0.2866	0.2921	2.21	0.2860
2	0.2860	0.2915	1.97	0.2861
3	0.2861	0.2916	2.00	0.2861

The carbon concentration based on the a- and c-value is calculated to be 2.0at% which corresponds to 0.44wt%. This is not in the range of the expected carbon

value in the weld which was estimated from the calculated concentrations in table 7.2 to be 0.18wt%. The upper limit of carbon in the weld comes from the TRIP steel which has a content of approximately 0.3wt% C and therefore the calculated carbon-content can not be correct. It was earlier described that calculations from diffraction patterns are associated with large uncertainties and the too high carbon content confirms this significant uncertainty.

7.4 Microstructure Characterisation

In the following sections the microstructure of the base materials of DP600 (DP) and TRIP700 (TRIP) are characterised along with the microstructure of the resistance welded combinations of DP to DP (DP-DP), TRIP to DP (TRIP-DP) and TRIP to TRIP (TRIP-TRIP).

7.4.1 DP Base Metal

The base material (BM) of DP is according to the manufacturer expected to be a two-phase microstructure containing ferrite and martensite. The BM microstructure of DP is shown in figure 7.5. The bright phase is ferrite and the dark phase is expected to be martensite. However, the microstructure image after etching with Modified LePera in figure 7.5b indicates a lamella structure which looks more like pearlite (marked with arrows). Before heat treatment DP steel consists of ferrite and pearlite, and the heat treatment will dissolve pearlite into austenite, and when quenching austenite will transform into martensite. It is possible that residual pearlite is present in the microstructure after heat treatment.

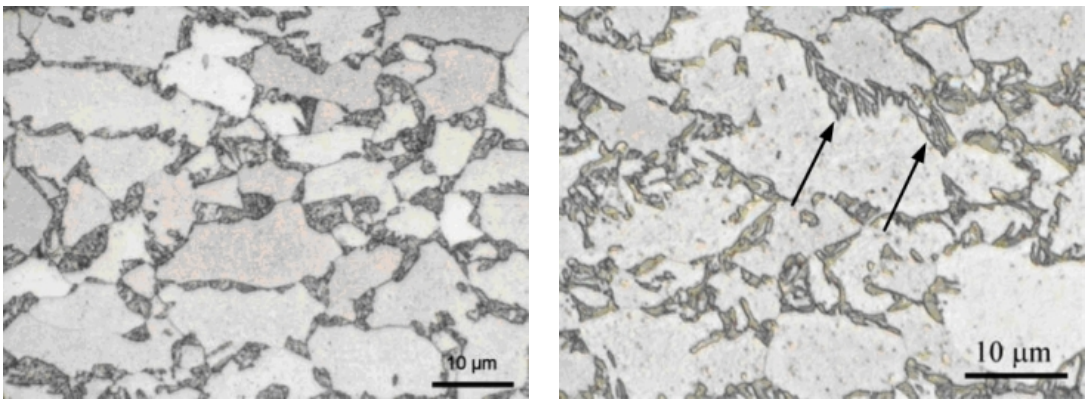

(a) Nital etch **(b)** Modified LePera etch

Figure 7.5: DP base metal

The hardness of DP base material used in this study is measured to be 220 HV100g and 200 HV5kg. In literature the Vickers hardness is measured as a function of volume fraction of martensite in an alloy comparable with the DP steel used in this study [115]. At a volume fraction of 20% martensite the hardness is approximately 200 HV30kg. This value is comparable with the 200 HV5kg measured in this study, although the indentation force is different. A microstructure containing 80 % ferrite and 20 % bainite is expected to have a hardness of 180 HV30kg according to Kumar et al. [115]. Based on this value it can be stated that if the microstructure was pure ferrite and pearlite the hardness would have been even lower than 180 HV30kg. Consequently the conclusion on the microstructure of DP base material is that ferrite and martensite is the main constituents. Some pearlite may be present, however, not a significant amount.

7.4.2 TRIP Base Metal

The base material of TRIP is more complicated than the base material of DP because of the presence of several phases. TRIP base material is shown in figure 7.6. The large bright grains are ferrite whereas the small grains are either bainite,

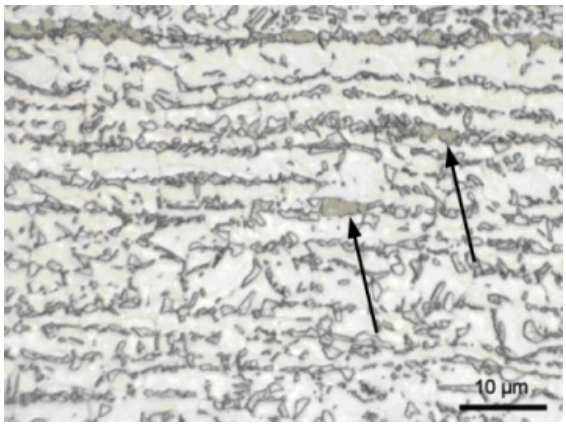

Figure 7.6: TRIP base metal - Modified LePera etch

residual austenite or martensite. The colour of the small grains varies and is related to the phase but the resolution in LOM is too low for examination of the small grained structure of TRIP BM. Therefore, it is difficult to verify the phases according to the colours. According to De et al. [97] bainite would appear blue or brown, retained austenite white, and martensite straw coloured. In figure 7.6 is observed many small grains with a bright appearance indicating it is austenite. However, the contrast of these small grains is very close to the large ferrite grains and it is therefore impossible to distinguish between austenite and ferrite. Several brown grains are also observed (arrow) and it is most likely bainite. No straw

coloured grains are observed which should be martensite but it is possible that there is no martensite in this as-received condition and that martensite therefore only forms upon deformation.

7.4.3 DP-DP

The Microstructure of DP from BM and into heat affected zone (HAZ) in the DP-DP weld is shown in figure 7.7. DP BM is included for easier overview and is similar to figure 7.5 but it is not the same image. The amount of dark areas is increased when shifting from BM to HAZ indicating that martensite or bainite has formed when the temperature is increased closer to the weld. Martensite and bainite can only be formed from austenite and therefore the temperature must have been above the eutectic temperature. When the temperature is rapidly decreasing, cooled from above eutectic temperature, martensite is formed. If the cooling rate is slightly lower, bainite will form.

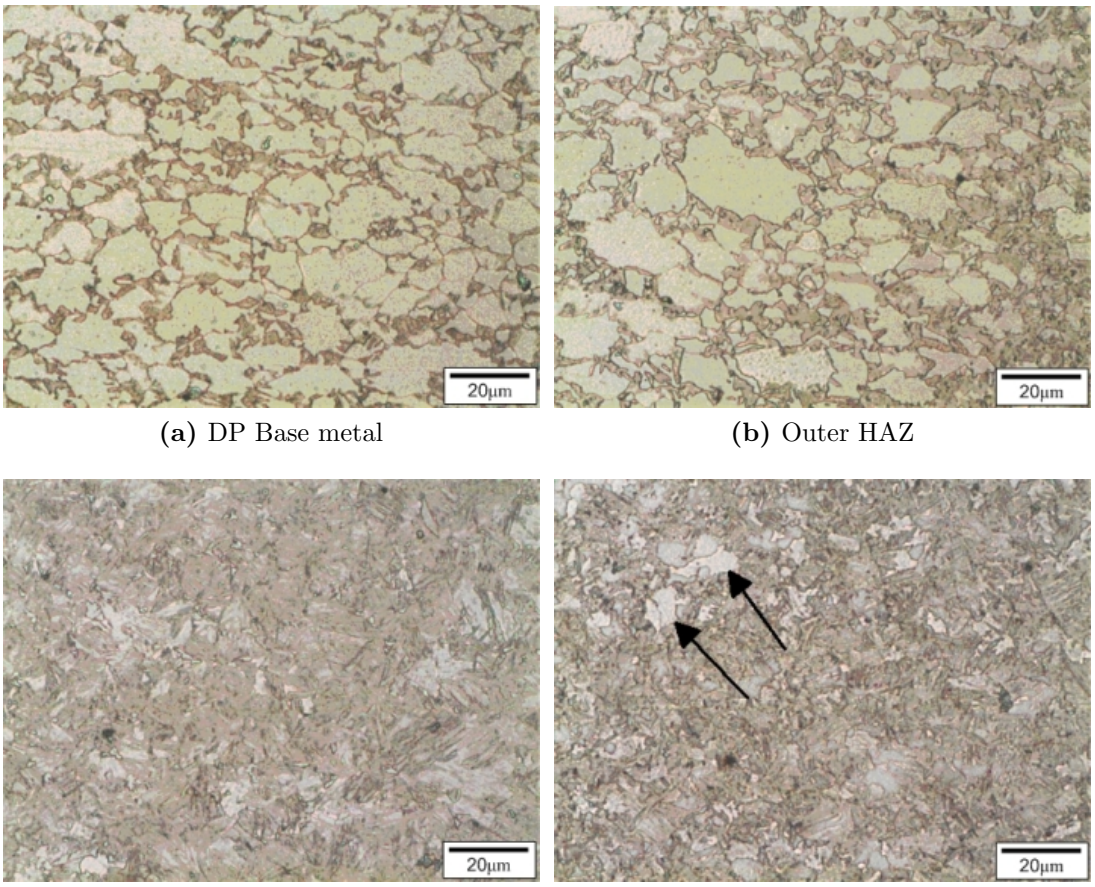

(a) DP Base metal **(b)** Outer HAZ

(c) Inner HAZ **(d)** Weld zone close to HAZ

Figure 7.7: Nital etch of DP-DP microstructure

As described in section 7.3 martensite is the only phase identified in the TRIP-DP weld. The carbon content in the DP-DP weld (0.08 wt%) is significantly lower than in the TRIP-DP weld (average of 0.3 and 0.08 wt%) and therefore the possibility of martensite to be formed is lower in DP-DP. The inner HAZ (figure 7.7c) and the weld close to HAZ (figure 7.7d) have very similar appearances containing small lamellas. However, both areas (most significant in figure 7.7d) also contain some equiaxed grains of bright appearance with irregular shape (arrows in figure 7.7d). It is not possible to determine which phase it is from EDS analysis but the appearance indicates that it is not bainite or martensite. These equiaxed areas are most likely retained austenite, however not determinable. Hardness measurements will most likely be able to identify austenite which is expected to be less hard than martensite. However, the size of the austenite grains complicates the hardness measurements in these grains.

In the centre of the weld nugget (WN) of DP-DP the lamella structure is larger than in HAZ which is illustrated in figure 7.8. It is clearly seen that the lamellas

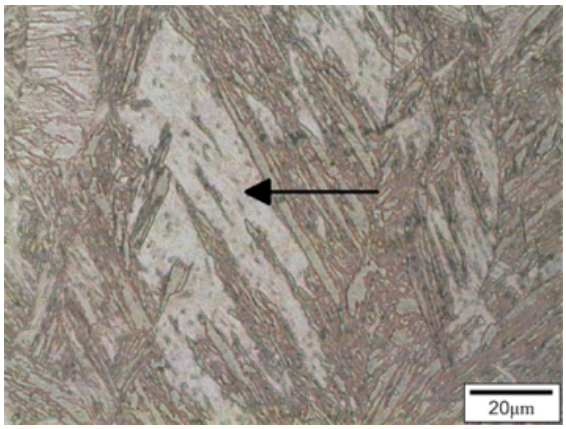

Figure 7.8: Nital etch of DP-DP weld nugget microstructure

are larger than in figure 7.7d. In the WN the material has been melted and the austenite grains have grown larger than in the HAZ and on subsequent cooling, martensite or bainite are formed and their size are controlled by the size of the austenite grains. Another observation in figure 7.8 is the presence of another apparently different type of structure appearing bright without the lamella structure, but rather a homogeneous structure (marked with arrow). It is possible that the bright area is still the lamella structure but seen from another angle. The colour difference between the lamella structure and the bright area could be due to the different orientation of the lamellas which influences the reaction upon etching. It is also possible that the bright area is another phase.

Microhardness is measured in the two different structures to verify if there is a significant difference. In figure 7.9 on the next page an example of the locations of the microhardness indentations is shown. It is seen that the size of the indentations

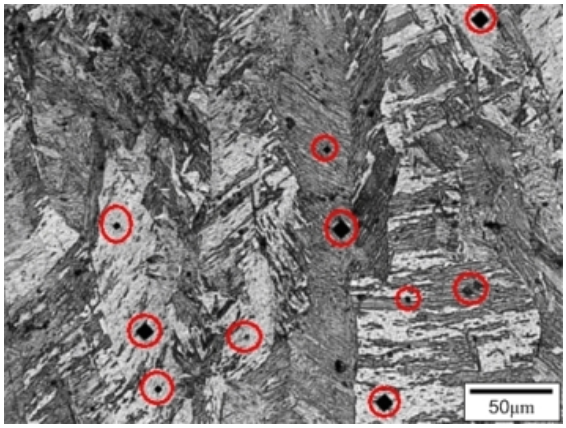

Figure 7.9: Example of microhardness indentations in the two different areas in the DP-DP weld nugget

are acceptable and are not too close to grain boundaries. For comparison the microhardness is also measured in the ferrite grains in the base material. The three different areas were hardness tested using a load of 5g and 25g. The results of the microhardness measurements are shown in table 7.7 where F, B and D represent the three different areas *ferrite in base material* (F), *bright area in weld nugget* (B) and *dark lamella area in weld nugget* (D).

Table 7.7: Results of microhardness measurements in DP-DP weld nugget

Indentation Load	**5g**			**25g**		
Measuring Areas	**F**	**B**	**D**	**F**	**B**	**D**
Average hardness [HV]	31.6	406.1	441.4	172.6	407.5	436.3
Standard deviation [HV]	2.4	22.0	15.4	18.5	18.2	9.3

There is a clear difference between ferrite and the two other areas and there is a slight difference between the bright areas and the dark lamella areas. To verify if there is a difference between these two areas (B) and (D) the results are tested by using the procedure known as the student one-sided t-test with unequal variances [88] which compares two means to see if they are equal or not. The test is shown in appendix D.3 and it shows that there is a statistically significant difference in hardness between the bright (B) and dark (D) areas of the microstructure in the nugget. However, the difference in hardness between the two different areas

does not necessarily imply that the two areas are different phases. The difference in hardness and visual appearance could still be caused by the size of the grains and the different orientations, but the different appearance could also be massive ferrite formed upon massive transformations. This corresponds well to the difference in hardness. The morphology of the grain in figure 7.8 looks like massive ferrite [116]. Massive ferrite is formed at a slightly slower cooling rate than martensite. Once a massive ferrite grain is nucleated the phase grows at extremely high rates in any direction which is the reason for the irregular shape. The transformation rate is still slower than martensite transformation which is the fastest phase transformation. Massive transformation and martensite transformation should not be confused with each other, because the transformations are quite different. Martensite transformation occurs as a sudden change in crystal structure by re-arrangement of atoms whereas massive transformation involves thermally activated jumping of atoms across the interface between the old and the new phase, with different crystal structure. Martensite is therefore termed military transformation whereas massive transformation is a civilian transformation. In both types of transformations the composition of the phase before and after transformation is the same which means that both transformations are diffusionless [67, 98].

In order to investigate how the hardness increases due to the thermal history experienced by the material during welding, a linear profile of hardness measurements is conducted from outside the HAZ and into the nugget. To get an indentation large enough to spread across many grains and grain boundaries (more than 5 grains are needed for a representative measurement) the indentation force was chosen to 50g. In order to increase the resolution of the profile and still have a minimum of 2.5 times the diagonal spacing between each measurement the profile was made in a zigzag profile with a stepwise movement of $\Delta X = +50\mu m$ and $\Delta Y = \pm 50\mu m$. In figure 7.10 is shown the hardness profile in the DP-DP weld. The hardness in the base material is around 220 HV50g and starts to increase slowly when approaching the weld nugget. From $X = 0.4$mm to $X = 0.65$mm the hardness increases to approximately 400 HV50g, which is the approximate hardness value in the weld nugget. These hardness values are representative for the temperature in the areas of the weld. From $X = 0$mm to $X = 0.4$mm the temperature is not high enough to cause any phase transformations. The HAZ starts from $X = 0.4$mm where phase transformations have occurred. The amount of transformed material is controlled by the increased temperature when approaching the weld. The fraction of transformed material is identified by the amount of remaining ferrite. Since it is not known what phase is formed in the weld, it is also not possible to state which phase is formed in the HAZ. Not before $X = 1$mm has the material actually been melted during the process but already from $X = 0.5$mm the hardness has been increased to the same level as the melted region which indicates that the entire microstructure is fully transformed at $X = 0.5$mm, but the HAZ continues to $X = 1$mm.

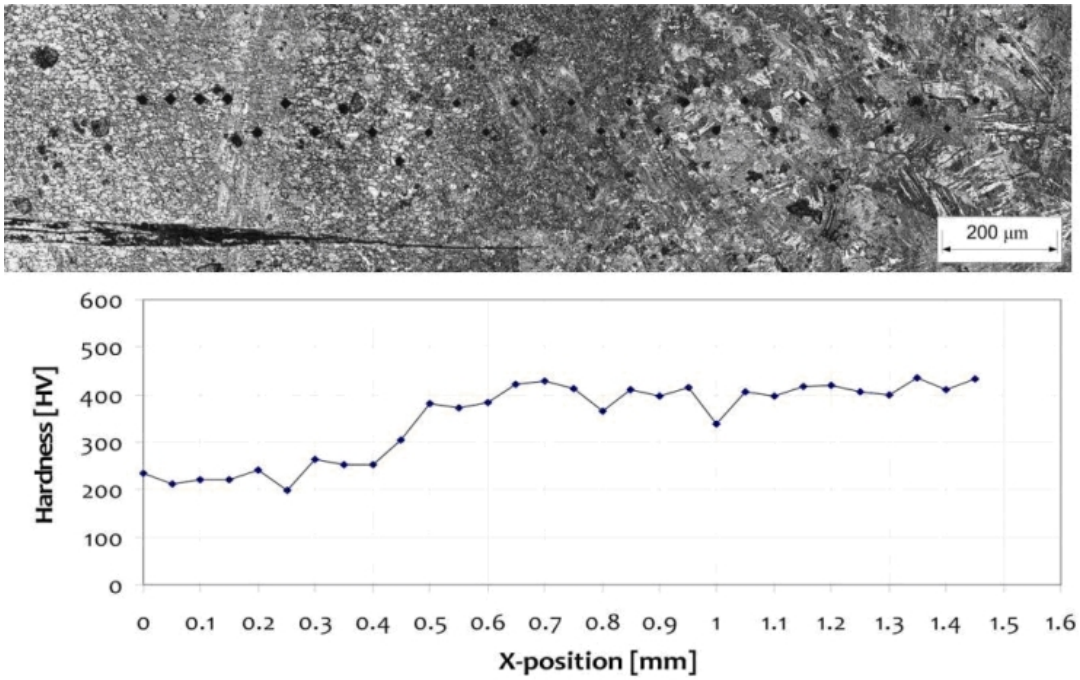

Figure 7.10: Microhardness profile of DP-DP weld. Indentation force is 50g

The eutectic temperature is related to the alloying elements, but since no CCT or TTT diagrams are available for the alloy it is not possible to state the precise temperature. However, approximately 700°C is a reasonable estimate of the eutectic temperature for many steels [55]. In figure 7.11 some hardness indentations are shown to illustrate how large the indentation are.

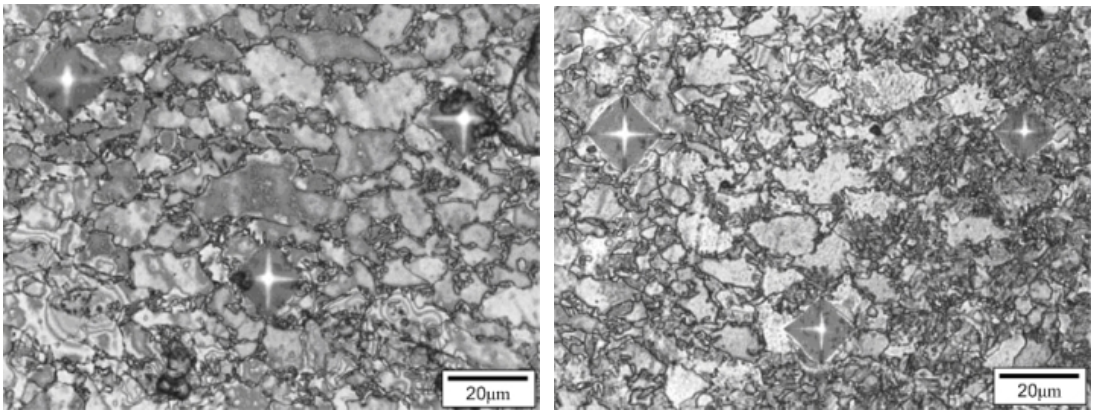

(a) $X-$position(mm) $= 0.25, 0.03, 0.35$ **(b)** $X-$position(mm) $= 0.4, 0.45, 0.5$

Figure 7.11: Close-up of hardness measurements in figure 7.10

Looking at the actual indentations in figure 7.11 it is possible to see that the high increase in hardness appears precisely in the zone where the large ferrite grains start to disappear. As described above, this zone has been heated up above the eutectic temperature where ferrite begins to transform into austenite. During the subsequent very fast cooling the austenite transforms to a much harder phase which is either martensite or bainite, and the hardness increases.

7.4.4 TRIP-TRIP

The TRIP HAZ in a TRIP-TRIP weld is shown in figure 7.12. TRIP BM is included for easier overview and is similar to figure 7.6 but with a different etching method. In figure 7.12 the microstructure is etched with Nital since it gives the best result in the HAZ and weld. The BM image in figure 7.12a looks completely different from the BM image in figure 7.6 which is etched with the Modified LePera approach. In figure 7.6 bainite, ferrite and austenite can be distinguished because

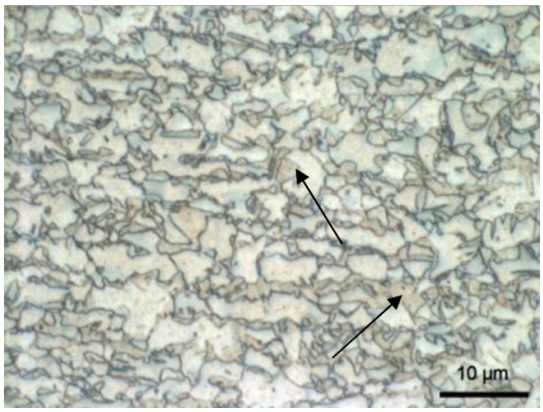

(a) TRIP Base metal

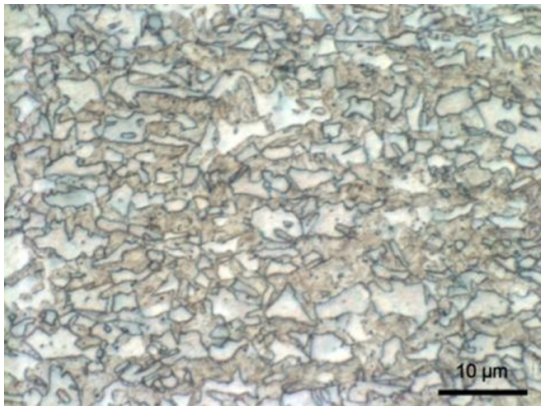

(b) Outer HAZ

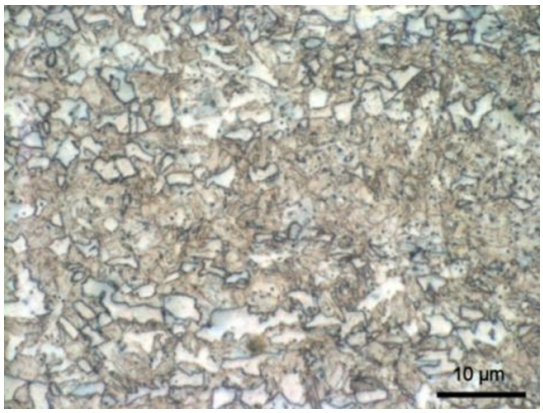

(c) Inner HAZ

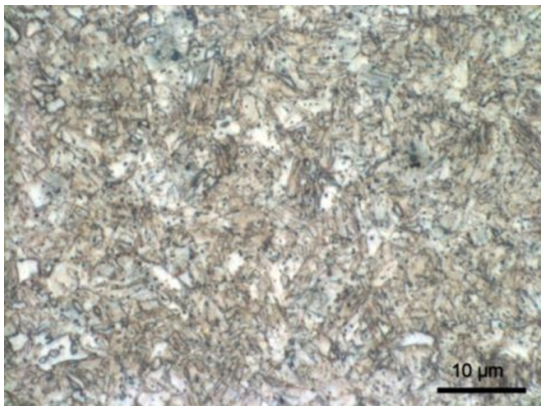

(d) Weld zone close to HAZ

Figure 7.12: Nital etch of TRIP-TRIP microstructure

of their contrast but here in figure 7.12a is only seen the ferrite grain boundaries, and probably the austenite grain boundaries. Some areas in figure 7.12a have a brown contrast (arrows) which could be bainite but this is purely based on the amount and morphology of these dark areas which are comparable to the bainite grains in figure 7.6. In figure 7.12b the amount of brown area is increased. It is possible that the brown areas are martensite since the amount of carbon in TRIP is higher (0.3 wt %) than in DP (0.08 wt%), and in TRIP-DP martensite was confirmed. When approaching the weld figure 7.12c and 7.12d the amount of dark areas is increased and the structure is more and more lamella. The amount of ferrite is simultaneously reduced and closest to the weld in figure 7.12d almost no ferrite is seen. When getting deeper into the weld nugget, the lamellas are increased

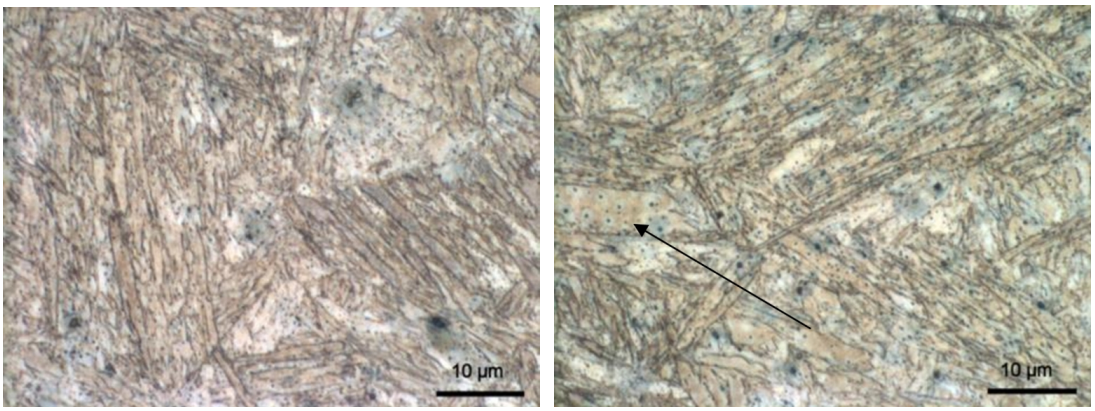

(a) **(b)**

Figure 7.13: Nital etch of TRIP-TRIP weld nugget microstructure

further in size. The weld nugget of TRIP-TRIP is shown in figure 7.13. In the weld nugget and inner HAZ microstructure is seen some black stains, that are not affiliated to a specific phase. This is most likely an over-etching effect and these stains were also seen in figure 7.12c and 7.12d. The microstructure in figure 7.13 is examined in SEM with secondary electrons and here the stains were seen as small holes which again indicates that they come from an etching effect. It is also possible that it is carbides which have been removed from the microstructure during etching. However, carbides are not expected to have formed in a martensitic microstructure and in bainite the carbides are expected to be much smaller than these carbides. Consequently it is concluded that these black stains is due to over-etching. Another observation in figure 7.13 is the presence of a rather equiaxed grain as marked with an arrow. This equiaxed area was also observed in the DP-DP weld nugget in figure 7.8 and it was proposed to be massive ferrite.

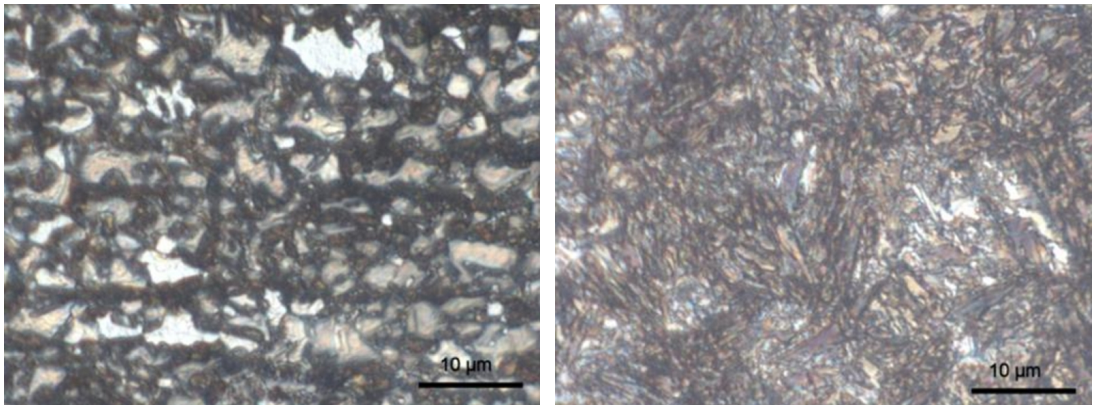

(a) TRIP-TRIP HAZ **(b)** TRIP-TRIP weld nugget

Figure 7.14: SMB etch of TRIP-TRIP microstructure

TRIP-TRIP is also examined with SMB etching and in figure 7.14 are shown microstructure images from the HAZ and the weld nugget. After etching with SMB austenite is expected to be clear, ferrite untouched, and martensite and bainite will attain dark colours. In HAZ there can be seen two types of bright phases; a white phase and a beige phase which could be austenite (white) and ferrite (beige). It is also possible that the colours are unreliable because they can be altered or faded. However, if the white colour of austenite is reliable then these images give a clear indication of the presence of austenite in the HAZ and to a lesser degree in the weld nugget. This was not found with any of the other etching methods.

7.4.5 TRIP-DP

BM and HAZ of DP in TRIP-DP weld is shown in figure 7.15 on the next page. DP BM (a) is enclosed for better overview and is the same image as in figure 7.5a. From figure 7.15a to 7.15b the amount of dark areas are increased. This was also observed in figure 7.7 where the BM was compared with outer HAZ in the DP-DP weld. Here it was not determined what phase was formed but since martensite is known to have formed in the weld nugget it is likely that the dark areas in figure 7.15 is martensite. When approaching the weld (figure 7.15c and 7.15d) the material is more strongly influenced by the heating and the fraction of ferrite grains are reduced. The microstructure is very comparable to DP-DP in figure 7.7 which is not surprising since the TRIP steel is not expected to have any influence on the HAZ of the DP steel. As noted in DP-DP in figure 7.7 it is also possible that some of the grains assumed to be ferrite are residual austenite in figure 7.15. However, this is not determinable using LOM. The martensite around the ferrite/austenite contain a fine lamella structure and approaching the weld (figure 7.15d) the width

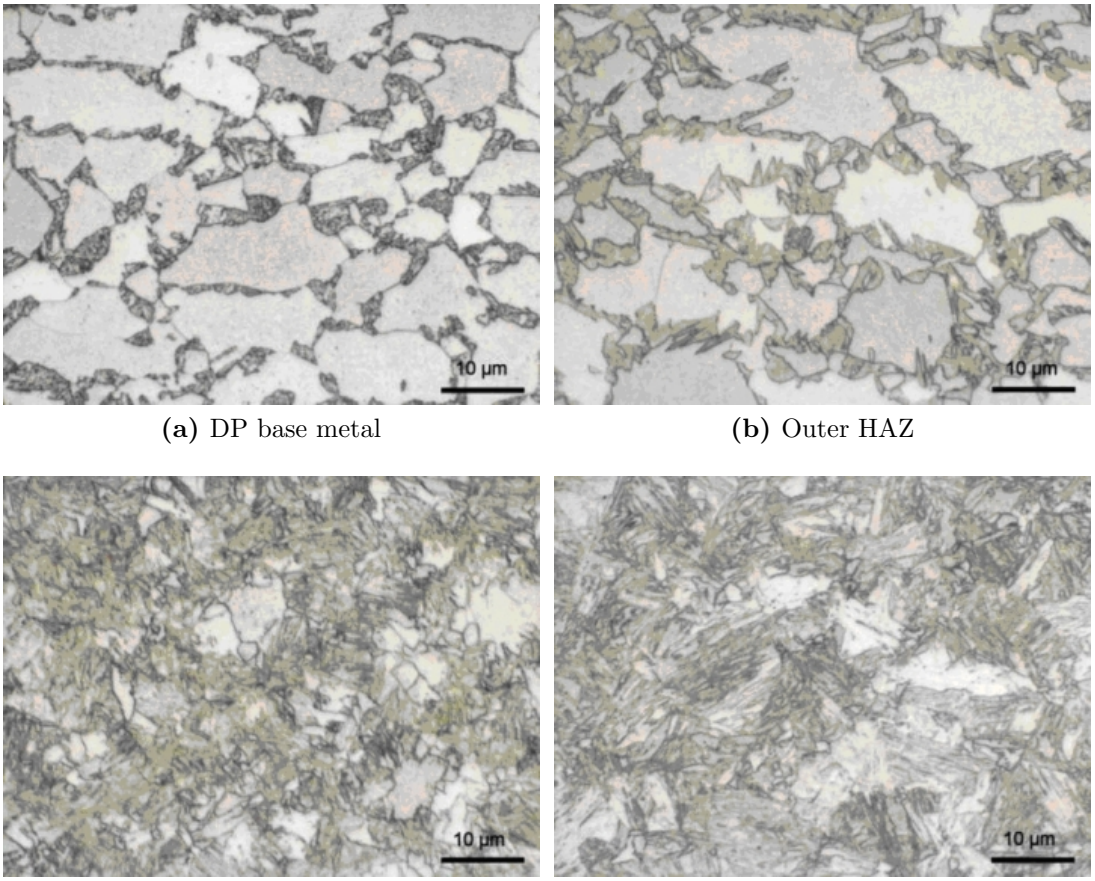

(a) DP base metal **(b)** Outer HAZ

(c) Inner HAZ **(d)** Weld zone close to HAZ

Figure 7.15: Nital etch of TRIP-DP microstructure - the DP side

of the lamellas increases corresponding to a higher temperature close to the weld and therefore the austenite grains, from which martensite are formed, are larger.

Before characterisation of the TRIP-DP weld nugget, the HAZ of the TRIP side is described. The HAZ of the TRIP is shown in the four micrographs in figure 7.16 on page 178. No BM image is included here but the TRIP BM can be seen in figure 7.6 and figure 7.12a. Figure 7.16a show the HAZ closest to the BM. Here, the dark areas are increased compared to the BM (in figure 7.6). As described in section 7.4.4 it is most likely martensite which is formed in the TRIP HAZ since the carbon content is significantly higher in TRIP (0.3 wt%) compared to the average of TRIP and DP (0.08 wt%) where martensite was measured in the weld nugget using diffraction (section 7.3). Approaching the weld the morphology of the dark areas become clearer and the lamella structure is easier seen. Residual ferrite is seen in figure 7.16c indicating that complete transformation has not oc-

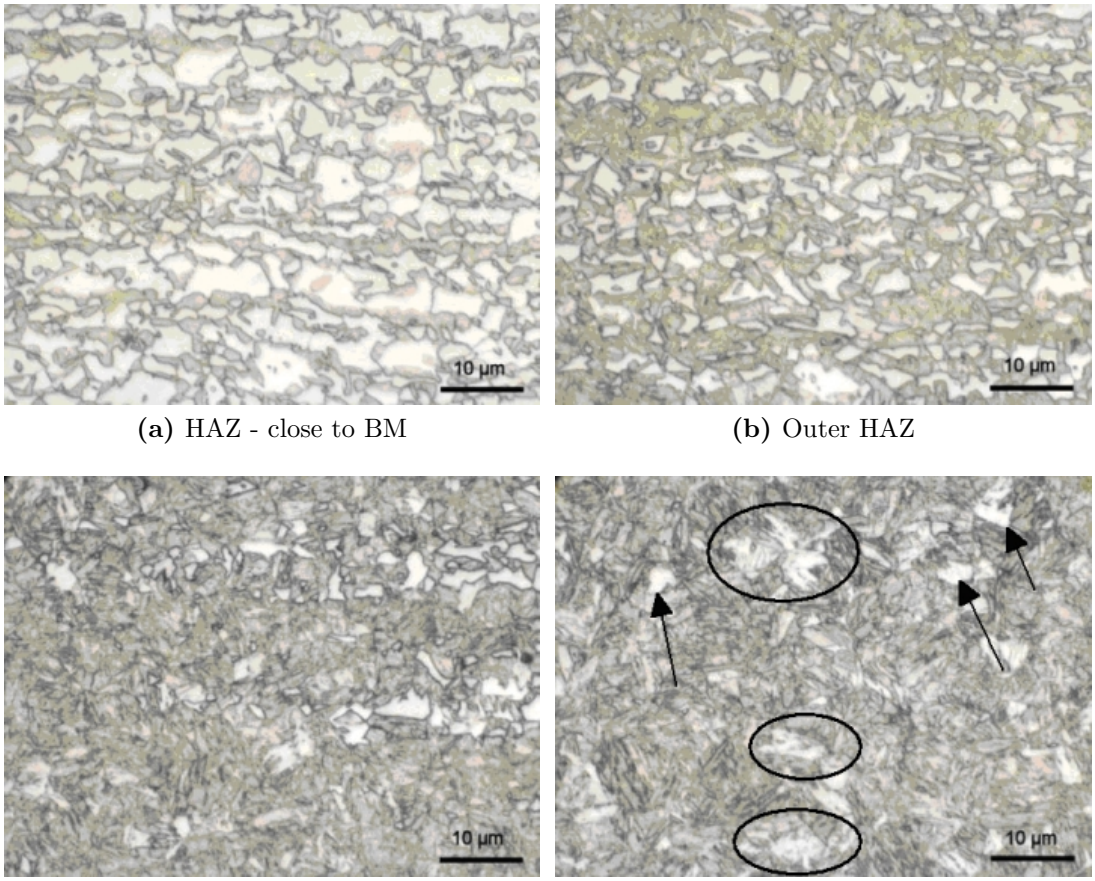

(a) HAZ - close to BM

(b) Outer HAZ

(c) Inner HAZ

(d) Weld zone close to HAZ

Figure 7.16: Nital etch of TRIP-DP microstructure - the TRIP side

curred yet whereas in figure 7.16d ferrite is almost absent. The few ferrite grains still present are marked with arrows in figure 7.16d, however, it is also possible that these grains are residual austenite. Some other bright grains are observed in figure 7.16d which are marked with circles. These grains are assumed to be massive transformations of ferrite as the structure is comparable to massive ferrite as already observed in the TRIP-TRIP weld nugget in figure 7.13. The difference between the ferrite/austenite grains and the massive ferrite is mainly seen as the shape and homogeneity of the grains. The ferrite/austenite grains are homogeneous and have a rather rounded shape whereas the massive transformed ferrite has a more angular shape with structure inside the grains. The massive ferrite grains were not observed in the TRIP HAZ in TRIP-TRIP (figure 7.12) but it is possible that small bright grains are early transformed massive ferrite.

Microhardness measurements are performed with the same procedure as described in section 7.4.3 to investigate the hardness profile in the TRIP steel in a TRIP-DP weld. The material has been etched using the Modified LePera and the profile is taken from the TRIP-side of the joint. The results are shown in figure 7.17. The hardness of the base material is approximately 250 HV50g. After $X = 0.2$mm the hardness clearly starts to increase but with a slightly smaller gradient than for DP (c.f. figure 7.10). The maximum level of the hardness around 500 HV50g is comparable with literature [117]. From the HAZ to the weld the hardness decreases slightly. This is due to the mixing of the two steel alloys which produces a hardness level in the nugget between the hardness levels of welded TRIP and welded DP joints. The HAZ corresponds to the interval from $X = 0.2$mm to 0.9mm and it is clear that the hardness decreases immediately when reaching the weld where TRIP and DP is mixed up during melting.

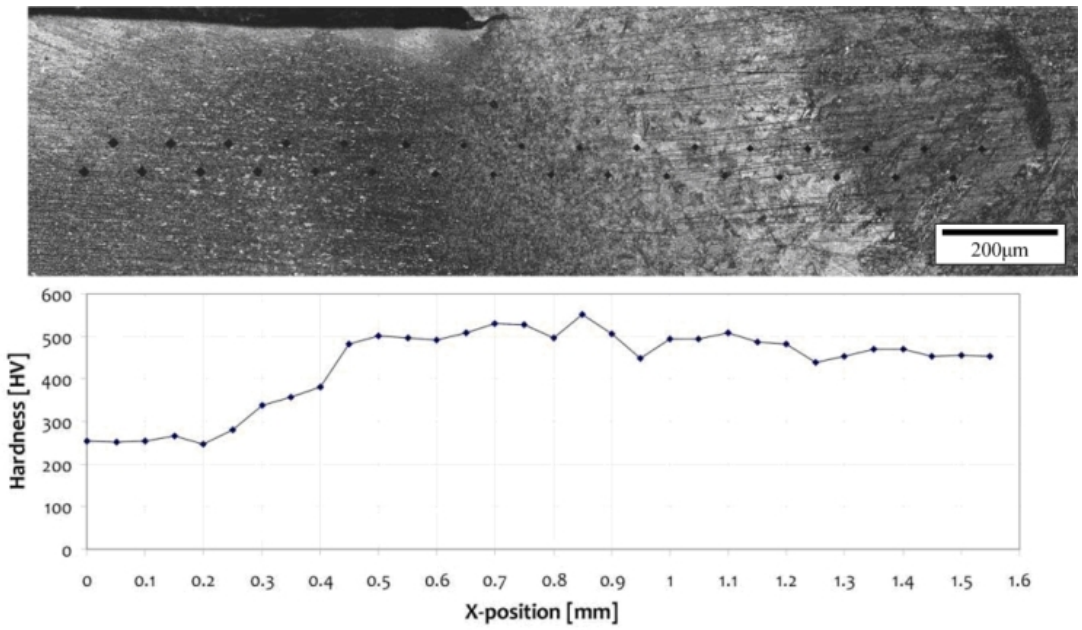

Figure 7.17: Microhardness profile of TRIP-DP weld (TRIP side). Indentation force is 50g

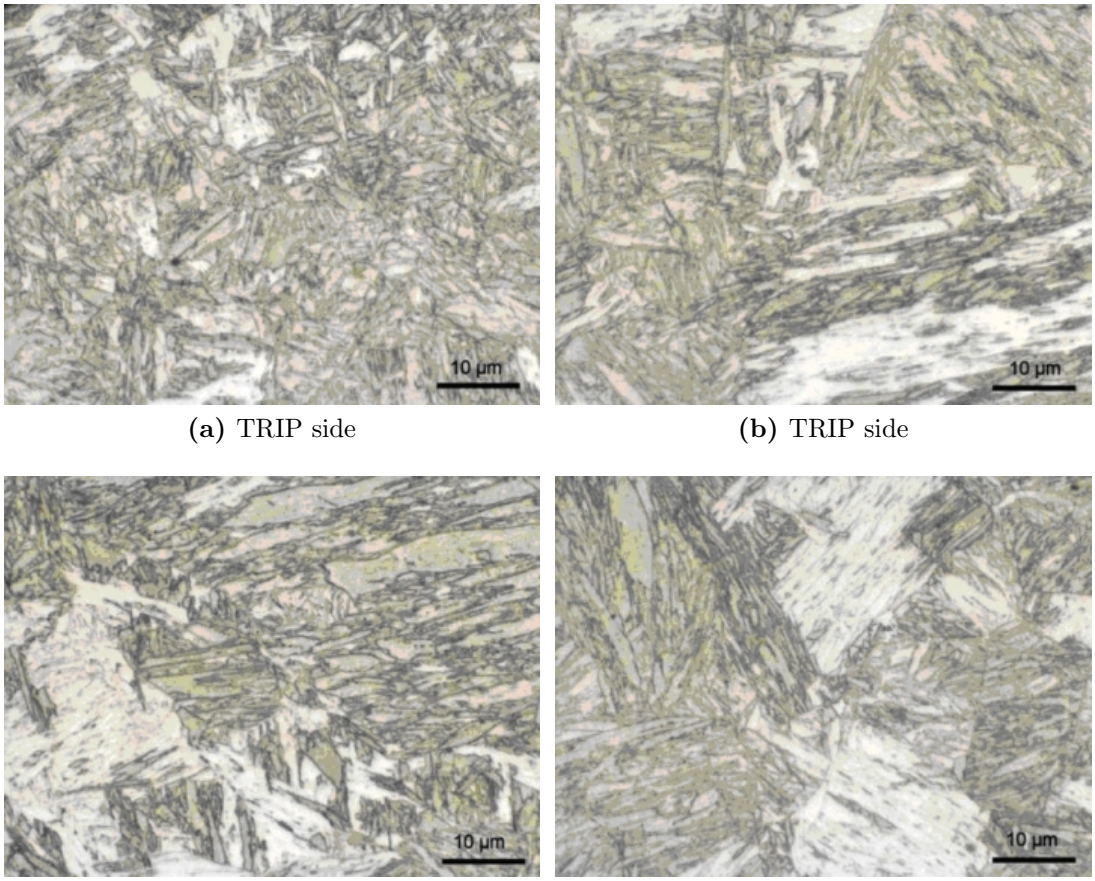

(a) TRIP side **(b)** TRIP side

(c) DP side **(d)** DP side

Figure 7.18: Nital etch of TRIP-DP weld nugget microstructure showing former TRIP and DP sides of the weld

Microstructure of the weld nugget in TRIP-DP is shown in figure 7.18. The images are divided into those areas which were originally TRIP (figure 7.18a - 7.18b) and DP (figure 7.18c - 7.18d) before welding. It is noted that the lamella structure generally is larger in the former DP side than in the TRIP side of the nugget. Large bright areas are also observed in the weld in both sides and this is assumed to be massive ferrite as previously observed in the weld nugget of both DP-DP and TRIP-TRIP (figure 7.8 and figure 7.13). It is furthermore observed that in the former DP side of the weld the massive ferrite grains are significantly larger than in the TRIP side. This is attributed to a likely difference in cooling rate during welding.

The sheet thickness of the DP steel is larger than the TRIP. This implies that the weld zone in the TRIP steel is closer to the electrodes during welding, which increases the cooling effect from the copper electrodes. Therefore, the massive

transformation may be favoured in DP rather than in TRIP. The difference in sheet thickness is assumed to be the primary reason for the different size of the massive ferrite grains in the weld nugget. The carbon content will normally be expected to play a role in the massive transformation, but the carbon content is expected to be similar in both sides of the weld nugget because the weld nugget is assumed to be fully mixed up during welding.

Another difference between the former TRIP and DP side of the weld nugget is the size of the martensite lamellas. The martensite lamellas are slightly larger in the DP side than in the TRIP side. This is probably related to the thickness of the sheet and the lower cooling rate in the DP side. When a lower cooling rate is present, the austenite grains are stabilised for a longer duration at high temperature and have grown larger. As a result, the martensite lamellas will also become slightly larger.

The microstructure in the TRIP-DP weld is also thoroughly investigated in TEM. Simultaneously diffraction of the various structures was performed as described in section 7.3. The weld was examined on the former TRIP side as well as the DP side, but since no differences were observed no distinction between the two sides will be done in the following descriptions. In figure 7.19 on page 182 several TEM images are shown. The images in figure 7.19a and 7.19b have a typical lath martensite appearance [118]. However, in figure 7.19b there is a tendency of some lamella to appear like bainite with carbide platelets aligned inside the lamellas (marked with an arrow). Since bainite is not identified in any diffraction pattern there is only a minor possibility of any bainite to be present in figure 7.19b. It is possible that the lamellas are twinned martensite, and this is also possibly the explanation to the structure in figure 7.19f, which appears like twinned martensite. In figure 7.19c and 7.19d large grains of irregular shape are observed which are most likely massive ferrite. Diffraction does not give any concluding information on this, but this cannot be expected due to the very close-related lattice of martensite, ferrite and massive ferrite. In figure 7.19e a magnified view of some large martensite lamella is seen. Inside of the lamella many small particles or what appears like particles can be observed. Since no other phases are identified with diffraction in these areas it can be concluded that they are neither carbides nor another phase. In certain points (marked with arrows) small lamella are observed and which are most likely twins.

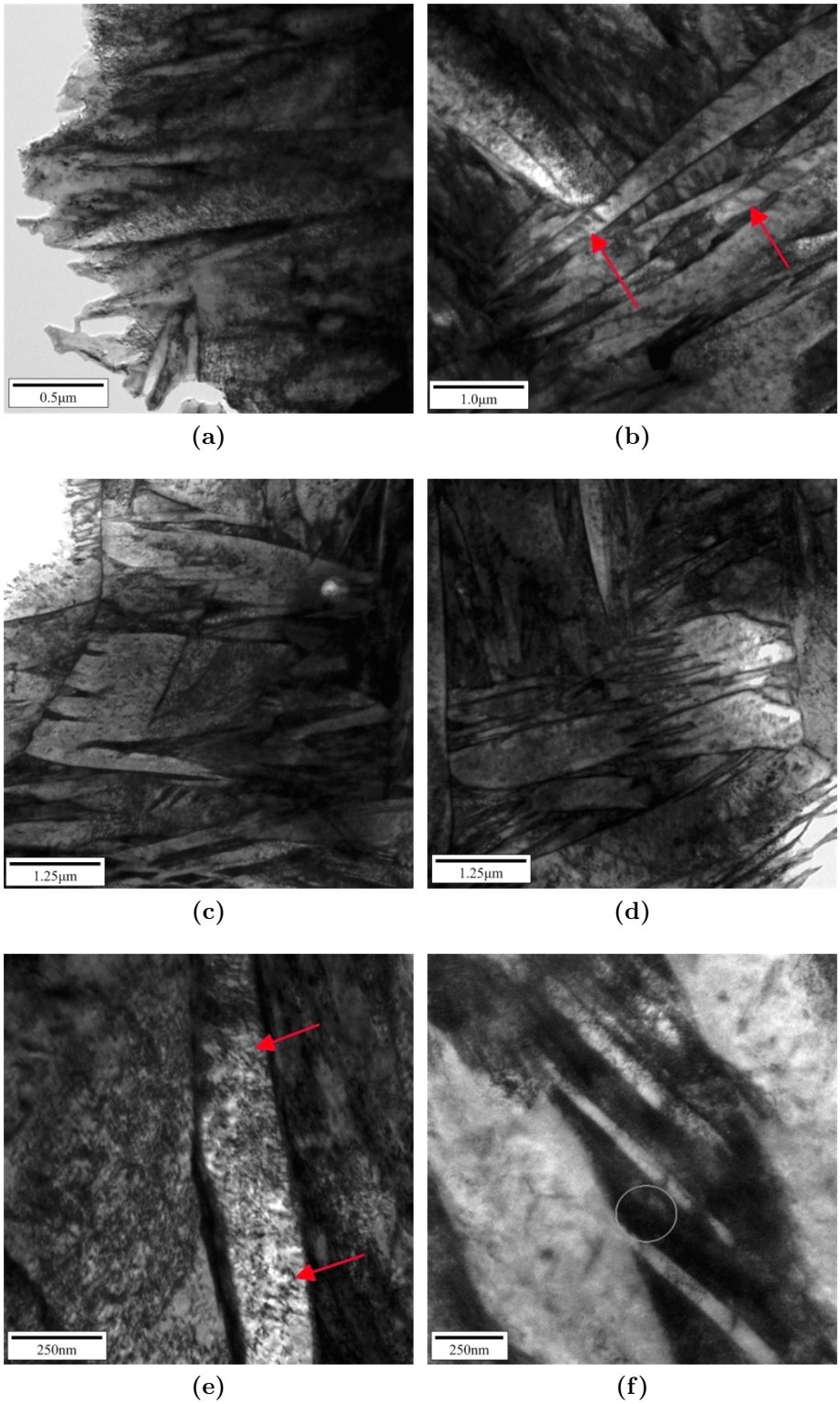

(a) **(b)**

(c) **(d)**

(e) **(f)**

Figure 7.19: TEM micrographs of TRIP-DP weld nugget

7.5 Comparison with Literature

From diffraction of phases in the TRIP-DP weld it was found that martensite is the only phase present in the weld. From the morphology examination it is desired to verify this statement. The descriptions of the morphology from figure 7.19 indicate that laths martensite is the main constituent and that massive ferrite is probably present. Comparison with literature will be done in the following.

In figure 7.20 are shown two TEM images from Zhang and Kelly [119] showing typical morphology of bainite. Cementite laths are clearly seen in figure 7.20b

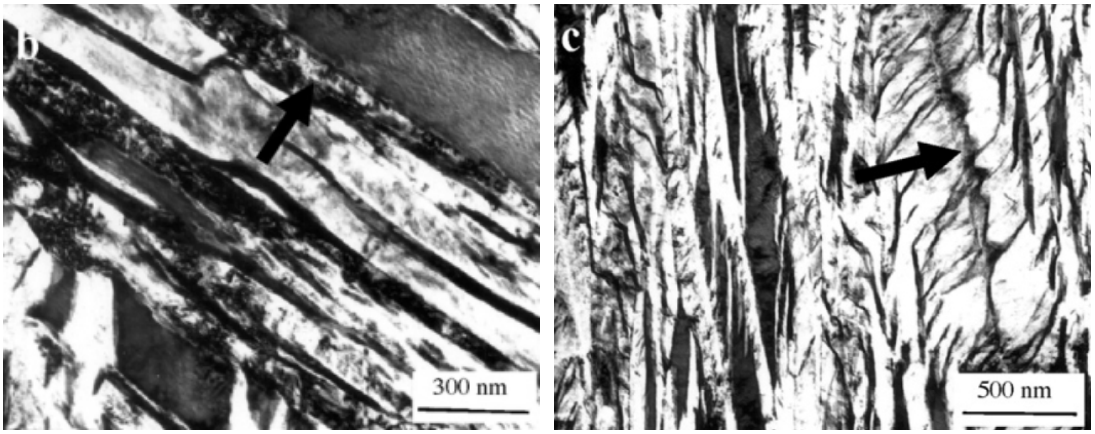

(a) **(b)**

Figure 7.20: TEM micrographs showing (a): Upper bainite, (b): Lower bainite [119]

and comparing these laths with the observed lamellas in figure 7.19 it is clear that the lamellas observed in this study are *not* cementite laths in a bainite structure. This confirms the diffraction analysis where no bainite was found. Another study by [103] uses TEM to investigate the morphology of water-quenched HSLA-80 steel (0.05wt% C), which is comparable to DP steel. From the images of the microstructure in figure 7.21 they identify (a): lath martensite, and (b): bainite, which is confirmed by diffraction measurements [103]. The morphology of the martensite laths is comparable with the morphology observed in this study. Bainite is identified as the structure in figure 7.21b and this type of morphology cannot be recognised from our study. Furthermore, diffraction from the bainite observed by Das et al. [103] clearly indicate two phases (c.f. figure 7.3) which was not found in any of the diffraction analysis in this study.

Babu et al. [120] investigates lath martensite using TEM and images from their work are shown in figure 7.22. The martensite laths in the two images have different size corresponding to the temperature from which they are quenched. The austenite

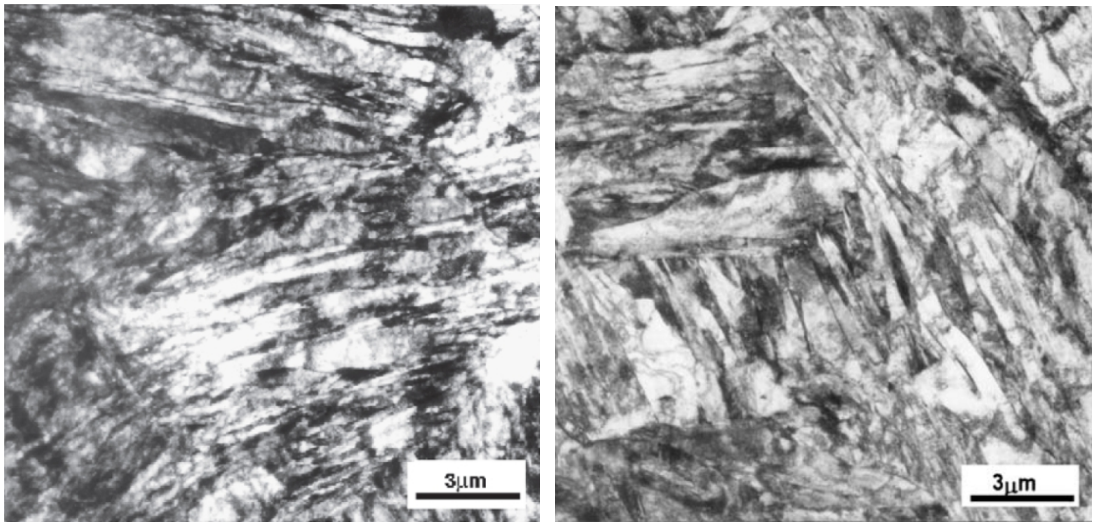

(a) Lath martensite **(b)** Bainite

Figure 7.21: TEM micrographs of water-quenched HSLA steel (0.05wt% C) [103]

grains will be large at high temperatures which result in large martensite laths and smaller for martensite from austenite at lower temperatures. This was also found in this study where the martensite laths are increasing in size when approaching the weld from the HAZ. Furthermore, as observed in figure 7.22a, and marked with a red circle, some lamellas are seen inside the large martensite lath which is found to be twins [120]. These lamellas are comparable to the lamellas observed in figure 7.19b and it confirms the presence of twins in this study. It also rejects the hypothesis that the observation was bainite in figure 7.19.

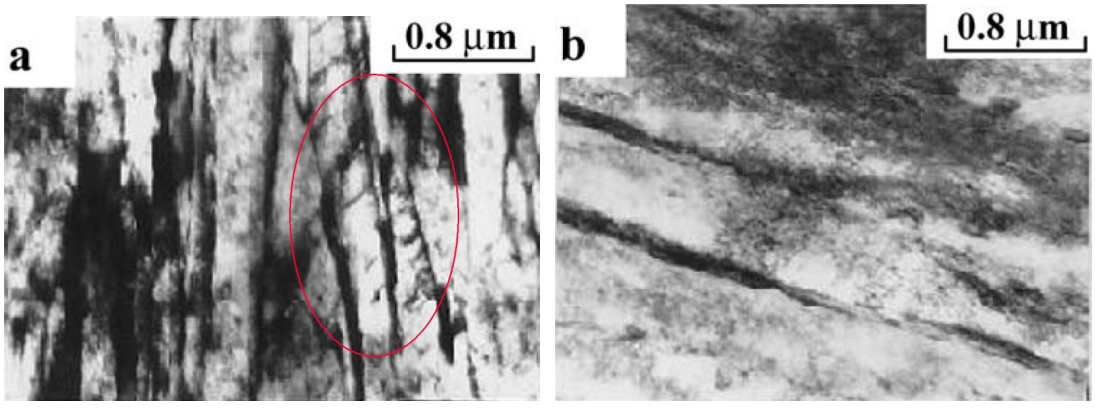

(a) **(b)**

Figure 7.22: TEM micrographs of low alloyed carbon steel (0.29wt% C) oil-quenched from (a): 925°C, (b): 1100°C [120]

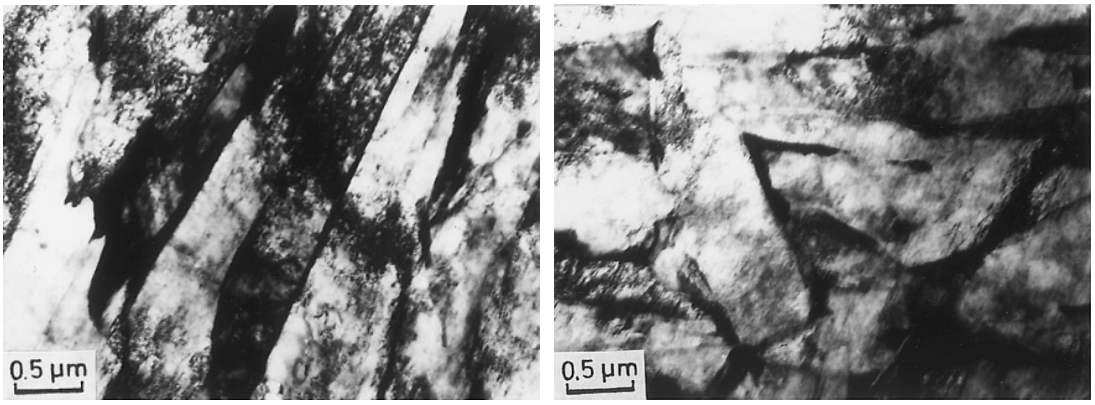

(a) **(b)**

Figure 7.23: TEM micrographs of arc welded low alloyed carbon steel (0.04wt% C) showing (a): martensite laths, (b): massive ferrite [121]

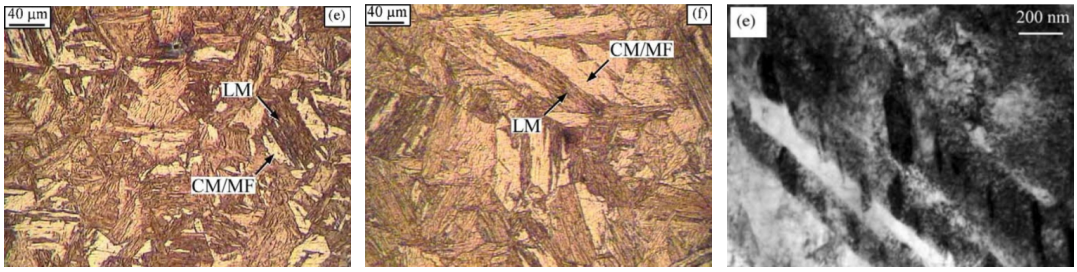

(a) **(b)** **(c)**

Figure 7.24: Optical micrographs of micro alloyed low carbon steel (0.08wt%) annealed at $1150 - 1250°C$ for (a): 4min and (b): 30min, and (c): a TEM image of 7.24b showing martensite twins [116].(LM: lath martensite, CM: coarse martensite, MF: massive ferrite)

Dhua et al. [121] investigates arc welded low carbon steel (0.04wt% C) using TEM and images are shown in figure 7.23. The appearance of the martensite lamellas (non-homogeneous structure) is comparable with the non-homogeneous structure of some martensite lamellas observed in this study (figure 7.19e). Furthermore, massive ferrite is observed by Dhua et al. [121] in figure 7.23b and the irregularity of this phase is comparable to the results in figure 7.19c and 7.19d. This indicates that the low carbon content (0.04wt%) will enhance the massive transformation in the steel [121]. Massive ferrite is also observed by Poorhaydari et al. [116] where another low-carbon steel (0.08wt% C) is investigated. Images are shown in figure 7.24. The optical micrographs in figure 7.24a and 7.24b are very comparable with the results with a lamella structure with large equiaxed grains of irregular shape found in this study. It was found to be martensite and massive ferrite.

Poorhaydari et al. [116] also observe lath martensite and twins which are confirmed by diffraction. The large bright grains are explained to be either massive ferrite or coarse martensite [116].

7.6 Discussion of Methods

7.6.1 Etching

In general Nital etching was found to be best suited for DP BM whereas the Modified LePera etch better shows the more complex microstructure in TRIP BM. In the HAZ and WN of both DP and TRIP the Nital etching is in general the most suitable method. Nital clearly shows the features of the microstructure in the HAZ and WN. Furthermore, the etching results are repeatable and not sensitive to colour differences as the Modified LePera etchant is. The advantage of the Modified LePera etch is its ability to show different phases due to different colours and contrast. However, the colour and contrast changes are not only related to different phases but are also influenced by residual stresses in the grains or grain orientation. With the Modified LePera etch the colouring of the grains is affected by many different factors and therefore the colours are not completely reliable. Furthermore, the details are sharper in a microstructure etched with Nital and therefore Nital is recommended for HAZ and WN of both steels. For DP BM the Modified LePera etch was not suitable since the morphology becomes significantly different from the Nital etched microstructure seen in figure 7.5. SMB etching is expected to be purely tint etching and therefore grain boundaries should not be etched and not clearly visible. However, in figure 7.25 the microstructure of TRIP BM is seen after SMB etching and the grain boundaries are clearly revealed after the tint etching.

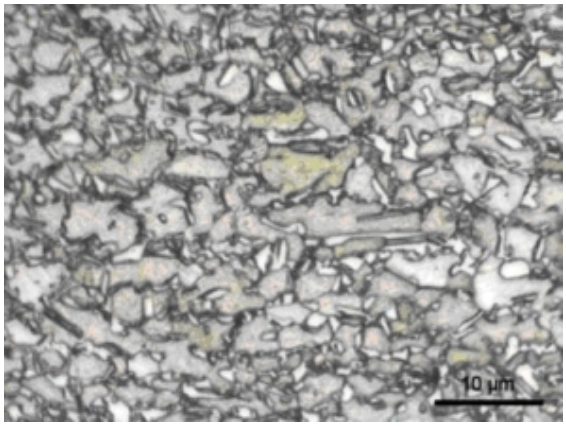

Figure 7.25: TRIP base metal SMB etched

It is possible that the mechanical polishing has influenced the material so that the harder phases protrude from the softer phases. If this effect occurs for TRIP BM in combination with the tint etching, the grain boundaries are revealed simultaneously with grains appearing in different colours. This is most likely the reason for the visible grain boundaries in figure 7.25. In general, the SMB etching gives rather unambiguous results because the colours vary a lot. This concerns BM as well as HAZ and WN. The only application where SMB could be very useful is to reveal austenite in a welded microstructure that also contain other phases like martensite. This is because austenite is the only phase which is seen as completely white after SMB etching. This was found in figure 7.14.

The Modified LePera etchant has shown to be very effective in revealing all phases in TRIP BM. However, by checking the reliability of the technique it was found that the results varied. In figure 7.26 is seen the microstructure of TRIP BM etched with the same Modified LePera technique, but the results are not completely similar. The large ferrite grains are bright in both images but the contrast of the small grains is different in the two images. The contrast difference between the small grains is exactly what is unique for the Modified LePera etching technique because bainite, austenite, and martensite can be distinguished. In figure 7.26a the contrast difference between the small grains is very large whereby bainite, austenite, and martensite can be distinguished. However, in figure 7.26b which is obtained by the exact same procedure on the same sample the contrast difference in the small grains are not quite as significant as in figure 7.26a. The conclusion is thus that the repeatability of the technique is poor.

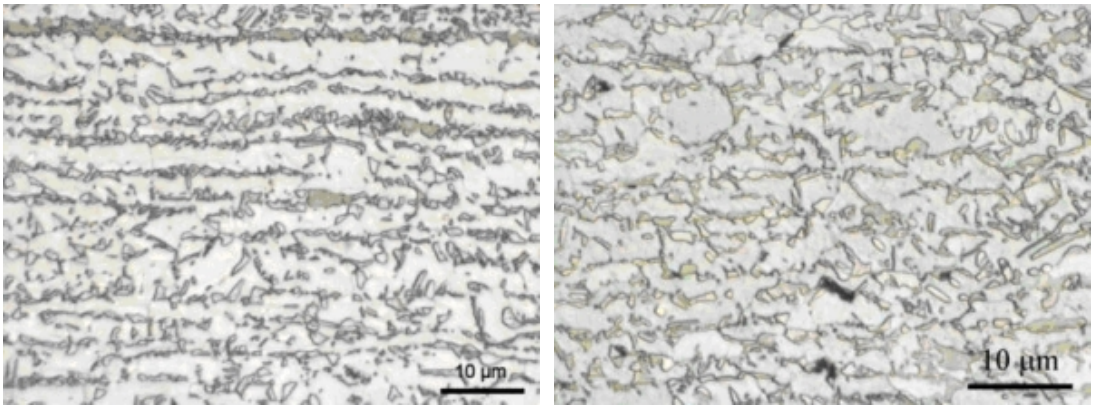

(a) **(b)**

Figure 7.26: TRIP base metal etched with Modified LePera etch resulting in two different results (a) and (b).

In literature the result of the Modified LePera method is reported to be much better in revealing all phases in TRIP compared to what was found in this study (c.f. figure 7.6) [97]. In figure 7.27 is shown the microstructure of TRIP steel after etching with a Modified LePera etchant done by De et al. [97]. Martensite is

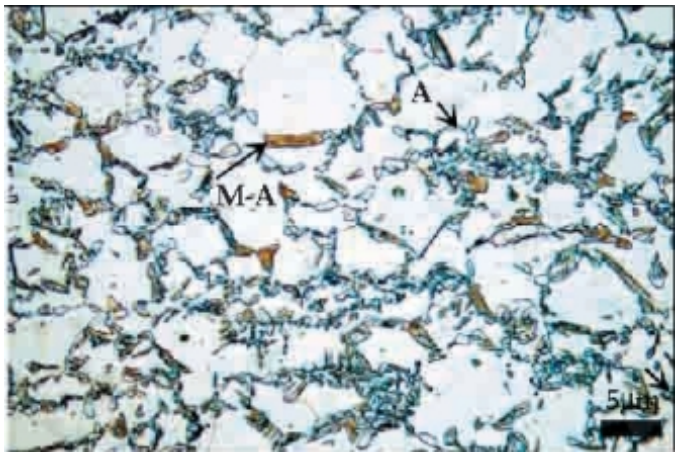

Figure 7.27: TRIP steel etched with Modified LePera etch by De et al. [97].

clearly identified in figure 7.27 as the straw-coloured phase which was not found in this study. Efficient use of the Modified LePera etchant might require more experimentation to achieve more consistent results.

7.6.2 LOM

The main challenge with LOM in this study is the resolution. The resolution is too low to clearly reveal the detailed microstructure of TRIP and DP steels. Another problem associated with the LOM is the contrast of the tint etched samples. When using high magnifications the colour sharpness becomes poor since the amount of wavelengths seen in an image is significantly reduced. As a result, identification of phases based on the tint etching technique was found to be difficult.

7.6.3 Diffraction

It was possible from diffraction to determine that the crystal structure was not pure BCC but rather BCT. However, large uncertainties of the methods rejected the possibility of determining the carbon content of the martensite. Comparing the results in table 7.6 obtained from the diffraction measurements with the preliminary estimates in table 7.5 calculated from the nominal composition values there is a relatively large difference in the estimates of a and c. Based on the nominal composition values the distortion of the BCC lattice should be much less than what is measured. Why is this so? The primary reason is supposedly the large

influence of the measuring uncertainty on the estimate of c. As shown previously even small errors in the measurements of spot radius can results in large errors in the estimates of c and a. The conducted investigation has shown that it is not possible to estimate the carbon content from the measured diffraction pattern without a significant amount of uncertainty. The uncertainty is so large that no reasonably conclusions can be made regarding the actual carbon content. However, it is believed that the results strengthen the hypothesis that the lattice indeed is BCT because the majority of the measurements indicate that the lattice parameter c is larger than a.

7.7 Conclusion

The three zones (BM, HAZ and WN) in the welded DP and TRIP steel have been investigated using different material characterisation techniques. The base material of the DP steel was found to consist primarily of ferrite grains surrounded by small areas of martensite. A small amount of areas resembling pearlite structure was noted, but the presence of pearlite could not be confirmed. In the HAZ of the DP steel the ferrite grains had been transformed to a supposedly martensitic structure which greatly increased the hardness of the material. Due to the relatively low carbon content (0.08wt% C) it cannot be precluded that the highly irregular and lamella structure also consists of some bainite.

The base material of the TRIP steel has a much finer microstructure than the DP steel. It was found to consist primarily of ferrite surrounded by austenite, bainite and possibly some martensite. When entering the HAZ the ferrite grains disappear at the expense of martensite and/or bainite which can be seen by the hardness increase of the material. It is concluded that martensite is the phase formed in the TRIP HAZ since the carbon content is high enough for martensite to be formed in this zone. Martensite was confirmed in the TRIP-DP WN which has a lower carbon content (0.18 wt%) than the TRIP steel alone (0.3 wt%) and it is thus likely that martensite is formed in the TRIP steel due to the higher carbon content.

The WN of the three different material combinations (DP-DP, TRIP-TRIP and TRIP-DP) had a very similar appearance. In the WN the material has been melted and then cooled down very rapidly. Upon solidification the initial microstructure is assumed to be austenitic. The very fast cooling favours a diffusionless phase transformation. The morphology of the WN is dominated by a lamella lath-martensitic structure together with relatively large irregular grains. TEM measurements confirm the microstructure to contain only martensite and not bainite. The irregular grains are supposedly massive ferrite, which is supported by hardness measurements and similar findings in literature. Furthermore, it is noted that the amount

of irregular grains in the DP side of a TRIP to DP weld is smaller than in the TRIP side. This is argued to be due to the unequal thickness of the sheets, thereby decreasing the cooling rate in the DP side of the weld. This corresponds well with the fact that massive ferrite forms at a lower cooling rate than the rate promoting martensite.

From the measured diffraction patterns it was attempted to estimate the carbon content of the alloy based on the distortion of the BCC lattice. It was found to be extremely challenging to get reliable results using this method and the measurement uncertainty was consequently too large to estimate the carbon content with a reasonable error margin, especially with the small amounts of carbon present in the alloys used in this work.

Nital etching was found best suited for DP BM whereas the Modified LePera proved more capable of revealing the more complex microstructure in TRIP BM. In HAZ and WN of both DP and TRIP the Nital etching was found to be the most suitable method.

Chapter 8

Three Sheet Spot Welding of AHSS

The automotive industry is constantly seeking for product and production optimisation. Resistance spot welding is a key technology in automotive assembly production. The process is fast and can easily weld many different material combinations which are difficult or even impossible to join by other welding techniques. The development of new advanced high strength steels (AHSS) for use in the automotive industry represent new challenges to the resistance welding of these steels. These new steel types are often used in supporting parts of the car and in parts which are designed to absorb the impact of a crash. The parts are typically joined to considerably thinner and softer low carbon sheet materials that act as the outer panels of the car.

The weldability of different AHSS in two layer lap joints has been investigated by several authors [45, 48, 49, 122]. Problems due to formation of hard martensite phases during the rapid cooling after welding increase the risk of brittle fracture of the joints. Joining of three sheets by resistance spot welding is an increasing trend in automotive assembly. Compared to two sheet spot welding, joining of three sheets is significantly more complicated because an extra interface is introduced. The use of different material combinations and different sheet thickness in the three layers complicate the process even further. Three layer joining of a thin low carbon steel sheet to two thicker high strength steels is a weld presenting large challenges and yet it is of increasing importance in car manufacturing.

When resistance spot welding three sheets the joint has two sheet-to-sheet (S/S) interfaces with positions relative to each other and to the electrodes depending on the individual sheet thicknesses. If one of the outer sheets is considerably thinner than the other two sheets, the interface between this and the centre sheet is located closer to the neighbouring electrode than the other interface. In this case the large heat conduction to the electrode creates an asymmetric heat distribution

causing problems achieving a successful weld. If the heat input is too small the nugget will not develop in the thinner sheet and the weld will be unsuccessful. If the heat input on the other hand is too large splash is often observed between the two thicker sheets. In some cases this implies unsatisfactory weld strength.

It is difficult to achieve the optimum parameter settings for such a joint and the robustness of the process might be poor and highly influenced by stochastic variations. When welding high strength steels the electrode force required to avoid splash is often high because of the high hardness of the steels. But when spot welding two layers of AHSS with a third layer of soft low carbon steel, the latter will typically experience significant electrode indentation due to the high load which in many cases is unacceptable for aesthetic reasons.

The present work deals with the weld mechanism and weldability of three layer spot welding of thin low carbon steel sheets to HSLA and AHSS sheets investigating different material combinations. The present work reflects spot welding with common conventional welding equipment. The objective is to study the influence of the main parameters on weld strength and nugget development in order to improve the understanding of the problems involved in three sheets spot welding and to estimate optimum welding parameters. Factorial experimentation is used to design and analyse the experiments with respect to the weld strength. Furthermore the nugget size and resulting bond type has been investigated. To investigate the possibility of simulating this problem, the experimental results are compared with numerical simulations.

8.1 Experimental

8.1.1 Experimental Procedure

Experiments were performed on a TECNA 8105 AC welding machine with a TE-180 weld controller. The electric system can deliver up to 85kA with 50Hz. The actual current was measured using a Rogowski coil together with a pre-calibrated TECNA-1430 conditioner. The mechanical system is pneumatically driven and can deliver up to 20kN weld force. The actual load during the welding process was measured using a piezo electric force transducer. The electrodes used were d=20mm and d=16mm ISO type B CuCrZr with tip diameters of d=8mm and d=6mm, respectively. During welding splash was recorded both visually and by observing irregular fluctuations in the measured weld force. The materials available for the investigation are listed in table 8.1 indicating sheet thickness as well as nominal composition. They include two types of advanced high strength steels (DP600 and TRIP700), a high strength, low alloyed steel (HSLA 340) and a low

Table 8.1: Specification of materials

Material	Supplier	Thk.	Coating	Nominal composition [wt%]						
		[mm]	[μm]	C	Mn	Cr	Si	P	S	Al
DP600	SSAB	1.5	-	0.08	0.9	-	0.4	0.015	0.002	0.04
HSLA340	SSAB	0.8	-	0.05	0.4	-	0.01	0.01	0.01	0.04
DC06	SSAB	0.6	-	0.002	0.15	-	-	0.01	0.01	0.04
TRIP700	ThyssenKrupp	1.2	Zn: 14	0.29	2	0.6	0.3	0.4	0.01	0.24

carbon steel (DC06). The sheets were cut into samples of 25x100mm and welded according to the set-up shown in figure 8.1. Reference code to a specific three sheet weld combination is abbreviated *sheet1-sheet2-sheet3* as for instance DC06-HSLA-TRIP, where the first mentioned material is the top sheet. In all experiments the top sheet is the thin, low carbon steel, while the two others vary.

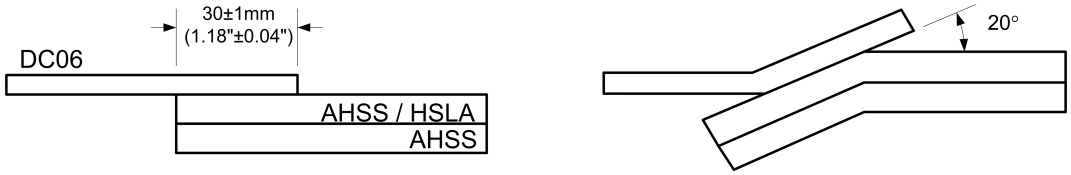

Figure 8.1: Specimen alignment during welding (left) and before tension shear testing (right)

The weld strength was tested in tension shear tests on a 100 kN Amsler universal testing machine. The sheet samples were bent 20 degrees prior to testing, as shown in figure 8.1, in order to ensure a uniform test condition. Testing was carried out by pulling the thin, low carbon steel sheet apart from the two high strength steels.

The influence of RMS current I, electrode force F and weld time in cycles T on the weld strength was investigated. Furthermore the effect of increasing tip diameter of the bottom electrode B from d=6mm to d=8mm was studied. No up- or down-slope of the current or force were used. The experimental investigations were designed as unreplicated 2^k full-factorial designs with $n_C = 3$ centre points. This design was chosen in order to get an overview of the influence of the main parameters as well as possible interactions on the quality of the weld. The centre points were used to estimate the variability due to stochastic error in the experiments. The experiments were divided into seven series. The first three series investigate welding of DC06 to HSLA as the middle sheet and either DP600 or TRIP as the bottom sheet. The four last series investigate welding of DC06 to DP600 and TRIP in the four possible combinations. An overview of the different weld series are given in table 8.2 and the factorial plan is given in table 8.3.

Series no. 1 and 2 were carried out as initial studies to test the overall weldability of DC06 to HSLA and AHSS. Furthermore the influence of increasing the size of the bottom electrode was included in these series. Based on the first two series the third series was carried out with identical process parameters for the two material combinations and using larger bottom electrode, d=8mm tip. The four last series no. 4-7 were made to increase complexity of the welding process even further by introducing AHSS next to DC06 in different combinations, but keeping the weld parameters the same for all combinations.

Performing the weld series 1-7 the weld current was entered on the control unit according to the values in table 8.3. Measurements of the actual RMS weld current showed this to be significantly lower than the prescribed current on the controller. This is due to the fact that the total resistance in the secondary circuit influences the actual current delivered by the machine. In the simulations the measured RMS value of the current is used and not the set value on the controller shown in table 8.3.

Table 8.2: Sheet combinations in the weld series

Series	**Three sheet combination**				
1	DC06	-	HSLA	-	DP600
2	DC06	-	HSLA	-	TRIP700
3	DC06	-	HSLA	-	*DP/TRIP*
4-7	DC06	-	*DP/TRIP*	-	*DP/TRIP*

Table 8.3: Overview of factorial investigation

	Current I - [kA]		**Force F - [kN]**		**Time T - [cycles]**		**Electrode B - [mm]**		**Material M**	
Series	Low	High	Low	High	Low	High	Low	High	Low	High
1	8	10	3	4	10	14	6	8	-	-
2	6	8	3	4	8	12	6	8	-	-
3	7	9	3	4	6	12	-	8	TRIP	DP
4-7	8	10	3	4	12	20	-	8	-	-

8.1.2 Numerical Procedure

The numerical software SORPAS was used to simulate the process of three layer spot welding. The program utilises the flow formulation in the mechanical analysis which is coupled to an electrical and a thermal model and updated throughout the analysis. The analysis relies on the material data inserted in the model. The stress-strain curves for varying temperatures of the low carbon steel DC06 and the two high strength steels DP600 and TRIP700 were determined by hot tensile testing as described in chapter 2. The electrical properties and the stress-strain-temperature curves for HSLA were taken from SORPAS own material database. A minimum of 2 elements in the thickness direction of the sheets were used and the time step was set to 0.2ms.

8.2 Results and Discussion

8.2.1 Weld Strength

In practically all the tension-shear tests the failure mode was identified as fracture in the base material of the low carbon steel, with subsequent nugget pull-out/tearing of the parent steel sheet. Only for the very weak welds the failure mode was interface failure between the low carbon steel and the high strength steels.

In tables 8.4, 8.5 and 8.6 on the next page the ANOVA tables of the reduced, fixed effects models for the experimental series 1 to 3 is collected employing the procedures described by Montgomery [88]. The significance level was chosen to be 2.5% and hence factors with a significance level larger than 2.5% were dropped from the model, and their sum of squares (SS) were pooled in the residual SS. The significance level (Prob.>F_0) for each significant factor and factor interaction is listed in table 8.4-8.6, together with the calculated sum of squares and its degree of freedom (DF)[1]. All factors only have two levels and hence all factors have one degree of freedom. The mean square is calculated and the F_0 ratio between factor mean square and the mean square of the total experimental variability (the residual) is calculated. Using the F distribution the null hypothesis is tested and the probability that the variance in the experimental data is caused by stochastic error alone and not by the variation of the factor levels is calculated. A low probability therefore implies that the factor or factor combination has a significant effect on the strength of the welds. The sum of squares of the residual consists partly of pure error calculated from the three centre point repetitions and partly of the sum of squares from the insignificant factors which is dropped from the model. Finally

[1]Factor abbreviations are listed in table 8.3.

Table 8.4: Series 1: DC06-HSLA-DP600 - ANOVA analysis

Factor	**SS**	**DF**	**MS**	$\mathbf{F_0}$	**Prob.** $> \mathbf{F_0}$
B	228711.1	1	228711.1	63.2	<0.00%
BF	32052.64	1	32052.6	8.9	1.07%
BT	48719.53	1	48719.5	13.5	0.28%
Residual	47027.37	13	3617.5		

Table 8.5: Series 2: DC06-HSLA-TRIP - ANOVA analysis

Factor	**SS**	**DF**	**MS**	$\mathbf{F_0}$	**Prob.** $> \mathbf{F_0}$
F	39951.5	1	39951.5	46.1	<0.00%
T	58356.7	1	58356.7	67.4	<0.00%
I	83041.2	1	83041.2	95.9	<0.00%
Residual	20839.6	13	1603.0		

Table 8.6: Series 3: DC06-HSLA-DP/TRIP - ANOVA analysis

Factor	**SS**	**DF**	**MS**	$\mathbf{F_0}$	**Prob.** $> \mathbf{F_0}$
M	29052.8	1	29052.8	9.5	0.80%
F	30748.9	1	30748.9	10.1	0.67%
T	56010.9	1	56010.9	18.4	0.07%
I	59547.6	1	59547.6	19.6	0.06%
Residual	42631.6	14	3045.1		

the overall mean weld strength and standard deviation is given in table 8.7 as well as the values of the centre point itself.

To illustrate how the models were reduced using a significance level of 2.5% the iteration of series no. 1 is shown in appendix E, where the significant factors are marked with gray. As can be seen from the table the electrode force and weld time is close to being significant, which is expected, but in the reduced model of series no. 1 the main factors contributing significantly to the increase of the weld strength is the electrode size B and the interactions between electrode size and force BF and electrode size and weld time BT shown in figure 8.2. Had the chosen parameter range been chosen differently (i.e. lowering the minimum values) the main parameters F, T, and I would most likely have had a significant effect. The fact that different factors have an effect depending on the chosen parameter range can be attributed to the experimental variation and errors introduced by the linearity assumption of the 2-level factorial design.

Table 8.7: Measured weld strength of series 1 to 3 (Results in [N]).

Series		Overall	Centre point
1	Mean	2488	2611
	Std.Dev.	151	12
2	Mean	2434	2403
	Std.Dev.	108	29
3	Mean	2594	2606
DP600	Std.Dev.	107	25
3	Mean	2594	2672
TRIP700	Std.Dev.	107	44

In series no. 1 (figure 8.2) it is seen how increasing weld time decreases strength using the small electrode while the strength is increased if using larger bottom electrode. This is contributed to the fact that the small electrode promotes splash at larger weld time. The larger electrode allows for the growth of a larger nugget which results in higher strength. The force has no effect on the weld strength using the small electrode while the strength decreases when increasing the load with a large bottom electrode. This is explained by considering the relation between pressure and contact resistance. Using the small electrode the pressure is higher compared to the large electrode and for high pressures the effect on contact resistance and heat generation levels out. Furthermore it can be seen from figure 8.2 that increasing electrode size alone raises the strength. The current shows no influence on weld strength. This is most likely because the actual current values in

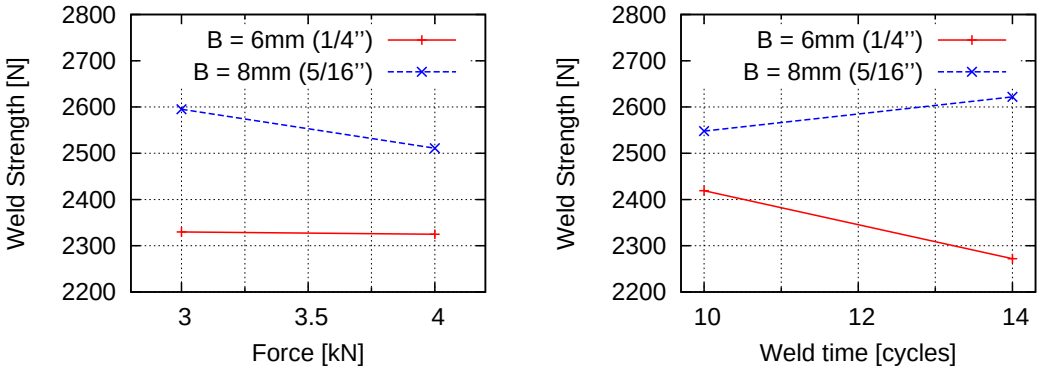

Figure 8.2: Plot of factor interactions between electrode size and weld time (left), and electrode size and electrode force (right) for weld series no. 1

the experiments were considerably lower and lying closer to each other (< 1kA) than prescribed on the controller. On top of this the nugget size becomes more robust in regard to the weld current when approaching the splash limit - which is the case here.

Series no. 2 involves welding of DC06 and HSLA with TRIP700 steel. The series use different weld parameter settings than the previous, cf. table 8.5. In the ANOVA analysis of series no. 2 the current I, force F and weld time T now have a significant effect on the weld strength, while the electrode size B on the other hand does not have an effect. The fact that influence of I, T and F is significant suggests that the range of the factor levels is wide enough to cover the nugget growth region where changes in these factors significantly affect the nugget growth. For higher levels of these factors their effect on nugget size and strength saturates and thereby becomes insignificant. For this material combination the weld strength did not increase when increasing the size of the bottom electrode. This could suggest that the nugget is not allowed to grow to its potentially full size and the effect of a smaller pressure due the larger electrode drowns in the main effect of changing the actual load itself. This is supported by the fact that the average weld strength of the centre points for series no. 2 is noticeably lower than for series no. 1 when considering the standard deviation of the results (c.f. table 8.7). It suggests that the nugget in series no. 2 could still be allowed to grow to obtain a larger nugget and thereby higher strength.

Due to the fact that increasing the size of the bottom electrode promoted higher strength and eliminated splash in series no. 1 as well as having no effect in series no. 2 it was chosen to apply the larger size bottom electrode with tip d=8mm in the remaining series 3-7, which were then focused on investigating the effect of the material combinations.

As such, series no. 3 was run with a large lower electrode and common factor levels for the two material combinations: DC06 - HSLA - TRIP or DP. The factor level range was set to overlap the ranges of the two previous series hereby increasing the average heat input when using TRIP steel and decreasing the average heat input when using DP steel. The ANOVA analysis in table 8.6 suggests that the factors material M, current I, force F and weld time T all have significant effects on the weld strength. Changing the material from TRIP to DP or increasing the electrode force decreases the average weld strength while an increase in current and weld time increases weld strength. For the high heat input settings using TRIP steel material splash starts being a problem - although the weld strength is not negatively influenced by this. Due to the fact that no interactions involving the material type of the bottom sheet are significant, the factors I, F and T have the same effect on the relative weld strength independent of material type.

This indicates that the lower absolute values of the factor level range for DP steel covers more of the nugget growth region than in series no. 1, and the strength is therefore now influenced by these factors. The standard deviations of the centre run experiments indicate that TRIP steel gives higher variability than DP steel.

The four series no. 4-7 were all carried out with the large bottom electrode tip of d=8mm. Analysis of the results from the factorial experiments using the ANOVA procedure presented problems. This is mainly due to the fact that the ANOVA analysis works best with process responses which are continuous. When a certain parameter configuration yields no weld strength the recorded weld strength is zero which gives a large discontinuous jump in the response. Furthermore some of the welds resulted in an abnormally high indentation of the top electrode which resulted in a highly increased nugget size and again a jump in weld strength. These jumps will corrupt the ANOVA analysis and, either show large effects from factors which are not expected to be significant, or show no effect due to a too high variability in the results.

In table 8.8 the results of the different series are collected showing the overall and centre point average and standard deviations. Looking at the overall averages and

Table 8.8: Results of experimental investigation series 4 to 7 (Results i [N])

Series No.	Bottom sheets	Overall		Centre point			
		Mean	S.Dev.	Mean	S.Dev.	Fail. mode	Splash
4	TRIP-TRIP	2169	973	2706	155	Tearing of base metal	Splash
5	TRIP-DP	1867	1467	2011	121	Weld interface failure	No splash
6	DP-TRIP	3062	632	2904	103	Tearing of base metal	No splash
7	DP-DP	2836	91	2830	25	Tearing of base metal	No splash

standard deviations it is obvious that the series 4-6 all including the TRIP steel has large variability in the chosen range of the factor levels. This means that changing the process parameters causes a large change in response of the process. Comparing with the standard deviations of the centre points it is clear that the main process parameters highly affect the results of these welds. The DC06-TRIP-TRIP combination showed splash at high heat input settings and no or weak welds at low heat input. Furthermore, splash was also observed for one of the low heat input settings indicating, that the TRIP steel itself is inducing variability into the process. This

can also be seen from the relatively large standard deviation of the centre point runs and the fact, that splash was not consistent for the repeated centre point runs.

Introducing the DP steel drastically changed the results and the effect was highly dependent on the order of the materials in the three layers. In the DC06-TRIP-DP combination (series no. 5) the factorial experiments resulted in an even larger variability. This was due to the fact that some of the weld configurations produced no joint between the DC06 and the TRIP steel while others resulted in splash and high strength. Looking at the centre points the strength is much lower compared to the other combinations and the failure mode is weld interface failure. If on the other hand the DP steel is inserted next to the DC06 steel in the DC06-DP-TRIP combination (series no. 6) the average weld strength increases and the process becomes much more robust strength-wise with successful welds at all factor level combinations, although with significant amount of splash at low force (3kA) settings. In series no. 7 the TRIP steel has been replaced by DP steel implying the material combination DC06-DP-DP. This combination is extremely robust in the chosen parameter range as the weld strength hardly changes and no splash is observed. An ANOVA analysis on this series suggests that only the current has noticeable influence and that the effect is small.

The experimental investigation of weld strength shows that the zinc coated TRIP steel makes the process more sensitive to process variations. The process window for making a successful weld is diminished when TRIP steel is involved in the material combination. The dominant failure mode during tension shear testing was identified as nugget pull-out and subsequent tearing of the thin low carbon steel sheet.

8.2.2 Nugget Formation

The nugget formation mechanism in a three layer welding of a low carbon sheet to two high strength steels was investigated using numerical simulation of the process. The simulations gave the actual temperature distribution in the material at a given time during the process. An analysis of temperature development during welding revealed that for the present configuration of materials and sheet thicknesses the heat generation was concentrated around the interface between the two thicker high strength steels, which was where the weld nugget started to form. Depending on the material combination and the thickness of the sheets the weld nuggets grow towards the interface of the thin low carbon steel. Conventionally the optimal weld is achieved if the nugget is allowed to grow a considerably amount into all the sheets being joined. However the problems regarding the investigated three sheet welds were to achieve nugget growth into the thin low carbon steel sheet without getting splash and internal defects in the weld.

Looking at the cross-section micrographs of the centre runs of series 1 through 7 presented in figure 8.3 and 8.4 on page 202 and 203, it is seen how the resulting weld nuggets compare. The simulated temperature distribution and weld nuggets size are shown for comparison, the white line drawn in the micrograph showing the predicted nugget. The micrographs indicate that the nugget has not been able to grow into the thin low carbon steel sheet in any of the weld series centre point runs. The nuggets tend to grow up close to the interface of the low carbon sheet but then it stops, in some cases practically at the interface. For other weld configurations than the centre-point settings the nugget might have been able to penetrate slightly into the low carbon steel, but this should be investigated by making micrographs of additional joints in order to confirm or dismiss this hypothesis. The microstructure morphology of the low carbon steel sheets do change appearance in the heat affected zone, but there is no proof of the presence of a liquid phase during welding. It appears as if the interface of the low carbon steel acts as a barrier to the nugget growth. This is especially obvious when looking at the nugget in series 3 using the DP600 steel. The nugget formation can be assumed to have started in the interface between the DP600 and the HSLA steel but from the shape of the nugget it is clear that it has been allowed to grow a longer, vertical distance downward into the DP600 steel than upward into the HSLA and DC06 steel.

Despite the fact that the nugget does not grow into the low carbon steel, a strong bond is still established as observed in the tension shear tests of the welds (cf. table 8.7 and 8.8). As the low carbon steel is assumed not to have reached the liquidus temperature the bond must be a bond between the nugget melt and the solid phase, low carbon steel, or a solid state bond between the high strength steel and the low carbon steel facilitated by the high pressure and high temperature.

It is furthermore observed from the simulations that the weld nugget generation is strongly influenced by the presence of the zinc coating on the TRIP steel. According to the simulations the initiation of the weld nugget formation is delayed due to the improved contact conditions in the interface and the resulting reduced heat generation. The simulations actually suggest that the nugget formation initiates in the bulk part of the sheets rather than at the interface, but then almost immediately after grows through the interface forming a weld nugget between the two high strength steels. In general, a rather good agreement between simulated and experimentally obtained nugget sizes is observed, see figure 8.3 and 8.4. The largest discrepancy is noticed in weld series 3 where the simulated nugget size is somewhat larger than the experimentally obtained. This is most likely caused by the modelling of the contact resistance between the two zinc coated surfaces of the TRIP steels where the simulated heat generation and the squeeze out of the liquid coating is overestimated compared to the real situation.

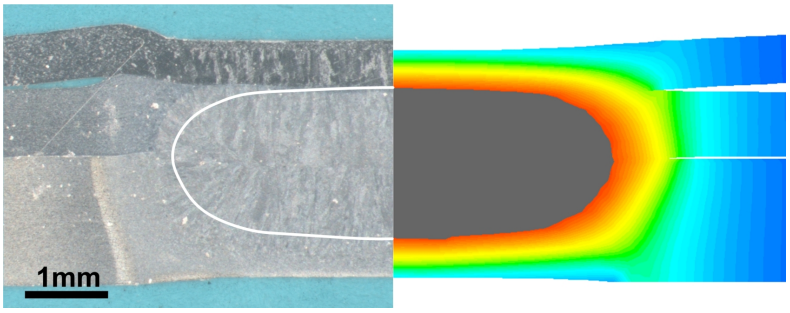

(a) Series 1: DC06 - HSLA - DP600

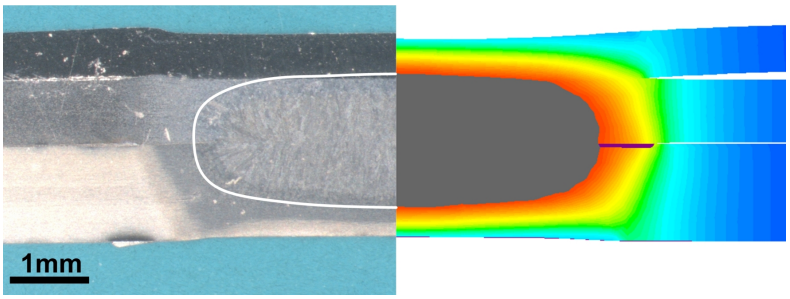

(b) Series 2: DC06 - HSLA - TRIP700

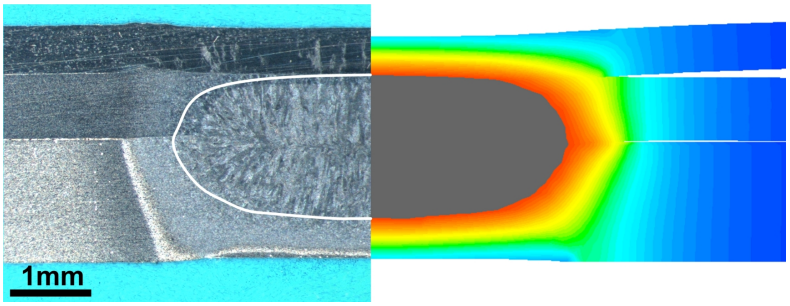

(c) Series 3(DP): DC06 - HSLA - DP600

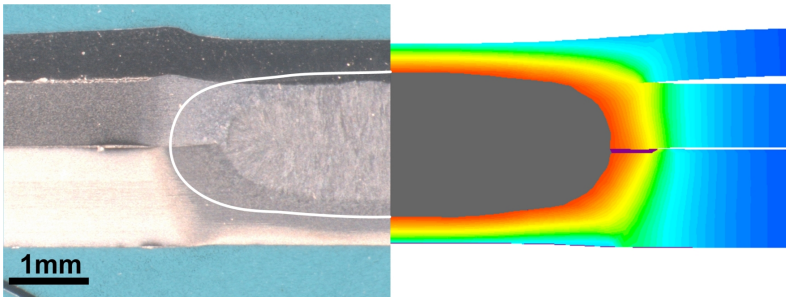

(d) Series 3(TRIP): DC06 - HSLA - TRIP700

Figure 8.3: Experimental and numerically calculated Cross-sectional views of centre-point welds in weld series 1, 2 and 3

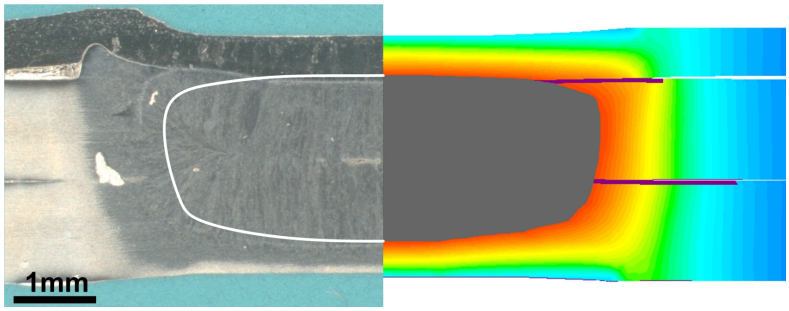

(a) Series 4: DC06 - TRIP700 - TRIP700

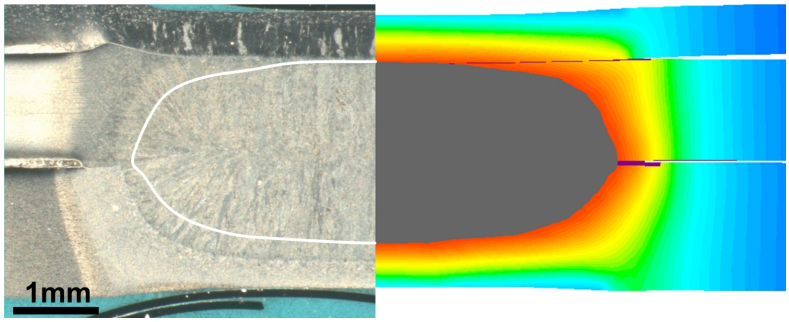

(b) Series 5: DC06 - TRIP700 - DP600

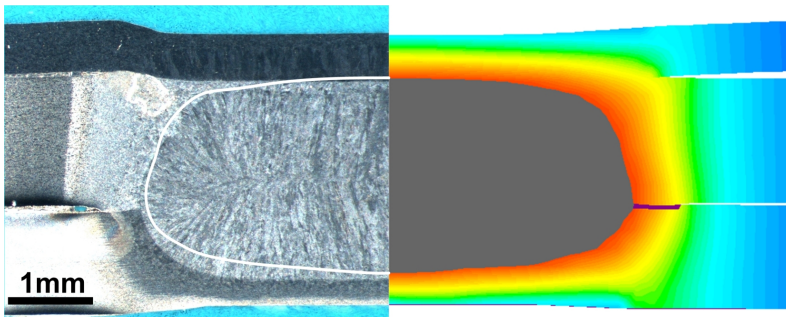

(c) Series 6: DC06 - DP600 - TRIP700

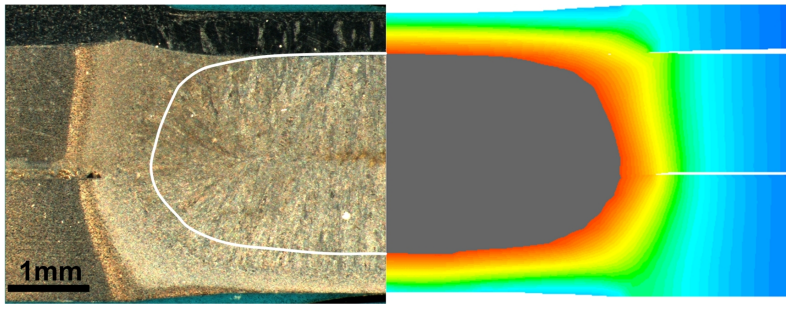

(d) Series 7: DC06 - DC600 - DC600

Figure 8.4: Experimental and numerically calculated Cross-sectional views of centre-point welds in weld series 4, 5, 6 and 7

8.2.3 Bonding Mechanism

Despite the fact that no nugget penetration into the thin low carbon steel was observed, the tension shear tests resulted in rather high strength of the joints compared to previous studies [3] as well as nugget pull-out and ductile fracture of the low carbon steel in most cases. This implies that the low carbon steel is effectively joined to the high strength steels. A closer inspection of the micrographs revealed several different weld interfaces between the low carbon steel and high strength steel.

Depending on the interface temperature during welding, bonding is established by solid bonding by growth of phases and/or grains across the interface. In some cases the entire interface is bonded while less favourable bonding conditions only allow for parts of the interface to form strong solid bonds. This is seen in figure 8.5 showing the interface between low carbon steel and HSLA steel in weld series 2.

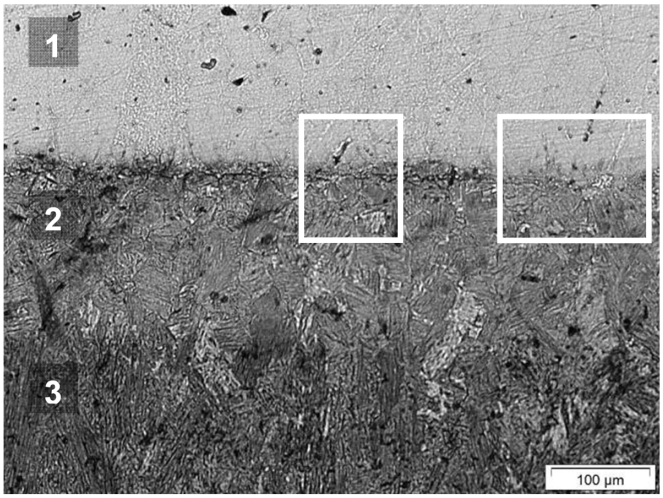

Figure 8.5: DC-HSLA interface in welds series no. 2

Outside the boxed areas the original interface is still intact and visible as a black line separating the two steels. Inside the boxes the interfaces have grown together and the interface line is no longer present as seen in figure 8.6. The larger bonding area, the higher is the expected tension shear strength of the welds. Three different material zones are distinguished in figure 8.5. Zone 1 consists of the low carbon steel, zone 3 is the weld nugget now transformed to martensite and zone 2 is the heat affected zone of the HSLA steel in contact with the low carbon steel. With reference to the tension shear strength of the centre point run of weld series 2, given in table 8.7, it is clear that a strong bond is created even though the weld nugget clearly has not reached the joining interface.

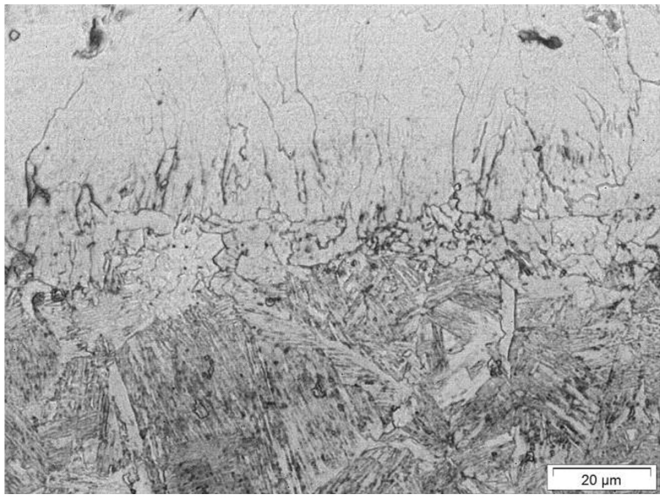

Figure 8.6: Area of bonded interface, series no. 2

8.2.4 Discussion

From the factorial experimental series 1 and 2 it is shown that increasing the tip diameter of the bottom electrode from 6mm to 8mm significantly increases the tension shear strength of the weld combinations with DP steel, but not with the TRIP steel. As proposed in section 8.2.1 the main reason for this is contributed to the fact that the maximum nugget size had been reached using the small electrode and a larger electrode could allow for the growth of a larger nugget. The process parameter range of the TRIP steel was however not chosen as close to the maximum nugget size and hence an increased electrode size could not generate a larger nugget for the chosen weld parameters. On the other hand it is noticed that a change in process parameters gave stronger welds and presumably larger weld nuggets.

As seen from the factorial experiments of especially series 4-7 (table 8.8) the three layer welding generally becomes less robust towards changes in process variables when TRIP steel is included in the material combination. Although the TRIP steel itself is stronger than the DP steel the difference is not significant and is not expected to cause significant changes to the weld results. This has been confirmed by numerical simulation where the material properties of DP steel in weld series 3 were replaced by the properties of TRIP steel. The difference in nugget diameter was less than 4%. The electrical properties of the bulk materials are furthermore not expected to differ significantly due to the fact that all the materials are steel alloys with relatively low amounts of alloying elements. Because the TRIP steel is thinner than the DP steel it affects the welding process, as the cooling capacity of the specimen itself is decreased, but on the other hand the interfaces moves closer

to the electrodes thereby facilitating cooling. However, the main factor influencing the weldability of TRIP steel is believed to be the 14μm zinc coating. The coating is soft and a good conductor resulting in low contact resistance of the interfaces and slower heat generation thereby delaying the nugget formation. This implies that longer weld times or higher currents are needed to initiate nugget growth. As the melting point of zinc is considerably lower than that of the steels the coating will in many cases melt and be squeezed out from the contact zone due to the high contact pressure. This will cause a change in contact conditions with time and the requirements for weld time and weld current are dynamically lowered increasing the risk of splash and weld defects due to the sudden excessive heat generation. This mechanism is believed to be the main factor contributing to decreasing the weldability window of the TRIP steel. This hypothesis was supported by numerical simulations. The coating was removed from the TRIP steel in weld series 3 and the simulation suggested that this would increase the nugget diameter by more than 23% due to the high increase in contact resistance in the TRIP and HSLA interface.

Indentation is a problem observed in the experiments but not addressed in the investigation. As the soft low carbon steel sheets typically are used as outer panels the aesthetic appearance is of importance. The problem of indentation becomes even more pronounced when joining hard and soft materials with RW. The high strength steels require some minimum electrode force in order to stabilise the process and avoid excessive splash. The relatively high force required to weld the high strength steels typically results in a non-negligible indentation in the low carbon steel. Furthermore the actual contact area at the interfaces are determined by the relative hardness of the materials, which implies that the electrical contact resistance is lowered considerably between the low carbon steel and the high strength steel. As described in section 8.2.2 this will significantly decrease the heat generation in this interface and the nugget formation is confined to the interface between the two harder steels. This problem is not easily resolved as it has roots in the basic functional properties of the process itself. However, by optimisation of the process it is under these circumstances possible to arrive at a reasonably trade-off between indentation, risk of splash and weld strength.

8.3 Conclusion

The mechanism of nugget formation has been identified to initiate between the two high strength steels from where it develops and grows into the sheets. Depending on the heat input the nugget might grow close to or in some cases even slightly penetrate into the thin low carbon steel.

It was found that increasing the size of the bottom electrode improved the strength of the joints by increasing the weld nugget diameter. This, however, was only observed for weld settings where the growth of the nugget was restricted, not due to a low heat input, but due to geometrical limitations solely.

By examining micrographs of the welds it was found that the bonding mechanism between the low carbon steel and the high strength steels predominantly consisted of solid state diffusional growth of micro structure grains across the interface rather than by a fusion nugget. The solid state bonding is facilitated by the high temperatures and pressure during the welding process. The strength of the welds were measured by tension shear test and was found to be relatively high compared with previous investigations utilising the same low carbon steel [122]. Furthermore, fracture was typically in form of ductile tearing of the low carbon steel around the weld nugget. Only few of the weaker welds failed in a brittle manner through the interface and this was mainly observed for interfaces with zinc coating involved, i.e. for the TRIP steel.

It was investigated whether it was possible to model the three layer welding process by numerical simulation using material models of the strength of the materials determined by hot tensile testing. The simulations proved to have a good correlation with the experimental results which shows that the numerical analysis could be used as a tool to optimise individual weld configurations of three layer spot welding of AHSS.

Chapter 9

Modelling of Hardness in AHSS Welds

Resistance spot welding is by far the most widely applied welding process in car assembly operations. With the introduction of new advanced steels in the production, detailed knowledge of the influence of the process on the microstructure and mechanical behaviour of the steels is essential for manufacturers. Several researchers have investigated the weldability and problems related to resistance welding of AHSS. Particularly hot-cracking and undesirable weld failure associated with high hardness have been investigated and optimised welding procedures and practises to prevent these problems have been proposed [45, 123–125].

The size of the weld nugget has traditionally been a practical measure of the strength of the weld. However, welding of AHSS has a dramatic effect on the microstructure in and around the weld. As a consequence a larger variation in mechanical properties occurs than for welds of traditional low-carbon steels. AHSS is manufactured using special heat treatment procedures resulting in an advantageous microstructure exhibiting both high strength and toughness. This microstructure is changed significantly during welding as described in chapter 7 with the formation of primarily martensite during cooling. This has a significant influence on the hardness and mechanical properties of the joint. Although martensite formation will enhance the tensile strength of the material it deteriorates its toughness. Brittle fracture due to martensite formation is unacceptable in the automotive industry where ductile failure is a safety design parameter. Empirical studies by Uijl and Smith [45] have shown that hardness levels exceeding 450HV correlate with an increased tendency towards brittle failure through the nugget. This is generally associated with a large degree of martensite in the microstructure. The accurate

prediction and modelling of the resulting microstructure after resistance welding of AHSS steels has a high priority when designing joints and evaluating the risk of brittle failure mechanisms.

The purpose of this work has been to investigate modelling of post-weld hardness of resistance welded AHSS. The focus has been to apply empirical formulae for hardness estimation and to include numerically calculated thermal history as well as the melted volume of the joint. Spot welded lap joints of similar and dissimilar material combinations are investigated and besides the AHSS a low carbon steel is included in the investigation.

Most of the content of the following chapter has been presented at the 5th International Seminar on Advances in Resistance Welding 2008 in Toronto, Ontario, Canada [122]. The simulations, however, has been improved by using the more recent version 10.1 of SORPAS.

9.1 Modelling of Post Weld Hardness

A few recent studies [47, 126] applied mathematical and numerical modelling to estimate the cooling rate in resistance spot welding to predict the resulting microstructure. Such models are typically simplified as compared to the complexity of the process, which is characterised by fast heating, inhomogeneous and unknown temperature in the weld, and fast cooling. One of the oversimplifications is that cooling is usually assumed to be unidirectional through the electrodes. This assumption only holds for the central part of the nugget while the outer part and the HAZ is characterised by cooling in 3 dimensions, through nugget and base material. With the use of advanced finite element methods it is possible to predict the actual thermal history in the entire nugget and HAZ with better accuracy. In this work the numerical program SORPAS is used for simulating thermal history and melted volume of the materials in the weld zone.

Several empirical models for predicting post-weld hardness in steels have been proposed in literature [45, 50, 127]. The most common way of modelling hardness in welds is by relating the alloying components of the steel to the post-weld hardness by a parameter commonly referred to as the Carbon Equivalent (CE). This parameter is calculated based on the alloying content of the steel and expresses the combined effect of the alloying elements on the specific steel hardenability. Khan et al. [50] compares several studies of hardness prediction and show that a linear relationship between CE and post-weld hardness can be assumed. This implies that the critical factor in determining post-weld hardness using these empirical models is the calculation of the CE.

The model originally proposed by Blondeau et al. [127] is utilised in this study as it has been shown to yield good agreement between predicted and experimental results for resistance welding of alloyed high strength steels [45], and because the model takes into account the effect of cooling rate on the hardness prediction. The model is given in equation (9.1) where HV is the Vickers hardness and t_r is the cooling rate at 700°C

$$\mathrm{HV} = 127 + 21\log(t_r) + 949(\mathrm{CE}) \tag{9.1}$$

The carbon equivalent (CE) is given by equation (9.2) where the variables are given in $wt\%$ of the alloying elements.

$$\mathrm{CE} = \mathrm{C} + \frac{28.5\mathrm{Si} + 11.6\mathrm{Mn} + 8.4\mathrm{Ni} + 16.9\mathrm{Cr}}{1000} \tag{9.2}$$

As can be seen from equation (9.2) the carbon content is the main factor influencing on the hardness prediction, whereas the other alloying elements have a minor, but still significant influence.

The model by Blondeau et al. [127] is based on the assumption of complete martensite formation of the material and therefore in reality predicts the hardness of the formed martensite. As described in chapter 7 martensite is formed by military transformation of austenite into martensite. Depending on its composition the steel has a certain temperature range where austenite is stable. The austenite initiation temperature and the temperature where all material is transformed are commonly referred to as $Ac1$ and $Ac3$, respectively. They can be estimated by the empirical formulae by Andrews [128] given in equation (9.3)

$$Ac1[^\circ\mathrm{C}] = 723 - 10.7\mathrm{Mn} - 16.9\mathrm{Ni} + 29.1\mathrm{Si} + 16.9\mathrm{Cr} + 290\mathrm{As} + 6.38\mathrm{W} \tag{9.3a}$$

$$Ac3[^\circ\mathrm{C}] = 910 - 203\sqrt{\mathrm{C}} - 15.2\mathrm{Ni} + 44.7\mathrm{Si} + 104\mathrm{V} + 31.5\mathrm{Mo} + 13.1\mathrm{W} \tag{9.3b}$$

As was seen in chapter 7 the fraction of martensite in the HAZ increases when approaching the nugget. This is directly related to the degree of austenization of the material, i.e. the fraction of material transformed to austenite during welding (and subsequently cooled to form martensite). In this work a linear relationship of material austenization of the form $Au\%(T_{max}) = (T_{max} - Ac1)/(Ac3 - Ac1)$ is adopted as a factor in the HAZ where the maximum temperature T_{max} in the material is within the austenization region, but less than $Ac3$. The critical cooling rates for martensite transformation are estimated by using the work by Gould et al. [47] which is comparable to similar investigations [87, 108]. The estimates predict that the AHSS steels form martensite while the DC06 does not [109].

When welding dissimilar materials the weld nugget will be a mixture of the two original alloys. In chapter 7 it was found that the hardness was close to constant throughout the weld nugget for the lap joint of DP600 and TRIP700. This indicates that the two alloys are completely mixed forming a homogeneous alloy with a hardness value lying between the hardness values of the parent individual materials. The following linear volume weighted mixing rule is proposed for calculation of the hardness in the nugget of dissimilar materials, as shown in equation (9.4)

$$\mathrm{HV}_{mix} = \frac{V_1 \cdot \mathrm{HV}_1 + V_2 \cdot \mathrm{HV}_2}{V_1 + V_2} \tag{9.4}$$

Because of the linear relationship between HV and CE the hardness can be used directly. Otherwise equation (9.4) should be substituted with a compositional weighted average rule. As explained later in section 9.2.3 this mixing rule is implemented in the numerical procedure allowing for calculation of the hardness in welds of dissimilar materials.

9.2 Method

9.2.1 Materials

The two AHSS steels investigated in chapter 7, DP600 and TRIP700, are also used in this study for modelling of hardness. Furthermore a low carbon steel DC06 is included in the analysis. The compositions of the three steel grades and their as-delivered conditions are collected in table 9.1. The DC06 and DP600 sheets have

Table 9.1: Composition of the steel grades as defined by the manufacturers. Compositions are given in wt%

Material	**Supplier**	**Thk.**	**Coating**	**Nominal composition [wt%]**						
		[mm]	**[μm]**	**C**	**Mn**	**Cr**	**Si**	**P**	**S**	**Al**
DP600	SSAB	1.5	-	0.08	0.9	-	0.4	0.015	0.002	0.04
DC06	SSAB	0.6	-	0.002	0.15	-	-	0.01	0.01	0.04
TRIP700	ThyssenKrupp	1.2	Zn: 14	0.29	2	0.6	0.3	0.4	0.01	0.24

a thickness of 1.5 mm and are uncoated. The TRIP steel sheet has a thickness of 1.2mm and is provided with a hot-dipped galvanised Zn-coating. The main effect of the zinc coating on the TRIP 700 steel is expected to be an initial decrease of the heat generation at the interfaces where the zinc coating is present. Due to the lower melting point of zinc compared to steel, the coating will typically melt and be expelled from the sheet to sheet interface in the early stages of the process. In this sense the zinc will be removed from the weld interface. If the coating was not

present, a lower current would typically have been required to achieve a similar weld, and so the influence of the coating on the resulting microstructure is assumed negligible. The zinc coating will, however, have a negative effect on the lifetime of the electrodes such that the electrodes need to be changed more frequently than for uncoated sheets. For this investigation the number of welds is limited and electrode wear is therefore not a problem.

9.2.2 Experimental Procedure

For the experiments the sheets were cut in samples of 100x25mm and welded as a lap joint. All possible two sheet combinations, 6 altogether, were welded and investigated. The welding parameters were chosen to achieve a strong weld with a large nugget, but without metal expulsion. The settings were found by numerical simulations followed by experimental verification. The settings were comparable to those used in similar studies [125, 129]. The welding was done on a TECNA 8105 AC welding machine with a TE- 180 weld controller. The electrical system can deliver up to 85kA with 50Hz. The actual current was measured using a Rogowski coil together with a pre-calibrated TECNA-1430 conditioner. The mechanical system is pneumatically driven and can deliver up to 20kN weld force. The actual load during the welding process was measured using a piezo electric force transducer. The electrodes used were of material CuCrZr and diameter of 20mm ISO 5821-1979 type B with a tip diameter of 8 mm and a 50 mm tip rounding radius. The weld strength was tested with tension shear tests on an Amsler tensile testing machine with a maximum pulling force of 100kN. The welding parameters and the weld tensile shear strength as determined in the tension-shear test are given in table 9.2. The micrographs of the weld cross-sections were made by mounting them in resin and grinding until the centre of the nugget was reached. Subsequently the samples were polished (final step 5min diamond 1μ) and etched with 2% Nital for about 3 seconds. Reflected light microscopy was performed with a Neophot 30 (Zeiss, Jena); micrographs were recorded with a CoolSnap CCD camera. The

Table 9.2: Overview of weld settings (RMS current, force, weld time in 50Hz cycles) and joint breaking force (JBF) of welds.

Material combination	Current [kA]	Force [kN]	Weld Cycles	JBF [kg]
DC06 – DC06	10.5	4.5	17	925
DP600 – DP600	9.8	6	17	2030
TRIP700 – TRIP700	9.5	4.5	17	1650
DC06 – DP600	9.4	4.5	17	1030
DC06 – TRIP700	9.8	4.5	17	1026
DP600 – TRIP700	9.8	5.2	17	1853

hardness profile across the weld nugget was measured using a Futuretech FM-700 micro indentation hardness tester with 100g load. Inspired by Gould et al. [47] the hardness measurements were made crosswise through the nugget as shown on figure 9.1.

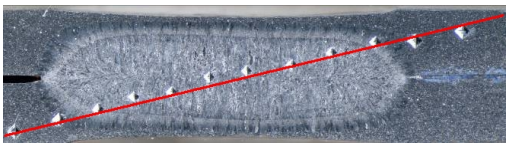

Figure 9.1: Hardness measurement profile

9.2.3 Numerical Procedure

In this work the commercial FE-program SORPAS ver. 10.1 for numerical modelling of resistance welding is used for numerical simulation of the process. The program is dedicated and optimised for simulating resistance welding and consists of 4 models: a mechanical, a thermal, an electrical and a metallurgical model. The metallurgical model has incorporated the ability to calculate the post-weld hardness based on an expression of the similar form as in equation (9.1), but with variable parameters. For this work the coefficients given by Blondeau et al. [127] is used according to equation (9.1) and the CE is calculated according to equation (9.2). The calculations are performed *after* the simulation has finished and any coupled effects of hardness on the simulation is therefore not taken into account. The total volume of melted material is calculated and used for calculation of the hardness in the mixed nugget according to equation (9.4). The calculated metallurgical data for the numerical simulation is given in table 9.3.

Table 9.3: Metallurgical data for simulation

Material	**CE**	**Ac1** [°C]	**Ac3** [°C]	t_r[°C/s]
DC06	0.004	721	900	13500
DP600	0.140	722	853	120
TRIP700	0.282	720	824	200

9.3 Results

9.3.1 Hardness

The hardness profiles of the different welds are plotted in figure 9.2 showing welds of similar material (figure 9.2a) and dissimilar material (figure 9.2b). The first

material in the labels show what material corresponds to the negative direction to the weld centre. As an example the label DC06-TRIP indicate that the weld was originally DC06 steel in the negative direction and TRIP steel in the positive direction on the plot. It is noted that the hardness is more or less homogeneous throughout the nugget, which indicates that during the welding process the melt forms a homogeneous alloy of the dissimilar materials being welded. This was also noted in chapter 7. The welds of similar materials show a rapid hardness increase across the HAZ and the hardness remains constant throughout the nugget. The higher alloyed the material the higher is the hardness in the nugget. For the dissimilar welds the hardness in the HAZ of the strongest material is higher than in the nugget. This is consistent with a molten nugget of different (less alloyed) composition and hence a softer microstructure than the parent material.

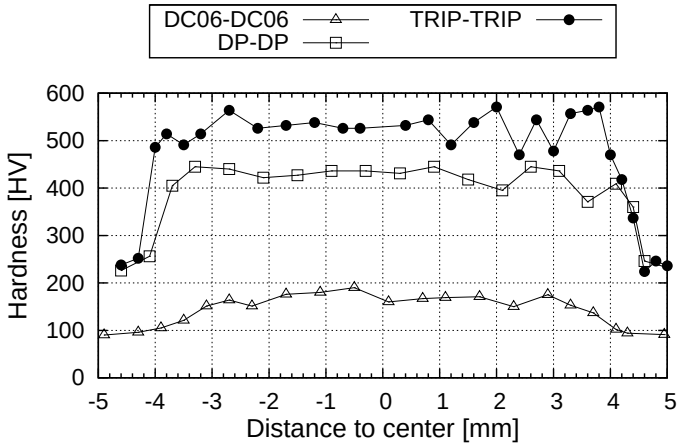

(a) Similar materials

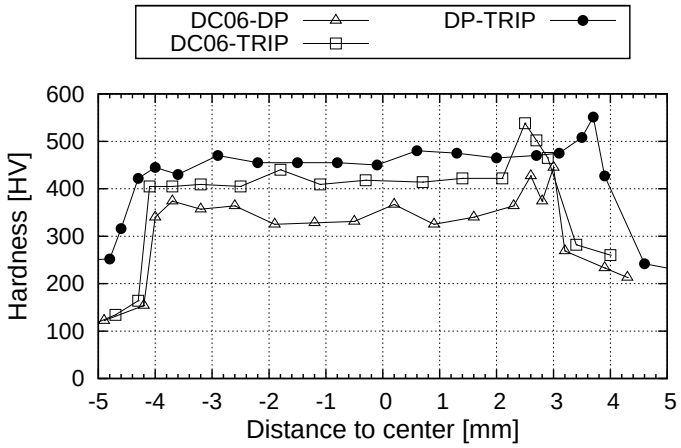

(b) Dissimilar materials

Figure 9.2: Experimental micro hardness of welds

9.3.2 Microstructure

The microstructure of the DP and TRIP steels have been characterised in chapter 7 so only the base metal and HAZ of the low carbon steel DC06 will be given here. During welding of DC06 the material in the HAZ reaches temperatures sufficiently high to (at least partly) transform ferrite into austenite. On subsequent cooling a back transformation to ferrite will occur. The micrographs in figure 9.3b and 9.3c show irregular ferrite grain boundaries in the HAZ, whilst smooth grain boundaries occur in the as-delivered microstructure far away from the weld nugget (figure 9.3a - note the scale difference). These irregular grain boundaries indicate the occurrence of a massive transformation from austenite to ferrite, which is a consequence of a fast transformation (but not fast enough to induce a martensitic transformation) that is rate controlled by thermally activated jumps of iron atoms across the austenite-ferrite interface [67]. Because the transformation is diffusion-

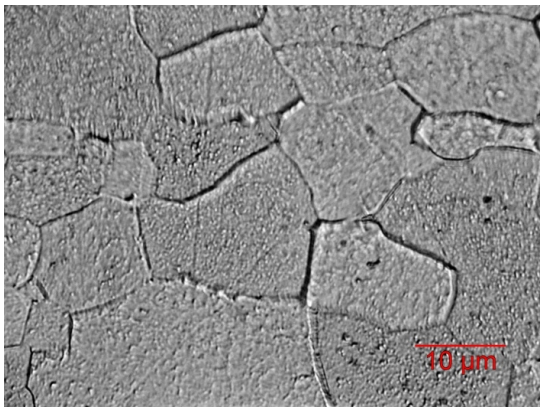

(a) DC06 Base metal

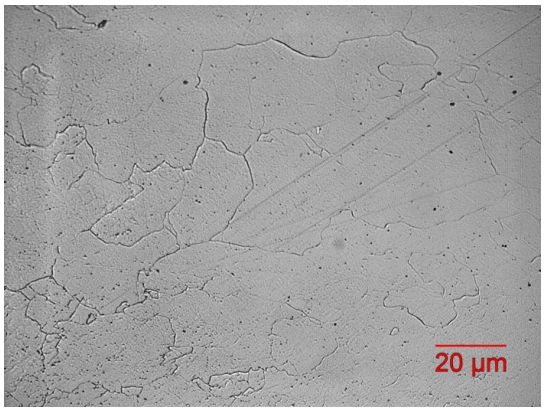

(b) Outer HAZ

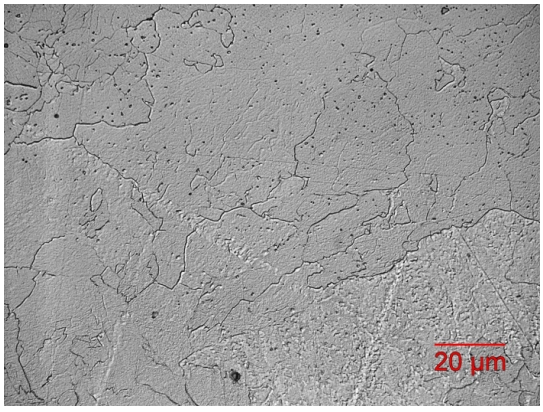

(c) Inner HAZ

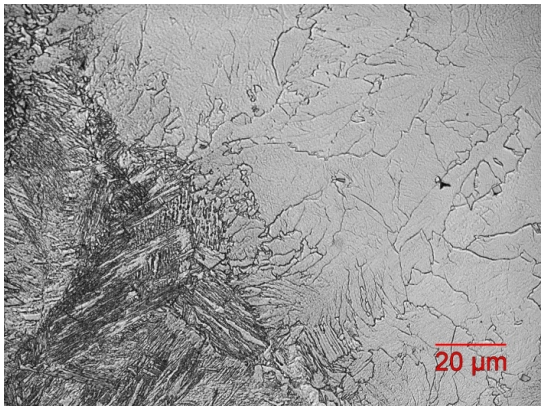

(d) Weld zone close to HAZ

Figure 9.3: Nital etch of microstructure of DC06 side of a DC06-DP600 weld

less the compositions of austenite and ferrite are identical and no partitioning of alloying elements occurs. The total grain boundary area is increased, which hinders dislocation motion and slightly increases the hardness. This material is a typical interstitial free steel alloyed with some carbide forming elements such as Ti, Mn etc. These elements will react with carbon and prevent the formation of cementite. The small black dots in the base material and outer HAZ (figure 9.3b and 9.3c) are probably alloying element carbides. In the inner HAZ close to the nugget the material has experienced temperatures close to the melting point and the cooling rate has been even faster than in the outer HAZ. It is noted how the microstructure abruptly changes going from the HAZ and into the nugget on figure 9.3d. This is mainly due to the mixing of DC06 and DP in the nugget creating a new alloy with much higher tendency to form martensite or other hard phases.

In figure 9.4 an overview of the microstructure morphology and average hardness of the weld nuggets are shown. The microstructure of the weld nuggets for the different welds, which were all characterised, show a highly irregular structure and a significantly higher hardness than in the as-delivered material (see figure 9.2). The microstructure of the welds of the high strength steels are largely martensitic as found in chapter 7. The irregular microstructure of DC06-DC06 is most likely the result of a massive austenite-ferrite transformation; the occurrence of a martensitic transformation at extremely high cooling rate cannot be excluded (despite the low carbon content) and the relatively large hardness increase indicates that some martensite is probably formed.

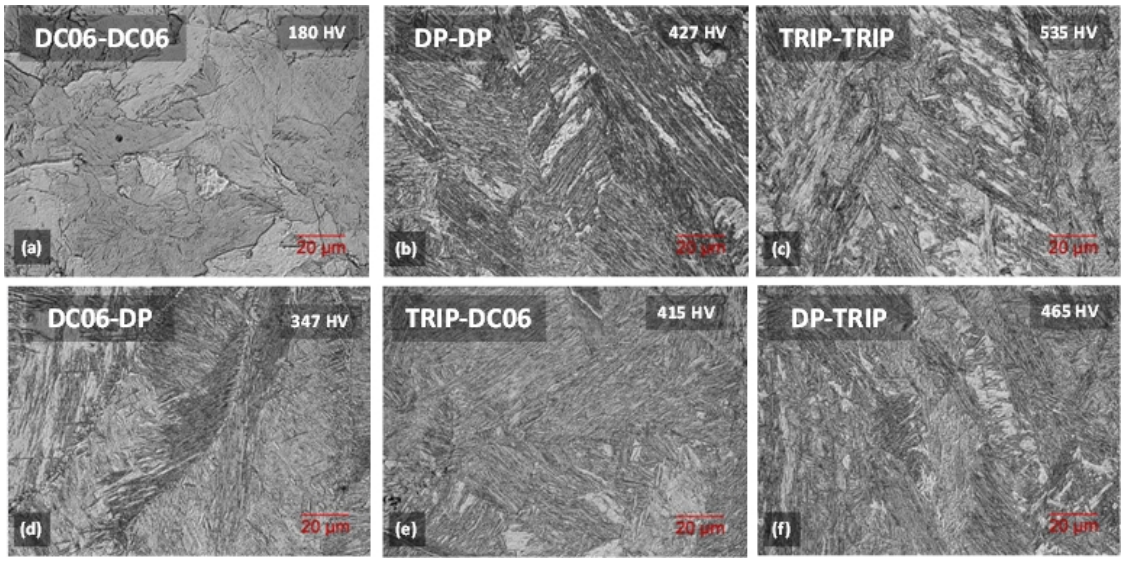

Figure 9.4: Overview of microstructure of the weld nuggets of all material combinations.

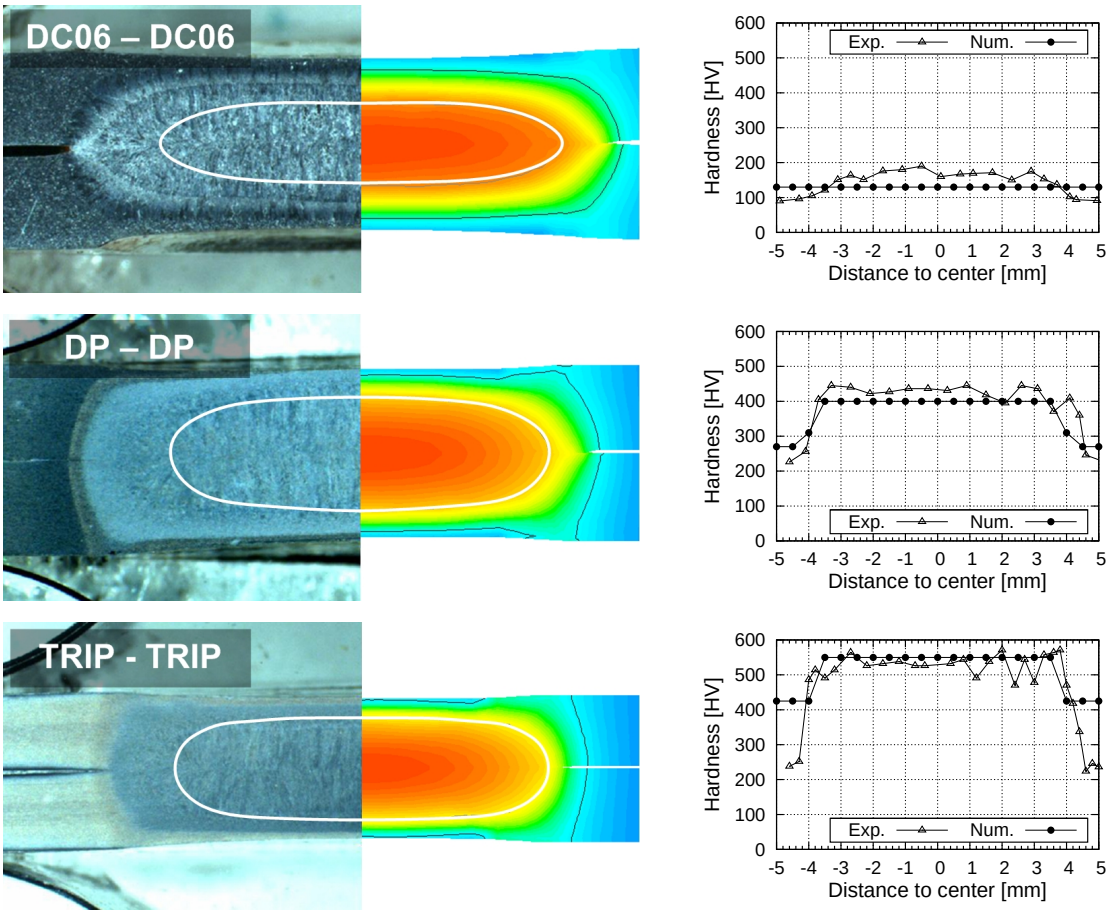

Figure 9.5: Numerical results for welding of combinations of similar materials

9.3.3 Numerical Results

The results from the numerical calculations of the temperature distributions in the welds of similar and dissimilar material combinations are shown in figure 9.5 and 9.6. In these graphs the colours indicate maximum temperature during welding, where red is the highest (≈1400°C) and the light blue is the minimum (≈400°C). The white line marks the liquid region, i.e. the size of the nugget, and the dark line indicate the austenized region (>720°C). The dynamic cooling rates are simulated during the cooling process. The highest cooling rates achieved for similar steel combinations are 4900°C/s for DC06-DC06, 4500°C/s for DP-DP and 5100°C/s for TRIP-TRIP. These rates can be compared to the critical cooling rate for martensite formation as presented in table 9.3. The cooling rates experienced in this investigation are much higher than the critical cooling rates for the DP and TRIP steels and much lower than the critical cooling rates for the low carbon DC06 steel.

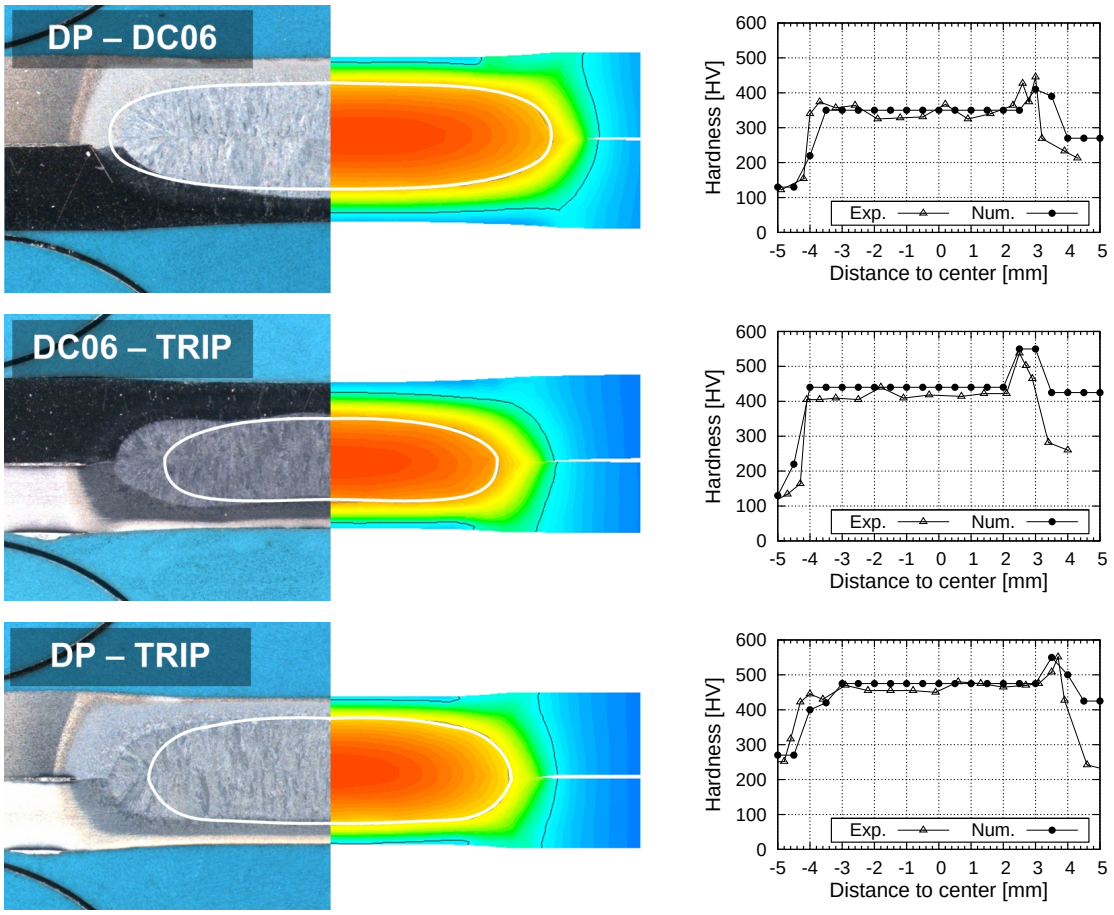

Figure 9.6: Numerical results for welding of combinations of dissimilar materials

9.4 Discussion

Comparing the reflected light micrographs (left) and the calculated temperature distributions (right) in figure 9.5 and 9.6 a satisfactory agreement between the sizes of HAZ and austenite regions emerge. The agreement between predicted and experimental shape of the molten part of the nugget is not as good as for the austenite regions. This is most likely due to inadequate description of materials properties such as resistivity, contact resistance, heat conductivity at elevated and high temperatures. This data is not commonly available in literature and usually is very costly to estimate and so the standard values from the materials database of the numerical program was used. Despite the fact that there is some disagreement between experimental and simulated nugget size, the relative fractions of melted material in the two sheets are seen to match rather well with the experiments, even though the nugget itself is different. In other words the ratio of molten material

from the two sheets are approximately the same for the simulated results which implies that the disagreement in nugget size is not expected to have any influence in estimating the nugget hardness using equation (9.4).

Comparing the calculated and simulated hardness profiles in figure 9.5 and figure 9.6 a reasonably agreement is found - especially for the DP and TRIP similar welds. For the DC06 to DC06 weld the correspondence is not so good, as the simulation predicts no increase in hardness. This is because the estimated critical cooling rate for martensite formation is not exceeded and hence no martensite is simulated. Whether the experimental observed hardness increase is due to minor martensite formation or due to massive formation of ferrite from austenite is unknown. The model by Blondeau et al. [127] is mainly applicable for steels of higher carbon content. Consequently more advanced models should be used to describe hardness formation for low carbon steels. Furthermore it is observed that the simulated hardness outside of the HAZ generally does not match the experimentally found value. This is because the model only calculates hardness based on thermal history and the original hardness values are thus not included in the model. It is seen how the proposed mixing rule in equation (9.4) successfully simulates the hardness value in the nugget and that surprisingly good agreement with experimental results are found. Especially for the cases of low carbon steel welded to AHSS the carbon content of the two alloys are significantly different but still the model captures the effect of alloy mixing extremely well.

The modelling of microstructural phase changes and resulting hardness distribution of different heat treatments of steels is the aim of many investigations in the field of material science. These models are usually derived by considering the principles of thermodynamic equilibrium and the driving force for phase changes. The resistance welding process is characterised by extremely high heating and cooling rates of the material compared to normal heat treatments of steels. This implies that the condition of the materials during the process generally is very far from the equilibrium condition, which makes it difficult to apply the normal theories for predicting phase transformation. The present work utilises a simple empirically based formula for the calculation of the resulting hardness as a function of composition and cooling rate, equation (9.1). As a first version, the model does not consider all possible phase changes but assumes a complete transformation to martensite if the critical cooling rate is exceeded. This is a reasonable assumption for spot welding of most types of steels due to the very high cooling rate. The present work considers the simple spot welding using a single pulse and no down slope nor tempering schemes. Applying more complicated welding schemes as mentioned above may not result in similar good agreements between the measured and numerically estimated hardness. In that case more detailed knowledge of the phase changes for different cooling paths is needed to improve the model. Another limitation which

is worth mentioning is the fact that the metallurgical model is not fully coupled with the thermal and other models during simulation, in the sense that the effect of phase changes (metallurgical effects) during the process on the mechanical and thermal properties of the material is not fully included. One could argue that the temperature dependency of the material models is able to capture some of the metallurgical effects during the process, though this is not a complete description.

By using the procedure described in this chapter it is shown how the post-weld hardness of lap joints of typical AHSS steels can be simulated. Several studies have investigated the relationship between hardness, size of weld and the maximum strength of the bond before failure initiates. Several authors have proposed failure criteria depending on weld size and hardness of the nugget [51, 130]. The combination of the ability to numerically predict weld size and hardness with known failure criteria opens for the possibility to estimate the strength of a given weld by numerical simulation. This could prove to be an important tool for engineers in designing new constructions assembled by resistance welding.

9.5 Conclusion

The hardness of the material across the weld zone in resistance welded lap joints of low carbon steel DC06 and high strength steels DP600 and TRIP700 and combinations hereof have been measured by micro hardness indentation tests of cross sectioned samples. The hardness profiles of the joints using high strength steels show a large increase in hardness in the weld nugget and the HAZ. Using reflected light microscopy the microstructural changes and the resulting hardness increase has been explained by visual inspection of the microstructure revealing predominantly martensitic structure due to extremely high cooling rates combined with high carbon content. Welding dissimilar materials produces a new alloy in the melted region with a well defined boundary to the non-melted region. The hardness throughout the melted region is observed to be constant indicating a complete mixture of the two materials resulting in a homogeneous alloy (and hardness) in the entire weld nugget with a new composition depending on the compositions of the two base materials. The experimentally performed lap-joints have been simulated using the commercial FE program SORPAS. In order to numerically estimate the hardness distribution of the welds the material compositions represented by the CE number and the thermal history obtained from the simulations were used together with the empirical model by Blondeau et al. [127]. When welding dissimilar materials the model was modified with the mixing of the materials in the weld nugget to account for the formation of a new homogeneous alloy in the melted region depending on the volume fraction of melted materials. The proposed model showed good agreement with the experimental data.

Chapter 10

Conclusion

The resistance welding process is influenced by a large number of process and material parameters. An essential step in any modelling context is to have an accurate description of the material parameters. In resistance welding the material is exposed to both electric currents and high stresses at a wide range of temperatures. Two methods for measuring material yield strength at discrete temperatures, the hot tensile test and the hot compression test, has been investigated. The hot tensile test is suited for testing sheet metal while the hot compression test is able to test bulk specimens of cylindrical shape, also at increased strain rate. Both tests were found suitable for measuring yield stress curves at temperatures ranging from room temperature to close to the melting temperature of the material.

The tensile yield strength of advanced high strength steel DP600 and TRIP700 as well as low carbon steel DC06 was tested and could be described by the standard Hollomon power-law equation at the different test temperatures. The compressive yield stress of round cylindrical samples of Nickel 200, Stainless Steel AISI 316, Aluminium 6060T6, and mild steel S235JR were tested. With the Hollomon equation it was possible to describe the behaviour of the materials at medium and high strains, while some discrepancy was found at low strains. The material models based on the Hollomon equation and table values of temperature dependent model parameters were readily implemented in the numerical software SORPAS.

A method for measuring the electrical resistivity cylindrical specimens were developed based on the thermo-mechanical Gleeble 1500 system. The resistance of the four previously mentioned materials (nickel, stainless, aluminium, and mild steel) were measured. The method showed good repeatability in measuring bulk resistivity and the results did generally agree well with reference measurements from literature. It was found that the measurements of the mild steel specimens were significantly disturbed by the ferromagnetic properties of the material creating a

self-induction effect resulting in erroneous measurements. It was proposed how this influence could possibly be decreased by reducing the cross section of the specimens.

The electrical contact resistance was measured applying the experimental procedure used for the resistivity measurement but also synchronising measurements of contact pressure between two specimens. Measurements were performed at constant temperature by step-wise increasing pressure, resulting in data describing the decrease of contact resistance with increasing pressure for chosen temperature levels. Three repetitions were made at each temperature. Test specimens were prepared using wire EDM and turning, resulting in two distinctively different surfaces. The measurements of contact resistance generally showed a low experimental variation that did not obscure the effects of changing the main parameters.

A literature study showed that the theory of contact resistance of a single cluster of contact spots, presented by Greenwood [7] in 1966, is widely used as the basis for deriving general applicable contact resistance models. However, as argued in this thesis, the derivation of the models involve significant simplifications and assumptions that are often not in agreement with the original theory by Greenwood. Despite the dubious derivation of the models the researchers are able to report reasonably agreement with experiments. In general the models describe the contact resistance as a function of pressure following an inverse power-law of the form: $R_{\mathrm{CR}} = R_0 p^n$, where n is a constant of either -1 or -0.5. The hardness or yield strength of the material is introduced by the relationship between pressure and true area of contact presented by Bowden and Tabor [71] which, together with the material resistivity, only influences the value of R_0 and not n. The effect of temperature is indirectly accounted for by its effect on material yield stress and resistivity.

The experimental measurements show that the specimen surface type (EDM or turned) is significantly influencing the behaviour of the contact resistance. This is explained by the way that the two processes affect the individual materials and produce surfaces of either high or low hardness and/or a thin or thick oxide layer. It is shown how the experimental results with good approximation all follow a straight line in a log-scale plot for pressures higher than 10MPa, implying an inverse power-law relationship of the data. However, the rate of decrease, or the n exponent, is not constant, as the theoretical models predict, but it is numerically smaller for surfaces with increased hardness and/or thickness of the oxide layer. This is explained by referring to the results by Nakamura and Minowa [77], which show that the decrease of constriction resistance with true contact area depends on the resistance of the spots in contact. The results thereby question the governing assumption that the effect of constriction resistance and film resistance can be modelled separately.

Micro resistance spot welding of 0.2mm stainless steel AISI 316 and Nickel 200 has been investigated with focus on the contact resistance. The method of estimating contact resistance by measuring the voltage drop across the sheet to sheet interface was analysed. It was found that, especially in the beginning of the process, the bulk resistance is negligible compared to the contact resistance, while after the initial contact resistance drop the measured bulk resistance becomes dominant. The influence of the current, electrode force, and current ramp rate on the joint breaking force was analysed through an ANOVA analysis. Although current and force has significant effect on weld strength no influence on the development of the contact resistance was observed. By varying the current ramp rate it was shown that the contact resistance on average is controlled by the value of the current at a given time during the process. By numerical simulation it was shown that the interface temperature was proportional to the value of the current. This indicates that the contact resistance during micro spot welding of foils to a large degree is controlled by the actual interface temperature rather than by factors such as electrode force or heating time. Numerical simulation of the process was investigated with special consideration to the contact conditions. Problems related to downscaling of the process was identified. The relatively low electrode force does not clearly define a contact area, as is the case in large scale resistance spot welding. This results in the simulations being very sensitive to small variations in electrode size and initial contact area.

The micro resistance welding of thin stainless steel 316L wire to a large block was investigated experimentally and numerically. The welding mechanism was detailed and it was found that melting initiated in the bulk of the wire and not at the interface. This was due to hot collapse of the wire projection, resulting in increased cooling of the interface. By choosing the optimal process parameters the nugget was able to grow into the block creating a strong fusion bond and the optimal joint breaking force was found comparable to the case of cross wire welding. Numerical simulation of the process was done with a 2D in-plane analysis. It was found that the mechanical simulation of the experimentally observed collapse was insufficient resulting in excessive heat generation at the interface. By manually increasing the wire to block contact area as well as decreasing electrical contact resistance and increasing the heat conductivity of the block, it was possible to achieve a weld mechanism similar to the experimentally observed. This indicate possible problems in the numerical software regarding simulation of downscaled joints, however, inaccurate values of material parameters could also contribute to the lack of correspondence with experiments. Overall the results indicate that numerical simulation of downscaled joints introduce problems not observed for large scale welding. Especially the relatively small electrode force and the formation of the actual contact area should receive special attention in simulation of micro resistance welding.

In relation to characterising the microstructure of welds of advanced high strength steels DP600 and TRIP700 different etching techniques were investigated. For the base metal of DP600 and TRIP700 the most suitable etch was the Nital and the modified LePera etch, respectively. In the HAZ and weld nugget the Nital etch was found most suitable for both materials. The microstructure of the base material of the TRIP700 steel was found to be much finer than the DP, containing primarily ferrite surrounded by austenite, bainite, and possibly some martensite, while the DP was ferrite surrounded by small areas of martensite. The high cooling rates in spot welding favours diffusionless transformation and in the HAZ and weld nugget the microstructure of both materials were found to consist of mainly lath martensite as well as large irregular grains. These grains are supposedly massive ferrite and hardness measurements confirm that the hardness of these grains is lower than for the lamella martensite. TEM measurements revealed only BCC crystal structure present in the weld nugget confirming the presence of martensite and possibly massive ferrite while precluding the presence of bainite. Due to measurement uncertainty it was not possible to estimate the carbon content from the distortion of the BCC lattice.

The weldability of three sheet spot welding of thin low carbon steel to two thicker high strength steels plates were investigated. Design of experiments and statistical analysis were applied to analyse the effect of changing main process parameters. Although limited fusion bonding of the low carbon steel was observed, the welds showed a significant joint breaking force indicating a strong solid state bond comparable to equivalent fusion bonds. It was shown that by using a larger bottom electrode the maximum joint breaking force could be increased. Numerical modelling of the process was investigated and generally a high degree of agreement with the experimental results were found indicating that numerical simulation may be readily used for simulation of three sheet spot resistance welding of advanced high strength steels.

Predicting strength and fracture modes of resistance welded high strength steels is of great industrial interest and is closely related to the hardness of the final joint. Based on the microstructure characterisation the post weld hardness can be estimated by assuming martensite formation as the primary hardening mechanism. The empirical formulae by Blondeau et al. [127] predicting the martensite hardness based on alloy content was combined with numerical simulation of the austenization region and cooling rate. By utilising a proposed weighting function based on melted volume fraction the post weld hardness of similar and dissimilar material combinations of DP600, TRIP700, and DC06 steels were estimated and showed excellent agreement with experimental measurements.

The modelling of material mechanical and electrical properties has been investigated in relation to simulating resistance welding. It has been shown how the introduction of advanced materials and welding of micro components increase the requirements for the numerical models and the models describing material properties. Several specific problems have been addressed to explore these initiatives, and possible solutions to these problems have been proposed. The problems addressed in this project has been simulated using the existing numerical software SORPAS. Modelling solutions to the problems should in future work be incorporated into the numerical software for testing and verification purposes, as well as for achieving further insight into the process and the numerical issues.

Proposal for Future Work

The results of the present project show that precise modelling of material behaviour is an important aspect of simulation of resistance welding. An accurate description of the physical models become of increasing importance, especially when downscaling the process, as even small variations in the process parameters can have significant impact on the outcome of the process. The contact resistance models were shown to be inadequate to describe the experimentally measured behaviour of the contact resistance. To improve the understanding of the phenomenas governing the contact resistance in resistance welding a more comprehensive study of this field is proposed. Using the Gleeble system the following points would be relevant to investigate:

- The correlation between the test specimen preparation method and its influence on relevant surface properties such as asperity and bulk hardness, white layer, oxide layer, and surface topography.
- Experimental investigation of the influence of the surface properties, pressure, and temperature on the contact resistance for relevant materials.
- Increasing the diameter of the test specimens to obtain more reliable measurements at lower values of the contact pressure relevant for small and micro scale welding. Alternatively dedicated equipment could be necessary for reliable measurements.

The simulation of resistance welding of micro components revealed that the estimation of the actual electrical contact area presented problems due to the low contact pressure compared to normal scale welding. A deeper experimental investigation into the formation of the contact area and the development of advanced numerical algorithms for estimating the contact area for low pressure contacts is proposed for future work.

In predicting post weld strength the modelling of the resulting microstructure is essential. It was shown how simple empirical based models were able to capture post weld hardness for simple two sheet lap joints assuming full martensite formation, with the carbon content being the most influential parameter. In order to be able to predict weld strength in steels that do not form martensite upon cooling, or in other materials such as aluminium or copper, more advanced models are needed which account for more complex phase changes depending on the heating and cooling during welding.

In the automotive industry a large part of the resistance welded joints is the rotational symmetric lap spot weld which can be simulated using 2D rotational symmetry. However, as soon as the geometry no longer can be assumed rotational symmetric it becomes difficult to approximate the problem with an equivalent 2D problem. The design and optimisation of increasingly advanced joints requires that 3D problems can be satisfactory simulated, and the development of numerical code for 3D resistance welding is therefore an area of large potential for both industry and the research community.

References

[1] W. Bernard Carlson. *Innovation as a Social Process: Elihu Thomson and the Rise of General Electric*. Cambridge University Press, 2003. ISBN 0521533120.

[2] Y. Zhou. *Microjoining and nanojoining*. Woodhead Publishing Limited, Cambridge, England, 2008. ISBN 978-1-84569-179-0.

[3] H. Zhang and J. Senkara. *Resistance Welding - Fundamentals and Applications*. Taylor and Francis Group, Florida, USA, 2006. ISBN 0-8493-2346-0.

[4] W. Zhang, H. H. Jensen, and N. Bay. Finite element modeling of spot welding similar and dissimilar metals. In *Seventh International Conference on Computer Technology in Welding*, page 364, 8-11 July 1997 1997.

[5] W. Zhang. Design and implementation of software for resistance welding process simulations. *SAE Publications*, Welding And Joining(SP-1766):105–113, 2003.

[6] N. Bay and W. Zhang. Thermomechanical modelling of resistance welding. In *Proceed. of Int. Conf. on Computational Methods for Coupled Problems in Science and Engineering*, pages 162–165, Ibiza, May 21-23 2007.

[7] J. A. Greenwood. Constriction resistance and the real area of contact. *British Journal of Applied Physics*, 17(12):1621–1632, 1966.

[8] R. Holm. *Electric Contacts*. Springer-Verlag, Berlin/Heidelberg, Germany, 1967.

[9] N. Jonassen. *Elektromagnetisme*. Polyteknisk Forlag, 2004. ISBN 87-502-0771-7.

[10] Q. Song. *Testing and modelling of contact problems in resistance welding*. PhD thesis, Technical University of Denmark, 2003.

[11] S. S. Jensen. *Modstandssvejsning - Strategiske overfladebelaegninger ved pressvejsning af komplekse metalkombinationer*. PhD thesis, Technical University of Denmark, 1994. MM94.40.

[12] R. L. O'Brien. *Welding Handbook - Welding Processes*, volume Volume 2. American Welding Society, Miami, FL, eighth edition edition, 1991.

[13] L. Kristensen. *Projection welding of complex geometries*. PhD thesis, Technical University of Denmark, 2000. MM99.81.

[14] K. P. Bentley, J. A. Greenwood, P. M. Knowlson, and R. G. Baker. Temperature distributions in spot welds. *British Welding Journal*, 10(12):613–619, 1963.

[15] H. S. Cho and Y. J. Cho. Study of the thermal behavior in resistance spot welds. *Welding Journal (Miami, Fla)*, 68(6):236s–244s, 1989.

[16] H. A. Nied. Finite element modeling of the resistance spot welding process. In *14th International AWS-WRC Brazing and Soldering Conference*, pages 171–173. AWS, 1983.

[17] W. Rice and E. J. Funk. Analytical investigation of temperature distributions during resistance welding. *Welding Journal*, 46(4):175–s, 1967.

[18] S. D. Sheppard. Thermal and mechanical simulations of resistance spot welding. *Welding Research Council Bulletin*, (356):34–41, 1990.

[19] X. Sun and P. Dong. Analysis of aluminum resistance spot welding processes using coupled finite element procedures. *Welding Journal (Miami, Fla)*, 79 (8):215s–221s, 2000.

[20] X. Sun. Modeling of projection welding processes using coupled finite element analyses. *Welding Journal (Miami, Fla)*, 79(9):244–s, 2000.

[21] E. Feulvarch, V. Robin, and J. M. Bergheau. Resistance spot welding simulation: a general finite element formulation of electrothermal contact conditions. *Journal of Materials Processing Tech.*, 153-154:436–441, 2004.

[22] B. H. Chang, Y. Zhou, I. Lum, and D. Du. Finite element analysis of effect of electrode pitting in resistance spot welding of aluminium alloy. *Science and Technology of Welding and Joining*, 10(1):61–66, 2005.

[23] Z. Hou, Ill-Soo Kim, Y. Wang, C. Li, and C. Chen. Finite element analysis for the mechanical features of resistance spot welding process. *Journal of Materials Processing Tech.*, 185(1-3):160–165, 2007.

[24] F. J. Studer. Contact resistance in spot welding. *Welding Journal (New York)*, 18(10):374–s, 1939.

[25] M. Vogler and S. Sheppard. Electrical contact resistance under high loads and elevated temperatures. *Welding Journal - Including Welding Research Supplement*, 72(6):231, 1993.

[26] S. S. Babu, M. L. Santella, Z. Feng, B. W. Riemer, and J. W. Cohron. Empirical model of effects of pressure and temperature on electrical contact resistance of metals. *Science and Technology of Welding and Joining*, 6(3): 126–132, 2001.

[27] P. Rogeon, P. Carre, J. Costa, G. Sibilia, and G. Saindrenan. Characterization of electrical contact conditions in spot welding assemblies. *Journal of Materials Processing Tech.*, 195(1-3):117–124, 2008.

[28] Q. Song. An experimental study determines the electrical contact resistance in resistance welding. *Welding Journal - Including Welding Research Supplement*, 84(5):73S, 2005.

[29] Dynamic Systems Inc. http://www.gleeble.com, 27 Nov. 2009.

[30] M. Merklein, J. Lecher, V. Godel, S. Bruschi, A. Ghiotti, and A. Turetta. Mechanical properties and plastic anisotropy of the quenchenable high strength steel 22mnb5 at elevated temperatures. *Key Engineering Materials*, 344: 79–86, 2007.

[31] Q. Guo, H. G. Yan, Z. H. Chen, and H. Zhang. Elevated temperature compression behaviour of mg-al-zn alloys. *Materials Science and Technology*, 22 (6):725–729, 2006.

[32] A. Turetta, S. Bruschi, and A. Ghiotti. Investigation of 22mnb5 formability in hot stamping operations. *Journal of Materials Processing Tech.*, 177(1-3): 396–400, 2006.

[33] Y. Zhou, S. J. Dong, and K. J. Ely. Weldability of thin sheet metals by small-scale resistance spot welding using high-frequency inverter and capacitor-discharge power supplies. *Journal of Electronic Materials*, 30(8):1012–1020, 2001.

[34] K. J. Ely and Y. Zhou. Microresistance spot welding of kovar, steel, and nickel. *Science and Technology of Welding and Joining*, 6(2):63–72, 2001.

[35] W. Tan, Y. Zhou, H. W. Kerr, and S. Lawson. A study of dynamic resistance during small scale resistance spot welding of thin ni sheets. *Journal of Physics D: Applied Physics*, 37(14):1998–2008, 2004.

[36] S. Fukumoto and Y. Zhou. Mechanism of resistance microwelding of crossed fine nickel wires. *Metallurgical and Materials Transactions A (Physical Metallurgy and Materials Science)*, 35A(10):3165–3176, 2004.

[37] S. Fukumoto, Z. Chen, and Y. Zhou. Interfacial phenomena and joint strength in resistance microwelding of crossed au-plated ni wires. *Metallurgical and Materials Transactions A*, 36A(10):2717–2724, 2005.

[38] W. Tan, S. Lawson, and Y. Zhou. Effects of au plating on dynamic resistance during small- scale resistance spot welding of thin ni sheets. *Metallurgical and Materials Transactions A*, 36A(7):1901–1910, 2005.

[39] Z. Chen and Y. Zhou. Joint formation mechanism and strength in resistance microwelding of 316l stainless steel to pt wire. *Journal of Materials Science*, 42(23), Dec 2007.

[40] M. I. Khan, J. M. Kim, M. L. Kuntz, and Y. Zhou. Bonding mechanisms in resistance microwelding of 316 low-carbon vacuum melted stainless steel wires. *Metallurgical and Materials Transactions A-Physical Metallurgy and Materials Science*, 40A(4):910–919, APR 2009.

[41] ISO10447. Resistance welding - peel and chisel testing of resistance spot and projection welds. *International Standard*, 2006.

[42] ISO14323. Resistance spot welding and projection welds - specimen dimensions and procedure for impact shear test and cross-tension testing. *International Standard*, 2006.

[43] ISO14324. Resistance spot welding - method for the fatigue testing of spot welded joints. *International Standard*, 2003.

[44] S. Donders, M. Brughmans, L. Hermans, and N. Tzannetakis. The effect of spot weld failure on dynamic vehicle performance. *Sound and Vibration*, 39 (4):16–25, 2005.

[45] N. Uijl and S. Smith. Resistance spot welding of advanced high strength steel for the automotive industry. In *4th International Seminar on Advances in Resistance Welding*, pages 30–62, 2006.

[46] M. Marya, K. Wang, L. G. Hector J., and X. Gayden. Tensile-shear forces and fracture modes in single and multiple weld specimens in dual-phase steels. *Transactions of the ASME.Journal of Manufacturing Science and Engineering*, 128(1):287–298, 2006.

[47] J. E. Gould, S. P. Khurana, and T. Li. Predictions of microstructures when welding automotive advanced high-strength steels. *Welding Journal*, 85(5): 111S–116S, MAY 2006.

[48] V. H. Baltazar Hernandez, M. L. Kuntz, M. I. Khan, and Y. Zhou. Influence of microstructure and weld size on the mechanical behaviour of dissimilar ahss resistance spot welds. *Science and Technology of Welding and Joining*, 13(8):769–776, NOV 2008.

[49] M. I. Khan, M. L. Kuntz, and Y. Zhou. Effects of weld microstructure on static and impact performance of resistance spot welded joints in advanced high strength steels. *Science and Technology of Welding and Joining*, 13(1): 49–59, JAN 2008.

[50] M. I. Khan, M. L. Kuntz, E. Biro, and Y. Zhou. Microstructure and mechanical properties of resistance spot welded advanced high strength steels. *Materials Transactions*, 49(7):1629–1637, 2008.

[51] D. J. VandenBossche. Ultimate strength and failure mode of spot welds in high strength steels. *SAE Publications*, February 1977. Document: 770214.

[52] J. Danckert. Yield criteria and flow rule for anisotropic materials. Technical Report JEP-1925-92/2, Technical University of Denmark, 1989. TEMPUS-Project.

[53] S. Kalpakjian and S. R. Schmid. *Manufacturing Processes for Engineering Materials*. Pearson Education, Inc., USA, 2003. ISBN 0-13-045373-0.

[54] S. Giversen. Material properties and contact resistance in resistance welding, 2009. M.Sc. thesis, Dept. of Mech. Eng., Tech. Uni. of Denmark.

[55] W. D. Callister. *Materials Science and Engineering - An Introduction*. Wiley, USA, 2003. ISBN 0-471-22471-5.

[56] E. Doege, H. Meyer-Nolkemper, and I. Saeed. *Fliesskurvenatlas Metallischer Werkstoffe*. Hanser Verlag, München, 1986.

[57] A. H. Cottrell and B. A. Bilby. Dislocation theory of yielding and strain ageing of iron. *Proceedings of the Physical Society.Section A*, 62(1):49–62, 1949.

[58] B. J. Brindley and J. T. Barnby. Dynamic strain ageing in mild steel. *Acta Metallurgica*, 14(12):1765–1780, 1966.

[59] H. J. Kleemola and M. A. Nieminen. On the strain-hardening parameters of metals. *Metallurgical Transactions A (Physical Metallurgy and Materials Science)*, 5(8):1863–1866, 1974.

[60] H. D. Young and R. A. Freedman. *University Physics - with Modern Physics*. Pearson Education Inc., 2004. ISBN 0-321-20469-7.

[61] W. H. Hayt and J. A. Buck. *Engineering electromagnetics*. McGraw-Hill Higher Education, 2006. ISBN 0073104639.

[62] F. E. Terman. *Radio engineers handbook*. McGraw-Hill, 1950.

[63] Inc Automation Creations. Matweb - material property data, 2010. http://www.matweb.com.

[64] J. R. Davis. *SM Speciality Handbook: Stainless Steels*. ASM International, Jan. 1994. ISBN 0-87170-503-6.

[65] Speciality Metals. Datasheet nickel 200 and nickel 201, 2010. http://www.specialmetals.com/index.php.

[66] G. Elert. Hypertextbook - the physics factbook - resistivity of aluminum, February 2010. http://hypertextbook.com/facts/2004/ValPolyakov.shtml.

[67] D. A. Porter and K. E. Easterling. *Phase Transformations in Metals and Alloys*. Taylor and Francis, 1992.

[68] R. S. Timsit. Electrical contact resistance: properties of stationary interfaces. *IEEE Transactions on Components and Packaging Technologies*, 22(1):85–98, 1999.

[69] J. G. Kaiser, G. J. Dunn, and T. W. Eagar. Effect off electrical resistance on nugget formation during spot welding. *Welding Journal (Miami, Fla)*, 61 (6):167. s–174. s, 1982.

[70] Z. Weimin. The electrical contact resistance in resistance welding evaluated by gleeble testing machine. *Materials Science Forum*, 575-578 PART 2:753–756, 2008.

[71] F. P. Bowden and D. Tabor. *The friction and lubrication of solids*. University Press, Oxford, 1950.

[72] T. Wanheim, N. Bay, and A. S. Petersen. A theoretically determined model for friction in metal working processes. *Wear*, 28(2):251–258, 1974.

[73] W. R. D. Wilson and S. Sheu. Real area of contact and boundary friction in metal forming. *International Journal of Mechanical Sciences*, 30(7):475–489, 1988.

[74] M. P. F. Sutcliffe. Surface asperity deformation in metal forming processes. *International Journal of Mechanical Sciences*, 30(11):847–868, 1988.

[75] M. Braunovic, V. V. Konchits, and K. N. Myshkin. *Electrical Contacts: fundamentals, applications and technology*. Taylor and Francis, Florida, 2007. ISBN 1-57444-727-0.

[76] M. Nakamura and I. Minowa. Computer simulation for the conductance of a contact interface. *IEEE Transactions on Components, Hybrids, and Manufacturing Technology*, 9(2):150–155, 1986.

[77] M. Nakamura and I. Minowa. Film resistance and constriction effect of current in a contact interface. *IEEE transactions on components, hybrids, and manufacturing technology*, 12(1):109–113, 1989.

[78] M. Nakamura, I. Minowa, and M. Kanno. Computer simulation for the conductance of a contact interface. ii. *IEEE Transactions on Components, Hybrids, and Manufacturing Technology*, 11(3):324–327, 1988.

[79] I. Minowa, M. Nakamura, and M. Kanno. Conductance of a contact interface depending on the location and distribution of conducting spots. In *Proceedings of Electrical Conference on Contacts, Electromechanical Components and Their Applications*, pages 19–25, 1986.

[80] M. Geiger, M. Kleiner, R. Eckstein, N. Tiesler, and U. Engel. Microforming. *CIRP Annals - Manufacturing Technology*, 50(2):445–462, 2001.

[81] C. Sommer and S. Sommer. *Complete EDM Handbook*. Advance Publishing, 2005. ISBN 978-1575373027.

[82] E. Feulvarch, P. Rogeon, P. Carre, G. Sibilia, and J. M Bergheau. Modeling of spot welding: definition of the interfacial contact conditions and experimental validation. *Mecanique and Industries*, 7(3):251–263, 2006.

[83] P. S. James, H. W. Chandler, J. T. Evans, J. Wen, D. J. Browne, and C. J. Newton. The effect of mechanical loading on the contact resistance of coated aluminium. *Materials Science and Engineering: A*, 230(1-2):194–201, 1997.

[84] E. Bardal. *Korrosjon og korrosjonsvern*. Tapir Akademisk Forlag, Trondheim, 2001.

[85] F. P. Bowden and J. B. P. Williamson. Electrical conduction in solids .1. influence of the passage of current on the contact between solids. *Proceedings of the Royal Society of London Series A-Mathematical and Physical Sciences*, 246(1244):1, 1958.

[86] Z. Luo, J. Wang, P. Shan, Z. Gao, and F. Zou. Asymmetric laplace law for distribution of aluminum contact resistance in spot welding. *China Welding (English Edition)*, 16(2):66–71, 2007.

[87] M. Zhang, L. Li, R. Y. Fu, D. Krizan, and B. C. De Cooman. Continuous cooling transformation diagrams and properties of micro-alloyed trip steels. *Materials Science and Engineering A*, 438-440:296–299, 2006.

[88] D. C. Montgomery. *Design and Analysis of Experiments*. John Wiley and Sons, United States of America, 2005. ISBN 0-471-48735-X.

[89] Y. Shmaliy. *Continuous-time signals*. Springer, Netherlands, 2006. ISBN 1402048173.

[90] B. Sighvatsson. Resistance welding of small scale components. Technical report, Technical University of Denmark, 2006. M.Sc. Thesis: MM06.18.

[91] American Welding Society. *Resistance Welding Manual*. Resistance Welder Manufacturers Association, USA, 1989.

[92] S. Fukumoto, T. Matsuo, D. Kuroda, and H. Tsubakino. Micro-resistance spot welding of nickel free austenitic stainless steel, 2007.

[93] S. Fukumoto, K. Fujiwara, S. Toji, and A. Yamamoto. Small-scale resistance spot welding of austenitic stainless steels. *Materials Science and Engineering A-Structural Materials Properties Microstructure and Processing*, 492(1-2): 243–249, SEP 25 2008.

[94] B. H. Chang and Y. Zhou. Numerical study on the effect of electrode force in small-scale resistance spot welding. *Journal of Materials Processing Technology*, 139(1-3):635–641, 2003.

[95] S. Fukumoto, H. Tsubakino, and Y. Zhou. Heat input and deformation control in resistance micro-welding of fine nickel wires. *Welding International*, 20(9):692–697, 2006.

[96] K. Tsuchiya, H. Kawamura, and G. Kalinin. Re-weldability tests of irradiated austenitic stainless steel by a tig welding method. *Journal of Nuclear Materials*, 283-287:1210–1214, 2000.

[97] A. K. De, J. G. Speer, and D. K. Matlock. Color tint-etching for multiphase steels. *Advanced Materials and Processes*, 161(2):27–30, 2003.

[98] A. K. Sinha. *Physical Metallurgy Handbook*. McGraw-Hill, 2003.

[99] L. Cheng. *Phase Transformations in Iron-based interstitial martensite*. PhD thesis, Technische Universiteit Delft, 1990.

[100] University of Cambridge Dept. of Materials Science. Homepage, July 2009. http://www.msm.cam.ac.uk/.

[101] Fateh Fazeli, Fateh Fazeli, and Xiang Wang. Some microstructural aspects of bainite in high-carbon si-mn steels. *ISIJ International*, 47(9):1341–1350, 2007.

[102] I. Madariaga, I. Gutierrez, and H. K. D. H. Bhadeshia. Acicular ferrite morphologies in a medium-carbon microalloyed steel. *Metallurgical and Materials Transactions A (Physical Metallurgy and Materials Science)*, 32A(9): 2187–2197, 2001.

[103] S. Das, A. Ghosh, S. Chatterjee, and P. R. Rao. Microstructural characterization of controlled forged hsla-80 steel by transmission electron microscopy. *Materials Characterization*, 50(4-5):305–315, 2003.

[104] P. J. Goodhew. *Electron Microscopy and Analysis*. Taylor and Francis, 2001.

[105] G. R. Speich, V. A. Demarest, and R. L. Miller. Formation of austenite during intercritical annealing of dual-phase steels. *Metallurgical Transactions A (Physical Metallurgy and Materials Science)*, 12A(8):1419–1428, 1981.

[106] E. Girault, P. Jacques, Ph Harlet, K. Mols, J. Van Humbeeck, E. Aernoudt, and F. Delannay. Metallographic methods for revealing the multiphase microstructure of trip-assisted steels. *Materials Characterization*, 40(2):111–118, 1998.

[107] S. Zaefferer, J. Ohlert, and W. Bleck. A study of microstructure, transformation mechanisms and correlation between microstructure and mechanical properties of a low alloyed trip steel. *Acta Materialia*, 52(9):2765–2778, 2004.

[108] P. J. Jacques. Transformation-induced plasticity for high strength formable steels. *Current Opinion in Solid State and Materials Science*, 8(3-4):259–265, 2004.

[109] A. Harthoej and K. R. Pedersen. Analyse og modellering af mikrostruktur og haardhed i staal ved modstandssvejsning. Technical report, Technical University of Denmark, 2008. B.Sc. Thesis.

[110] S. Oliver, T. B. Jones, and G. Fourlaris. Dual phase versus trip strip steels: comparison of dynamic properties for automotive crash performance. *Materials Science and Technology*, 23(4):423–431, 2007.

[111] T. Lyman. *Metals Handbook*. American Society for Metals, 1972.

[112] F. S. LePera. Improved etching technique to emphasize martensite and bainite in high-strength dual-phase steel. *Journal of Metals*, 32(3):38–39, 1980.

[113] P. H. Jouneau and P. Stadelmann. Ems-online, electron microscopy image simulation, August 1998. Centre Interdepartemental de Microscopie Electronique, EPFL, Lausanne, http://cecm.insa-lyon.fr/CIOL/.

[114] J. M. Zou and J. C. Mabon. Web-based electron microscopy application software: Web-emaps, 2004. Microsc Microanal 10(Suppl 2), University of Illinois, USA, http://emaps.mrl.uiuc.edu/.

[115] A. Kumar, S. B. Singh, and K. K. Ray. Influence of bainite/martensite-content on the tensile properties of low carbon dual-phase steels. *Materials Science and Engineering A*, 474(1-2):270–282, 2008.

[116] K. Poorhaydari, B. M. Patchett, and D. G. Ivey. Transformation twins in the weld haz of a low-carbon high-strength microalloyed steel. *Materials Science and Engineering A*, 435-436:371–382, 2006.

[117] R. Grange, C. Hribal, and L. Porter. Hardness of tempered martensite in carbon and low-alloy steels. *Metallurgical and Materials Transactions A*, 8(11): 1775–1785, 11/01 1977. URL `http://dx.doi.org/10.1007/BF02646882`. M3: 10.1007/BF02646882.

[118] H. F. Lan, W. J. Liu, H. F. Lan, and X. H. Liu. Ultrafine ferrite grains produced by tempering cold-rolled martensite in low carbon and microalloyed steels. *ISIJ International*, 47(11):1652–1657, 2007.

[119] M. X Zhang and P. M. Kelly. Crystallography of carbide-free bainite in a hard bainitic steel. *Materials Science and Engineering A*, 438-440:272–275, 2006.

[120] N. K. Babu, M. R. Suresh, P. P. Sinha, and D. S. Sarma. Effect of austenitizing temperature and cooling rate on the structure and properties of a ultra-high strength low alloy steel. *Journal of Materials Science*, 41(10):2971–2980, 2006.

[121] S. K. Dhua, D. Mukerjee, and D. S. Sarma. Weldability and microstructural aspects of shielded metal arc welded hsla-100 steel plates. *ISIJ International*, 42(3):290–298, 2002.

[122] K. R. Pedersen, A. Harthoej, K. L. Friis, N. Bay, Marcel A. J. Somers, and W. Zhang. Microstructure and hardness distribution of resistance welded advanced high strength steels. In *The 5th International Seminar on Advances in Resistance Welding*, 24-26 September 2008.

[123] Cs Orosz, B. Palotas, and J. Dobranszky. Welding investigations of modern high strength dual phase and trip-steel for automotive industry application. *Materials Science Forum*, 537-538:431–438, 2007.

[124] C. Ma, D. L. Chen, S. D. Bhole, G. Boudreau, A. Lee, and E. Biro. Microstructure and fracture characteristics of spot-welded dp600 steel. *Materials Science and Engineering A*, 485(1-2):334–346, 2008.

[125] M. Marya, M. Marya, and X. Q. Gayden. Development of requirements for resistance spot welding dual-phase (dp600) steels part 1 - the causes of interfacial fracture. *Welding Journal (Miami, Fla)*, 84(11):172–s, 2005.

[126] J. E. Gould, S. P. Khurana, and T. Li. Numerical microstructural analysis of automotive-grade steels when joined with an array of welding processes. volume 712, page 1236, 2004. ISBN 0094243x.

[127] R. Blondeau, Ph Maynier, and J. Dollet. Prediction of the hardness and strength of plain and low-alloy steels from their structure and composition. *Memoires Scientifiques de la Revue de Metallurgie*, 70(12):883–892, 1973.

[128] K. W. Andrews. Empirical formulae for calculation of some transformation temperatures. *Iron and Steel Institute – Journal*, 203:721–727, 1965.

[129] American Iron and Steel Institute. The steel industry technology roadmap for automotive. Technical report, Southfield, USA, 2008.

[130] K. L. Nielsen. 3d modelling of plug failure in resistance spot welded shear-lab specimens (dp600-steel). *International Journal of Fracture*, 153(2):125–139, 2008.

Appendices

Appendix A
Contact Resistance

A.1 Nickel 200

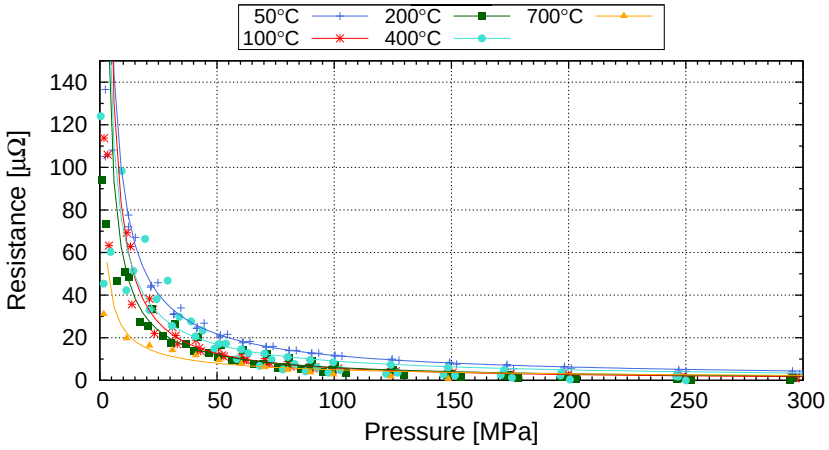

Figure A.1: Measured contact resistance for turned Nickel 200 specimens

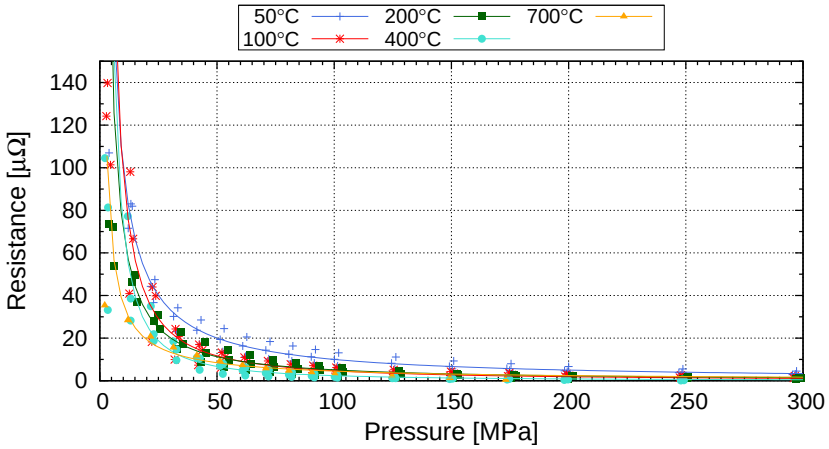

Figure A.2: Measured contact resistance for EDM cut Nickel 200 specimens

A.2 Stainless steel AISI 316L

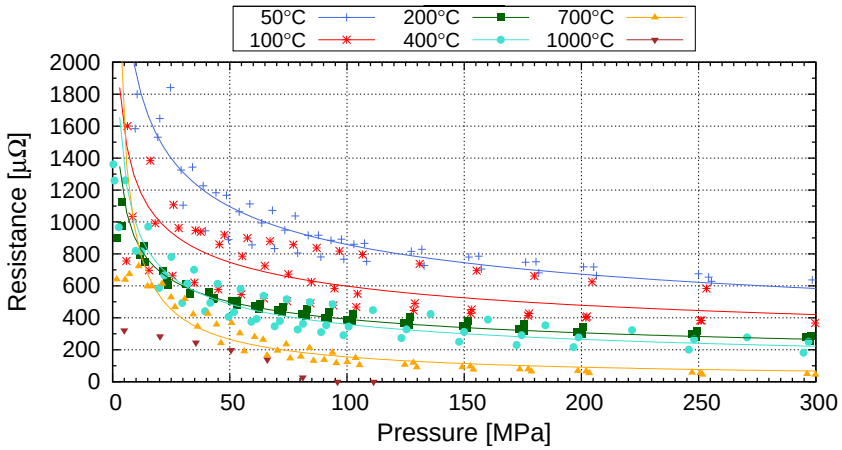

Figure A.3: Measured contact resistance for turned stainless steel 316 specimens

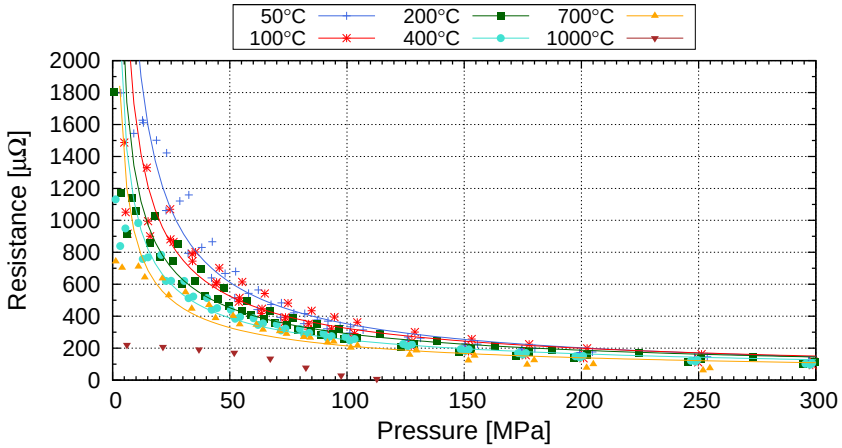

Figure A.4: Measured contact resistance for EDM cut stainless steel 316 specimens

A.3 Aluminium 6060 T6

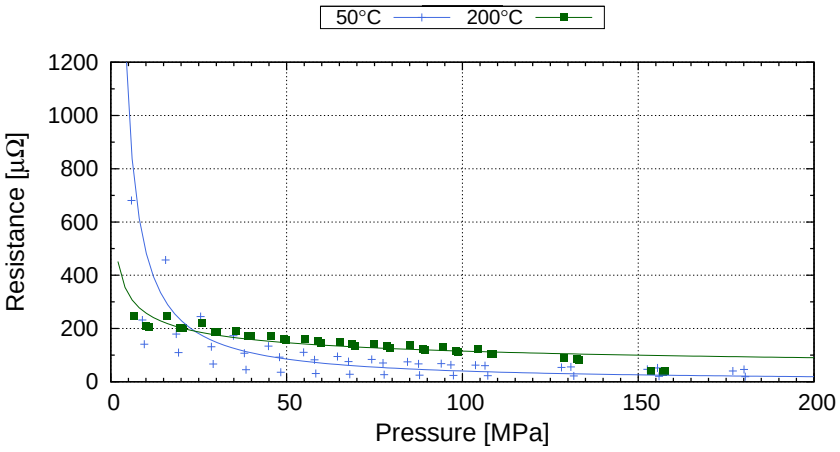

Figure A.5: Measured contact resistance for turned aluminium 6060 specimens

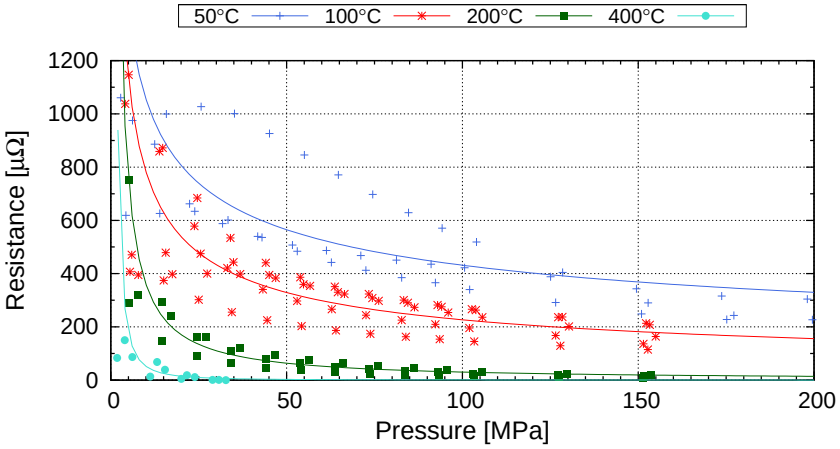

Figure A.6: Measured contact resistance for EDM cut aluminium 6060 specimens

A.4 Mild steel S235JR

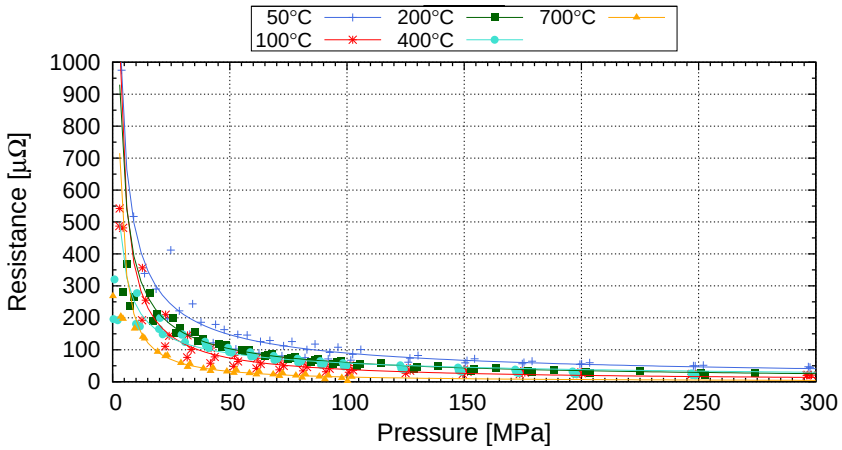

Figure A.7: Measured contact resistance for turned steel S235JR specimens

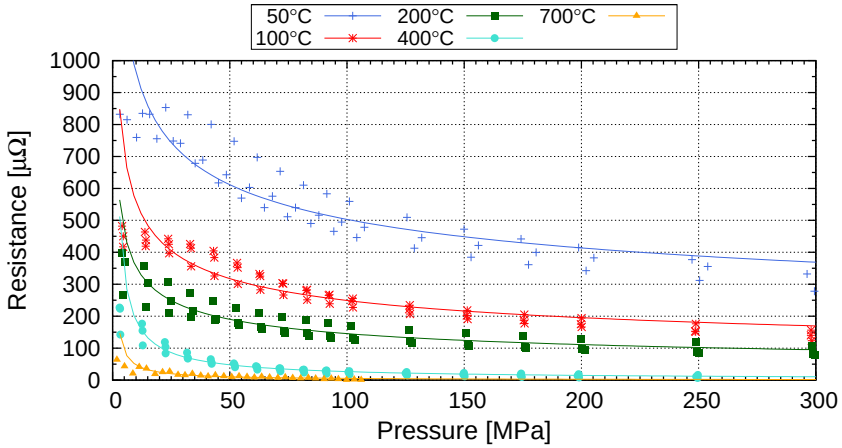

Figure A.8: Measured contact resistance for EDM cut steel S235JR specimens

A.5 Fitting Parameters

Table A.1: Fitting parameters and estimated parameter standard errors

Material	Temperature	C	n	C_{err}	n_{err}
Ni200	50	720	-0.89	27.9	0.012
Turned	100	948	-1.10	127.5	0.045
	200	518	-0.96	66.7	0.042
	400	533	-0.88	135.6	0.078
	700	109	-0.66	30.0	0.084
Ni200	50	1004	-1.00	101.1	0.032
EDM	100	2021	-1.32	604.1	0.103
	200	987	-1.14	142.9	0.046
	400	2224	-1.48	776.5	0.126
	700	286	-0.90	61.5	0.069
SS316	50	4944	-0.38	315.9	0.015
Turned	100	2631	-0.32	320.9	0.028
	200	1994	-0.35	63.5	0.008
	400	2689	-0.44	252.2	0.023
	700	5355	-0.77	599.6	0.033
	1000	2900	-0.75	2917.7	0.290
SS316	50	13916	-0.80	1080.0	0.023
EDM	100	8082	-0.70	722.3	0.025
	200	5480	-0.64	400.2	0.020
	400	4423	-0.62	230.7	0.014
	700	3643	-0.61	445.6	0.034
	1000	2525	-0.77	2279.3	0.250
Al6060	50	5885	-1.08	2518.3	0.128
Turned	200	578	-0.35	71.5	0.033
Al6060	50	2583	-0.39	503.3	0.050
EDM	100	2705	-0.54	480.2	0.049
	200	4284	-1.08	1239.3	0.091
	400	3358	-1.81	6922.3	0.778
S235	50	3206	-0.73	117.5	0.049
Turned	100	4170	-0.98	254.6	0.060
	200	2948	-0.81	141.2	0.024
	400	1327	-0.64	83.7	0.032
	700	4535	-1.15	259.0	0.034
S235	50	1842	-0.28	136.7	0.018
EDM	100	1250	-0.35	87.8	0.018
	200	867	-0.39	86.6	0.025
	400	1306	-0.84	151.7	0.036
	700	416	-0.94	75.4	0.058

Appendix B
Dynamic Contact Resistance in MRSW

B.1 Experimental Weld Results

[Extension] = mm

[JBF] = N

[Nugget diameter] = mm

F	I	A	Extension			Max JBF			Nugget diameter		
-1	-1	-1	0.30	0.16	0.33	205	105	210	0.82	0.72	0.78
1	-1	-1	0.12	0.37	0.09	124	213	78	0.71	0.82	0.53
-1	1	-1	0.58	0.58	0.47	375	365	228	0.96	1.06	0.81
1	1	-1	0.53	0.53	0.61	362	335	347	0.90	0.90	0.96
-1	-1	1	0.29	0.40	0.38	218	230	198	0.77	0.80	0.75
1	-1	1	0.16	0.12	0.09	172	109	98	0.78	0.70	0.62
-1	1	1	0.72	0.63	0.70	359	357	364	1.07	0.98	1.08
1	1	1	0.54	0.62	0.59	342	374	342	1.02	1.15	0.95

F	I	A	IF.			Splash		
-1	-1	-1	1	1	1	1	0	1
1	-1	-1	1	1	1	0	1	0
-1	1	-1	0	0	1	1	1	1
1	1	-1	0	0	0	1	1	1
-1	-1	1	1	1	1	1	1	1
1	-1	1	1	1	1	0	0	0
-1	1	1	0	0	0	1	1	1
1	1	1	0	0	0	1	0	1

Table B.1: Weld results for experimental series of SS316 showing: Factor combination; Extension at JBF; Max JBF; Estimated nugget diameter; IF - Interface Failure (1=true,0=false); Observed Splash (1=true,0=false)

F	I	A	Extension			Max JBF			Nugget diameter		
-1	-1	-1	0.10	0.00	0.12	93	0	66	0.52	0.00	0.44
1	-1	-1	0.00	0.00	0.00	0	0	0	0.00	0.00	0.00
-1	1	-1	0.67	0.58	0.64	240	235	255	1.03	1.09	1.08
1	1	-1	0.28	0.14	0.10	121	119	94	0.74	0.46	0.45
-1	-1	1	0.08	0.13	0.44	83	109	169	0.25	0.40	0.95
1	-1	1	0.04	0.04	0.00	79	45	0	0.00	0.00	0.00
-1	1	1	0.52	0.58	0.59	220	224	224	0.95	0.99	0.96
1	1	1	0.22	0.17	0.22	132	136	130	0.62	0.55	0.69

F	I	A	IF.			Splash		
-1	-1	-1	1	1	1	0	0	0
1	-1	-1	1	1	1	0	0	0
-1	1	-1	0	0	0	1	0	0
1	1	-1	1	1	1	0	0	0
-1	-1	1	1	1	1	0	0	1
1	-1	1	1	1	1	0	0	0
-1	1	1	0	0	0	0	1	1
1	1	1	1	1	1	0	0	0

Table B.2: Weld results for experimental series of Ni200 showing: Factor combination; Extension at JBF; Max JBF; Estimated nugget diameter; IF - Interface Failure (1=true,0=false); Observed Splash (1=true,0=false)

Appendix C
Micro Welding Wire to Block

C.1 Simulated Temperature Profile

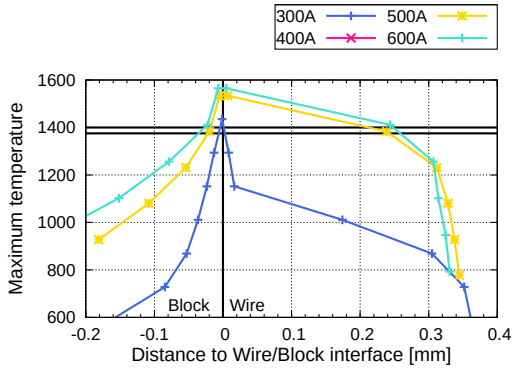

(a) $F = 1.5\text{kp}$, $W_c = 0.01\text{mm}$

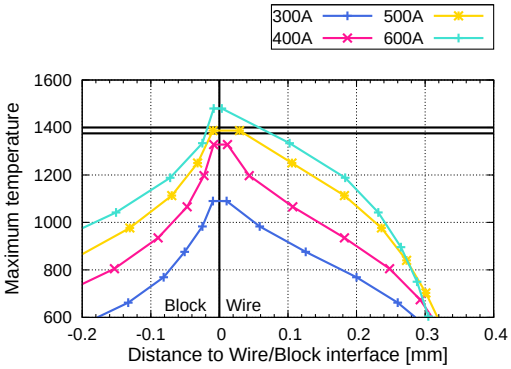

(b) $F = 5\text{kp}$, $W_c = 0.01\text{mm}$

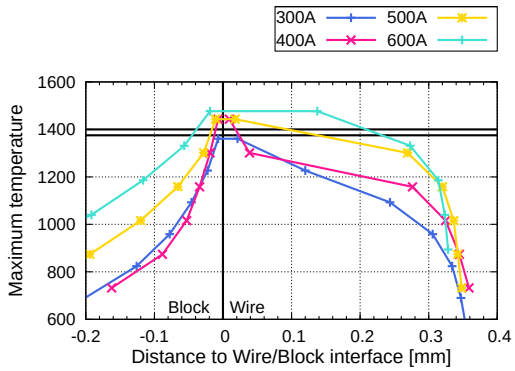

(c) $F = 1.5\text{kp}$, $W_c = 0.07\text{mm}$

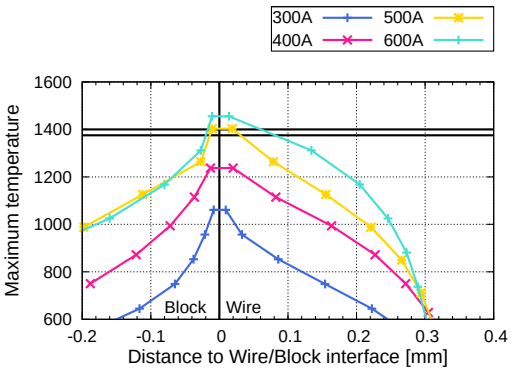

(d) $F = 5\text{kp}$, $W_c = 0.07\text{mm}$

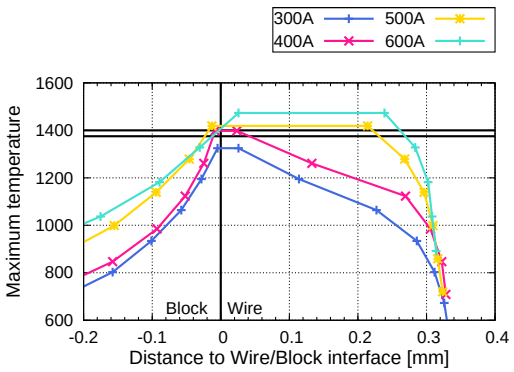

(e) $F = 1.5\text{kp}$, $W_c = 0.15\text{mm}$

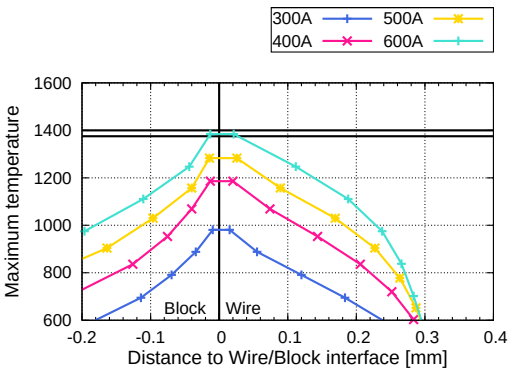

(f) $F = 5\text{kp}$, $W_c = 0.15\text{mm}$

Appendix D
Characterize AHSS

D.1 Recipies of Etchants

Nital [111]
2ml HNO_3 98ml ethanol

SMB [110, 111]
10g SMB 90ml water SMB solutions must be freshly prepared before use.

Modified LePera [110]
Part 1: 4% picral with few drops HCl (1ml per 100 ml) Part 2: 10% aqueous solution of SMB Method: 12-15 sec. in Part 1 and 5 sec. in Part 2.

D.2 Results of Diffraction Measurements

No.	a	Zone Axis	Calculation of λL				Calc. c (1. spot)			Calc. c (2. spot)		
			Spot	Indices		λL	Spot	Indices	c	Spot	Indices	c
	[nm]		*[px]*	*h k l*		*[px*nm]*	*[px]*	*h k l*	*[nm]*	*[px]*	*h k l*	*[nm]*
1	0.2866	111	332	1 1 0		67.36	339	0 1 1	0.27575	339	1 0 1	0.27575
2	0.2866	101	488	2 0 0		69.93	339	0 1 1	0.29715	594	2 1 1	0.29776
3	0.2866	102	489	0 2 0		70.07	592	1 1 2	0.29166	592	1 1 2	0.29166
4	0.2866	111	340	1 1 0		69.00	336	1 0 1	0.29418	334	1 0 1	0.29806
5	0.2866	313	343	1 1 0		69.51	750	0 1 3	0.29383	750	0 1 3	0.29383
6	0.2866	101	339	1 1 0		68.70	470	0 0 2	0.29234	580	1 1 2	0.29196
7	0.2866	111	333	1 1 0		67.57	338	0 1 1	0.27895	338	0 1 1	0.27895
8	0.2866	313	760	1 3 0		68.87	334	1 0 1	0.29652	894	1 3 2	0.29248
9	0.2866	53-1	761	1 3 0		68.97	579	1 2 1	0.32270	587	2 1 1	0.29407

D.3 Comparison of Means of Hardness Measurements in DP-DP

Student One-Sided t-test with Unequal Variances

The test compares two means to see if they are equal or not Montgomery [88]. The test requires that the variation can be assumed to follow a normal distribution, which in most cases is a reasonably assumption. The results of the t-tests are shown in table D.1. The t_0 value is the *test statistic* which together with the relevant t-distribution determined from the calculated degrees of freedom (DOF) gives the *P-value*. The p-value (the Power) of the test is the probability that the two compared means are equal and comes from the same normal distribution. Thus a low p-value implies a high probability that the two means *do* differ. The results show that the hardness of the B and D areas in the nugget both clearly differ from the F phase in the base material (pairs: F-B and F-D). Comparing B and D (pair: B-D) show that the hardness in the two areas is different with a probability of 99% in both load cases. Normally a 95% confidence level is assumed adequate to conclude a significant difference between the means, and so the test shows a significant difference in hardness between the bright and dark areas of the microstructure in the nugget.

Table D.1: One-sided students t-test on the mean hardness of the areas in DP-DP

Load	Pairs	t_0	v (DOF)	P-value
5g	F - B	37.9	4.1	0.000
	F - D	58.8	4.2	0.000
	B - D	2.9	7.2	0.011
25g	F - B	20.3	8.0	0.000
	F - D	28.6	5.9	0.000
	B - D	3.2	5.9	0.013

Appendix E
Three Sheet Spot Welding of AHSS

Table E.1: Example on iteration scheme for dropping factors (2.5% significance level)

	Iteration 1			Iteration 2			Iteration 3		
Factor	**DF**	**MS**	**P**	**DF**	**MS**	**P**	**DF**	**MS**	**P**
B	1	228711.1	0.07%	1	228711.1	0.00%	1	228711.1	0.00%
F	1	13286.6	1.13%	1	13286.6	2.88%	-	-	-
T	1	5413.3	2.70%	-	-	-	-	-	-
I	1	1178.9	10.86%	-	-	-	-	-	-
BF	1	32052.6	0.47%	1	32052.6	0.25%	1	32052.6	1.07%
BT	1	48719.5	0.31%	1	48719.5	0.05%	1	48719.5	0.28%
BI	1	10610	1.41%	1	10610	4.62%	-	-	-
FT	1	4066	3.55%	-	-	-	-	-	-
FI	1	1178.9	10.86%	-	-	-	-	-	-
TI	1	2652.5	5.29%	-	-	-	-	-	-
BFT	1	5413.3	2.70%	-	-	-	-	-	-
BFI	1	216.5	35.55%	-	-	-	-	-	-
FTI	1	1353.3	9.66%	-	-	-	-	-	-
BFTI	1	1353.3	9.66%	-	-	-	-	-	-
Pure Err.	2	152.4		2	152.4		2	152.4	
Lack of fit	4	8336.5		9	2536.2		11	4248.5	
Residual	6	8488.9		11	2102.8		13	3617.5	